University of California
Los Angeles

Longitudinal Spin Transfer to Λ and $\bar{\Lambda}$ Hyperons Produced in Polarized Proton-Proton Collisions at $\sqrt{s} = 200$ GeV

A dissertation submitted in partial satisfaction
of the requirements for the degree
Doctor of Philosophy in Physics

by

Ramon Cendejas

2012

Abstract of the Dissertation

Longitudinal Spin Transfer to Λ and $\bar{\Lambda}$ Hyperons Produced in Polarized Proton-Proton Collisions at $\sqrt{s} = 200$ GeV

by

Ramon Cendejas

Doctor of Philosophy in Physics

University of California, Los Angeles, 2012

Professor Huan Z. Huang, Chair

Studies on the spin structure of the proton have been an active area of research; after the EMC experiment and subsequent experiments found that only about 30% of the total proton spin is carried by quark spins. The Relativistic Heavy Ion Collider (RHIC) is the world's first and only polarized proton collider. The Solenoidal Tracker At RHIC (STAR) has full azimuthal acceptance and is ideally suited to advance studies of the proton spin. Jets and pions are being used to study the spin contribution from gluon spins to the proton spin, while measurements of leptonic W boson decay make it possible to directly measure the d, u, $\overline{d}$, and $\overline{u}$ quark polarizations. The longitudinal spin transfer, D_{LL}, of Λ and $\overline{\Lambda}$ hyperons in longitudinally polarized proton-proton collisions is sensitive to quark and anti-quark polarization in the polarized proton; as well as to polarized fragmentation; and has been proposed as a possible probe of s and $\overline{s}$ quark polarization.

The STAR collaboration has previously reported an initial proof-of-concept measurement of D_{LL} of Λ and $\overline{\Lambda}$ hyperons from a data sample obtained at $\sqrt{s} = 200$ GeV in 2005. The data correspond to an integrated luminosity of 2 pb^{-1} with 50%

beam polarization. Considerably larger data samples corresponding to 6.5 pb^{-1} and 25 pb^{-1} with beam polarizations of 57% at $\sqrt{s} = 200$ GeV were obtained in 2006 and 2009 using an upgraded instrument. Improvements were made on the analysis procedure to reduce background contribution to the $\Lambda(\overline{\Lambda})$ measurements. These new measurements of D_{LL} form the main topic of this dissertation. The sample of hyperons residing within a jet that triggered the experiment are classified as near-side hyperons, and are analyzed separately from an away-side sample that has similar precision. In addition to D_{LL}, the double longitudinal spin asymmetry, A_{LL}, for the production of Λ and $\overline{\Lambda}$ hyperons has been extracted. The near-side D_{LL} at forward pseudo-rapidity, $\eta = 0.5$, in the highest hyperon transverse momentum p_T interval at 7 GeV is measured to be $D_{LL}^{\Lambda} = -0.03 \pm 0.04_{stat} \pm 0.01_{syst}$ and $D_{LL}^{\overline{\Lambda}} = -0.06 \pm 0.05_{stat} \pm 0.01_{syst}$ from 2009 data. The dependences of D_{LL} on η, p_T, and the fragmentation ratio, z, are studied. The stated D_{LL} from Λ and $\overline{\Lambda}$ each disfavor one of the published model predictions for D_{LL} for a combined Λ and $\overline{\Lambda}$ sample, and are consistent with other predictions as well as with the preceding data. The disfavored model prediction is based on the assumption that up, down, and strange (anti-)quark spins contribute equally to polarized fragmentation into $\Lambda + \overline{\Lambda}$ hyperons. Future data with improved statistical precision, including data at $\sqrt{s} = 500$ GeV, are needed to discriminate between the other models.

The dissertation of Ramon Cendejas is approved.

Ernest Abers

John B. Garnett

George J. Igo

Ernst P. Sichtermann

Huan Z. Huang, Committee Chair

University of California, Los Angeles

2012

To my family

Table of Contents

List of Figures

List of Tables

Acknowledgments

I would like to thank Huan Huang, Charles Whitten, and George Igo for giving me the opportunity to join the Intermediate Energy Experiment Group at UCLA. To Charles Whitten's, thank you for sharing your love of physics and life with me. I would also like to thank Ernst Sichtermann for giving me the opportunity to pursue my dissertation at the Lawrence Berkeley Laboratory. Thank you for your support and encouragement during my doctorate. To all my colleagues at UCLA, LBL, and elsewhere, thank you, for making me feel welcomed in the STAR Collaboration. Thank you Stephen Trentalange and Oleg Tsai for training and helping me out during my stays at STAR as the BEMC detector expert.

To my family and friends, thank you, especially to my parents Juan and Susana who supported me throughout all my many projects and goals, including my PhD. My sisters and brothers, Rocio, Remedios, Richard, Paula, and Vincent whom I bothered every night with the light and music while I worked on homework during my undergraduate and graduate studies. David W. Eaton, Armando and Ana Maria Ducoing played an integral part in completing my studies. For that I thank you.

Vita

2001	**M.S., Physics** University of California, Los Angeles, USA
2000	**B.S., Physics** University of California, Los Angeles, USA
2000	**B.S., Applied Mathematics** University of California, Los Angeles, USA
2008 - 2012	**Graduate Student Research Assistant** Lawrence Berkeley National Laboratory, USA
2007 - 2008	**Graduate Student Research Assistant** Intermediate Energy Physics Group Physics and Astronomy Department, UCLA
2007 - 2008	**Barrel Electromagnetic Calorimeter (BEMC) Detector Expert** Brookhaven National Laboratory, USA On-site contact to detector operators for STAR BEMC operations and troubleshooting. Update the expert operating manual. Implement mirroring and backup scheme to the STAR BEMC computer systems.
Fall 2007	**Teaching Assistant** Physics and Astronomy Department, UCLA Preside over discussion section, prepare and grade quizzes, grade homework and midterms for the upper division nuclear physics undergraduate course.

CHAPTER 1

Introduction

1.1 Proton Spin

The proton is a spin $\frac{1}{2}$ baryon with $+1$ charge. The proton is a composite particle, consisting of two valence up quarks (u), one valence down quark (d), sea quarks, and gluons [par87, par00]. Theoretical models and experiments have been designed and carried out to study how the proton's constituent particles contribute to its overall spin. In Quantum Chromodynamics (QCD), the proton's spin can be decomposed [Ji97] as

$$S = \frac{1}{2} = \frac{1}{2}\Delta\Sigma + \Delta G + L_z, \tag{1.1}$$

where $\Delta\Sigma$ is the quark helicity distribution, ΔG the gluon helicity distribution, and L_z the angular momentum. The (light-cone) parton helicity distributions are defined as

$$\Delta f = f^+ - f^-, \tag{1.2}$$

where the superscripts $+(-)$ refer to the helicity state. An illustration, including also the unpolarized (spin-averaged) parton distributions (PDFs), is shown in Figure 1.1. The (total) quark spin contribution consists of contributions from the three light quarks and anti-quarks,

$$\Delta\Sigma = \Delta u + \Delta d + \Delta s + \Delta\overline{u} + \Delta\overline{d} + \Delta\overline{s}, \tag{1.3}$$

(a): $f = f^+(x) + f^-(x)$ **(b):** $\Delta f = f^+(x) - f^-(x)$

Figure 1.1: (a) Unpolarized and (b) polarized parton distribution functions.

where the up quarks are denoted by u, the down quarks by d, and the strange quarks by s. The corresponding anti-quark distributions are denoted as $\overline{u}$, $\overline{d}$, and $\overline{s}$.

The European Muon Collaboration (EMC) conducted an experiment which measured the contribution of quark and anti-quark spins to the proton spin [Ash88, Ash89]. The experiment consisted of deep inelastic scattering (DIS) of longitudinally polarized muons off a fixed target that contained longitudinally polarized protons. The DIS cross section can be written as a linear combination of the polarized structure functions $g_1(x, Q^2)$ and $g_2(x, Q^2)$ of the nucleon,

$$\frac{d^2\sigma^{++}}{dQ^2dx} - \frac{d^2\sigma^{+-}}{dQ^2dx} = \frac{16\pi\alpha^2}{Q^4}\left[g_1(x,Q^2)y\left(\frac{y}{2} - 1 + \frac{Mxy}{E}\right) + g_2(x,Q^2)\frac{Mx}{E}\right], \tag{1.4}$$

where the superscripts $+(-)$ denote the lepton and nucleon helicity states, and the lepton mass and parity-violating terms are neglected. The other variables are

$$\begin{aligned} M &: \text{ mass of the struck nucleon,} \\ E &: \text{ initial lepton energy,} \\ x &: \text{ Bjorken scaling variable,} \\ y &: \text{ photon virtuality.} \end{aligned}$$

In experiments with high beam energies, the effects from $g_2(x, Q^2)$ are kinematically suppressed and can typically be neglected. The parity-conserving unpolarized DIS cross section can be similarly expressed in terms of structure functions $F_1(x, Q^2)$ and $F_2(x, Q^2)$ [par00]. The unpolarized and polarized structure func-

tions have intuitive leading-order interpretations in terms of the parton distribution functions,

$$F_1(x) = \sum_q e_q^2 q(x), \tag{1.5}$$

$$F_2(x) = 2x \sum_q e_q^2 q(x), \tag{1.6}$$

$$g_1(x) = \sum_q e_q^2 \Delta q(x), \tag{1.7}$$

$$g_2(x) = 0, \tag{1.8}$$

where e_q denotes the quark charge and $q(x)$ and $\Delta q(x)$ are the unpolarized and polarized quark distribution functions. Gluons do not enter in these leading order expressions, since the DIS photon does not couple directly to gluons. The leading order expressions furthermore show the well-known Bjorken scaling behavior, the (leading order) independence of the structure functions on Q^2, and the Callan-Gross relation $2xF_1(x) = F_2(x)$ [Bjo69, Cal68]. Beyond leading order, the structure functions acquire a dependence in Q^2 that is logarithmic.

The first moment of $g_1^p(x, Q^2)$ can be expressed using the linear combination of a_3, a_8, and $a_0(Q^2)$,

$$\begin{aligned} \Gamma_1^p\left(Q^2\right) &= \int_0^1 g_1^p\left(x, Q^2\right) dx \\ &= \frac{1}{12}\left[\left(1 - \frac{\alpha_s(Q^2)}{\pi}\right)\left(a_3 + \frac{a_8}{\sqrt{3}}\right)\right. \\ &\quad \left. + \sqrt{\frac{8}{3}}\left(1 - \frac{33 - 8n_f}{33 - 2n_f}\frac{\alpha_s(Q^2)}{\pi}\right) a_0(Q^2)\right], \end{aligned} \tag{1.9}$$

where a_3, a_8, and a_0 are the proton matrix elements of the axial vector currents, $A_{5\mu} = \bar{\psi}\gamma_u\gamma_5\psi$, n_f is the number of active quark flavors, and α_s is the strong coupling constant [Clo93]. Terms of $\mathcal{O}(\alpha_s^2)$ are neglected. At leading order, the

matrix elements are related to the helicity quark distributions as follows:

$$a_3 = \sqrt{\frac{2}{3}}\left[(\Delta u + \Delta\overline{u}) - (\Delta d + \Delta\overline{d})\right], \tag{1.10}$$
$$a_8 = (\Delta u + \Delta\overline{u}) + (\Delta d + \Delta\overline{d}) - 2\,(\Delta s + \Delta\overline{s}),$$
$$a_0 = \sqrt{\frac{1}{3}}\left[(\Delta u + \Delta\overline{u}) + (\Delta d + \Delta\overline{d}) + (\Delta s + \Delta\overline{s})\right].$$

Experimental results from polarized neutron decay [Bou83] and hyperon beta decay [Hsu88] are used to determine a_3 and a_8 respectively [Clo88, Clo93]. The quark spin contribution to the proton spin, $\Delta\Sigma$, is then extracted from the measured value of Γ_1^p, using the values of a_3 and a_8 from neutron and hyperon leptonic decay. The first moment of g_1^p is extrapolated for $x < 0.01$ and $x > 0.7$ to cover $0 < x < 1$. The EMC obtained $\Gamma_1^p = 0.126 \pm 0.010_{\text{stat.}} \pm 0.015_{\text{syst.}}$, well below the value of 0.192 ± 0.002 anticipated from the Ellis-Jaffe sum rule [Ell74]. The Ellis-Jaffe sum rule assumes $\Delta s = \Delta\overline{s} = 0$ and SU(3) flavor symmetry. Conversely, the quark and anti-quark spin contributions for the individual quark flavors can be obtained from the measured moment, the hyperon leptonic decay couplings, and the relations from Equation 1.10. In this way, only $(12 \pm 9 \pm 14)\%$ of the proton spin is found to arise from the spin of its constituent quarks. The strange quark spin contribution is found to be $\frac{1}{2}(\Delta s + \Delta\overline{s}) = -0.095 \pm 0.016_{\text{stat.}} \pm 0.023_{\text{syst.}}$, hence the strange quarks are found polarized anti-parallel to the proton spin. The above EMC results and implications, as well as the implication that g_1^n is negative, have motivated substantial follow-up research.

Other DIS experiments have been performed, extending the x range coverage. Targets with polarized neutrons and deuterons have been used in addition to targets with polarized protons which have allowed to confirm the validity of the more fundamental spin sum rule by Bjorken [Bjo69]. Figure 1.2 shows a recent compilation of results from several experiments for the polarized structure function of both the proton and deuteron [Has09]. The experimental results confirm the EMC

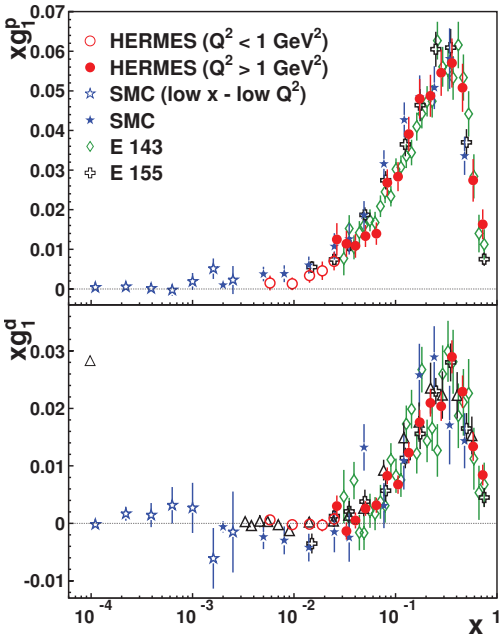

Figure 1.2: A recent compilation world data on the polarized structure function for both the proton and deuteron. Figure taken from [Has09].

data with better precision and larger x coverage, and therefore confirm that the quark spin contribution to the proton spin is surprisingly small.

In addition to the above inclusive polarized DIS experiments, polarized semi-inclusive DIS (SIDIS) experiments have been performed. In SIDIS experiments, a hadron is observed in the final state in addition to the scattered lepton. Such experiments, in particular those with identified hadrons, make it possible to more selectively study individual quark and anti-quark spin contributions to the proton spin. For example, the HERMES experiment has obtained SIDIS data with identified charged kaons in positron scattering off a polarized deuterium target [Air08]. The double spin asymmetry of the charged kaon production was used, together with fragmentation functions, in a leading-order analysis to determine $(\Delta s + \Delta\overline{s})$ for $0.023 < x < 0.06$ at Q^2=2.5 GeV^2. Figure 1.3 shows the results for $\Delta Q = \Delta u + \Delta\overline{u} + \Delta d + \Delta\overline{d}$ and $\Delta S = \Delta s + \Delta\overline{s}$. The obtained strange quark helicity distri-

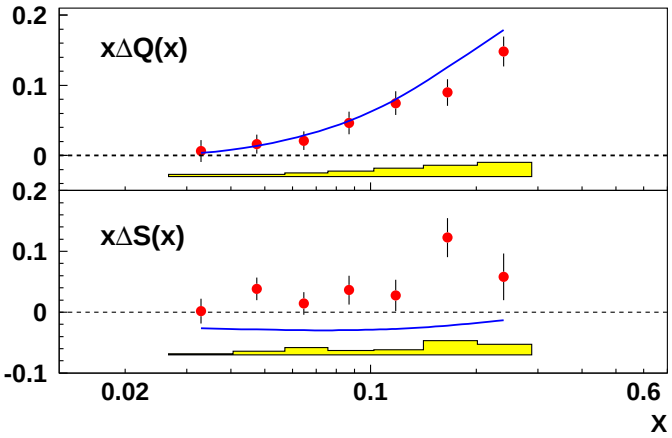

Figure 1.3: HERMES non-strange ($x\Delta Q(x)$) and strange ($x\left[\Delta s(x) + \Delta\overline{s}(x)\right]$) quark helicity distributions at Q^2=2.5 GeV^2 as a function of Bjorken x. The curves are the LO polarized PDF results from Leader et al. [Lea06].

bution is found slightly *positive* throughout the range in x covered by the measurements, $0.03 < x < 0.3$. The HERMES SIDIS data provides no evidence for the *negative* strange quark spin contribution to the proton spin that is found from the inclusive polarized measurements.

More recently, the COMPASS experiment at CERN has extracted flavor dependent spin contributions from SIDIS measurements off a target with polarized deuterons [Ale09]. The measured asymmetry for parallel and anti-parallel beam and target spin configurations is related by photon-depolarization to the asymmetry

$$A_1^h\left(x, Q^2, z\right) = \frac{\sum_q e_q^2 \Delta q\left(x, Q^2\right) D_q\left(z, Q^2\right)}{\sum_q e_q^2 q\left(x, Q^2\right) D_q\left(z, Q^2\right) + \mathcal{O}(\alpha_s)}, \tag{1.11}$$

where e_q is the quark charge, q and Δq the unpolarized and polarized quark distributions, and D_q^h the fragmentation distribution for hadron h with momentum fraction z from the parton. Similar to HERMES, the double spin asymmetry of charged kaon production was used to extract the strange quark spin contribution.

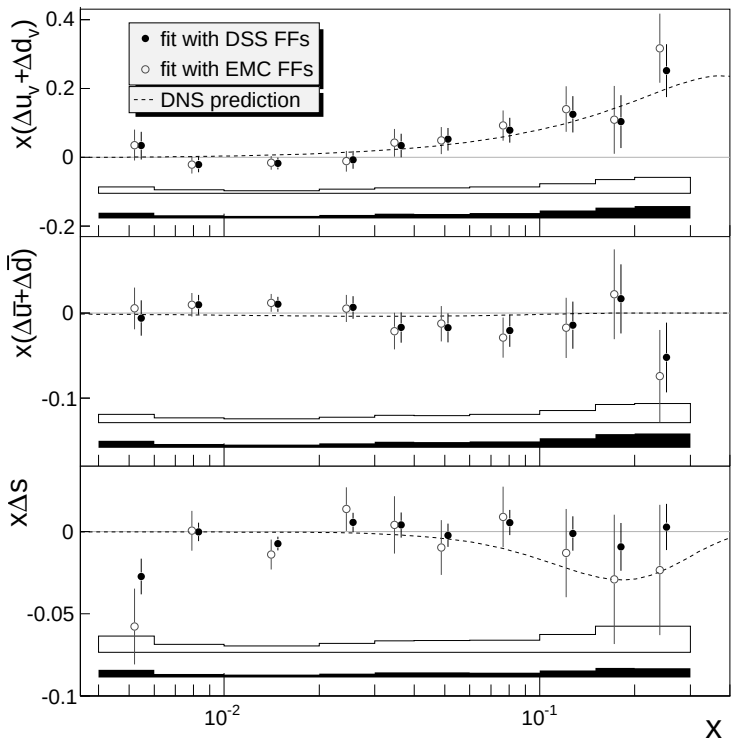

Figure 1.4: COMPASS quark helicity distributions at Q^2=3 GeV^2 for two different fragmentation functions. The fitted curves describe the LO polarized DNS PDFs [Flo05].

The COMPASS results are shown for two sets of fragmentation functions in Figure 1.4. The strange quark contribution is found to be $(\Delta s + \Delta\overline{s}) = -0.01 \pm 0.01_{\text{stat.}} \pm 0.02_{\text{syst.}}$ for $0.004 < x < 0.2$. Recent SIDIS measurements seem to indicate the strange quark and anti-strange quark spin contribution, ΔS, is small. The exact sign of the ΔS has not been unambiguously established with the current experimental data.

Figures 1.5–1.6 contain a compilation of all inclusive and semi-inclusive deep-inelastic scattering data that, together with RHIC data on spin dependence in the inclusive hadroproduction of jets and pions, were incorporated in the most recent next-to-leading order global analysis of polarized parton distribution functions, the DSSV analysis [Flo09]. The results of the DSSV analysis, in terms of NLO

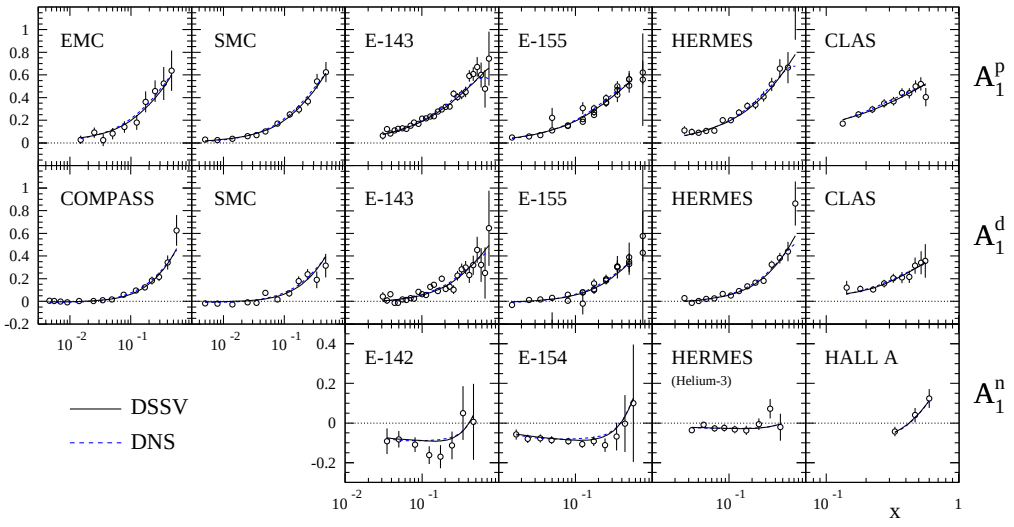

Figure 1.5: Comparison of DSSV NLO results with inclusive DIS experimental data. The DSSV fits are shown as the continuous curves. The results of a previous global analysis, DNS [Flo05], are shown as dashed lines for comparison. The uncertainties on the data are statistical.

polarized parton distributions, are shown in Figure 1.7. The up quark and anti-quark spins are seen to be preferentially aligned along the proton spin, whereas the net down quark and anti-quarks are preferentially aligned opposite the proton spin. These quantities are well determined from the data. The polarized gluon distribution is seen to be least well constrained. The negative value obtained for the net strange quark polarization from the integral of the inclusive structure function $g_1(x, Q^2)$ and the marginally positive net strange quark polarization from SIDIS measurements are reconciled by means of a negative $\Delta\bar{s}(x, Q^2) = 10$ GeV^2 for the SIDIS unmeasured small-x region. The indicated uncertainties on $\Delta\overline{s}$ do not include effects of alternative fragmentation functions, which are anticipated to be particularly important in the strange sector, or a range of scenarios for $\Delta s(x, Q^2) \neq \Delta\bar{s}(x, Q^2)$, and are therefore likely substantially smaller than the true uncertainties in this quantity. These effects are comparatively less important for the up and down quark distributions, and for gluons.

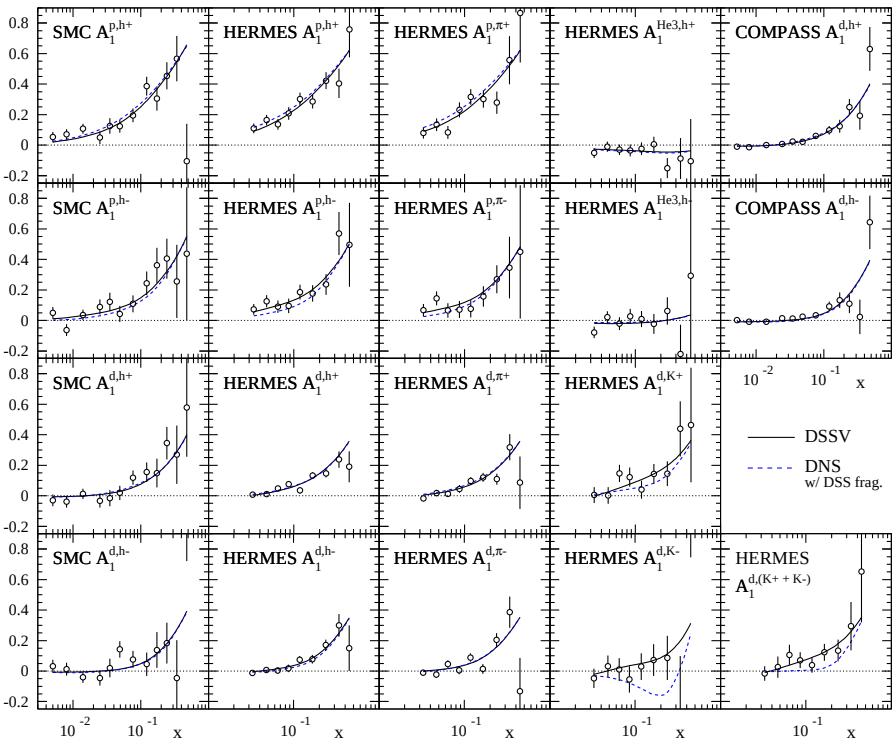

Figure 1.6: Comparison of DSSV NLO results with semi-inclusive DIS experimental data. The DSSV fits are shown as continuous curves. The results of a previous global analysis, DNS [Flo05], are shown as dashed lines for comparison. The uncertainties on the data are statistical.

Ample motivation thus exists to advance study of the net strange quark polarization with independent measurements and techniques.

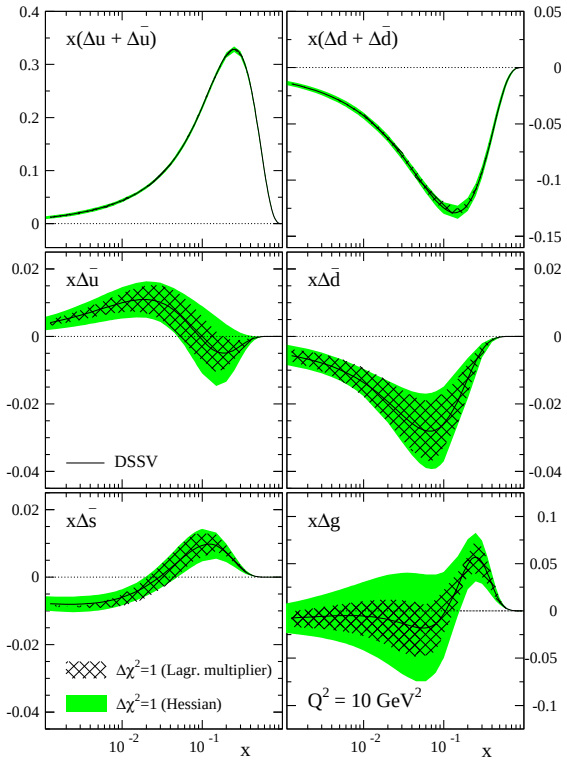

Figure 1.7: NLO polarized PDFs of the proton at Q^2=10 GeV^2 from the DSSV analysis. The DSSV analysis incorporates the inclusive and semi-inclusive data shown in the preceding figures, as well as RHIC hadroproduction data on jets and pions.

1.2 QCD Factorization, Universality, and Proton-Proton Scattering

The factorization theorem addresses short-distance and long-distance behaviors in high energy cross sections and universality [Col88, Col93]. For the purposes of this dissertation, the parton distributions in an initial state hadron and the fragmentation functions of a final state parton are long-distance behaviors. The partonic scattering process is a short-distance behavior, and is calculable in perturbative QCD. The parton distribution functions (PDFs) are non-perturbative properties of the nucleon and cannot currently be calculated from first principles. Instead,

they must be obtained from measurements. Much of the current knowledge of PDFs originates from unpolarized and polarized DIS measurements. Likewise, the fragmentation functions (FFs) are non-perturbative objects. They are typically determined from e^+e^- scattering measurements, with a particularly important role of the LEP data. LEP data currently provides the only experimental constraints on polarized fragmentation [Bor98b, Flo98b]. Factorization is closely related to universality and makes it possible to relate deep-inelastic lepton-nucleon scattering with other scattering processes, such as the process of main interest in this dissertation, that of $\Lambda(\overline{\Lambda})$ production in high-energy polarized proton-proton scattering.

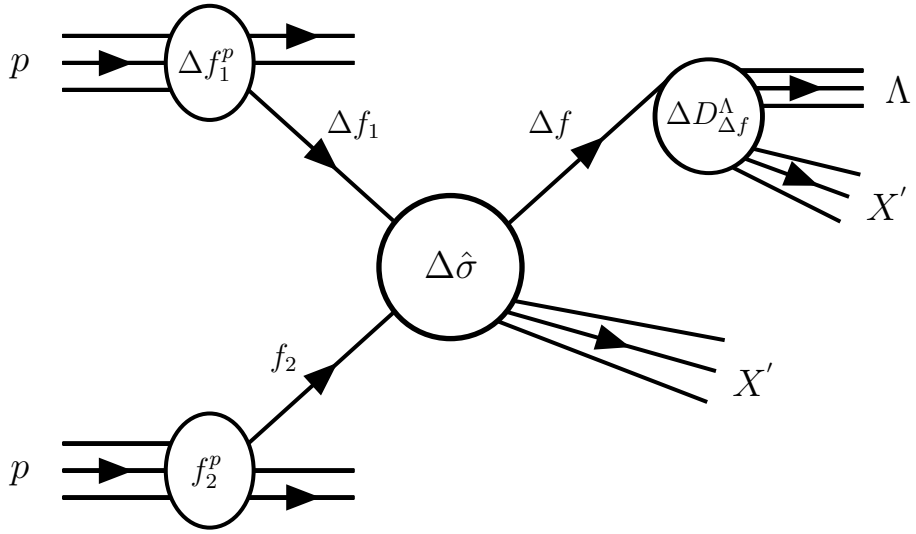

Figure 1.8: Production of polarized Λ from a singly longitudinally polarized $p+p$ collision at RHIC. Factorization and universality allow to separate the collision into separate components which could be determined by experimental results and pQCD calculations. The unpolarized and polarized PDFs are shown as f_2^p and Δf_1^p respectively. The longitudinally polarized sub-process cross section is shown as $\Delta\hat{\sigma}$ while the polarized fragmentation function responsible for the outgoing Λ particle is shown as $\Delta D_{\Delta f}^{\Lambda}$.

The production process of a polarized Λ from a singly longitudinally polarized

$p+p$ collision at RHIC is shown in Figure 1.8. A highly energetic polarized proton scatters off a highly energetic unpolarized proton and an observed $\Lambda(\overline{\Lambda})$ hyperon is produced in the hard scattering. The differential production cross section for a polarized Λ produced in a singly polarized $p+p$ collision is expressed in factorized form as

$$d\sigma^{pp\to\Lambda X'}(p_T) = \sum_{\Delta f_1, f_2, \Delta f} \Delta f_1^p\left(x_1, Q^2 = p_T^2\right) \otimes f_2^p\left(x_2, Q^2 = p_T^2\right) \otimes d\Delta\hat{\sigma}^{\Delta f_1 f_2 \to \Delta f X'} \otimes \Delta D_{\Delta f}^{\Lambda}\left(z, Q^2 = p_T^2\right), \tag{1.12}$$

where Δf_1^p (f_2^p) are the polarized(unpolarized) parton distribution functions in the proton. The scale, Q^2, is typically taken equal to the transverse momentum, $\mathrm{p_T}$, of the produced Λ. The polarized hard scattering cross section, $\Delta\hat{\sigma}$, is the calculable cross section for the inclusive production of a final state Δf in the hard scattering of an initial state polarized parton Δf_1 and an unpolarized parton f_2 [Che08]. Its kinematic dependencies have been omitted for clarity. The polarized fragmentation function, $D_{\Delta f}^{\Lambda}$, describes the probability of creating a longitudinally polarized Λ with a momentum fraction z from the polarized parton f in the final state. The polarized fragmentation function is defined as

$$\Delta D_{\Delta f}^{\Lambda}(z) = D_{\Delta f}^{\Lambda^+}(z) - D_{\Delta f}^{\Lambda^-}(z), \tag{1.13}$$

where the subscript Δf is used to denote a polarized parton of a particular flavor and the superscripts denote the Λ with positive $(+)$ and negative $(-)$ helicity.

The expression for the unpolarized differential production cross section for Λ hyperons is similar to that for the polarized production above; it is obtained trivially by omitting the Δ symbols from the parton distribution and fragmentation functions, and by using the unpolarized hard scattering cross section. The unpolarized cross section is therefore calculable using inputs for the unpolarized parton

distributions and fragmentation functions. Commonly used examples for both quantities are shown in Figure 1.9 (PDFs) and in Figure 1.10 (FFs).

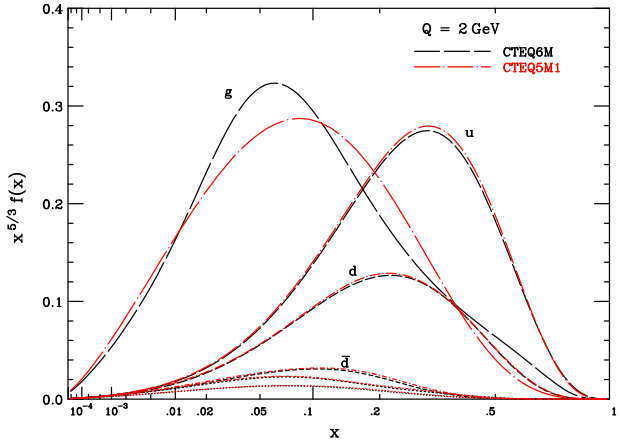

Figure 1.9: Comparison between CTEQ6M and CTEQ5M1 PDF fit curves at Q=2 GeV. CTEQ6M(CTEQ5M1) fit curves are shown as dashed(dot-dashed) lines. The smaller unlabeled curves correspond to $\overline{d}$ and s=$\overline{s}$. The largest difference between the fitted curves is seen for the gluon PDFs.

Agreement between predictions and production data obtained at RHIC allows to verify if the RHIC data can indeed be described with perturbative QCD techniques or, conversely, may allow one to provide better constraints. In the next section, the predicted and observed unpolarized production cross sections are compared. Subsequently, polarized production at RHIC will be used to gain insights in polarized parton distributions and polarized fragmentation.

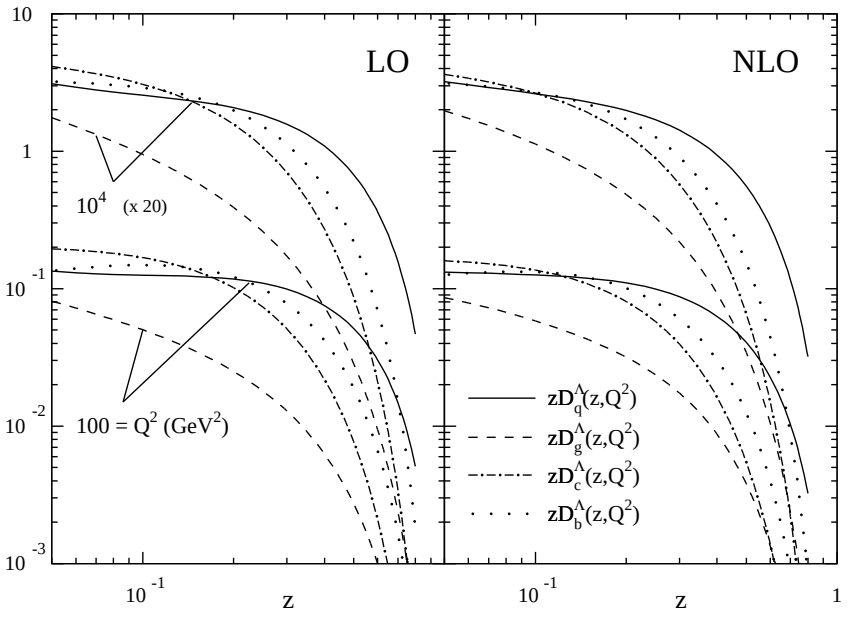

Figure 1.10: Dependence of unpolarized LO and NLO Λ fragmentation functions on z at Q^2=100 GeV^2 and Q^2=10^4 GeV^2.

1.3 Hyperon Production in Perturbative QCD Regime

STAR has published studies on strange particle production at RHIC for unpolarized p+p collisions at $\sqrt{s}$ = 200 GeV from data obtained in run year 2001 [Abe07]. Specifically, measurements of Λ, $\overline{\Lambda}$, and K^0_s p_T spectra were presented and compared with perturbative QCD calculations. Figure 1.11 shows the comparison of K^0_s and $\Lambda + \overline{\Lambda}$ particle spectra with various NLO pQCD calculations as a function of p_T. Adequate agreement of the NLO pQCD calculations based on the AKK fragmentation [Alb05] functions with the data is found, whereas the WV calculations based on the Λ fragmentations functions from de Florian et al. [Flo98a] under-predict the Λ spectra. The better description originates from the flavor separated AKK fragmentation functions [Alb05], which incorporate the OPAL quark flavor-tagged e^+e^- data in the analysis. It should be noted the AKK analysis has since been updated to include data from $p + p(\overline{p})$ collisions from CDF and

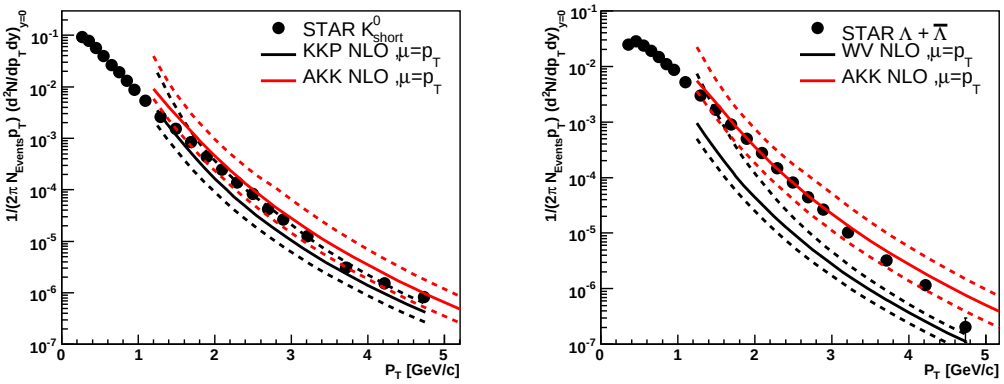

Figure 1.11: Comparison of NLO pQCD calculations by Werner Vogelsang to K^0_s and Λ particle spectra for data taken in run year 2001 $p+p$ collisions at $\sqrt{s} = 200$ GeV. The dashed lines describe the factorization and renormalization scale uncertainty. The NLO curves were generated using different fragmentation functions. The particle spectras for both K^0_s and Λ is best described by AKK which uses the latest OPAL experimental results to further constrain the fragmentation functions.

RHIC [Alb08]. However, for our purpose, the production of Λ hyperons at moderately high p_T from unpolarized $p+p$ collisions at STAR can be described within pQCD. This provides a basis for interpreting the polarized measurements in this dissertation in the pQCD framework.

1.4 Λ Polarization Models at RHIC

Few pQCD-inspired model calculations have been published for polarized proton collisions at RHIC. In one calculation, predictions are obtained for a Λ spin asymmetry in singly longitudinally polarized $p+p$ collisions at $\sqrt{s} = 500$ GeV [Flo98a]. This spin asymmetry is defined as

$$A^{\Lambda} = \frac{d\Delta\sigma^{pp^+\to\Lambda^+}/d\eta}{d\sigma^{pp^+\to\Lambda^+}/d\eta} \tag{1.14}$$

for a $\Lambda + \overline{\Lambda}$ sample where the numerator is the polarized cross section and the denominator is the unpolarized cross section. Therefore, it equals the observed

Λ polarization, P_Λ, or longitudinal spin transfer, D_{LL}, in singly longitudinally polarized proton-proton collisions. Within this model calculation, the LO GRSV "standard" polarized PDFs [G01] and three LO fragmentation scenarios [Flo98b] were used to generate the A^Λ curves. The first scenario (SU(6)) describes a non-relativistic naive quark model, where only a polarized strange quark contributes to the polarized fragmentation. That is, the Λ spin is carried solely by the strange quark spin. In the second scenario (DIS), contributions from polarized u and d quark fragmentation are incorporated with a size that is derived from the polarized Δu, Δd, and Δs distributions obtained from polarized DIS experiments and flavor rotation in the $S = 1/2,\ L = 0$ baryon octet. The third scenario (eq. contrib.) assumes all quarks contribute equally to the fragmentation which could be attributed if the Λ was primarily produced from feed-down decays. The asymmetries for the various fragmentation scenarios were generated for $\sqrt{s} = 500$ GeV $p + p$ collisions and are shown for Λ with $p_T > 13$ GeV in Figure 1.12. Positive pseudo-rapidity is defined along the momentum of the polarized beam. The curves describe the asymmetry for a combined $\Lambda + \overline{\Lambda}$ sample. Asymmetry measurements, in particular at forward pseudo-rapidity, in principle allows one to discriminate between these fragmentation scenarios.

An alternative analysis was published by Xu et al. [Xu06], who studied high p_T polarized $\overline{\Lambda}$s from a singly polarized $p+p$ collisions at $\sqrt{s} = 200$ GeV. The analysis complements [Flo98a] by separating the contribution from $\overline{\Lambda}$. The $\overline{\Lambda}$ polarization is defined as the inclusive production cross section difference ratio between the positive and negative helicity $\overline{\Lambda}$

$$P_{\overline{\Lambda}} = \frac{d\sigma\left(p^+p \to \overline{\Lambda}^+X\right) - d\sigma\left(p^+p \to \overline{\Lambda}^-X\right)}{d\sigma\left(p^+p \to \overline{\Lambda}^+X\right) + d\sigma\left(p^+p \to \overline{\Lambda}^-X\right)}, \tag{1.15}$$

where the superscript $+(-)$ denote the positive(negative) helicity of particle. The polarization relation is the same as the defined asymmetry relation from Equa-

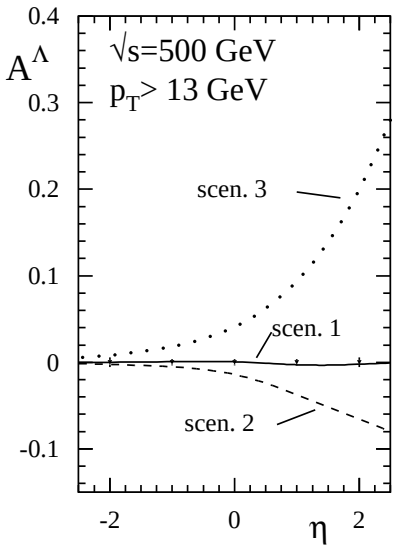

Figure 1.12: Asymmetry A^{Λ} curves for different fragmentation scenarios at $\sqrt{s} = 500$ GeV singly longitudinally polarized $p + p$ collisions and $p_T > 13$ GeV. Scenario 1 (SU(6)) describes when only strange quarks contribute to the Λ fragmentation. Scenario 2 (DIS) describes the asymmetry when only the u and d quarks negatively contribute to the Λ fragmentation. The last scenario, scen. 3 (Eq. contrib.), describes when all quark spins contribute equally to the polarized Λ fragmentation.

tion 1.14 and is equal to the spin transfer, D_{LL}, used in this dissertation. The model calculations were performed as simulations using PYTHIA 6.20 with an "after-burner" to incorporate spin effects and the leading-order GRSV2000 polarized PDFs. At higher p_T, the anti-strange quarks become the dominant contributor to the $\overline{\Lambda}$ production as seen in Figure 1.13 for $p_T > 8$ GeV and pseudo-rapidity similar to the detector acceptance of STAR. The two leading order GRSV2000 sets of polarized PDFs, "standard" and "valence" were used. For each set, two fragmentation scenarios were considered, an SU(6) and DIS scenario as in the above model calculation by Vogelsang et al. Figure 1.14 shows the generated longitudinal $\overline{\Lambda}$ polarizations for $p_T > 8$ GeV. The $\overline{\Lambda}$ polarization is seen to increase with (large) positive pseudo-rapidity in this range, where positive pseudo-rapidity is again taken to be along the momentum of the polarized beam. The different

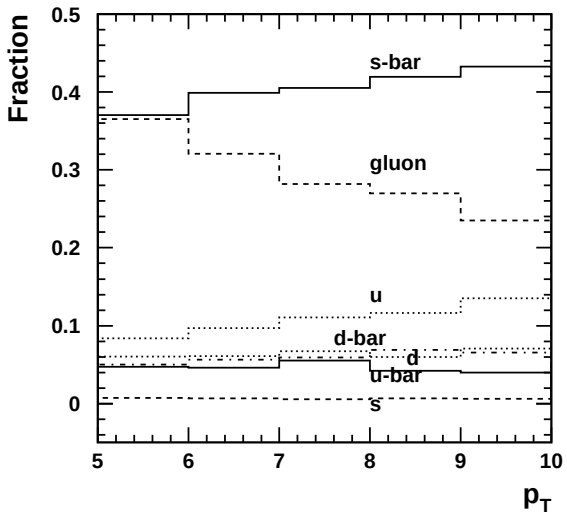

Figure 1.13: Parton contributions to $\overline{\Lambda}$ production for $|\mu| < 1$ for $\sqrt{s} = 200$ GeV $p + p$ collisions. At higher p_T, the anti-strange quark becomes the dominant contributor to the $\overline{\Lambda}$ production.

sets of polarized PDFs are seen to give rise to a larger spread than the different fragmentation scenarios in this model calculation and in the region of the STAR acceptance, $-1.2 < \eta < 1.2$. In this sense, the Δs contribution to the proton spin can therefore be studied in $\overline{\Lambda}$ spin transfer measurements in polarized p+p collisions at $\sqrt{s} = 200$ GeV. The measurement of Λ and $\overline{\Lambda}$ spin transfer may, furthermore, give insight in polarized fragmentation.

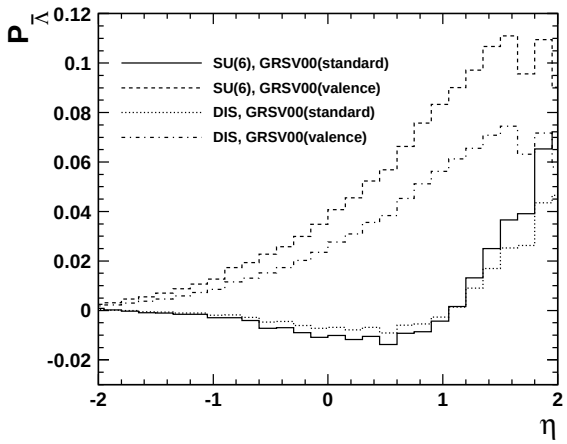

Figure 1.14: Expected longitudinal $\overline{\Lambda}$ polarization curves for different scenarios with $p_T > 8$ GeV in singly longitudinally polarized $p + p$ collisions at $\sqrt{s} = 200$ GeV. Positive η is taken along the longitudinally polarized beam direction.

1.5 Λ Self Analyzing Properties

The principal modes of decay for Λ are through weak decay channels with branching ratios (BR) of

$$\begin{aligned} \Lambda &\rightarrow p + \pi^- \quad (\text{BR } 63.9 \pm 0.5)\% \ , \\ \Lambda &\rightarrow n + \pi^0 \quad (\text{BR } 35.8 \pm 0.5)\% \ . \end{aligned}$$

Conservation of total angular momentum for Λ, $J^P_\Lambda = \frac{1}{2}^+$, in the decay into its daughters, which have total angular momentum of $J^P_p = \frac{1}{2}^+$ and $J^P_\pi = 0^-$, implies that the wave function contains L=0,1 values. The L=0 wave function (s-wave) is parity violating while the L=1 wave function (p-wave) conserves parity. This is a consequence of the parity transformation on the spherical harmonics component. Parity violating weak decays allow both s-waves and p-waves to exist [Eis57].

In the Λ rest frame, the decay protons will therefore have an angular distribution of

$$\frac{dN}{d\cos(\theta^*)} = \frac{N_{Total}}{2}\left[1 + \alpha_w P_\Lambda \cos(\theta^*)\right], \tag{1.16}$$

where

α_w : $\Lambda(\overline{\Lambda})$ weak decay parameter,

P_Λ : Λ polarization,

θ^* : Angle between decay proton and quantization axis.

The quantization axis is defined to be in the direction of the Λ momentum and gives rise to the above $P_\Lambda \cos(\theta^*)$ term. The amplitudes of the s-wave and p-wave are related to the weak decay parameter,

$$\alpha_w = \frac{2Re(AB*)}{|A|^2 + |B|^2}, \tag{1.17}$$

where A and B are the s-wave and p-wave amplitudes, respectively. With knowledge of the weak decay parameter and the decayed proton's angular distribution, the polarization of Λ can be determined [Lee57]. A detailed description on one of the experiments which extracted the weak decay parameter for Λ is given in [Cro63] where an unpolarized π^- beam was collided with an unpolarized proton beam. The weak decay parameter was extracted by evaluating the proton's up-down asymmetries from $\pi^- + p \rightarrow \Lambda + \mathrm{K}^0 \rightarrow p + \pi^-$. The decayed protons showed a preference to decay in the same direction as the polarization vector and α_w thus has a positive value. The current weak decay value extracted from global data is $\alpha_w = 0.642 \pm 0.013 (-0.642 \pm 0.08)$ [Ams08] for $\Lambda(\overline{\Lambda})$. The decay proton angular distribution and α_w can therefore be used to determine the Λ polarization in experiment.

1.6 Longitudinal Spin Transfer $\mathrm{D_{LL}}$ Measurements

In 2005, an initial $\mathrm{D_{LL}^{\Lambda(\overline{\Lambda})}}$ measurement from longitudinally polarized $p + p$ collisions was made at RHIC using the STAR detector at $\sqrt{\mathrm{s}} = 200$ GeV and average

beam polarization values of 52 ± 3% and 48 ± 3% [Abe09]. The D_{LL} values were extracted by measuring in small $\cos(\theta^*)$ intervals of

$$D_{LL} = \frac{1}{\alpha_w P_{beam} \langle \cos(\theta^*) \rangle} \frac{N^+ - RN^-}{N^+ + RN^-}, \tag{1.18}$$

where

$$\begin{aligned} \alpha_w &: \Lambda(\overline{\Lambda}) \text{ weak decay parameter,} \\ P_{beam} &: \text{measured beam polarization,} \\ \langle \cos(\theta^*) \rangle &: \text{central value of } \cos(\theta^*) \text{ interval,} \\ N^+,\, N^- &: \text{single spin } \Lambda(\overline{\Lambda}) \text{ yields,} \\ R &: \text{relative luminosity ratio.} \end{aligned}$$

Several data triggers were used to extract the $D_{LL}^{\Lambda(\overline{\Lambda})}$ values at different p_T^{Λ} intervals. The statistical uncertainties for D_{LL} are comparable to the spread between the various model predictions. Figure 1.15 shows the extracted $D_{LL}^{\Lambda(\overline{\Lambda})}$ values for different triggered data sets. The recorded longitudinally polarized $p+p$ collisions were limited in statistics.

During the 2006 and 2009 RHIC program, STAR recorded additional longitudinally polarized $p+p$ collisions at $\sqrt{s} = 200$ GeV. Advances were made in increasing the beam polarization at RHIC. The beam polarizations increased to 56 ± 4(58 ± 3) percent and 57 ± 3(57 ± 4) percent for the blue(yellow) beam in 2006 and 2009, respectively. In 2006, the Barrel Electromagnetic Calorimeter (BEMC) was completed, which increases its pseudo-rapidity coverage from $0 \leq \eta \leq 1$ to $-1 \leq \eta \leq 1$. The increase in pseudo-rapidity coverage allows to study jet associated $\Lambda(\overline{\Lambda})$s which travel in the opposite direction with respect to the triggered jet. An upgrade was performed on the Time Projection Chamber (TPC) data acquisition system in 2009 allowing to record data at rates of up to 1000 Hz [Lan05]. The number of jet patch regions in the BEMC detector used for

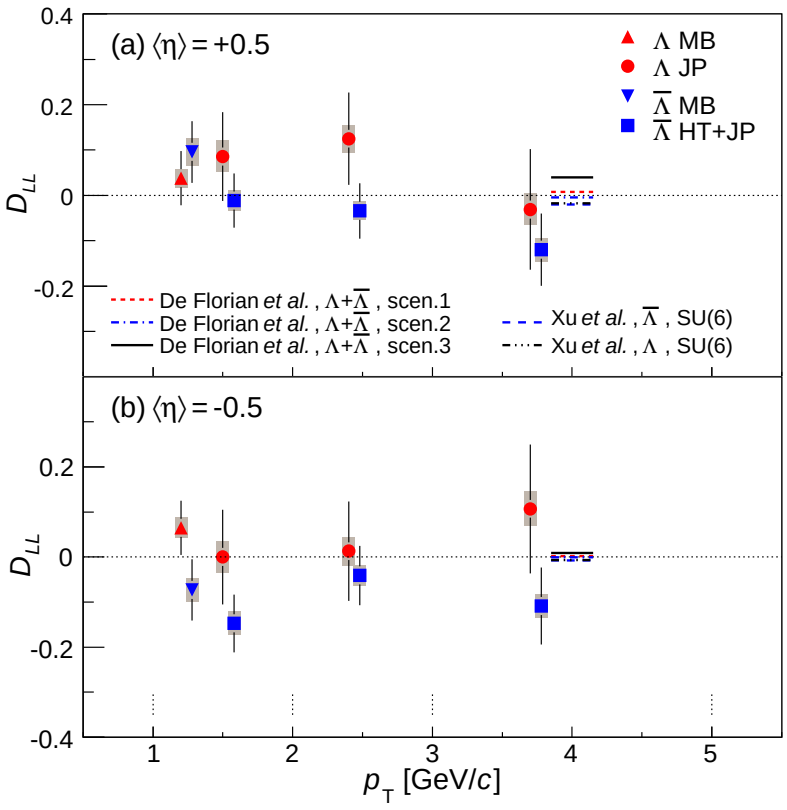

Figure 1.15: 2005 D_{LL} measurements of Λ and $\overline{\Lambda}$ for different triggered data sets in longitudinally polarized $p + p$ collisions. The various D_{LL} model expectations for the largest p_T and corresponding η are shown for comparison.

determining triggered jets in an event were increased from 6 to 12 in 2006 to 18 in 2009, creating a more uniform jet acceptance in η. Reducing the D_{LL} statistical uncertainty contribution is a key component in improving the precision for the extracted $D_{LL}^{\Lambda(\overline{\Lambda})}$ values at STAR. The analysis of run 2006 and 2009 data forms the main topic of this dissertation.

CHAPTER 2

Experiment

2.1 RHIC

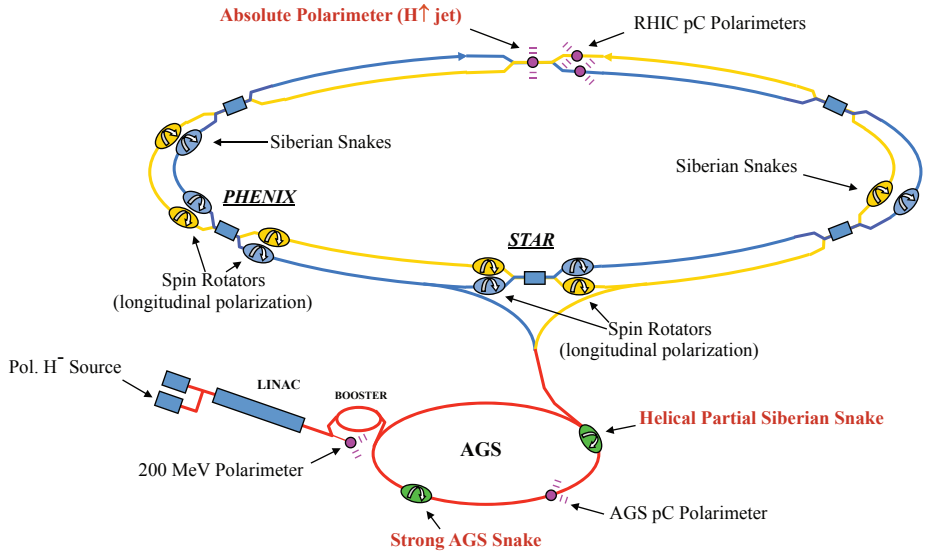

Figure 2.1: Schematic view of the RHIC apparatus. The analyses in this dissertation were performed using the STAR detector located at 6 o'clock (IP6). The RHIC polarimeters are located at IP12. The Siberian Snakes in RHIC are at the 3 and 9 o'clock locations.

The Relativistic Heavy Ion Collider (RHIC) is a proton and heavy ion collider located at Brookhaven National Laboratory (BNL) in Upton, NY. RHIC is the world's only polarized proton collider, able to collide polarized protons with beam polarizations of up to 70% for each beam at center of mass energies of up to $\sqrt{s} = 500$ GeV. Besides polarized protons, RHIC has also collided deuterons and

gold ions up to center of mass energies of $\sqrt{s} = 200$ GeV [Ale03]. RHIC enables studies of the spin structure of the proton through polarized proton collisions and of hadronic interactions through heavy ion collisions, including signatures of the Quark-Gluon Plasma (QGP) phase transition. This chapter focuses on an introduction to the RHIC facility and the Solenoidal Tracker at RHIC (STAR) detector for polarized proton collisions.

RHIC contains two acceleration rings with 3.8 km of circumference and six interaction points (IP)s [Sai01]. Figure 2.1 shows the layout of RHIC with the main components relevant to polarized proton collisions labeled. The acceleration ring with the beam traveling clockwise(counter-clockwise) is referred to as the blue(yellow) beam. The interaction points are labeled as the hour positions on a clock. The STAR (IP6) and PHENIX (IP8) experiments are still active [Ale03]. RHIC polarimetry is performed at IP12.

2.1.1 Siberian Snakes and Spin Rotators

The acceleration and storage of polarized proton beams has greatly benefited from the development of magnetic configurations named Siberian Snakes [Oka00]. Siberian snakes serve to counteract the depolarization effects caused while accelerating and maintaining the polarized beam at high energies. There are two main sources of depolarization, namely, imperfections from magnet errors and misalignments, and intrinsic resonances from focusing fields. Siberian Snakes at RHIC rotate the spin direction of the proton using four helical dipole fields. Helical dipole magnets allow for a compact design, 10.6 m in length, and are able to produce a 4 T field used to manipulate the direction of the proton spin. Figure 2.2 shows the proton orbit and spin direction as it traverses through a full Siberian Snake. The stable vertical spin direction is preserved when the spin direction of

the protons is rotated with the pair of Siberian Snakes [Ale03] and magnet imperfections are counter-acted. A partial Siberian Snake with 9° rotation was installed at the AGS which removed the need of implementing harmonic corrections to correct for depolarization effects [Hua94]. For AGS energies, a partial Siberian Snake works well while the higher energies on the RHIC rings require the use of full Siberian Snakes to counteract the larger orbital distortions [Ale03]. Two Siberian Snakes were installed in the straight sections of the collider lattice at the 3 and 9 o'clock locations. The Siberian Snakes rotate the polarized proton's spin direction 180° for every half revolution, canceling the accumulated spin precession without influencing the overall beam orbit. The Siberian Snakes at RHIC have made it possible to preserve proton polarization during acceleration and maintain the proton polarization during the beam storage period.

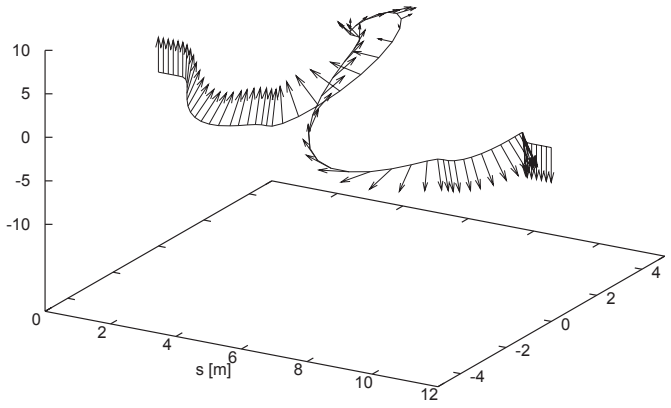

Figure 2.2: Position and spin polarization tracking for a proton with energy of E=23 GeV as it traverses through a full Siberian Snake. The spin direction completely rotates 180°. All three axis are in meters.

The polarization direction of the proton beams are (anti-)perpendicular to the proton orbit in the rings. To study longitudinally polarized proton collisions, spin rotators were installed at each beam fore and aft the STAR and PHENIX interaction regions. These magnets and the DX magnets are set to rotate the transverse polarized proton spins such that they become longitudinal at the interaction region

and the spins are then rotated back to transverse direction after the interaction region. Similar to the Siberian Snakes, the spin rotators are constructed using helical dipole magnets but instead of using four right handed helical dipole magnets, a configuration that alternates from right-handed to left-handed magnets is used as shown in Figure 2.3 [Ale03]. The currents through the spin rotator magnets are set and tuned individually for STAR and PHENIX. Hence, the polarization directions at each experiment need not be identical, and in the case of longitudinal spin configurations each experiment can minimize the size of residual transverse spin components.

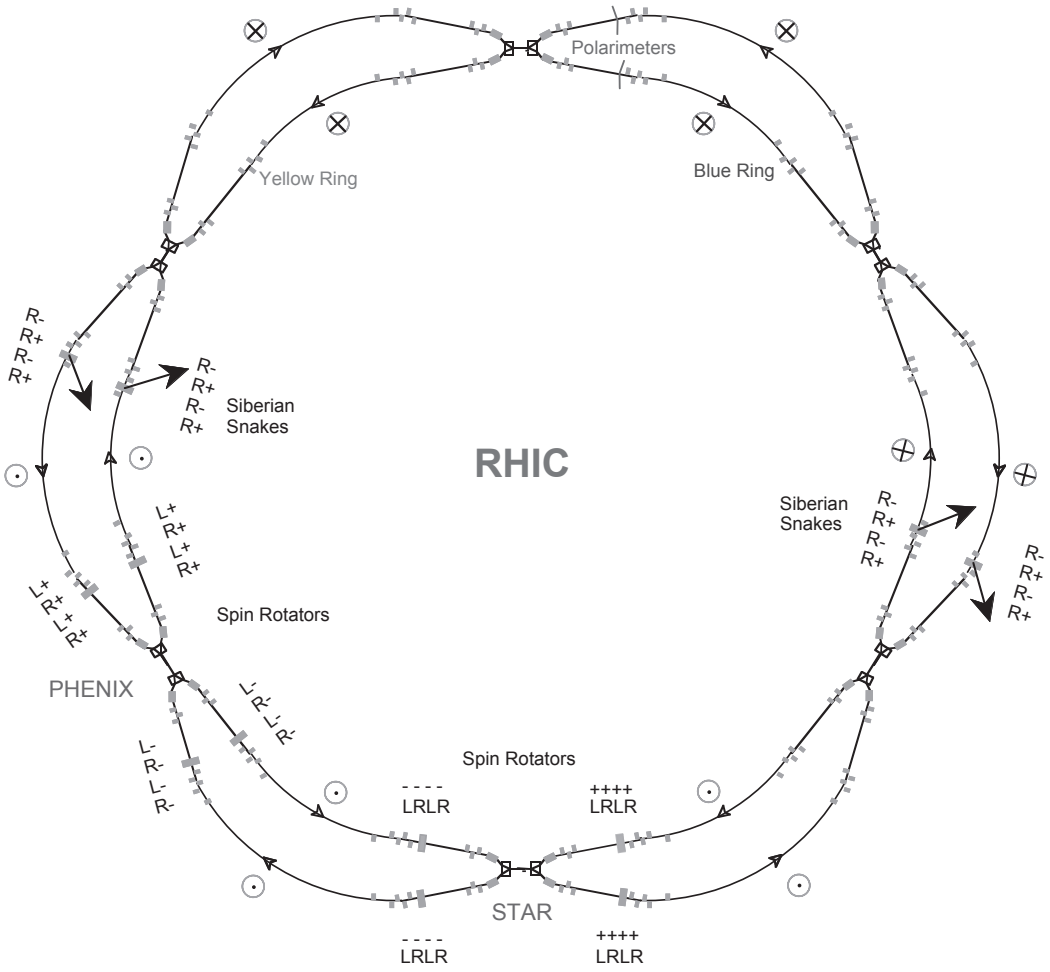

Figure 2.3: Schematic layout of Siberian Snakes and spin rotators at RHIC. The handedness of the dipole magnets that constitute the Siberian Snakes and spin rotators is denoted by L(R) for left(right) handedness.

2.1.2 Polarized Proton Beams

The RHIC rings can have up to 112 of the 120 available RF buckets filled. Each filled beam bunch typically contains up to 2×10^{11} protons. The bunches have a 2 ns duration and are 106 ns apart [Ale03]. Polarized protons are produced using an Optically Pumped H^- Ion Source (OPPIS). In this source, rubidium vapor is optically pumped by a pulsed laser to produce polarized electrons. The unpolarized ionized hydrogen gas picks up the polarized electrons and a hyperfine interaction results in the transfer of polarization from the electron to the proton [Zel07]. OPPIS is capable of producing a H^- 0.5 mA current with 80% polarization in a 300 μs pulse corresponding to 9×10^{11} polarized protons [Ale03]. The polarized H^- are then stripped of their electrons and accelerated to 200 MeV using a Radio Frequency Quadrupole (RFQ) and the 200 MHz LINAC before being injected to the AGS Booster [Ale01]. Further acceleration to 1.5 GeV and capturing to a single bunch is performed in the AGS Booster. The proton bunch is injected and accelerated to 25 GeV in the AGS before being injected to a RHIC ring. Beam bunches are injected one at a time into the RHIC rings, allowing to configure the spin direction of each beam bunch independently. Once in the RHIC ring, proton bunches are accelerated to their final energies of 100 GeV or 250 GeV.

2.1.3 RHIC Polarimetry

Polarization measurements are performed periodically for both RHIC beams independently. Two elastic scattering measurements are performed in the Coulomb Nuclear Interference (CNI) region to obtain a complete picture of the polarization for each beam [Rus07]. The CNI region occurs for a small four-momentum transfer squared, -t, of $0.001 \leq$ -t ≤ 0.02 GeV^2. The relative beam polarization is measured by analyzing the proton-Carbon (pC) elastic scattering measure-

ments [Kur02, Jin04, Hua08]. These are then normalized by the absolute beam polarization measured in elastic $p + p$ scattering off a transversely polarized hydrogen gas jet (H-jet) target [Zel05, Oka06b, Oka06a, Rus07]. Only the recoiled carbons and protons are observed in these measurements since the forward scattered protons are only slightly kicked and therefore generally remain within the region of the beam. The p-Carbon and H-jet polarimeters are located at IP12. Relative polarization measurements are fast, typically taking only a couple of minutes, and are performed multiple times during the lifespan of a beam store. The absolute polarization measurement typically require data accumulation for about a day and typically, this calibration is performed during multiple beam stores. This measurement then serves to normalize the relative polarization measurements.

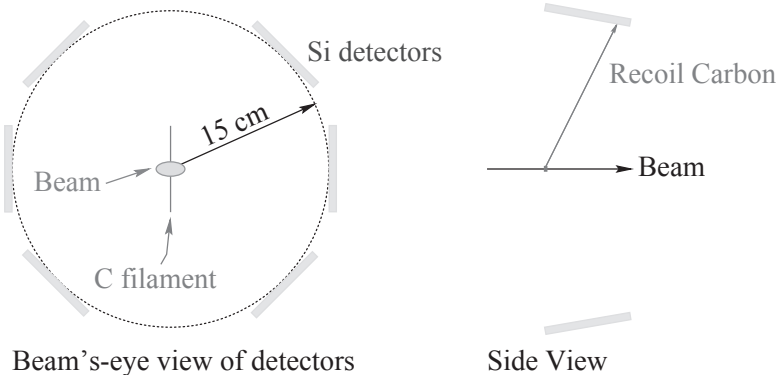

Figure 2.4: Schematic layout of the p-Carbon polarimeter. The thin carbon ribbons are movable and are positioned to intersect the beam during the measurement. The silicon detectors are placed perpendicular to the beam direction, at slightly forward angles along the beam directions.

The thin carbon ribbons used as targets for pC elastic scattering in CNI region with the polarized beam are 6-8 μg/cm^2 in diameter and 2.5 cm in length. The recoiling carbon ions are measured using six silicon detectors located transverse from the beam direction, 15 cm away from the target as shown in Figure 2.4. The silicon detectors are located at 45°, 90°, and 135° on each side of the beam. Each

silicon detector contains 12 individual 10 mm×2 mm strips which detect recoil carbon ions with kinetic energy $0.4 \leq \mathrm{E} \leq 0.9$ MeV [Nak08a]. For each strip, an asymmetry measurement pertaining to the number of counts from p^+ and p^- bunches is performed. The average strip polarization is measured by fitting the measured asymmetries, A_i, for each silicon detector strip i with respect to their azimuthal angle as

$$P_B(\phi) = \frac{A_i}{\overline{A}_N} = P_B \sin\phi, \tag{2.1}$$

where $\overline{A}_N$ is the weighted average analyzing power within the energy range, and P_B is the strip averaged polarization [Nak08b, Nak08a]. The pC polarimeters measure average beam polarization from multiple measurements to a relative uncertainty of about 10% without input from the H-jet polarimeters.

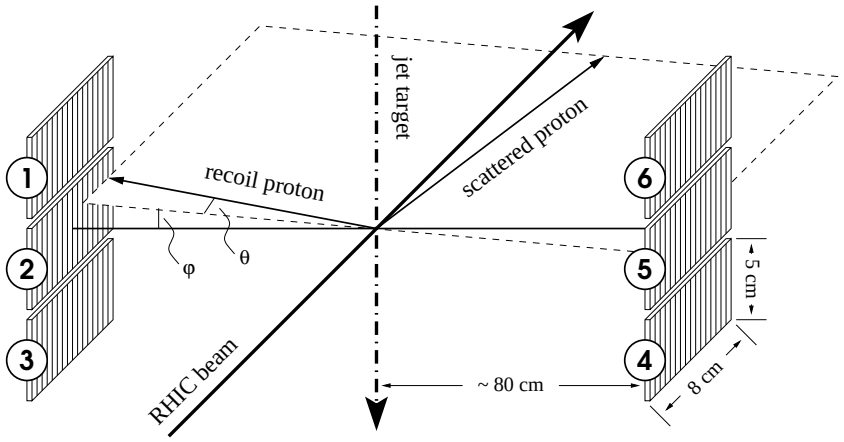

Figure 2.5: Schematic layout of the H-jet polarimeter silicon detectors. The silicon detectors are placed centered to the intersection region and perpendicular to the beam direction.

The transversely polarized hydrogen jet is produced by an Atomic Beam Source (ABS). The H-jet travels in the vertical direction and intersects with only one of the RHIC polarized proton beams. The other beam is displaced. The absolute polarization values of the target protons in the H-jet are measured with a Breit-Rabi polarimeter [Rus07]. Six silicon detectors are placed 80 cm away, centered

on the left and right side of the intersection point, perpendicular to the beam direction. Figure 2.5 shows the layout of the silicon detectors with respect to the intersection point of the beam and H-jet. Each silicon detector consists of sixteen individual strips, allowing the eight forward strips, with respect to the beam to be used for measuring the recoiled protons, while the eight backwards strips are used for background measurements. The silicon detectors are able to detect recoil protons with kinetic energies of $0.6 \leq \mathrm{E} \leq 17$ MeV. The absolute analyzing power, A_N, is measured using the absolute target polarization, P_{target}, and raw scattering asymmetries,

$$A_N = \frac{\epsilon_{target}}{P_{target}}. \tag{2.2}$$

The measured absolute analyzing power can be used to extract the absolute RHIC beam polarization since the protons between the polarized proton beam and hydrogen jet target are scattering elastically. The absolute RHIC beam polarization is extracted using the relation

$$P_{beam} = -\frac{\epsilon_{beam}\left(T_R\right)}{\epsilon_{target}\left(T_R\right)} P_{target}, \tag{2.3}$$

where ϵ are the observed asymmetries as a function of recoil energy, T_R, and P_{target} is the measured absolute target polarization [Oka08, Eys07]. The observed asymmetries are typically calculated using the square-root relation,

$$\epsilon = \frac{\sqrt{N_L^+ N_R^-} - \sqrt{N_R^+ N_L^-}}{\sqrt{N_L^+ N_R^-} + \sqrt{N_R^+ N_L^-}}, \tag{2.4}$$

where N are the recoiled proton counts from the left(right) side denoted by the subscript L(R) and the superscript $+(-)$ denotes the beam polarization state [Oka08]. The relative beam polarization measurements from the pC polarimeters are calibrated by the H-jet polarimeter measurement to a relative uncertainty of about 5%.

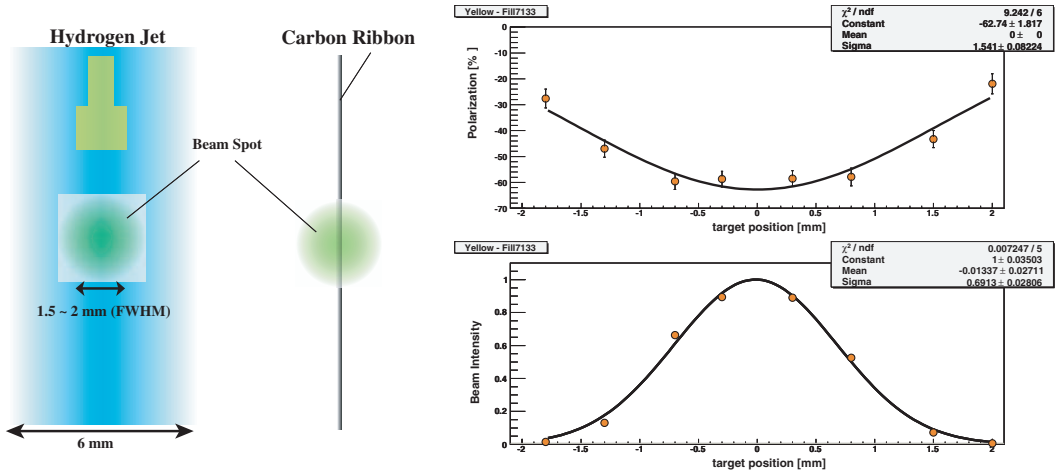

Figure 2.6: Beam spot coverage of H-jet and p-Carbon polarimeter target. The horizontal intensity and polarization profile are shown for the yellow beam for a representative beam fill in run year 2005. The target position is the relative position with respect to the beam center.

The carbon ribbon targets are 10-20 μm wide. This is smaller than the typical beam size of 1.5-2.0 mm at FWHM. The measurements locally sample the proton polarization where the target intersects the beam [Nak08b]. Figure 2.6 illustrates the typical coverage for a carbon target and for the H-jet target compared to the beam profile. Horizontal intensity and polarization profiles for the yellow beam are shown for a representative fill in run year 2005. The H-jet target measures the average beam polarization compared to the localized beam polarization measured by the pC polarimeter. To achieve better understanding of the polarization profile, the carbon ribbon is moved in 0.5 mm steps across the horizontal and vertical beam profile. A similar number of events are accumulated in each step, and the local measurements are combined to obtain an average for the full beam profile. Both vertical and horizontal scanning are used to reduce the systematic uncertainty associated with the beam polarization profile.

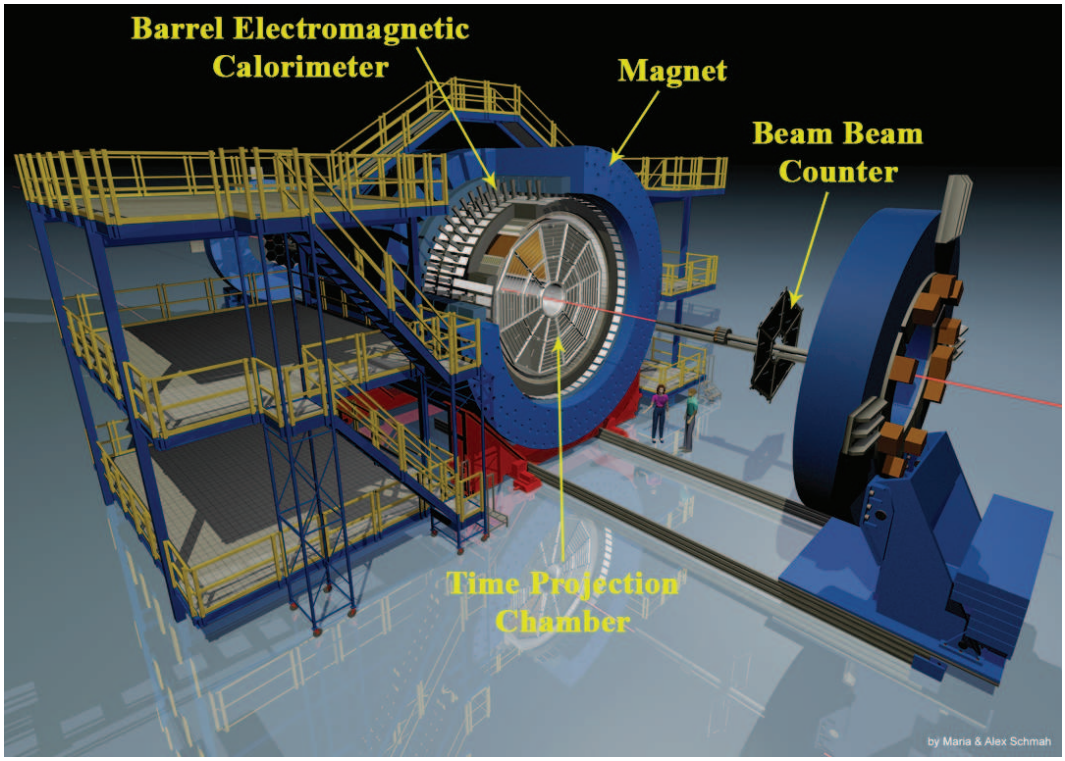

Figure 2.7: Layout of the STAR detector. STAR detector subsystems are labeled. Persons shown for scale.

2.2 STAR Detector

The Solenoidal Tracker At RHIC (STAR) is a full azimuthal particle and jet detector for proton-proton and heavy ion collisions. STAR is located in the Wide Angle Hall at IP6 at RHIC and is comprised of mid rapidity detector subsystems spanning a pseudo-rapidity range of $|\eta| < 1.2$ and forward detector subsystems with a maximum pseudo-rapidity of 7.5. Mid rapidity detector subsystems are labeled in the STAR schematic layout shown in Figure 2.7. The Time Projection Chamber (TPC) is the largest STAR detector subsystem which tracks and identifies charged particles. The STAR magnet is a 7.25 m long solenoid with an inner and outer diameter of 5.27 m and 7.32 m [Ber03]. The TPC is surrounded by the STAR magnet which generates a uniform full(half) magnetic field of 0.5(0.25) T within

the TPC detector. The data used in this dissertation were obtained with the magnet configured in full field mode. Detector subsystems relevant to the dissertation are further described in the following sections.

2.2.1 TPC

The largest detector subsystem of STAR is the Time Projection Chamber (TPC) which tracks and identifies charged particles [And03]. The analysis performed in the dissertation uses the TPC detector to reconstruct the hyperons and jets produced in the $p+p$ collision events. The TPC is a full azimuthal and $|\eta| < 1.1$ particle tracker, 4.2 m long and 4 m in diameter, able to detect particles with minimum transverse momentum of $p_T > 100$ MeV. The TPC detector consists of a high voltage central cathode membrane kept at 28 kV and ground end planes on both ends. The cylinder is constructed from 182 metals rings connected by 2 MΩ resistors, creating a uniform electric field gradient of 135 V/cm between the central membrane and end planes. Figure 2.8 shows the TPC inner and outer field cage, central membrane, and end planes. The field cage is filled with a 90%/10% mixture of argon/methane gas kept at 2 mbar above atmospheric pressure.

The TPC gas is ionized when a charged particle traverses it. The freed electrons drift in the electric field to the end plates, where their signal is amplified and collected with pad planes. The typical drift velocity is 5.45 cm/μs. The drift velocity is dependent on the electric field gradient, temperature, pressure, and gas content. Measurements of the drift velocity are performed several times a day using an ultraviolet (UV) laser. Trace organic molecules can be ionized with the UV laser, simulating a traversing charge particle [Hil86]. The measured time difference between ionized tracks and the known positions of the laser beams are used to determine the drift velocity [Leb02, Abe03]. At STAR, the laser beam is

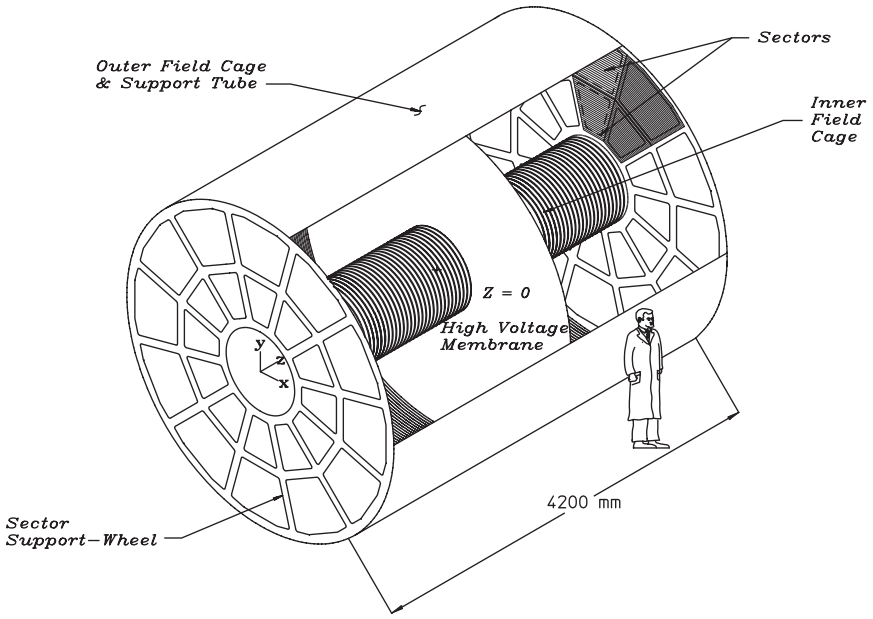

Figure 2.8: Schematic view of the TPC detector at STAR. The diagram shows the position of the outer and inner field cages, high voltage central membrane, and anode end pads. The 24 sub-sector anode pad positions are shown for one end. Person shown for scale.

split into 504 beams with similar intensities using mirror bundles placed at known locations as shown in Figure 2.9.

Ground end pads are subdivided into 2 rows of 12 sub-sectors placed in the clock hour positions. The inner(outer) sector contains 13(32) pad rows with 1750(3942) pads. The 45 pad rows on a 2 row sub-sector schematic layout are shown in Figure 2.10. Multi-Wire Proportional Chambers (MWPCs) are used to readout the pads. When the TPC is triggered, it reads out the pads in intervals of 512 time bins resulting in a z position resolution of 0.5-3.0 mm. A three dimensional charge point reconstruction of an event can be determined from the x-y positions determined by the MWPC readouts while the z positions are determined from the drift

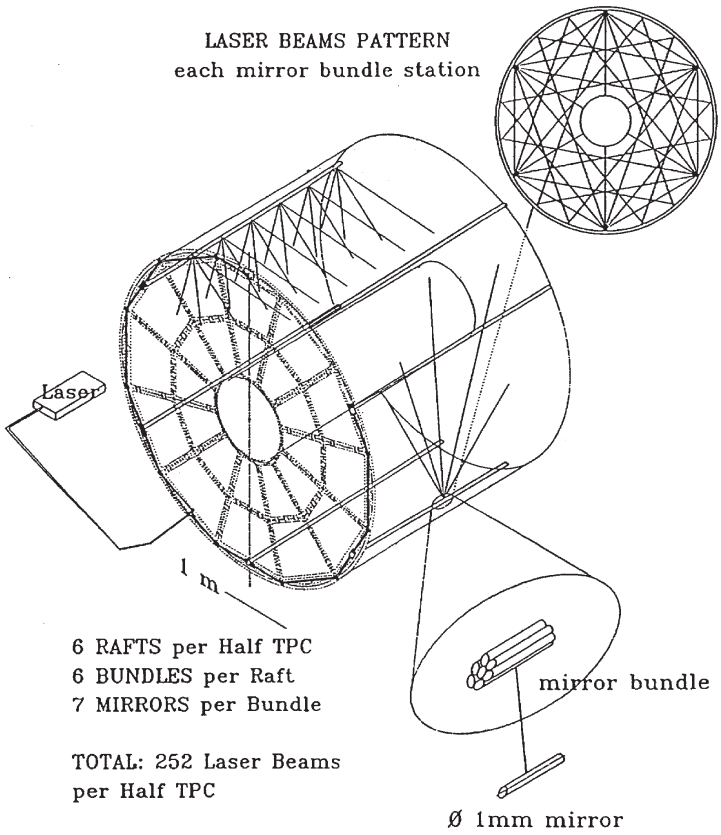

Figure 2.9: Schematic layout of the TPC laser system. Laser beams split by the mirror bundles. Side view laser beams pattern are shown on the top right diagram.

time.

Charged particles tracks are reconstructed using the charge points detected in the TPC detector. The magnetic field from the STAR magnet bends the charged particles into a helical curvature trajectory. Pattern recognition software is used to fit helical curvature tracks through the charge points. The event primary vertex is defined by locating the crossing point from the majority of reconstructed tracks. A primary vertex resolution of 350 μm is obtained using 1000 reconstructed tracks. The transverse momentum from the charged particles can be extracted using the measured radius of curvature

$$p_T = 0.3Br|q|, \tag{2.5}$$

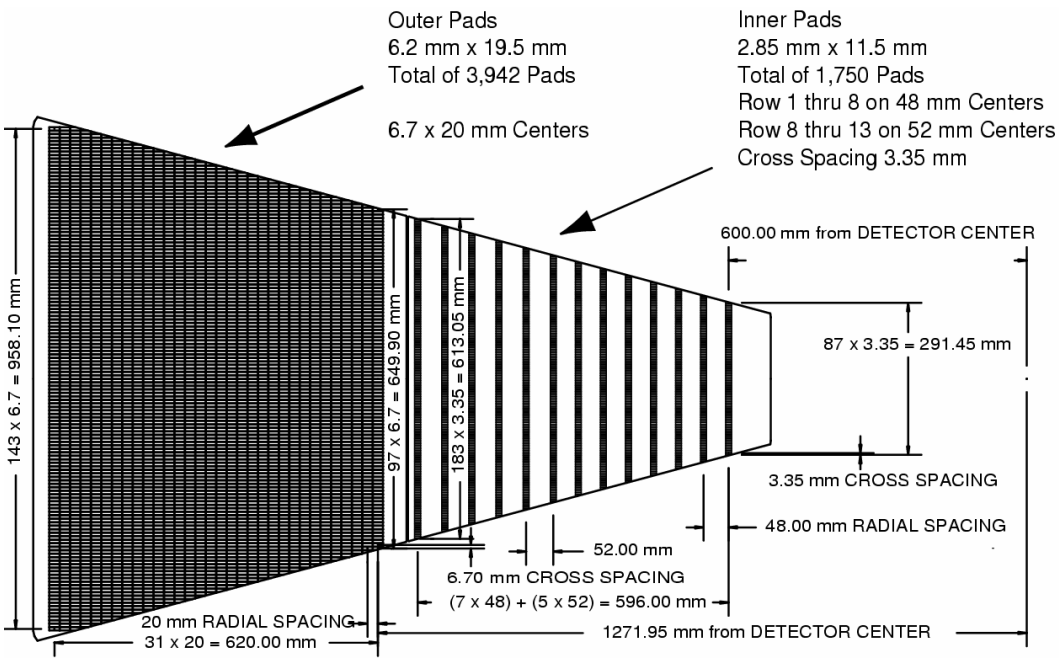

Figure 2.10: Schematic view of an TPC inner and outer sub-sector anode pad. The outer sub-sector on the left contains larger pads than the inner sub-sector on the right.

where B is the magnetic field strength, r is the radius of curvature, and q is the particle charge. The actual reconstruction software refines on this method by taking into account particle energy loss along the track and in some cases also by using a beam line constraint. At a transverse momentum of 2 GeV, the typical single-track transverse momentum resolution is about 4% [And03].

Particle charge and identification are determined using the TPC detector and STAR magnet. The direction the charged particle curves while traversing through the magnetic field allows to define the particle charge. Low momentum charged particles are identified by looking at the energy loss behavior as they traverse through the TPC gas. The ionization energy loss, dE/dx, is proportional to the sum of the drift electrons divided by the track path length across the pad length.

The mean energy loss is described using the Bethe-Bloch formula [Ams08]

$$-\frac{dE}{dx} = Kz^2 \frac{Z}{A}\frac{1}{\beta^2}\left(\frac{1}{2}\ln\left[\frac{2m_e c^2\beta^2\gamma^2 T_{max}}{I}\right] - \beta^2 - \frac{\delta}{2}\right), \tag{2.6}$$

where

$$\begin{aligned}
z &: \text{Particle charge,}\\
K &: \text{Constant,}\\
Z &: \text{Atomic number of absorber,}\\
A &: \text{Atomic mass of absorber,}\\
m_e &: \text{Electron mass,}\\
c &: \text{Speed of light,}\\
I &: \text{Average ionization of absorber,}\\
T_{max} &: \text{Max free electron recoil kinetic energy,}\\
\delta &: \text{Density correction,}\\
\beta,\, \gamma &: \text{Relativistic variables.}
\end{aligned}$$

The Bethe-Bloch expectation curves identified the various particle species at half field as shown in Figure 2.11.

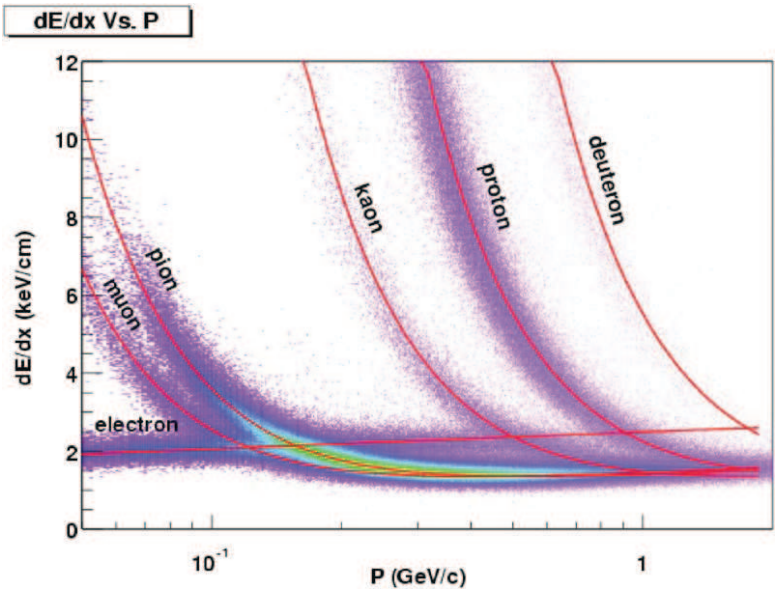

Figure 2.11: Particle energy loss distribution versus transverse momentum measured in the STAR TPC detector with a magnetic field 0.25 T. Bethe-Bloch expectation curves are shown in red for different particle species.

2.2.2 BEMC

The Barrel Electromagnetic Calorimeter (BEMC) is a projective lead scintillator calorimeter [Bed03] located between the TPC and the STAR magnet which measures the electromagnetic energy deposits associated with jets, leading hadrons, direct photons, and electrons produced in large p_T processes. The BEMC detector is 586 cm long with an inner and outer radius of 223 cm and 263 cm, and has full azimuthal acceptance for $|\eta| < 1$. BEMC measures the transverse energy deposited in electromagnetic showers from neutral and charged particles. Charged hadrons deposit a minimum amount of energy as a narrow electromagnetic shower in the lead scintillator material. Photons pair produce in the lead material and Bremsstrahlung resulting in further pair production creating a wider electromagnetic shower than hadrons.

The BEMC is made up of 120 modules. Each module is 26×293 cm^2 and

23.5 cm deep covering $\Delta\eta\times\Delta\phi = 1.0\times0.6^{\circ}$. The modules consist of 40 towers. A tower covers $\Delta\eta\times\Delta\phi = 0.05\times0.05$ and consists of 20 layers of lead and 21 layers of Kuraray SCSN-82 scintillator layers interleaved as shown in Figure 2.12. A "megatile" is used for each scintillation layer in a module. To separate the scintillator for each tower, groves are machined 95% deep and filled with an opaque epoxy. A Wavelength Shifting (WLS) fiber is inserted in the scintillator to transfer the light collected to a Photomultiplier Tube (PMT) located outside the STAR magnet.

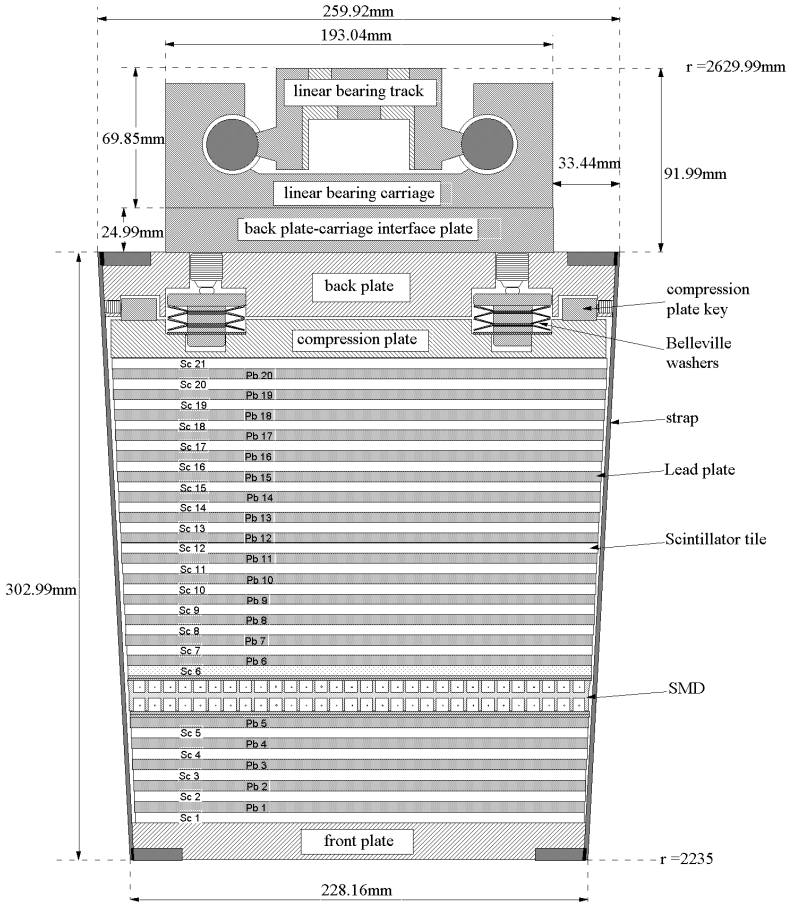

Figure 2.12: Side view schematic of a BEMC module. The two layers comprising the shower maximum detector are labeled between the lead and scintillator layers.

A Shower Maximum Detector (SMD) was installed $5X_0$ between the 5th and

6th scintillator/lead layer as shown in Figure 2.12. Improved spatial resolution of the calorimeter from the SMD allows to separate two gamma showers from π^0 and η meson decay. The SMD is a multi-wire proportional counter with gas amplification for the two dimensional cathode strip readout. The gas mixture is a 90%/10% of argon and carbon dioxide kept at fixed pressure of 15 psi. The cathode strip system is two independent cathode plane strips running perpendicular from each other along the η and ϕ direction as shown in Figure 2.13. The SMD contains 36,000 strips. Each strip contains thirty 50 μm gold plated tungsten wires. The cathode strips allow to recreate electromagnetic showers in two dimensions. Beam tests performed at the AGS show the SMD responds linearly as a function of energy [Cor02]. The ionization from the back plane of the SMD is 10% lower compared to the front plane. Energy resolution from the front plane is $\sigma/\mathrm{E} = 12\% + 86\% /\sqrt{\mathrm{E}}$ GeV while the black plane shows 3-4% degradation compared to the front plane.

The innermost first and second scintillating layers in each BEMC tower comprise the Pre-Shower Detector (PSD). A second WLS fiber is inserted to sample the scintillation light in each layer. The thickness of the two scintillation layers are increased from 5 mm to 6 mm to compensate the light reduction of 20% from having two WLS fibers. The two extra fibers are connected each to a single pixel on a 16-pixel multi-anode PMT. 300 multi-anode PMTs provide the pre-shower signals from the 4800 sampled towers.

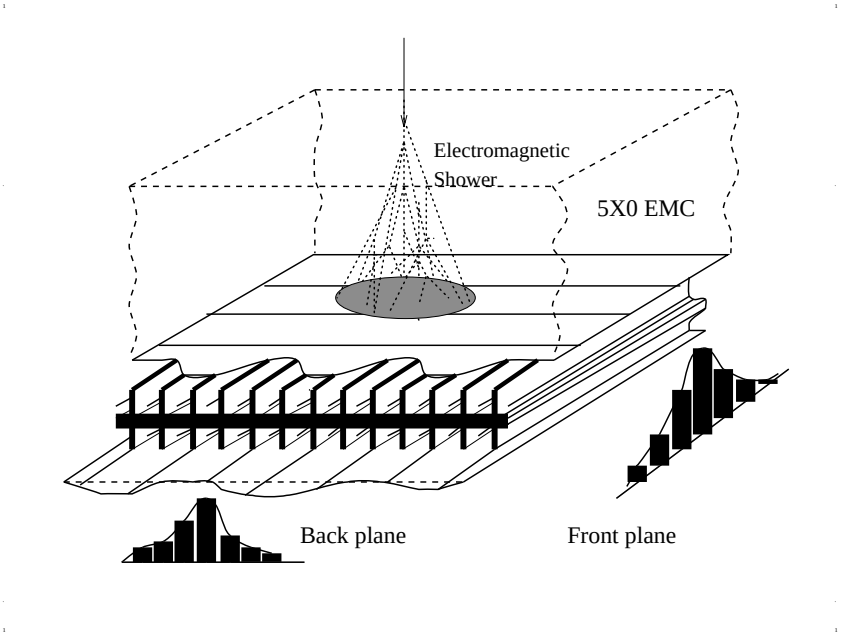

Figure 2.13: Schematic view of the BEMC shower maximum detector. Two independent wire layers in the η and ϕ direction allow to measure electromagnetic showers more precisely.

2.2.3 BBC

The Beam-Beam Counters (BBCs) are detector annuli around the beam pipe that are located on each end 3.7 m away from the interaction point, residing outside the STAR magnet. The BBCs are constructed of 18 large and 18 small hexagonal scintillator tiles. The small tiles make up an outer radius of 48 cm while the larger tiles reside with an outer radius of 193 cm as shown in Figure 2.14 This is equivalent to a pseudo-rapidity range of $2.1 < \eta < 3.6$ for the small tiles and $3.4 < \eta < 5.0$ for the large tiles. Each scintillator tile is constructed from 1 cm thick Kuraray SCSN-81 scintillator material. The sides of the tiles are painted with a reflective white paint and covered by a 1 μm thick aluminized mylar on the surface. The tile is finished by wrapping it with 10 μm thick black construction paper to seal it from outside light.

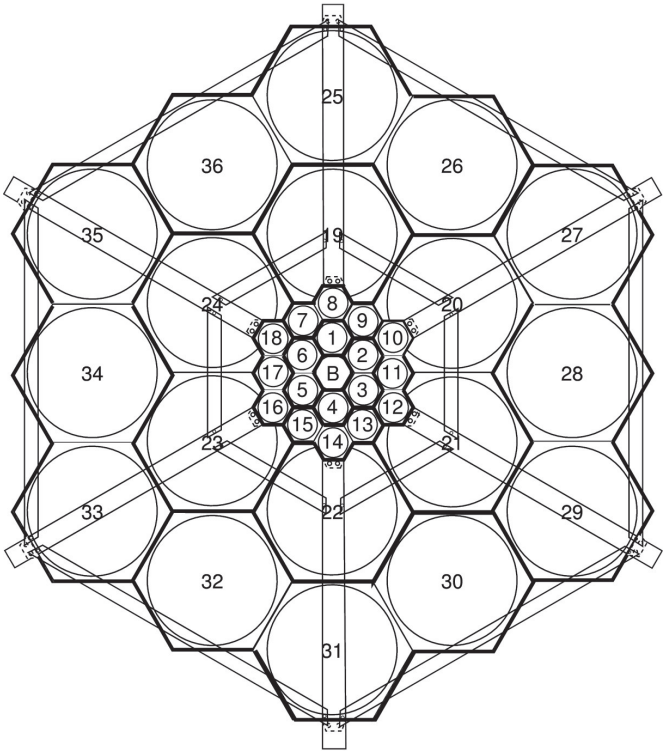

Figure 2.14: Schematic layout of the BBC detector tiles. The central small tile denoted by B is left empty to allow for the beam pipe.

The BBC detectors perform different roles in data taking such as trigger detectors, absolute and relative luminosity monitors, vertex finders, and local polarimeters. Rejecting events which do not have at least one small tile coincidence given within an allotted time window, reduces the amount of beam-gas events recorded. The fast response of the BBC detectors allow them to be used for event triggering which includes the L0 trigger and minimum bias trigger. The primary vertex can be determined from the measured time difference between the two BBC detector signals in a beam-collision event and known locations of the detector planes. The combined BBC acceptance amounts to about 53% of the total proton-proton cross section of 51 mb at $\sqrt{s} = 200$ GeV and the coincidence counting rate from the BBC detectors is used to determine the absolute luminosity, relative luminosity

and local polarimetry for polarized beam configuration [Kir05, Kir03].

2.2.4 ZDC

Zero Degree Calorimeters (ZDCs) are hadronic tungsten calorimeters used for detecting primarily neutrons. Two ZDC detectors are located 18 m away, past the DX magnets, on either side from the interaction point as shown in Figure 2.15. The DX magnets bend the charged particles allowing mostly neutral charged par-

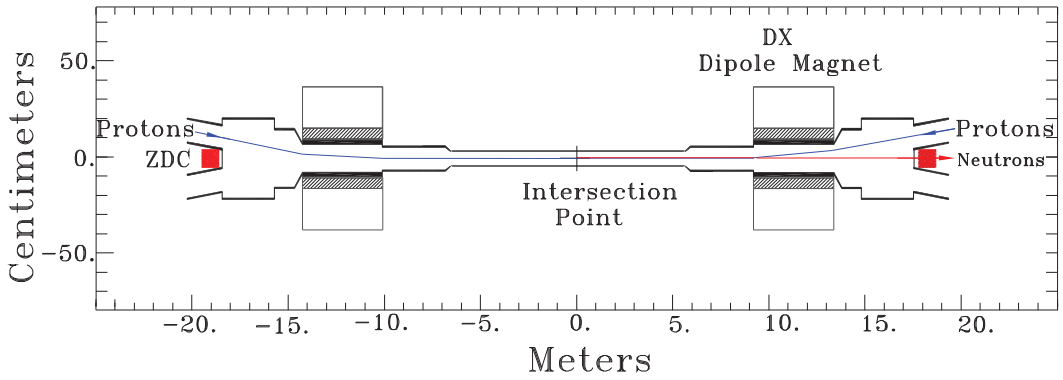

Figure 2.15: Schematic layout of the ZDC detector at STAR. The red boxes show the location of the ZDC detectors. The charged proton beam shown by the blue line are bent by the DX magnets allowing only neutrons shown by the red line to traverse into the ZDC detectors.

ticles to hit the ZDC detectors. The ZDC detectors sample with a transverse area of 10×13.6 cm^2 with respect to the beam. ZDCs are composed of three modules made from alternating layers of tungsten absorber and Cerenkov fiber ribbons placed 45° relative to the incident beam as shown in Figure 2.16. The fiber angle optimize the collection of Cerenkov light produced from the secondary showers [Bai03]. A Shower Maximum Detector (SMD) resides between the first and second ZDC module. The SMD is composed of eight horizontal and seven vertical slats. Each horizontal(vertical) slat comprises of four(three) fiber strips. The signal collected from the strips go to 16-pixel multi-anode photomultiplier tubes.

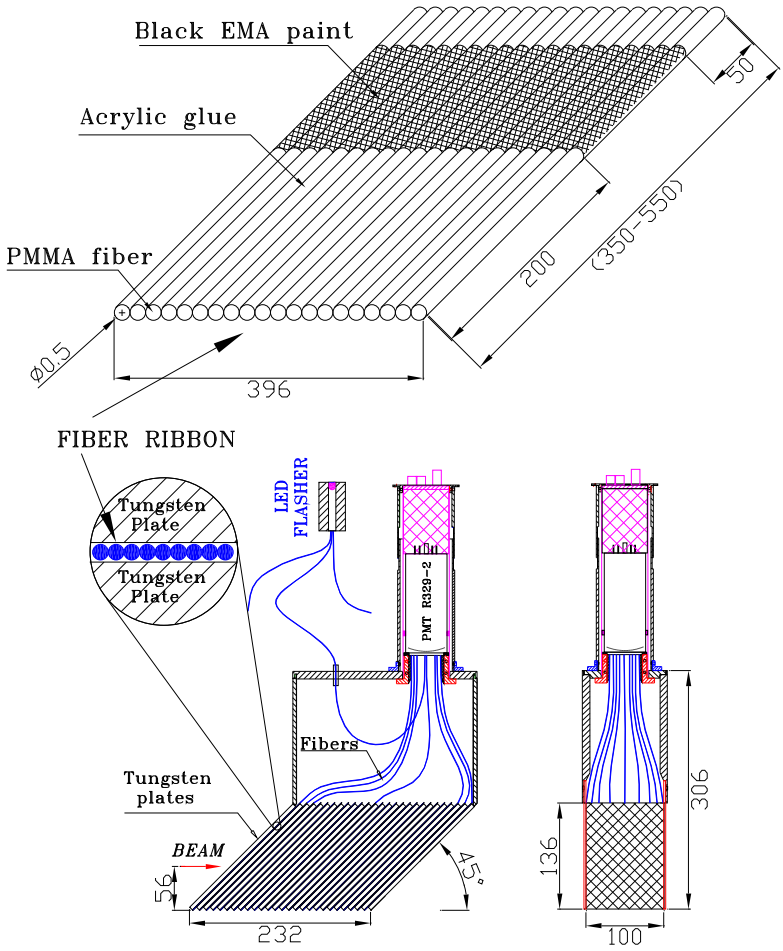

Figure 2.16: Schematic layout of a ZDC detector module. The diagram shows the angle the direction the tungsten absorber and PMMA fiber is located with respect to the beam.

The SMDs allow to determine the initial shower positions. The ZDC detectors are used for triggering events including minimum bias trigger events. During run year 2009, the ZDC-SMDs were utilized as a local polarimeters [Bit09].

2.2.5 Local Polarimetry

Local polarimetry measurements were performed at the STAR interaction region during both beam operation with transverse and longitudinal polarizations. The

currents of the spin rotators during longitudinal data taking periods are tuned using the CNI polarization values and local polarimetry measurements. The local polarimetry measurements are subsequently used to monitor any residual transverse polarization components. The BBC local polarimetry measurements were confirmed by measurements with the ZDC-SMD detectors for the data presented in this dissertation. The BBC detectors are readout with a scaler system, allowing to collect orders of magnitude better statistics in a shorter period of time than the ZDC-SMD for run year 2009. The ZDC measurement, however, has about a one order of magnitude larger analyzing power. Dedicated runs were performed for ZDC-SMD local polarimetry data.

The analyzing power, A_N, is defined by the ratio of the raw asymmetry, ϵ, and the beam polarization, P_{beam},

$$A_N = \frac{\epsilon}{P_{beam}}. \tag{2.7}$$

Three asymmetries can be extracted from the BBC and ZDC-SMD detector data. The geometrical asymmetry

$$\epsilon_{geo} = \frac{\sqrt{N_L^+ N_L^-} - \sqrt{N_R^+ N_R^-}}{\sqrt{N_L^+ N_L^-} + \sqrt{N_R^+ N_R^-}}, \tag{2.8}$$

luminosity asymmetry

$$\epsilon_{lum} = \frac{\sqrt{N_L^+ N_R^+} - \sqrt{N_L^- N_R^-}}{\sqrt{N_L^+ N_R^+} + \sqrt{N_L^- N_R^-}}, \tag{2.9}$$

and physics asymmetry

$$\epsilon_{phys} = \frac{\sqrt{N_L^+ N_R^-} - \sqrt{N_L^- N_R^+}}{\sqrt{N_L^+ N_R^-} + \sqrt{N_L^- N_R^+}}, \tag{2.10}$$

where $N_{L(R)}$ are the number of counts in the left(right) region and the polarization state is denoted by the superscript $+(-)$. The above asymmetries are expressed in the so-called square-root form. In this form, many false asymmetries cancel and,

in particular, false asymmetries from luminosity and geometrical acceptance are canceled for the physics asymmetry measurement. The asymmetry measurements are performed for each beam and each run. For run year 2006 and 2009, the counts for each polarization state on each beam are defined as

$$\begin{aligned} N_Y^+ &= n^{++} + n^{+-}, \\ N_Y^- &= n^{--} + n^{-+}, \\ N_B^+ &= n^{++} + n^{-+}, \\ N_B^- &= n^{--} + n^{+-}, \end{aligned} \tag{2.11}$$

where $Y(B)$ denote the yellow(blue) beam and n is the number of counts for the yellow and blue beam polarization state are denoted by the superscripts "$++$", "$-+$", "$+-$", and "$--$" respectively. In addition to the left-right asymmetries, similar asymmetries for top-bottom can also be extracted. The geometrical and luminosity asymmetries were typically not far from zero, as were the top-bottom physics asymmetries. A sizeable left-right physics asymmetry is expected for transverse polarization. The left-right physics asymmetry in the local polarimeters vanishes as the rotator magnets are powered, while the polarization value determined with the CNI persists.

The scaler data from the BBC detectors are used for the local polarimetry analysis [Kir05, Whi08]. The small tiles measure a sizeable asymmetry of 10^{-3}. Multiple tiles may receive a hit in a single beam collision event. Figure 2.17 shows the selection rules for a right scattering event in a left-right asymmetry measurement. An event is considered a right scattered event if at least one right tile shown in green is hit and no left tiles shown in red are hit. The top and bottom tiles shown in blue are ignored during the selection process. A similar approach is taken when selecting events for a top-bottom asymmetry. The top and bottom tiles are used for determining the scattered region while the left and right tiles are

ignored.

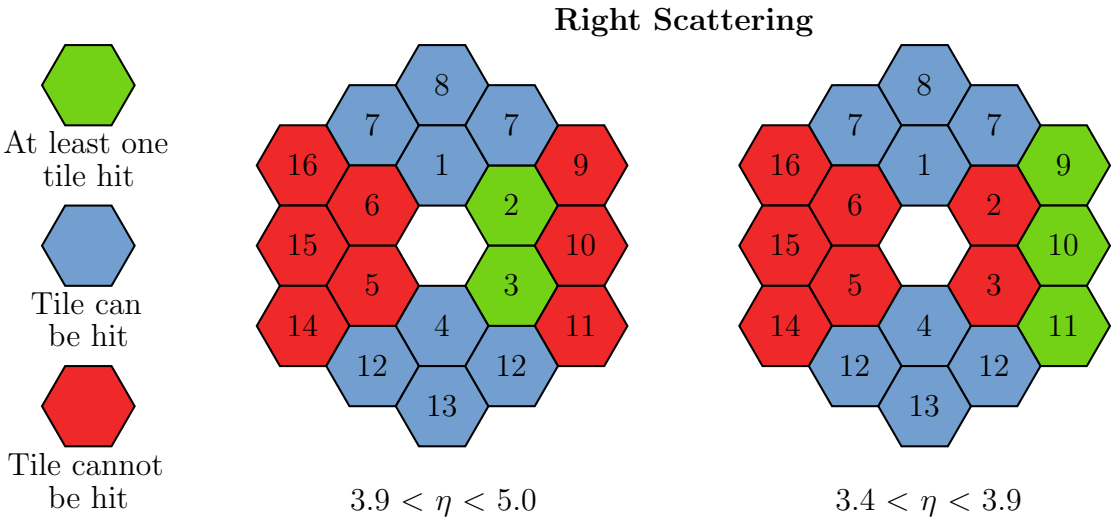

Figure 2.17: Diagram of BBC right scattering event selection rule for asymmetry measurements. Only right tiles shown in green can contain a hit while the tiles shown in red are not allowed to contain any hits. The top and bottom tiles shown in blue are not considered during the event selection.

As mentioned above, in run year 2009, the ZDC-SMD was utilized as a local polarimeter in addition to the BBC detectors. Previous experiments have shown the viability of using forward region calorimeters as local polarimeters. An experiment in IP12 was performed which measured the neutron production in the forward region [Baz07]. The detectors were positioned after the DX magnets, similar to the ZDC detectors at STAR. The PHENIX Collaboration have also performed local polarimetry analysis using their ZDC detectors [Tog08]. A polarimetry study was performed with the ZDC-SMD at STAR using a data sample from run year 2004 [Bit09].

For run year 2009, the slat ADC values from the ZDC-SMD were used. Pedestal and gain corrections are performed before imposing a minimum threshold on the ADC values for all SMD slats. The vertical and horizontal slat with the highest

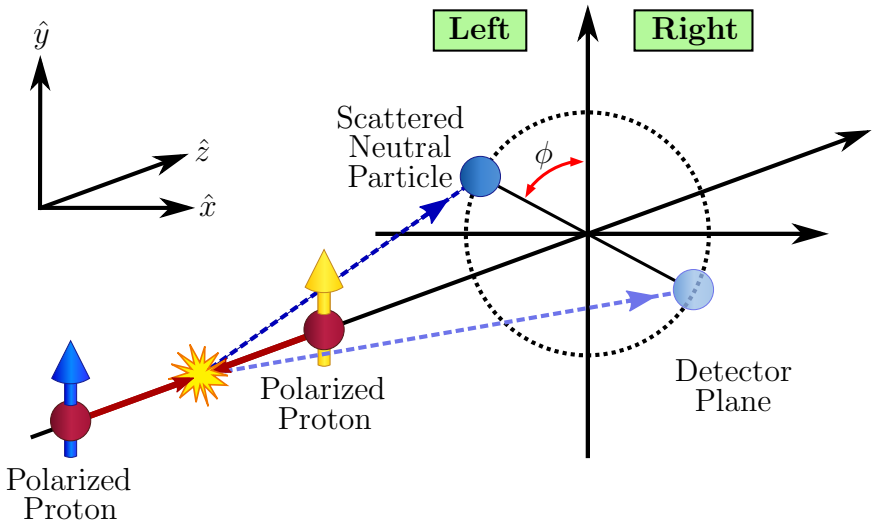

Figure 2.18: Diagram of transverse single spin asymmetry. The azimuthal angle from the detected neutrons is defined counter clockwise from the vertical direction.

ADC values for the event from the SMD are used as the position of the neutral particle. The 7 vertical and 8 horizontal slats allow to create a position matrix. For left-right asymmetries, the vertical slats 1-3 and 5-7 are combined to define the left-right regions while the horizontal slats 1-4 and 5-8 are combined to define the top-bottom regions for top-bottom asymmetries. In addition to measuring the geometrical, luminosity, and physics analyzing powers, the SMD allows to measure the azimuthal left-right physics analyzing power as shown in Figure 2.18. The SMD matrix and the defined sub-groups used for the azimuthal left-right azimuthal physics asymmetry are shown Figure 2.19. A left-right physics asymmetry measurement was performed for each sub-group. The left-right physics asymmetries are plotted as a function of the azimuthal angle and a sine function was fitted. The analyzing power is extracted by dividing the amplitude of the fitted function by the beam polarization.

The transverse polarized protons are rotated by the spin rotators fore and aft the STAR interaction point to perform longitudinally polarized proton-proton

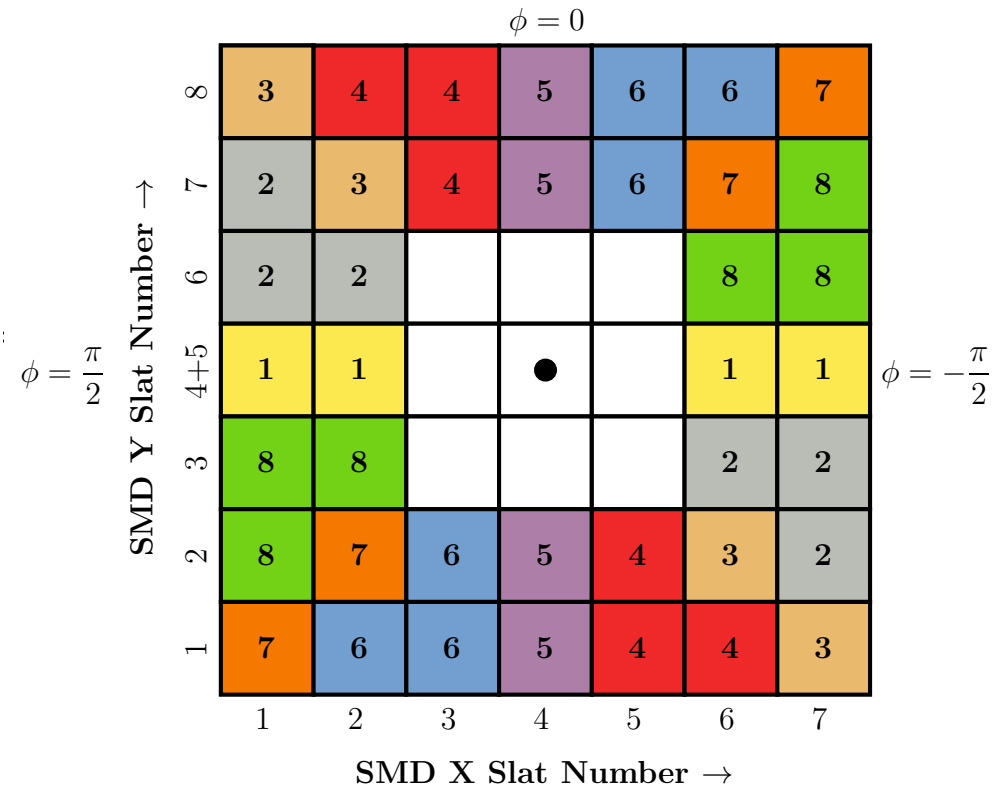

Figure 2.19: Diagram of the ZDC-SMD position matrix. Horizontal slats 4 and 5 are merged. For the azimuthal left-right physics asymmetries, the matrix is further broken to 8 sub-groups. Each sub-group is labeled by the group number and are color coded.

collisions. For longitudinally polarized proton collisions, the residual vertical and azimuthal transverse polarization components can be extracted using the left-right and top-bottom physics asymmetry results from the local polarimeters. The residual transverse azimuthal and vertical polarization angles from the longitudinally polarized beam are extracted using

$$\phi = \tan^{-1}\left[\frac{\epsilon_{LR}}{\epsilon_{TB}}\right], \tag{2.12}$$

$$\theta = \sin^{-1}\left[\frac{P_{beam,T}}{P_{beam}}\right], \tag{2.13}$$

where ϵ_{LR} and ϵ_{TB} are the left-right and top-bottom physics asymmetries, $P_{beam,T}$ is the transverse beam polarization component and P_{beam} is the beam polarization.

The transverse beam polarization component and beam polarization ratio is related to the analyzing powers

$$\left(\frac{P_{beam,T}}{P_{beam}}\right)^2 = \left(\frac{A_{LR}^{long}}{A_{LR}^{trans}}\right)^2 + \left(\frac{A_{TB}^{long}}{A_{LR}^{trans}}\right)^2, \tag{2.14}$$

where A_{LR} and A_{TB} are the analyzing powers for left-right and top-bottom. The longitudinal(transverse) beam polarization state at the interaction point is denoted by the superscript $long(trans)$.

2.2.6 Relative Luminosity

The extraction of spin asymmetries from the observed yields requires the classification of the recorded events by beam spin configuration, so called spin-sorting. In addition, corrections are made for the luminosities for the different beam-spin configurations. These corrections are implemented through relative luminosity ratios, defined by

$$R_1 = \frac{\mathcal{L}^{++} + \mathcal{L}^{+-}}{\mathcal{L}^{--} + \mathcal{L}^{-+}}, \quad R_2 = \frac{\mathcal{L}^{++} + \mathcal{L}^{-+}}{\mathcal{L}^{--} + \mathcal{L}^{+-}}, \quad R_3 = \frac{\mathcal{L}^{++} + \mathcal{L}^{--}}{\mathcal{L}^{+-} + \mathcal{L}^{-+}},$$
$$R_4 = \frac{\mathcal{L}^{++}}{\mathcal{L}^{--}}, \qquad R_5 = \frac{\mathcal{L}^{+-}}{\mathcal{L}^{--}}, \qquad R_6 = \frac{\mathcal{L}^{-+}}{\mathcal{L}^{--}},$$

where $\mathcal{L}$ is the sampled luminosity with superscripts, $+(-)$, defining the proton spin state for the yellow and blue beams respectively. Coincident signals from the BBC and ZDC detectors afore and aft the IP are counted to determine the relative luminosity ratios [Kir03]. These counts are recorded with a fast scaler system for each STAR run of approximately 20-30 minutes duration. Besides coincident counts, single counts are recorded to allow for corrections for event pile-up and background using techniques [Cro00] similar to those employed at the Tevatron CDF experiment. The statistical uncertainty of BBC measurements is at the level of 10^{-4} in $R_{1\cdot6}$ for each run. Comparison with the (independent) ZDC measurements gives a systematic uncertainty estimate at the level of 10^{-3}. Further details

of the run 2006 relative luminosity analysis may be found in Ref. [Sak11]. Additional details on the run 2009 relative luminosities may be found in Ref. [Hay11].

CHAPTER 3

Analysis

3.1 $\Lambda(\overline{\Lambda})$ and K^0_s Reconstruction

The particles of primary interest for this analysis, the spin-$\frac{1}{2}$ $\Lambda(\overline{\Lambda})$ hyperons, weakly decay to a p and π^- ($\overline{p}$ and π^+) with a branching ratio (BR) of $63.9 \pm 0.5\%$ [Ams08]. The spin-zero K^0_s meson decays, also weakly and with a similar decay topology, to a π^+ and a π^- with a BR of $69.20 \pm 0.05\%$ [Ams08]. The spin-zero K^0_s sample are used for control measurements. In this section, the reconstruction procedure for both $\Lambda(\overline{\Lambda})$ and K^0_s particles is presented.

3.1.1 Reconstruction Algorithm

The neutral $\Lambda(\overline{\Lambda})$ and K^0_s particles are reconstructed via their decay topology by combining a measured track with an oppositely charged particle at a secondary vertex. The decay particles, protons and pions, are identified using the particle identification method presented in Section 2.2.1. The decay length is the average distance a particle travels before decaying. The average proper decay length for Λ is 7.89 cm [Ams08] and 2.68 cm [Ams08] for K^0_s particles. To identify potential decay vertices, the charged particle helices observed with the TPC were extrapolated beyond the inner field cage of the TPC towards the primary vertex.

The Λ and K^0_s particles have similar decay topologies, allowing one to use a

common reconstruction scheme in the laboratory frame as shown in Figure 3.1. The reconstructed particle is referred to as a V^0 after its zero charge and the shape of its decay particle trajectories. The charged decay products are denoted by $(+)$ for positive, and $(-)$ for negative charged particles. The continuous lines indicate the reconstructed particle tracks from the detected TPC points which are then extrapolated back towards the primary vertex and are shown in blue dashed lines. The Distance of Closest Approach (DCA) is the shortest distance between two trajectories in three dimensional coordinate space. The positions for the decay particles at DCA to the decay vertex are shown in Figure 3.1 as the red and blue points, and are denoted by r^+ for the positive and r^- for the negative particle. The momentum vector, $\mathbf{p}_{V^0}$, is determined by summing the reconstructed momentum vectors $\mathbf{p}^{+(-)}$ of the decay particles at the decay vertex,

$$\mathbf{p}_{V^0} = \mathbf{p}^+ + \mathbf{p}^-. \tag{3.1}$$

An initial set of topological and kinematic requirements to the reconstructed V^0 candidate and decay products reduces combinatorial background. The reconstructed decay vertex position, r_{DV}, shown as the orange point in Figure 3.1, is defined as the midpoint distance between the decay particles at their DCA,

$$r_{DV} = \frac{r^+ + r^-}{2}. \tag{3.2}$$

The selection of events with a maximum reconstructed DCA of 1.5 cm between the decay particles reduces the number and fraction of incorrectly identified decay vertices in the retained event sample. The angle between the V^0 momentum and the vector pointing from the primary vertex to the decay vertex, $\mathbf{r}$, is given by

$$\phi_{RP} = \cos^{-1}\left[\frac{\mathbf{r}\cdot\mathbf{p}_{V^0}}{|\mathbf{r}|\,|\mathbf{p}_{V^0}|}\right], \tag{3.3}$$

is required to be small so as to select V^0 candidates moving outward from the primary vertex and collinear to $\mathbf{r}$. Two additional topological quantities, the DCA

of V^0 to the primary vertex and V^0's decay length are derived using

$$\text{DCA } V^0\text{–PV} = \big||\mathbf{r}|\sin(\phi_{RP})\big|, \tag{3.4}$$

$$\text{Decay Length} = \big||\mathbf{r}|\cos(\phi_{RP})\big|. \tag{3.5}$$

An upper limit on the DCA of V^0 to the primary vertex reduces the contamination of V^0's originating from so-called feed-down decays, an indirect source of Λ and $\overline{\Lambda}$ hyperons originating from the decays of heavier hyperons. The decay length of the V^0 in the laboratory frame is typically of the order of several (tens of) cm because of the time scale for weak decays. The requirement of a lower threshold on the decay length ensures that the decay vertex is away from the primary vertex, and thus reduces backgrounds from processes such as $\gamma \rightarrow e^+ + e^-$ in which the decay tracks were misidentified. The DCA of the decay particles to the primary vertex is determined by extrapolation of their reconstructed helix trajectory. A minimum distance for the DCA of the decay particles to the primary vertex is imposed to reduce the combinatorial from decay particles originating from the primary interaction vertex whose trajectories happen to intersect randomly with those of another particle.

The energy-momentum four-vector,

$$P^\mu = (E, p_x, p_y, p_z), \tag{3.6}$$

for each decay particle is reconstructed using the momentum vector at the decay vertex and the invariant mass [Ams08] of the identified particle species. The sum of the energy-momentum four-vectors of both decay products gives the energy-momentum four-vector of the V^0. The invariant mass, M_{V^0}, is reconstructed as follows,

$$M_{V^0}c = \sqrt{\left(E^+ + E^-\right)^2 - \left(\mathbf{p}^+ + \mathbf{p}^-\right)^2}. \tag{3.7}$$

When its value is in a range around the mass of interest, the V^0 particle is retained for further analysis.

	$\Lambda(\overline{\Lambda})$	K^0_s
DCA C^+-PV cm	> 0.15	> 0.15
DCA C^--PV cm	> 0.15	> 0.15
DCA between daughters cm	< 1.5	< 1.5
DCA V^0-PV cm	< 1.5	< 1.5
Decay Length cm	> 3.0	> 2.0
ϕ_{RP} rad	< 0.25	< 0.25
M_{V^0} Range GeV	$1.075 < M_\Lambda < 1.160$	$0.380 < M_{K^0_s} < 0.620$

Table 3.1: Initial topological and kinematic threshold values

An initial set of relaxed topological and kinematic selections are chosen to reduce the bulk of the combinatorial background. The topological and kinematic threshold values are referred to as selection cut values. Table 3.1 summarizes the initial relaxed selection cut parameters and their values. Although the combinatorial background is large, an invariant mass peak is visible for both $\Lambda(\overline{\Lambda})$ and K^0_s as shown in Figures 3.2(a)–(f) for data from run year 2006 and 2009. The reconstructed V^0 candidates that pass the initial selection cuts are saved for further analysis.

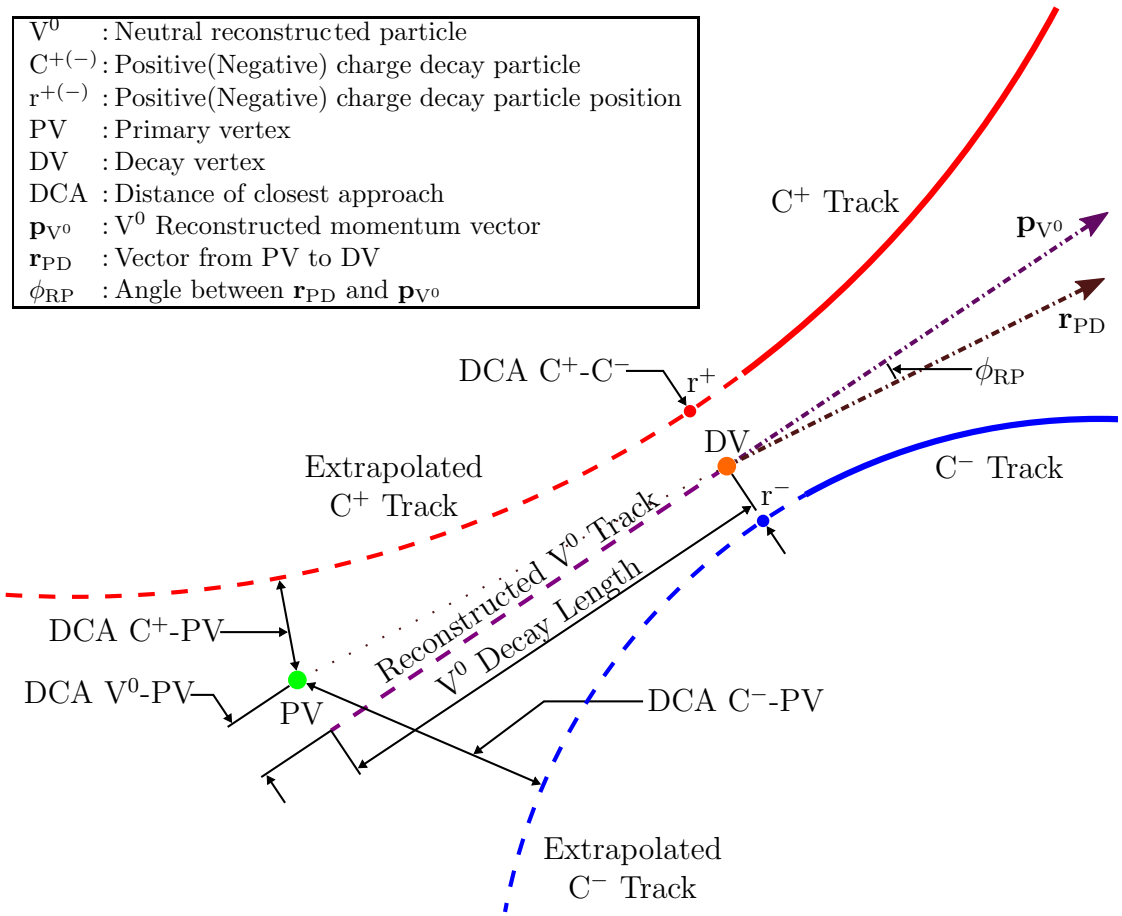

Figure 3.1: Reconstruction diagram for the hadronic decays of the Λ, $\overline{\Lambda}$, and K^0_s particles. In each case, jointly denoted by V^0, the particle decays into two oppositely charged particles. The red and blue points give the position for the decay particles when their reconstructed tracks are nearest to each other. This point determines the decay vertex, DV, as described in the text.

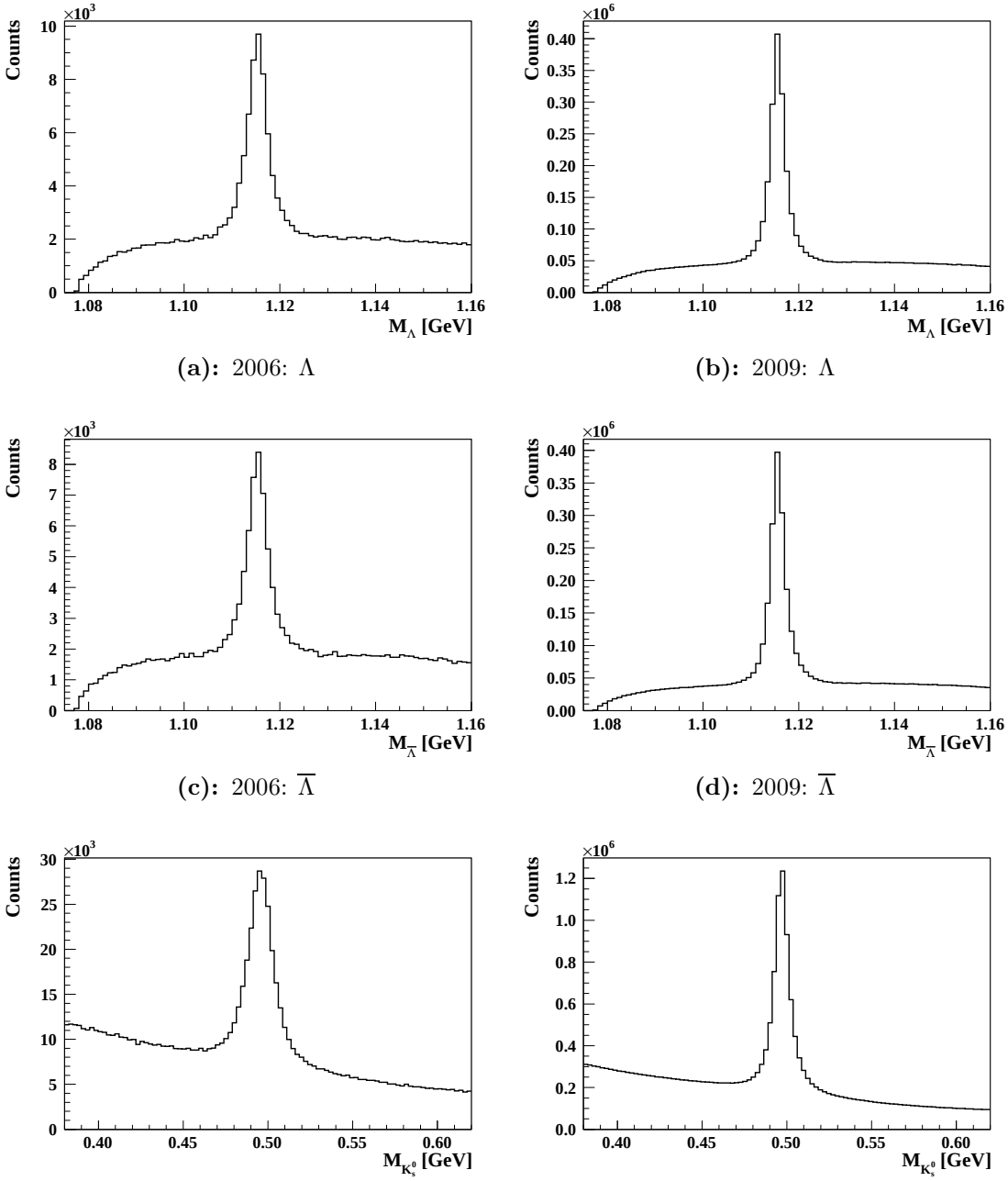

(a): 2006: Λ **(b):** 2009: Λ

(c): 2006: $\overline{\Lambda}$ **(d):** 2009: $\overline{\Lambda}$

(e): 2006: K^0_s **(f):** 2009: K^0_s

Figure 3.2: Invariant mass spectra of $\Lambda(\overline{\Lambda})$ and K^0_s candidates for run year 2006 and 2009 that satisfied triggers of interest and initial selections cuts in Table 3.1.

3.1.2 Selection Parameter Tuning to Further Reduce Combinatorial Background

The background in the initial V^0 candidate yields can be further reduced by tuning the selection cut parameters. For example, several of the topological and kinematic parameters are expected to vary with transverse momentum p_T. By separating the V^0 particles for different p_T intervals, the selection cuts can be tuned for each p_T interval.

The signal and background region in the invariant mass spectrum are first defined for each V^0 species prior to tuning the topological and kinematic parameter values. The background region for the three V^0 species is defined by two fixed sideband ranges in the invariant mass spectrum on either side of the nominal mass for all p_T intervals . The signal region is determined for each p_T interval by fitting a Lorentzian function to the mass spectrum. The signal range is defined as 1.75 times the full width half maximum (FWHM) centered at the fitted pole mass value for each p_T interval. Table 3.2 shows the signal and background range values for all V^0 species for run year 2006 and 2009.

The combinatorial background in the initial particle samples are further reduced prior to tuning the selection cut parameters. A minimum threshold of 0.2 rad is imposed to the opening angle of the decay daughter tracks with $n\sigma_e > -2$ to reduce electron contamination. By identifying V^0 candidates with an improbable decay length, one can further remove backgrounds from the particle yields [Tan86]. The decay length probability, P_d, for V^0 is defined as

$$P_d = 1 - e^{-\frac{M_{V^0} \cdot d}{|\mathbf{p_{V^0}}| \cdot c \cdot \tau}}, \tag{3.8}$$

where

	Λ	$\overline{\Lambda}$	K^0_s
p_T GeV	Signal Range GeV		
	JP1–6		
$0.5 \leq p_T < 1.0$	[1.1092, 1.1209]	[1.1102, 1.1199]	[0.4751, 0.5111]
$1.0 \leq p_T < 1.5$	[1.1094, 1.1208]	[1.1095, 1.1206]	[0.4775, 0.5133]
$1.5 \leq p_T < 2.0$	[1.1097, 1.1210]	[1.1094, 1.1213]	[0.4779, 0.5148]
$2.0 \leq p_T < 2.5$	[1.1091, 1.1219]	[1.1094, 1.1216]	[0.4777, 0.5159]
$2.5 \leq p_T < 3.0$	[1.1090, 1.1221]	[1.1096, 1.1218]	[0.4769, 0.5174]
$3.0 \leq p_T < 4.0$	[1.1083, 1.1232]	[1.1076, 1.1239]	[0.4749, 0.5195]
$4.0 \leq p_T$	[1.1047, 1.1274]	[1.1052, 1.1271]	[0.4656, 0.5302]
	JP1–9		
$0.5 \leq p_T < 1.0$	[1.1122, 1.1190]	[1.1124, 1.1190]	[0.4875, 0.5059]
$1.0 \leq p_T < 1.5$	[1.1119, 1.1192]	[1.1120, 1.1192]	[0.4860, 0.5082]
$1.5 \leq p_T < 2.0$	[1.1114, 1.1198]	[1.1114, 1.1199]	[0.4840, 0.5105]
$2.0 \leq p_T < 2.5$	[1.1106, 1.1207]	[1.1106, 1.1207]	[0.4816, 0.5130]
$2.5 \leq p_T < 3.0$	[1.1099, 1.1216]	[1.1097, 1.1218]	[0.4797, 0.5152]
$3.0 \leq p_T < 4.0$	[1.1084, 1.1233]	[1.1085, 1.1232]	[0.4772, 0.5178]
$4.0 \leq p_T$	[1.1049, 1.1275]	[1.1053, 1.1270]	[0.4686, 0.5273]
	L2JH–9		
$0.5 \leq p_T < 1.0$	[1.1120, 1.1192]	[1.1123, 1.1191]	[0.4872, 0.5063]
$1.0 \leq p_T < 1.5$	[1.1117, 1.1193]	[1.1118, 1.1194]	[0.4856, 0.5086]
$1.5 \leq p_T < 2.0$	[1.1112, 1.1200]	[1.1112, 1.1201]	[0.4836, 0.5110]
$2.0 \leq p_T < 2.5$	[1.1102, 1.1210]	[1.1105, 1.1209]	[0.4813, 0.5133]
$2.5 \leq p_T < 3.0$	[1.1094, 1.1221]	[1.1095, 1.1220]	[0.4793, 0.5154]
$3.0 \leq p_T < 4.0$	[1.1079, 1.1237]	[1.1081, 1.1236]	[0.4764, 0.5184]
$4.0 \leq p_T$	[1.1048, 1.1275]	[1.1048, 1.1275]	[0.4675, 0.5282]
p_T GeV	Background Range GeV		
$0.5 \leq p_T$	[1.076, 1.089]	[1.076, 1.089]	[0.382, 0.416]
	[1.146, 1.159]	[1.146, 1.159]	[0.584, 0.618]

Table 3.2: Initial signal and background ranges for run year 2006 and 2009 by trigger condition.

$$
\begin{aligned}
c &= \text{speed of light,} \\
d &= \text{V}^0 \text{ decay length,} \\
\text{M}_{\text{V}^0} &= \text{V}^0 \text{ invariant mass,} \\
\tau &= \text{V}^0 \text{ mean lifetime,} \\
\mathbf{p}_{\mathbf{V}^0} &= \text{V}^0 \text{ momentum.}
\end{aligned}
$$

A peak is observed near one for P_d as shown in Figure 3.3(a). The increase in V^0 particles near one can be attributed to background as seen from Figure 3.3b. A

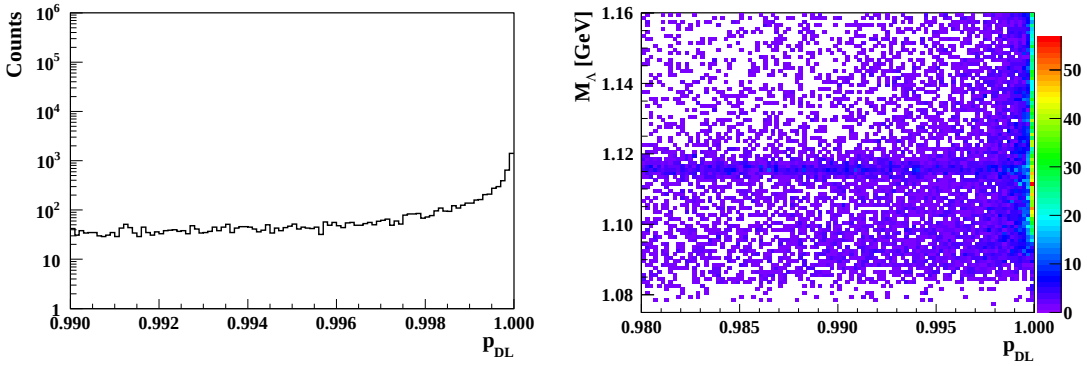

(a): Decay length probability.

(b): Decay length probability vs. invariant mass

Figure 3.3: Decay length probability for Λ candidates with $\text{p}_\text{T} < 0.5$ GeV from data obtained in run year 2006.

maximum value of 0.999 is imposed on the decay length probability. The majority of rejected V^0 candidates are made up of background V^0 particles as shown in Figures 3.4(a)–(f) for both run years. The visible mass peaks come from V^0 candidates which reside within the background and disappear after imposing the tuned parameter thresholds.

The following selection cut parameters are tuned per p_T interval to further reduce the background levels:

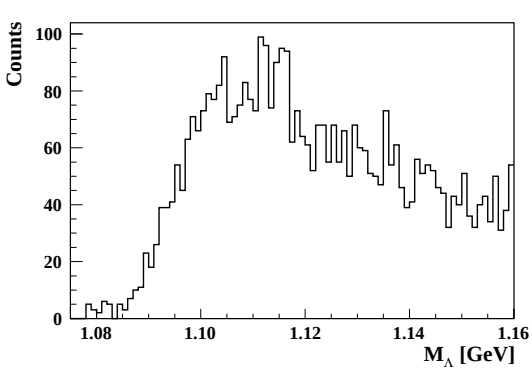

(a): 2006: Λ

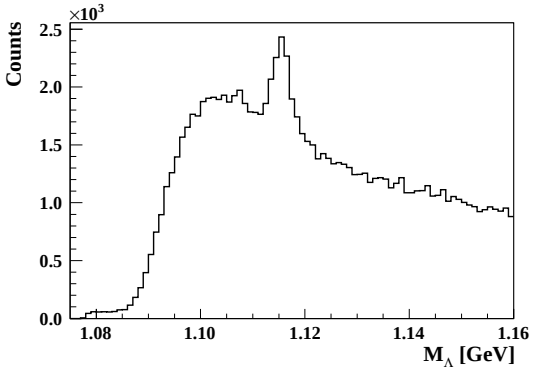

(b): 2009: Λ

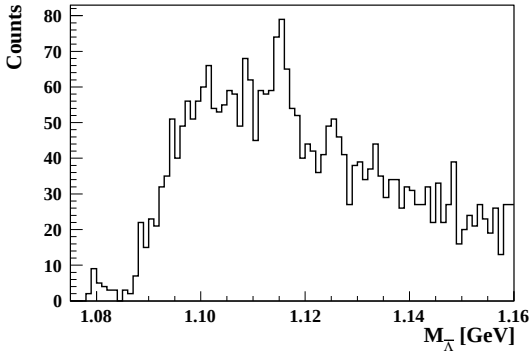

(c): 2006: $\overline{\Lambda}$

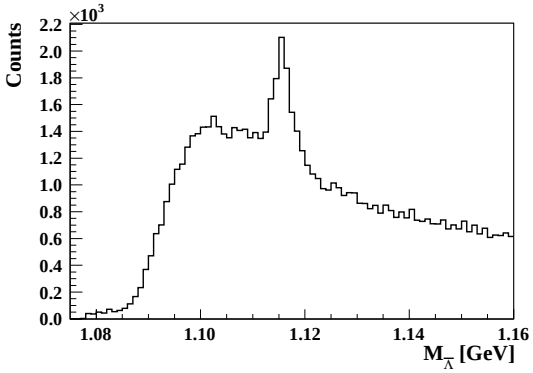

(d): 2009: $\overline{\Lambda}$

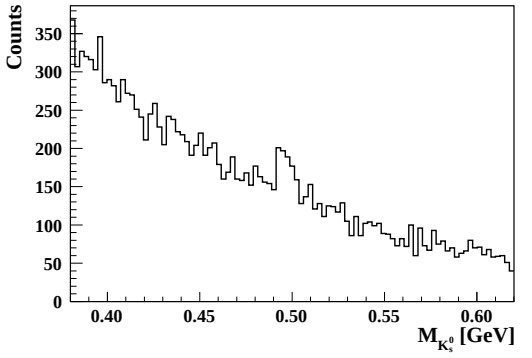

(e): 2006: K^0_s

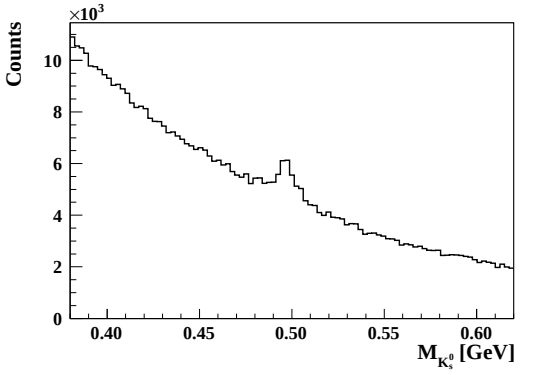

(f): 2009: K^0_s

Figure 3.4: Invariant mass yields for rejected $\Lambda(\overline{\Lambda})$ and K^0_s by decay length probability constraint for run year 2006 and 2009 which satisfied triggers of interest for $0.5 < p_T$ GeV.

DCA C^--C^+cm ,

DCA V^0-PV cm ,

ϕ_{RP} rad ,

Decay Length (DL) cm ,

DCA C^+-PV cm ,

DCA C^--PV cm .

The selection cut parameters are tuned by first sweeping the selection parameters for a selected range. In each step, V^0 particles that satisfy the selection cut requirements and reside in either the invariant mass signal or the background region are counted. The background counts are scaled using

$$\text{Scaled Bkg. Counts} = \text{Bkg. Counts} \times \frac{\text{Sig. Range}}{\text{Bkg. Range}}, \tag{3.9}$$

such that the invariant mass signal and background range are equal in size. The signal and background counts are each normalized using the maximum value for each region. A distribution,

$$\epsilon = (\text{Normalized Sig.} - \text{Normalized Bkg.}) \times \text{Normalized Sig.}, \tag{3.10}$$

is calculated for each selection parameter and used to tune the selection parameter values. The multiplication by the normalized signal counts serves to preserve signal counts. The distributions of ϵ are not always smooth. A Lowess smoothing procedure is a local weighted regression method used to smooth the points and improve the determination of the selection cut value. The maximal point is not used but rather the value were the slope starts to level out towards the maximal value, again with the aim to preserve signal counts.

The DCA between the decay daughters, the angle ϕ_{RP} rad, the DCA between the $p(\overline{p})$ and the PV, and the DCA of the $\pi^+(\pi^-)$ to the PV are tuned separately for

the $\Lambda(\overline{\Lambda})$ and K^0_s samples. The decay length was tuned per p_T interval but was not imposed for $\Lambda(\overline{\Lambda})$ and K^0_s samples. A combined selection cut parameter threshold is also computed and imposed. The reject and accept regions for each selection cut parameter are scaled to have an equal range of size one each. The rejection region is scaled to fit in (0,1) while the acceptance region is scaled and shifted to reside within (1,2). The V^0 particle parameter values are also scaled according to what region they reside in. The selection parameters are multiplied and a minimum threshold value is determined using the same method for determining the individual selection cut parameters. The following combined condition is imposed for each V^0 species,

$$\begin{aligned} \text{Mix-Plus} &< (\text{DCA } C^+\text{-}C^-) \times (\text{DCA } V^0\text{-PV}) \times (\text{DL}) \times (\text{DCA } C^+) \times \phi_{\text{RP}}, \\ \text{Mix-Neg} &< (\text{DCA } C^+\text{-}C^-) \times (\text{DCA } V^0\text{-PV}) \times (\text{DL}) \times (\text{DCA } C^-) \times \phi_{\text{RP}}, \end{aligned}$$

Figures 3.5(a)–(f) show examples of the selection parameter vs. invariant mass 2D plots on the left column and their corresponding tuning plots generated using Equation 3.10 on the right column at $1.5 < p_T < 2.0$ GeV for run year 2006. The arrow on the top corner signifies the direction the threshold selection parameter is scanned for. The vertical red line is the maximal value while the green vertical line is the value chosen for the given slope criteria. The black points are the raw values while the red points are the Lowess smooth points used to determine both the red and green lines and the green line is set as the threshold value for p_T interval. Candidates residing within the red hatched area are rejected.

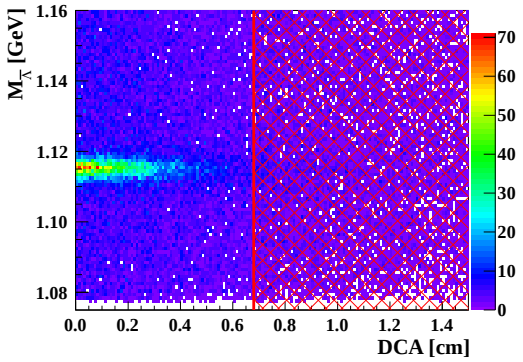

(a): $\overline{\Lambda}$: DCA $\overline{p}$-π^+

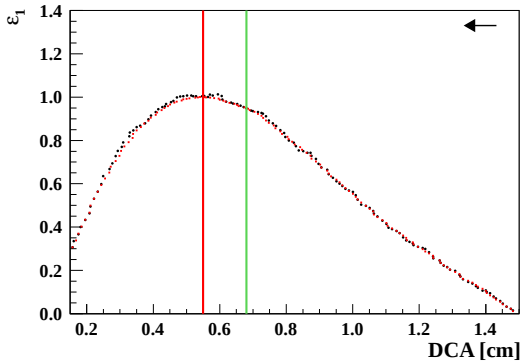

(b): $\overline{\Lambda}$: DCA $\overline{p}$-π^+

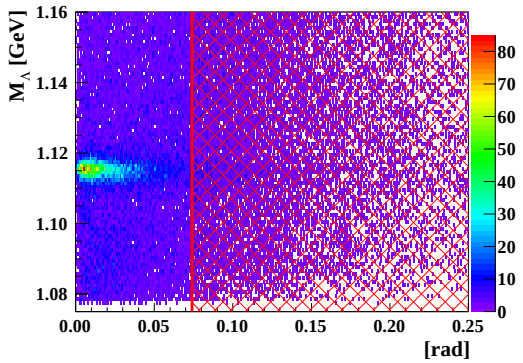

(c): Λ: ϕ_{RP}

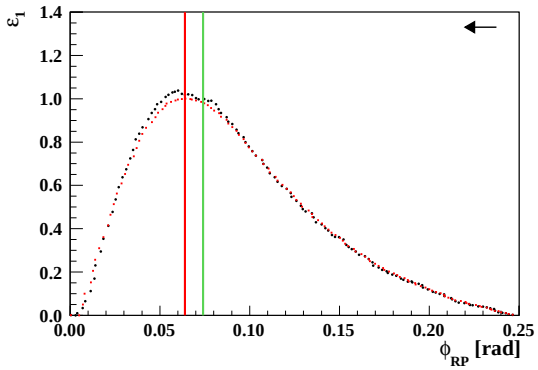

(d): Λ: ϕ_{RP}

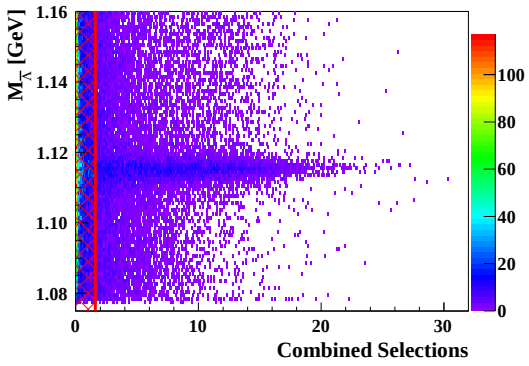

(e): $\overline{\Lambda}$: Combined Selections

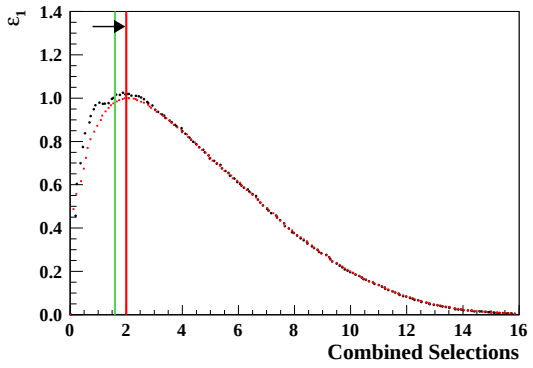

(f): $\overline{\Lambda}$: Combined Selections

Figure 3.5: 2D selection parameter versus invariant mass and tuning plots at $1.5 < \mathrm{p_T} < 2.0$ GeV for run year 2006. The vertical red line is the maximal value while the green vertical line is the value chosen for the given slope criteria. The threshold value used is given by the green vertical line. Candidates residing within the red hatched area are rejected.

3.1.3 Armenteros-Podolanski Relation

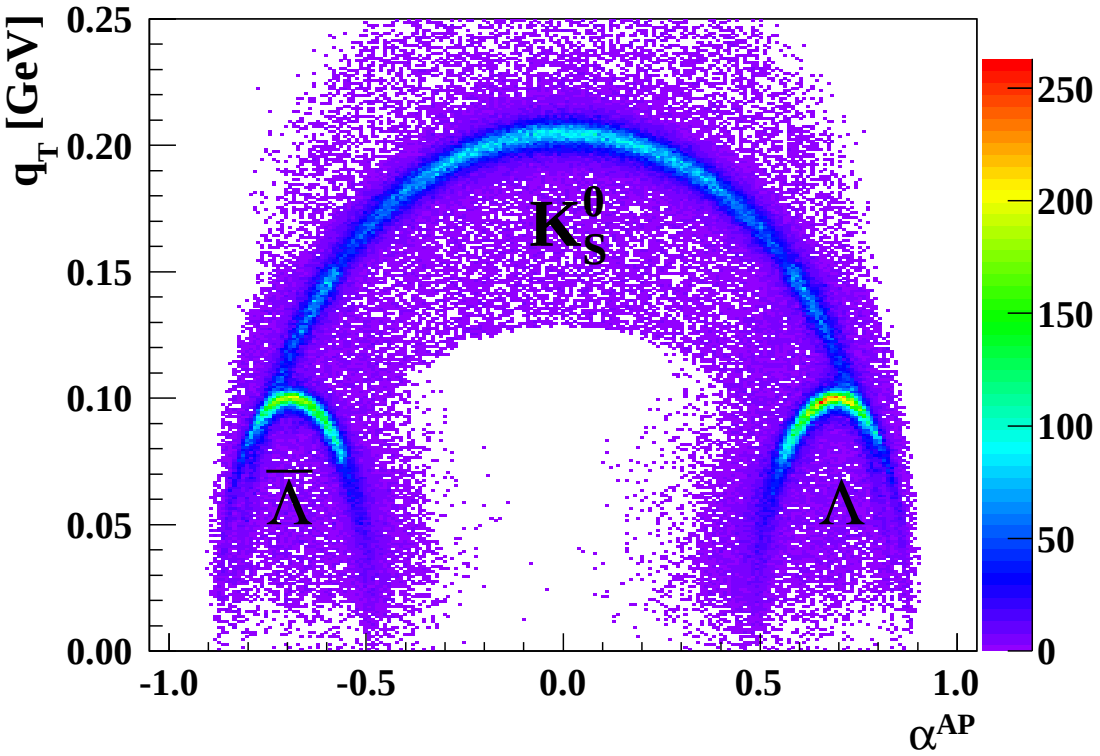

Figure 3.6: Run year 2006 Armenteros-Podolanski plot shows V^0 particles create visible structures. The Armenteros-Podolanski relation, α^{AP}, describes the asymmetry between the longitudinal momenta of the decay particles with respect to the direction of V^0 in laboratory frame. The quantity, $\mathbf{q}_T$, is the transverse momentum of the decay particles with respect to the direction of V^0 in laboratory frame.

The Armenteros-Podolanki relation, α^{AP}, describes the asymmetry between the longitudinal momenta of the decay particles with relation to the direction of V^0 in laboratory frame [Pod94], separating the V^0 particles into structures as illustrated in Figure 3.6. Two inertial frames are used to derive a parameterization of the Armenteros-Podolanski plot. The position and momentum measurements are taken in laboratory frame. By converting to a center of mass (CM) frame, a simplified description of the decay process can be used. Figure 3.7a shows a

V^0 decay in laboratory frame while Figure 3.7b shows the same decay in a CM frame. The CM frame, denoted by the (*) superscript, is created by boosting the laboratory frame with velocity, $\mathbf{v}$, determined from the V^0's momentum. This transformation places the V^0 at rest at the origin. The boost velocity,

$$\boldsymbol{\beta} = \frac{\mathbf{v}}{c}, \tag{3.11}$$

and Lorentz factor,

$$\gamma = \frac{1}{\sqrt{1-\boldsymbol{\beta}^2}}, \tag{3.12}$$

are used to transform between these inertial frames. $\boldsymbol{\beta}$ is collinear with $\mathbf{p}_{V^0}$ as seen from

$$\boldsymbol{\beta} \cdot \hat{\mathbf{q}}_L = \beta \hat{\mathbf{q}}_L \cdot \hat{\mathbf{q}}_L = \beta. \tag{3.13}$$

The momentum and energy for the V^0 and its decay particles in the CM frame are defined as

$$\begin{aligned} \mathbf{p}^*_{V^0} = 0 \quad &, \; E^{*2}_{V^0} = M^2_{V^0} c^4, \\ \mathbf{p}^*_{+} = \mathbf{p}^* \quad &, \; E^{*2}_{+} = m^2_{+} c^4 + \mathbf{p}^{*2} c^2, \\ \mathbf{p}^*_{-} = -\mathbf{p}^* \; &, \; E^{*2}_{-} = m^2_{-} c^4 + \mathbf{p}^{*2} c^2, \end{aligned} \tag{3.14}$$

and are used to define the energy-momentum four-vectors

$$P^{\mu *}_{V_0} = (M_{V^0} c, 0) \; , \; P^{\mu *}_{+} = \left(\frac{E^*_{+}}{c}, \mathbf{p}^* \right) \; , \; P^{\mu *}_{-} = \left(\frac{E^*_{-}}{c}, -\mathbf{p}^* \right), \tag{3.15}$$

where the subscripts $+(-)$ denote the particle charge.

The decay particle's momentum is projected longitudinally and transversely with respect to V^0's momentum in the CM frame. The momentum projections are denoted by $\mathbf{q}$ to differentiate them from the particle's momentum and are defined

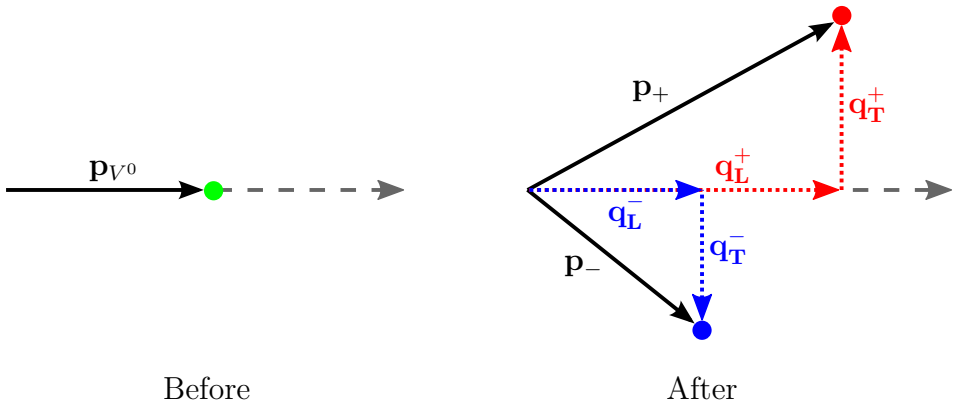

(a): Laboratory frame

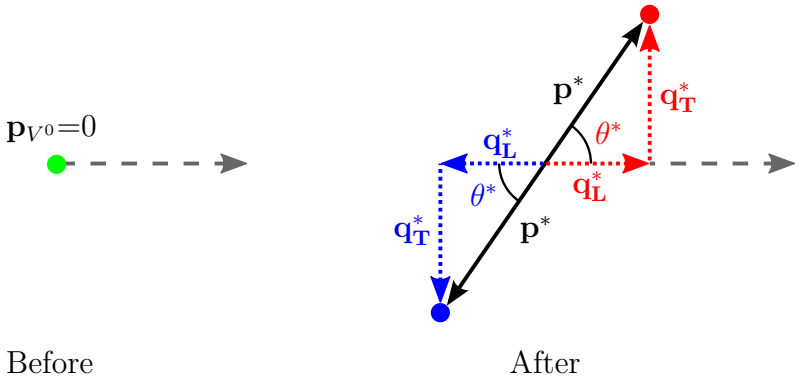

(b): Center of mass frame

Figure 3.7: V^0 decay in laboratory and center of mass inertial frames.

as

$$\mathbf{q}_L^* = |\mathbf{p}^*|\hat{\mathbf{q}}_L \cos\theta^*, \tag{3.16}$$

$$\mathbf{q}_T^* = |\mathbf{p}^*|\hat{\mathbf{q}}_T \sin\theta^*. \tag{3.17}$$

The definition of the projection vectors in the CM frame simplifies the vectors since they depend only on $\mathbf{p}^*$ and θ^* for both decay particles. In order to use the center of mass $\mathbf{q}_L^*$ and $\mathbf{q}_T^*$ for the Armenteros-Podolanski relation, the vectors are transformed to laboratory frame using a Lorentz transformation. The components in the transverse direction from the boost are unchanged in this transformation.

A Lorentz transformation tensor is used to transform $\mathbf{q}_L^*$ to the laboratory frame. The projected momentum vectors are defined in the laboratory frame as

$$\mathbf{q}_L = \frac{\gamma\boldsymbol{\beta}E^*}{c} + \gamma p^*\hat{\mathbf{q}}_L\cos\theta^*, \tag{3.18}$$

$$\mathbf{q}_T = p^*\hat{\mathbf{q}}_T\sin\theta^*. \tag{3.19}$$

The longitudinal components of the vectors specific to the decay particles are

$$\mathbf{q}_L^+ = \frac{\gamma\boldsymbol{\beta}E_+^*}{c} + \gamma p^*\hat{\mathbf{q}}_L\cos\theta^*, \tag{3.20}$$

$$\mathbf{q}_L^- = \frac{\gamma\boldsymbol{\beta}E_-^*}{c} - \gamma p^*\hat{\mathbf{q}}_L\cos\theta^*. \tag{3.21}$$

The Armenteros-Podolanski parameter, α^{AP}, in terms of the center-of-mass vectors is thus given by

$$\begin{aligned}\alpha^{AP} &= \frac{\left(E_+^* - E_-^*\right)}{M_{V^0}c^2} + \frac{2p^*\cos\theta^*}{\beta M_{V^0}c} \\ &= \alpha_0^{AP} + \zeta\cos\theta^*,\end{aligned} \tag{3.22}$$

where

$$\zeta = \frac{2p^*}{\beta M_{V^0}c}, \tag{3.23}$$

$$\begin{aligned}\alpha_0^{AP} &= \frac{\left(E_+^* - E_-^*\right)}{M_{V^0}c^2} \\ &= \frac{m_+^2 - m_-^2}{M_{V^0}^2},\end{aligned} \tag{3.24}$$

which gives the dependence of α^{AP} to θ^* and p^*. The combination of Equation 3.19 and Equation 3.22 with the trigonometric relation

$$\cos\theta^{*2} + \sin\theta^{*2} = 1 \tag{3.25}$$

results in the elliptical form

$$\left(\frac{\alpha^{AP} - \alpha_0^{AP}}{\zeta}\right)^2 + \left(\frac{q_T}{p^*}\right)^2 = 1. \tag{3.26}$$

The elliptical curve is offset by α_0^{AP} and has a semi-major and a semi-minor axis of ζ and p^*. The p^* dependence of the semi-minor axis and the parameter ζ can be eliminated by using the energy-momentum four-vectors in the CM frame

$$\begin{aligned} P_{V_0}^{\mu *} &= P_+^{\mu *} + P_-^{\mu *} \\ &= \left(\frac{E_+^* + E_-^*}{c}, 0 \right) \end{aligned} \tag{3.27}$$

so that

$$\left(P_{V_0}^{\mu *} \right)^2 = \left(\frac{E_+^* + E_-^*}{c} \right)^2 \tag{3.28}$$

$$\begin{aligned} {M_{V^0}}^2 c^4 &= E_+^{*2} + E_-^{*2} + 2E_+^* E_-^* \\ &= m_+^2 c^4 + m_-^2 c^4 + 2\mathbf{p}^{*2} c^2 \\ &\quad + 2\sqrt{\left(m_+^2 c^4 + \mathbf{p}^{*2} c^2\right)\left(m_-^2 c^4 + \mathbf{p}^{*2} c^2\right)} \end{aligned} \tag{3.29}$$

and

$$p^* = \frac{\sqrt{{M_{V^0}}^4 + m_+^4 + m_-^4 - 2{M_{V^0}}^2 m_+^2 - 2{M_{V^0}}^2 m_-^2 - 2m_+^2 m_-^2}}{2M_{V^0}}. \tag{3.30}$$

For a particular V^0 species the elliptical curve that parameterizes the Armenteros-Podolanski structures depends only on the invariant masses of the V^0 particle and of its decay products. The expected elliptical curves for $\Lambda(\overline{\Lambda})$ and $\mathrm{K}_{\mathrm{s}}^0$ are calculated in the limit that they are ultra-relativistic particles ($\beta \to 1$). Table 3.3 summarizes the calculated values [Ams08] used to create Figure 3.8 and compares the calculated α_0^{AP} with the values observed in the data. The two pions from $\mathrm{K}_{\mathrm{s}}^0$ decay each carry half of $\mathrm{p_L}$, which results in a symmetrical structure about the α^{AP} axis. The p and $\overline{p}$ from Λ and $\overline{\Lambda}$ decay carry most of $\mathrm{p_L}$, thus separating the structures along the α^{AP} axis.

The measured momenta of the decay particles and the reconstructed V^0 momentum are used to calculate the longitudinal and transverse components with

	ζ	p^*	α_0^{AP} (Calculated)	α_0^{AP} (Measured)
Λ	0.180	0.101	0.692	0.642
$\overline{\Lambda}$	0.180	0.101	-0.692	-0.642
$\mathrm{K}_{\mathrm{s}}^0$	0.828	0.206	0.0	–

Table 3.3: Expected values for ζ, p^*, and α_0^{AP} at ultra-relativistic speeds ($\beta \rightarrow 1$). α_0^{AP} (measured) was determined from the analyzed data.

respect to the V^0's reconstructed momentum vector,

$$q_L^{+(-)} = \frac{\mathbf{p}_{V^0} \cdot \mathbf{p}_{+(-)}}{|\mathbf{p}_{V^0}|}, \tag{3.31}$$

$$q_T = \sqrt{\mathbf{p}_+^2 - q_L^{+2}}, \tag{3.32}$$

which are then used to construct the Armenteros-Podolanski plot. The structures seen in the Armenteros-Podolanski plots are then compared to the expected elliptical curves. The agreement of the expected curve with the data can be improved by using the actual β instead the ultra-relativistic limit ($\beta \rightarrow 1$) for different $\mathrm{p_T}$ intervals. The average β value for each V^0 $\mathrm{p_T}$ interval is used to create the expected curve. Figures 3.9(a)–(b) shows the expected elliptical curves with realistic β values for two $\mathrm{p_T}$ intervals in comparison with the distributions observed in the analyzed data.

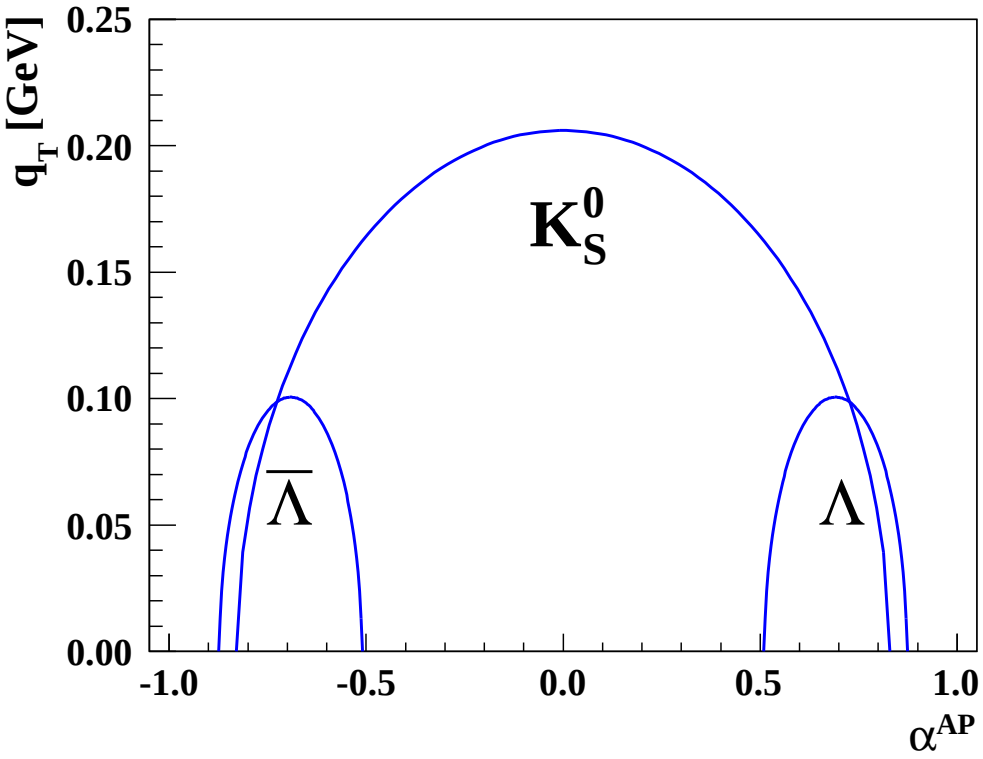

Figure 3.8: The expected Armenteros-Podolanski elliptical curves for ultra-relativistic $\Lambda(\overline{\Lambda})$ and K^0_s particles ($\beta \rightarrow 1$). α^{AP} describes the p_L asymmetry between the decay particles. Half of p_L is carried by $\pi^+(\pi^-)$ for a K^0_s decay, resulting in the K^0_s's curve to be symmetrical about the α^{AP} axis. The Λ and $\overline{\Lambda}$ curves reside in opposite quadrants since the p and $\overline{p}$ carry most of p_L in the decay.

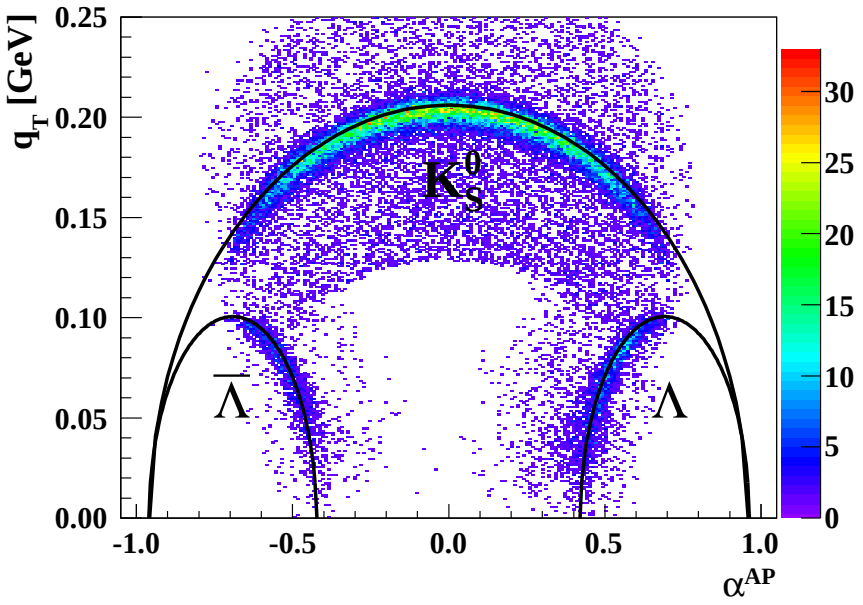

(a): $0.5 \leq p_T < 1.0$ GeV

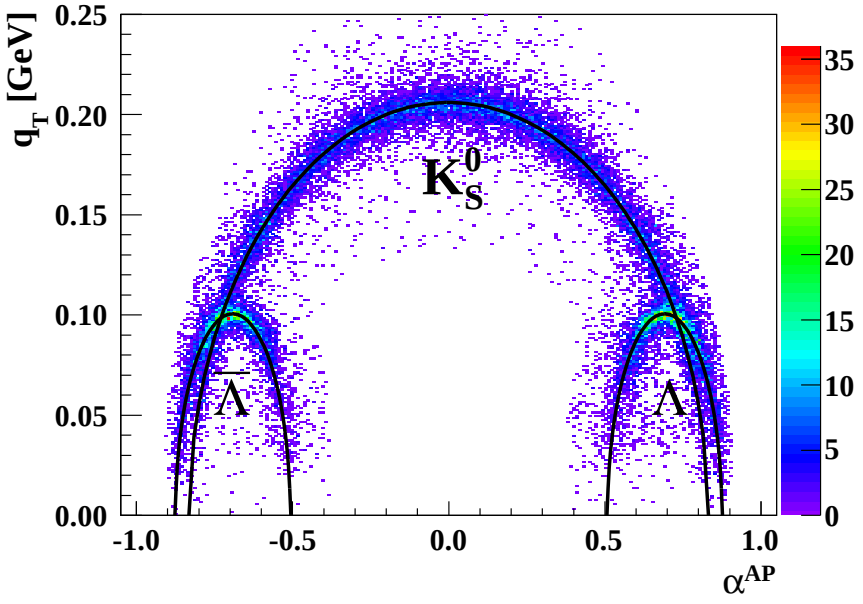

(b): $4.0 \leq p_T$ GeV

Figure 3.9: Armenteros-Podolanski distributions for tuned $\Lambda(\overline{\Lambda})$ and K^0_s candidates from run year 2006 data for two p_T intervals. Slower particles have a smaller β, broadening the elliptical curve.

3.1.4 Reduction of Contamination Between $\Lambda(\overline{\Lambda})$ and K^0_s Yields

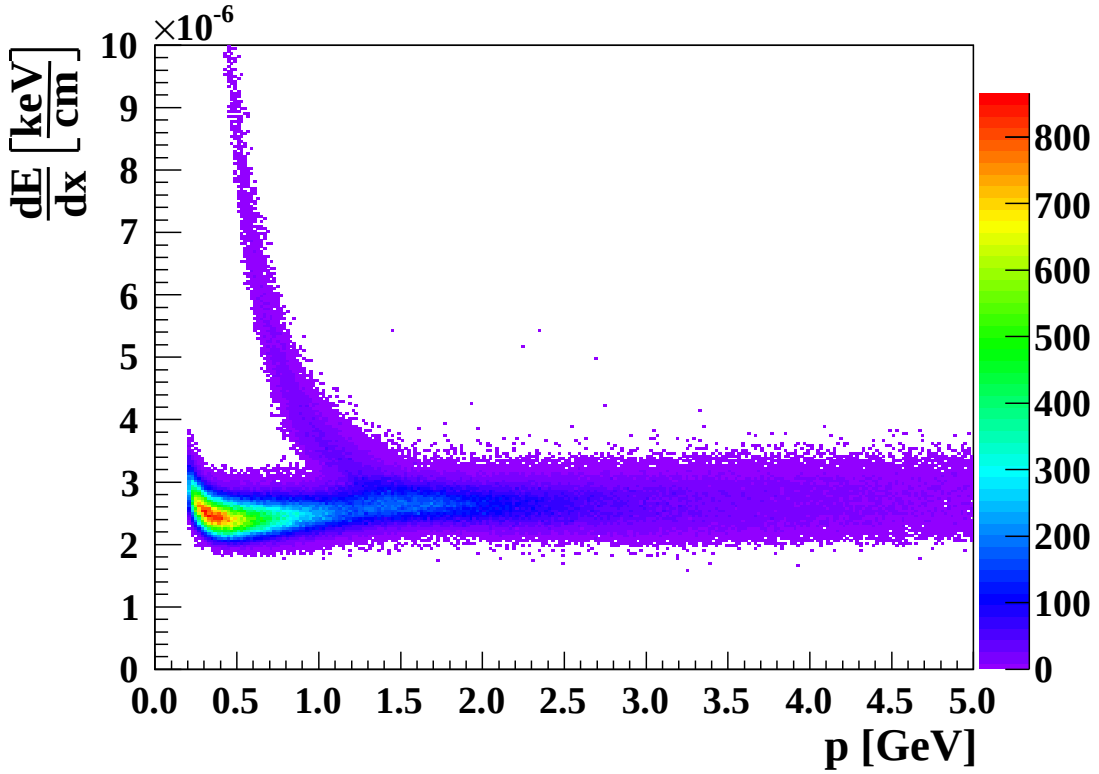

Figure 3.10: Run year 2006 dE/dx versus momentum scatter plot shows proton and pion particle bands begin to merge at 1.0 < p GeV

Decay particles can be misidentified. Figure 3.10 shows the ionization energy loss observed in the TPC for proton and pion candidates. For p > 1 GeV, the proton and pion distributions begin to overlap. V^0 particles reconstructed from misidentified decay particles can satisfy topological, kinematics, and reconstructed invariant mass requirements. Figure 3.11 shows the $\Lambda(\overline{\Lambda})$ Armenteros-Podolanski distribution for $2.0 < p_T < 2.5$ GeV. The $\Lambda(\overline{\Lambda})$ and K^0_s bands partially overlap. In the overlap regions, the identified $p(\overline{p})$ from $\Lambda(\overline{\Lambda})$s have similar kinematics as $\pi^+(\pi^-)$ from the reconstructed K^0_ss. The K^0_s particles are spin-zero, and if left in the analyzed $\Lambda(\overline{\Lambda})$ sample, will dilute the extracted D_{LL} values for $\Lambda(\overline{\Lambda})$. The

$\Lambda(\overline{\Lambda})$ particles in the K_s^0 sample may contribute to an unphysical non-zero D_{LL} value extracted for the K_s^0 sample. The following procedure was used to reduce the contamination from the incorrectly identified particle species.

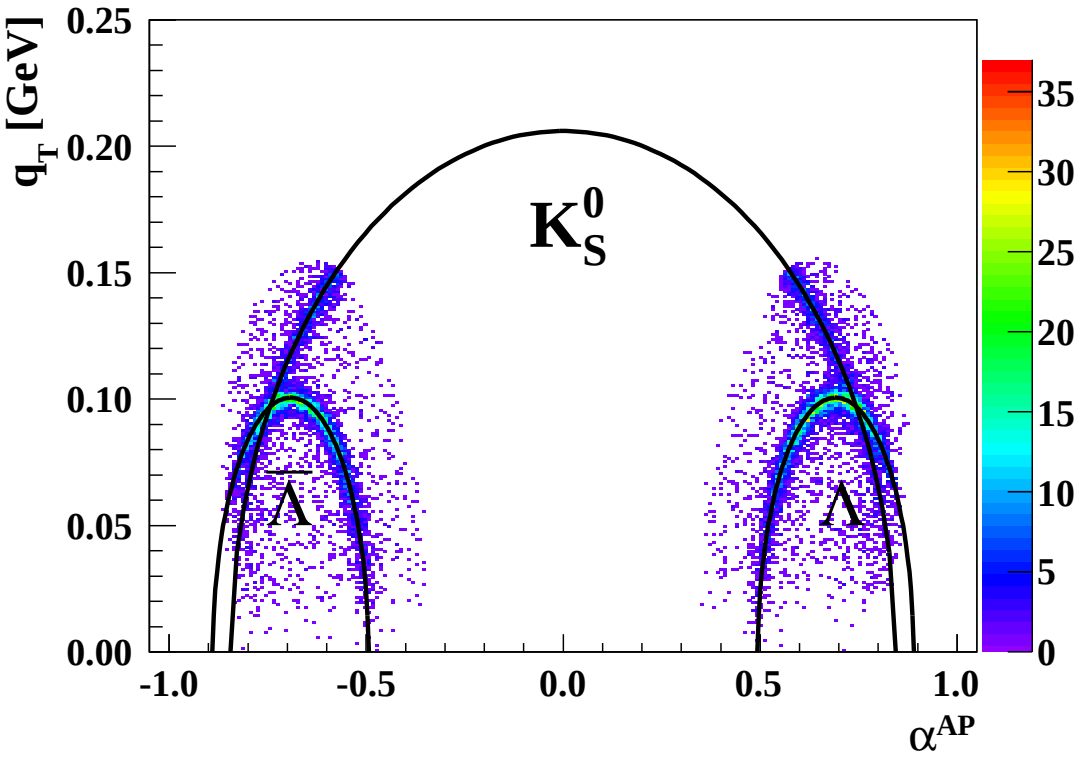

Figure 3.11: Run year 2006 Armenteros-Podolanski plot shows K_s^0 particle band overlaps with $\Lambda(\overline{\Lambda})$ particle bands for $2.0 < p_T < 2.5$ GeV.

The decay daughters from $\Lambda(K_s^0)$ candidates are reconstructed using the particle identification assumptions and invariant mass hypothesis for a $K_s^0(\Lambda)$ particle. Figures 3.12(a)–(f) show the reconstructed invariant mass spectra for $\Lambda(\overline{\Lambda})$ and K_s^0 particles for 2006 and 2009. A mass peak is visible in all cases. The reconstructed particles are required to satisfy the selection parameter cuts for the corresponding particle species. Particles which are within 3σ from the PDG invariant mass value are kept for further analysis.

The alternate reconstruction was used to develop more stringent particle identification criteria. The particles that reside within the invariant mass background range were used to restrict the range on $n\sigma_\pi$ and $n\sigma_p$. Alternately reconstructed K^0_s particles for which the original $p(\overline{p})$ satisfies $-1.4 < n\sigma_\pi < 1.8$ or $n\sigma_\pi < n\sigma_p$ are removed from the original $\Lambda(\overline{\Lambda})$ candidate sample. Similarly, the alternately reconstructed $\Lambda(\overline{\Lambda})$ particles which have an original $\pi^+(\pi^-)$ satisfying $|n\sigma_p| < 2.0$ or $n\sigma_p < n\sigma_\pi$ are removed from the original K^0_s candidate sample. Figures 3.13(a)–(d) show the scatter plots of the proton $n\sigma_p$ vs. $n\sigma_\pi$ for the original $\Lambda(\overline{\Lambda})$ candidates residing within the invariant mass signal and background region for JP1–6. The red hatched regions contain the rejected $\Lambda(\overline{\Lambda})$s from the original $\Lambda(\overline{\Lambda})$ sample. Figures 3.14–3.15 show the invariant mass vs. $\cos(\theta^*)$ 2D plots for the decontaminated particle samples and the invariant mass spectra for the alternately reconstructed particles for $\Lambda(\overline{\Lambda})$ and K^0_s particles. The blue line shows the particles which survive this decontamination procedure. The mass peak from the contaminated particle species has largely been eliminated. Table 3.4 shows the number of rejected $\Lambda(\overline{\Lambda})$ and K^0_s candidates after the contamination reduction.

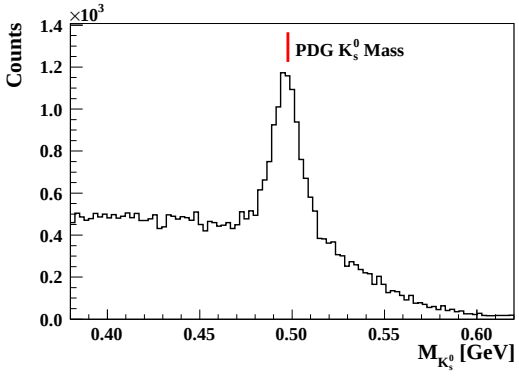

(a): 2006: Λ

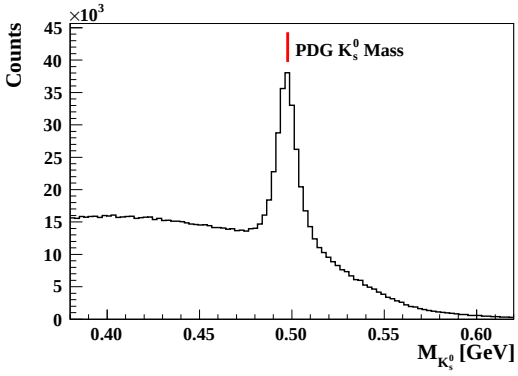

(b): 2009: Λ

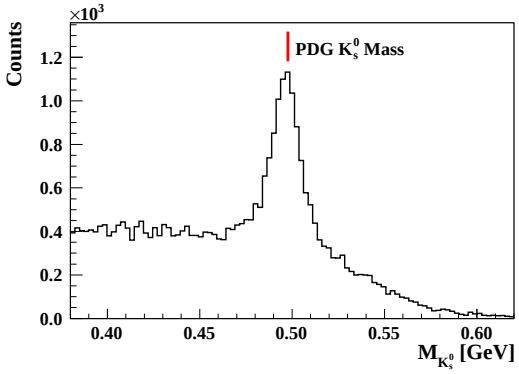

(c): 2006: $\overline{\Lambda}$

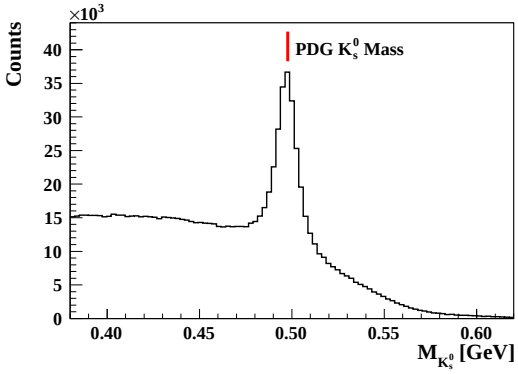

(d): 2009: $\overline{\Lambda}$

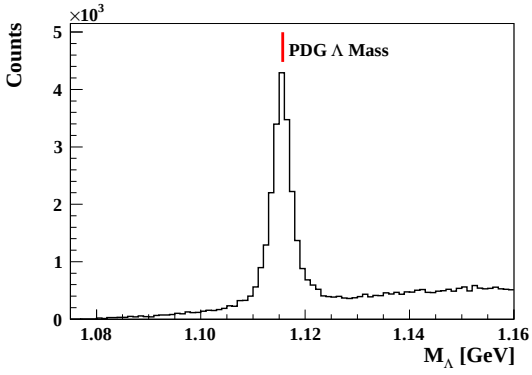

(e): 2006: K^0_s

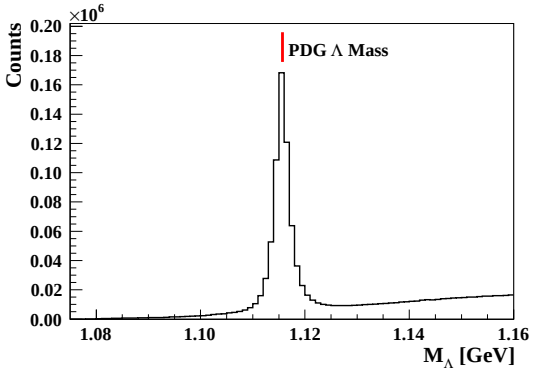

(f): 2009: K^0_s

Figure 3.12: Invariant mass spectra of reconstructed particles with different particle identification assumptions and invariant mass hypothesis for run year 2006 and 2009 which satisfied triggers of interest.

p_T GeV	Λ		$\overline{\Lambda}$		K_s^0	
	Signal (%)	Bkg. (%)	Signal (%)	Bkg. (%)	Signal (%)	Bkg. (%)
			JP1–6			
$0.5 \leq p_T < 1.0$	0.2	1.9	0.4	7.5	0.2	1.3
$1.0 \leq p_T < 1.5$	3.8	23.1	3.3	26.4	1.9	24.4
$1.5 \leq p_T < 2.0$	14.0	36.5	14.1	40.5	9.0	62.2
$2.0 \leq p_T < 2.5$	14.4	43.8	14.4	43.1	11.5	69.8
$2.5 \leq p_T < 3.0$	10.4	46.6	10.8	54.6	9.9	65.4
$3.0 \leq p_T < 4.0$	7.1	47.8	8.5	40.5	8.3	62.8
$4.0 \leq p_T$	7.6	26.0	7.4	39.1	6.9	47.4
			JP1–9			
$0.5 \leq p_T < 1.0$	0.0	4.5	0.1	4.8	0.1	1.9
$1.0 \leq p_T < 1.5$	1.9	24.9	1.7	24.8	1.3	33.4
$1.5 \leq p_T < 2.0$	9.5	37.1	9.1	38.8	8.2	71.5
$2.0 \leq p_T < 2.5$	11.4	43.3	11.4	44.5	12.2	75.7
$2.5 \leq p_T < 3.0$	8.6	43.6	8.4	45.0	11.3	72.7
$3.0 \leq p_T < 4.0$	6.2	38.1	6.3	40.1	9.2	68.3
$4.0 \leq p_T$	6.0	25.6	6.0	29.9	6.4	49.9
			L2JH–9			
$0.5 \leq p_T < 1.0$	0.1	3.5	0.0	4.5	0.1	1.7
$1.0 \leq p_T < 1.5$	2.1	23.7	2.1	24.8	1.3	26.8
$1.5 \leq p_T < 2.0$	10.5	36.1	10.2	38.0	7.3	65.8
$2.0 \leq p_T < 2.5$	12.5	42.8	12.3	45.1	10.4	71.3
$2.5 \leq p_T < 3.0$	9.4	43.6	8.9	46.0	9.4	69.6
$3.0 \leq p_T < 4.0$	7.0	37.4	6.9	40.6	7.9	63.5
$4.0 \leq p_T$	6.6	25.7	6.4	26.7	5.7	41.0

Table 3.4: Percentage of rejected candidates after the reduction of misidentified particle contamination in the signal and background regions for run year 2006 and 2009.

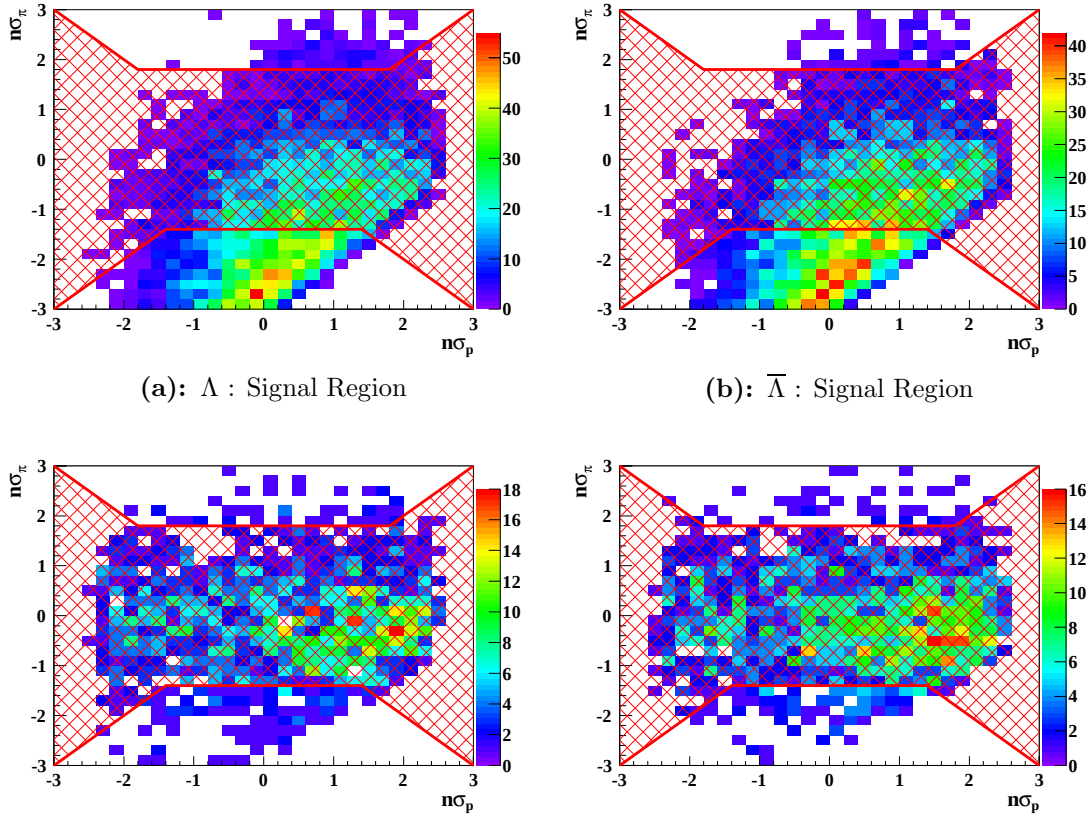

(a): Λ : Signal Region

(b): $\overline{\Lambda}$: Signal Region

(c): Λ : Background Region

(d): $\overline{\Lambda}$: Background Region

Figure 3.13: Run year 2006 nσ_{p} vs. nσ_{π} scatter plots for $\Lambda(\overline{\Lambda})$ particles residing in the signal and background regions. $\Lambda(\overline{\Lambda})$s which make up the background signal contain a large sample of $\mathrm{K}^0_{\mathrm{s}}$ particles. Particles that reside within the red meshed area and satisfy the $\mathrm{K}^0_{\mathrm{s}}$ particle selection parameter conditions are removed from the sample.

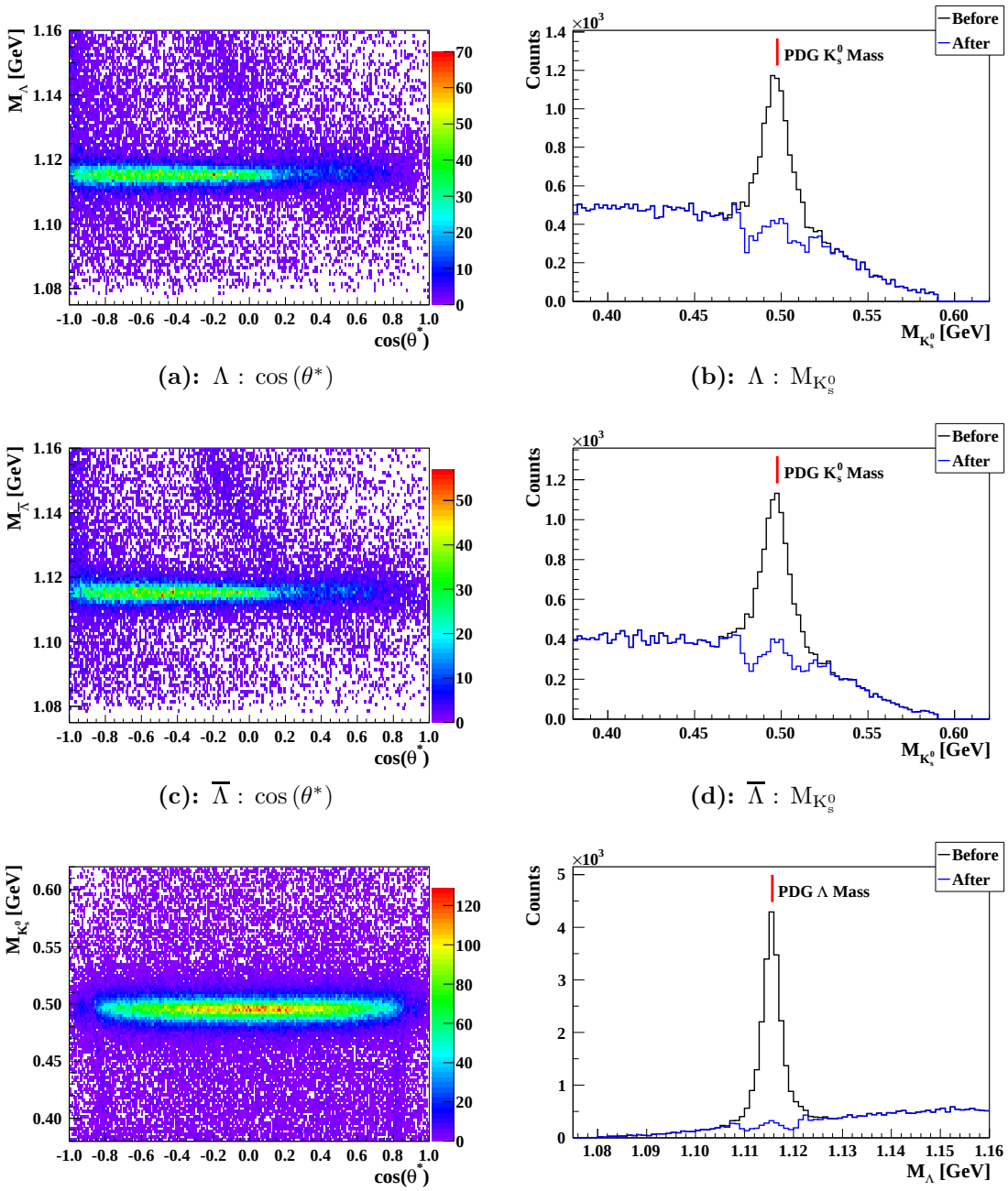

(a): Λ : $\cos(\theta^*)$ **(b):** Λ : $M_{K^0_s}$

(c): $\overline{\Lambda}$: $\cos(\theta^*)$ **(d):** $\overline{\Lambda}$: $M_{K^0_s}$

(e): K^0_s - $\cos(\theta^*)$ **(f):** K^0_s : $M_{\Lambda(\overline{\Lambda})}$

Figure 3.14: Invariant mass versus $\cos(\theta^*)$ and invariant mass spectra for $\Lambda(\overline{\Lambda})$ and K^0_s particles with different invariant mass hypotheses before and after the reduction of misidentified particle contamination for run year 2006. The blue lines describe the reconstructed invariant mass spectra for different invariant mass hypotheses after the contamination had been reduced as described in the text.

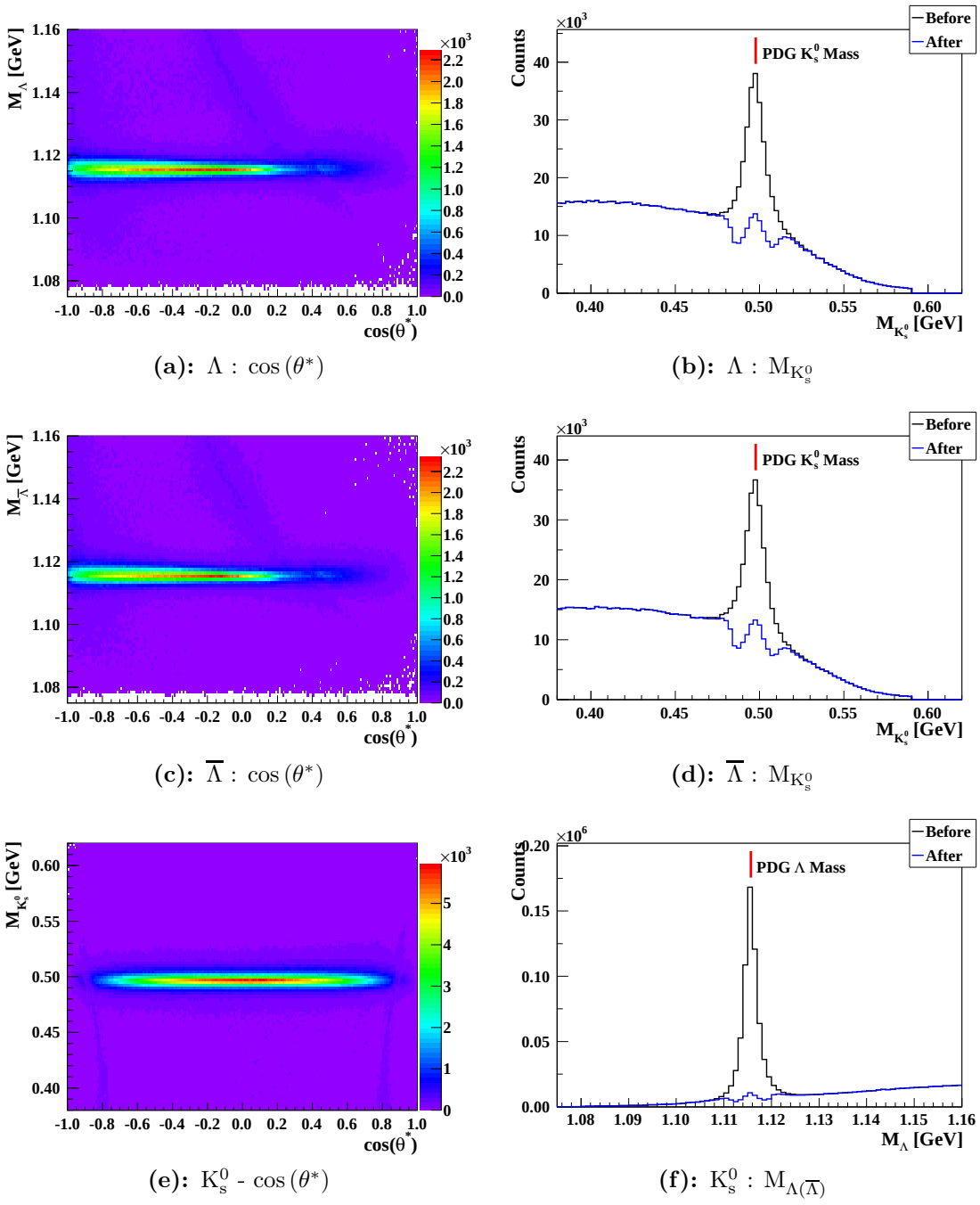

(a): Λ : $\cos(\theta^*)$ **(b):** Λ : $M_{K^0_s}$

(c): $\overline{\Lambda}$: $\cos(\theta^*)$ **(d):** $\overline{\Lambda}$: $M_{K^0_s}$

(e): K^0_s - $\cos(\theta^*)$ **(f):** K^0_s : $M_{\Lambda(\overline{\Lambda})}$

Figure 3.15: Invariant mass versus $\cos(\theta^*)$ and invariant mass spectra for $\Lambda(\overline{\Lambda})$ and K^0_s particles with different invariant mass hypotheses before and after the reduction of misidentified particle contamination for run year 2009. The blue lines describe the reconstructed invariant mass spectra for different invariant mass hypotheses after the contamination had been reduced as described in the text.

3.2 Jet Reconstruction

Jets quantify the flow of energy in the hard scattering of particles [Ste77]. Operationally, jets are observed as a cluster of particles traveling in the same direction, away from the collision point. It is convenient to classify jets by the parton stage, the hadron stage, and the detector stage as illustrated in Figure 3.16. During the parton stage, the jet is comprised of partons from the hard scattering collision, while at the hadron stage the partons have hadronized. At the detector stage, jets are composed of reconstructed tracks and energy deposits in the detector.

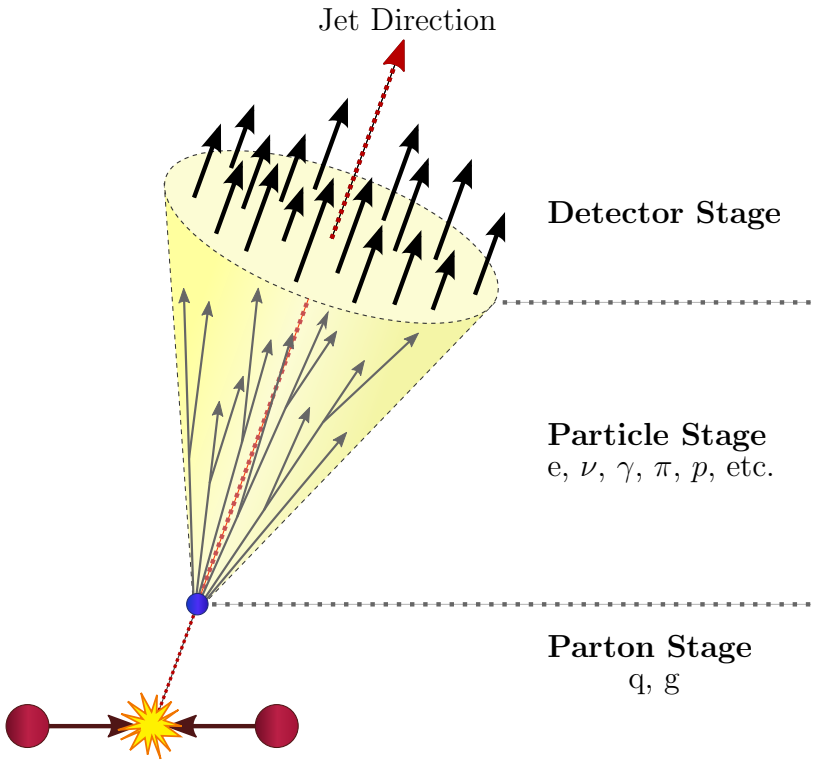

Figure 3.16: The classification of jets at the parton stage, the hadron stage, and the detector stage.

3.2.1 Reconstruction Algorithm

The STAR jet reconstruction software contains several reconstruction algorithms, including the midpoint cone algorithm [Bla00] that has been used in thus far published results and is used for the analysis. Jets are defined as a cluster of particles residing within a jet cone of radius,

$$R = \sqrt{(\Delta\eta)^2 + (\Delta\phi)^2}. \tag{3.33}$$

The workflow for the midpoint cone algorithm can be seen in Figure 3.17. It uses both a seeded and a midpoint approach to search for proto-jets. Proto-jets are

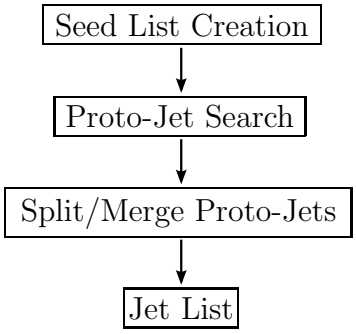

Figure 3.17: Midpoint Cone Algorithm Workflow

jets that satisfy the jet requirements but do not take into account the existence of any neighboring jets that may share constituent particles. The algorithm first starts by looking for towers in the detector with a minimum E_T seed energy and ranking them in decreasing order to create a seed list. Proto-jets are searched for near the seeds. Using the proto-jets, midpoints are found between all proto-jet pairs within $2R$ from each other. The midpoints are then used as separate seeds. Once all proto-jets have been identified, a split/merge procedure is implemented in order to create a final set of jets which do not share their constituent particles with other jets. If two proto-jets share 50% of E_T energy with each other, then the

two proto-jets are merged. Otherwise the particles are split between the jets. The split particles are assigned to the proto-jet cone they are closest to. The process of split/merge is performed until there are no proto-jets sharing constituent particles. The list of surviving proto-jets then becomes the final list of jets.

General Parameters	
Min Track p_T GeV	0.2
Min Tower p_T GeV	0.2
Minimum track hits	12
Jet η_{det}	[−0.7,0.7]
Min p_T^{Jet} GeV	5.0
Jet Cone Parameters	
R	0.7
Min Seed E_T GeV	0.5
Split Fraction	0.5

Table 3.5: Jet reconstruction parameters for run year 2006 and 2009

A jet cone radius of $R = 0.7$ was used for both 2006 and 2009 run years. In STAR, the primary tracks reconstructed in the TPC and energy deposits in the BEMC towers form the candidate particles are used in the jet reconstruction. If a hit BEMC tower is pointed at by a TPC track, an energy deposit corresponding to that of a minimum-ionizing particle is subtracted from the tower energy to reduce double counting. In order to build the 4-momentum vectors, the primary tracks reconstructed in the TPC are assigned a π mass while the particles depositing the energy in the BEMC towers are assigned to be photons. Particle tracks are also required to have a track-to-hit ratio (track hits/total possible hits) of at least 0.51 to reduce track splitting in the TPC. The parameter values used for jet reconstruction are the same for both run years and are summarized in Table 3.5.

3.3 Beam Polarization

Relative beam polarization measurements are done at the beginning of each RHIC beam fill, about every 2 hours afterwards, and before beams are dumped using the pC polarimeters [Nak08a]. A mean relative beam polarization is calculated for each fill. The mean relative beam polarization values are normalized against the mean absolute beam polarization values from the polarized hydrogen gas jet polarimeter measurement [Oka06a, Gro11a, Gro11b]. Runs from fills with beam polarizations less than 40% are rejected. Figures 3.18–3.19 show the beam polarization values for both run years. The beam crossings are classified according to the spin

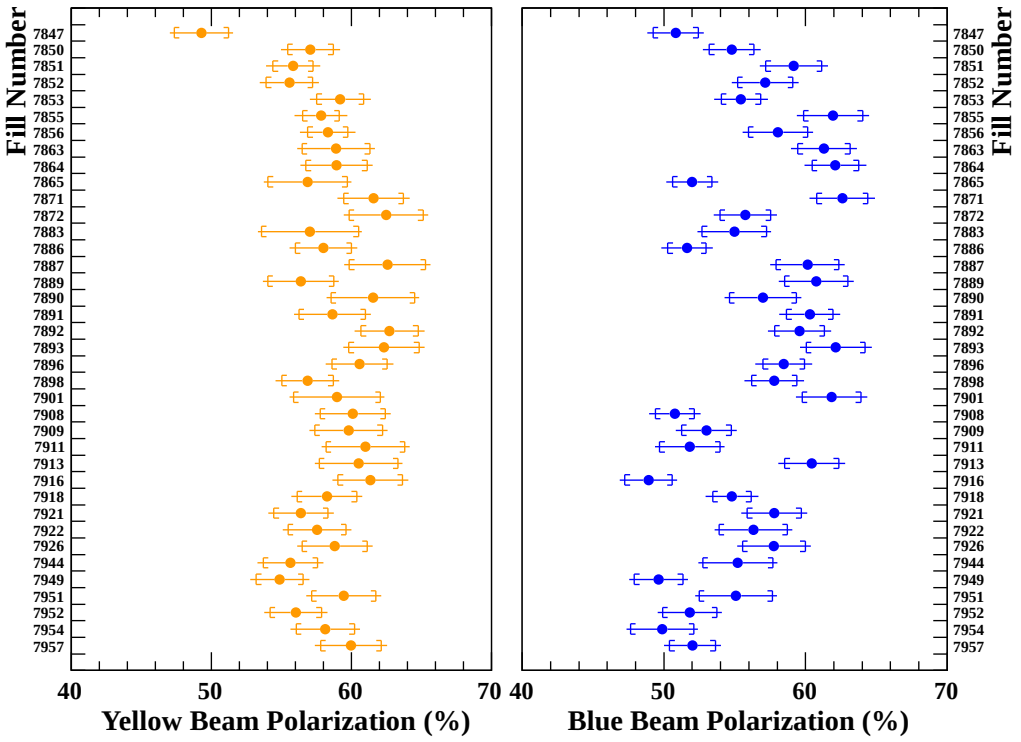

Figure 3.18: Beam polarization values per fill for run year 2006. The error bars show statistical and systematic uncertainties summed in quadrature. The inner error brackets indicate the size of the statistical uncertainty contribution. The systematic uncertainty is dominated by uncertainty in the hydrogen-jet calibration, which is common to all fills.

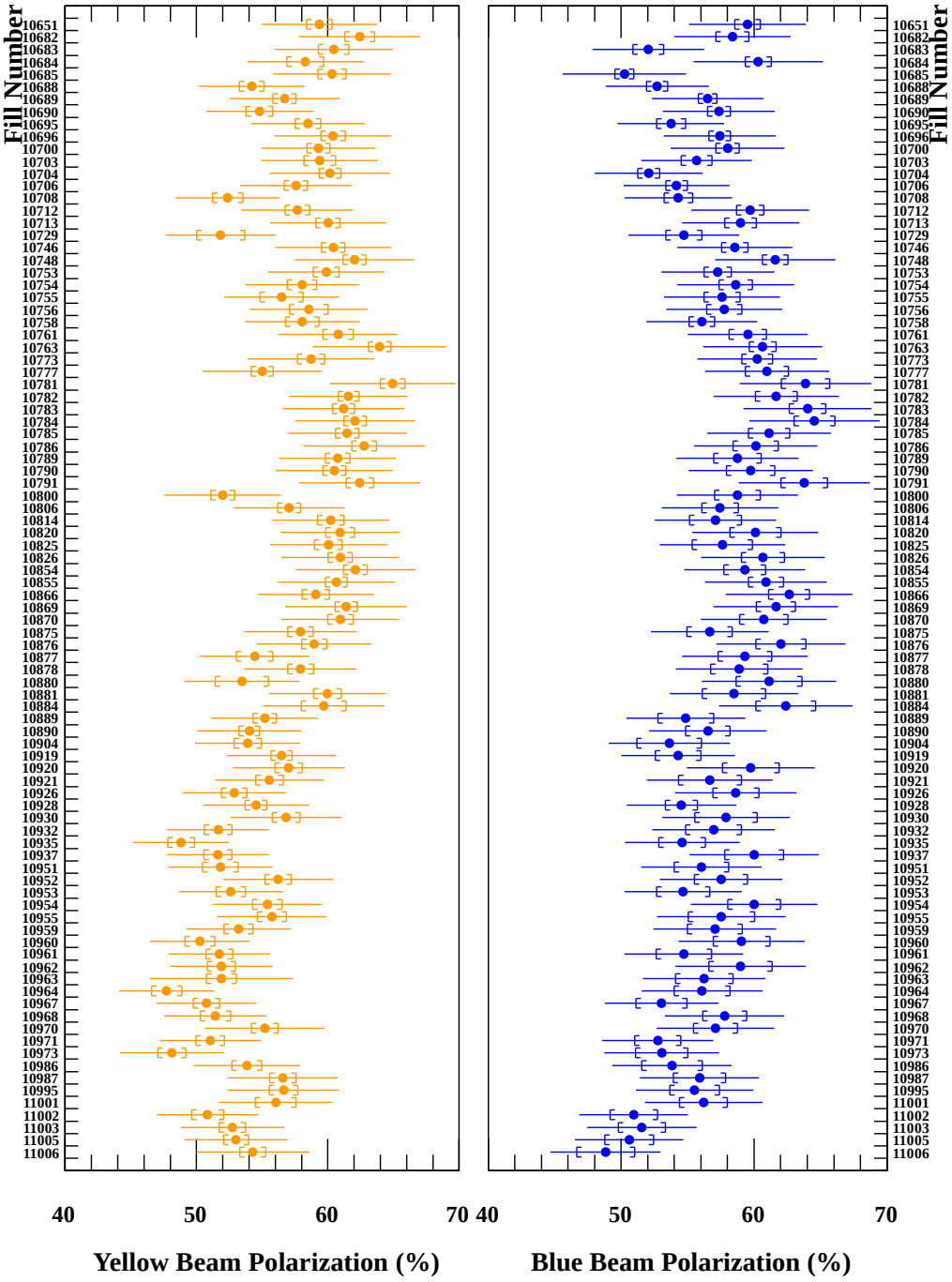

Figure 3.19: Beam polarization values per fill for run year 2009. The error bars show statistical and systematic uncertainties summed in quadrature. The inner error brackets indicate the size of the statistical uncertainty contribution. The systematic uncertainty is dominated by uncertainty in the hydrogen-jet calibration, which is common to all fills.

configuration of the colliding beam bunches with a spin pattern that is applied separately for each proton bunch and beam. The possible spin state combinations are shown in Table 3.6. The four double spin polarized states (spin 4-bits 5, 6, 9, 10) are of interest to the analysis.

Yellow Beam	Blue Beam	Spin 4-Bit
↑	↑	5
↓	↑	6
↑	↓	9
↓	↓	10
↑	–	1
↓	–	2
–	↑	4
–	↓	8
–	–	0

Table 3.6: Possible spin states at STAR interaction point.

3.4 Relative Luminosity

The BBC detectors are used to determine the relative luminosities of the beam bunches colliding at STAR [Kir05]. The relative luminosity ratios are defined in Section 2.2.6 and are determined for each run [Sak11, See11, Hay11]. Figures 3.20–3.21 show the various relative luminosity values for both run years. The run numbers have been indexed for visual clarity. The run indices can be found in Appendix A. The vertical dashed lines indicate the separations between fills. The horizontal green lines show the 2σ range, evaluated from the root-mean-square of the values for each run year. Runs with relative luminosity values outside the 2σ limit are removed from the list.

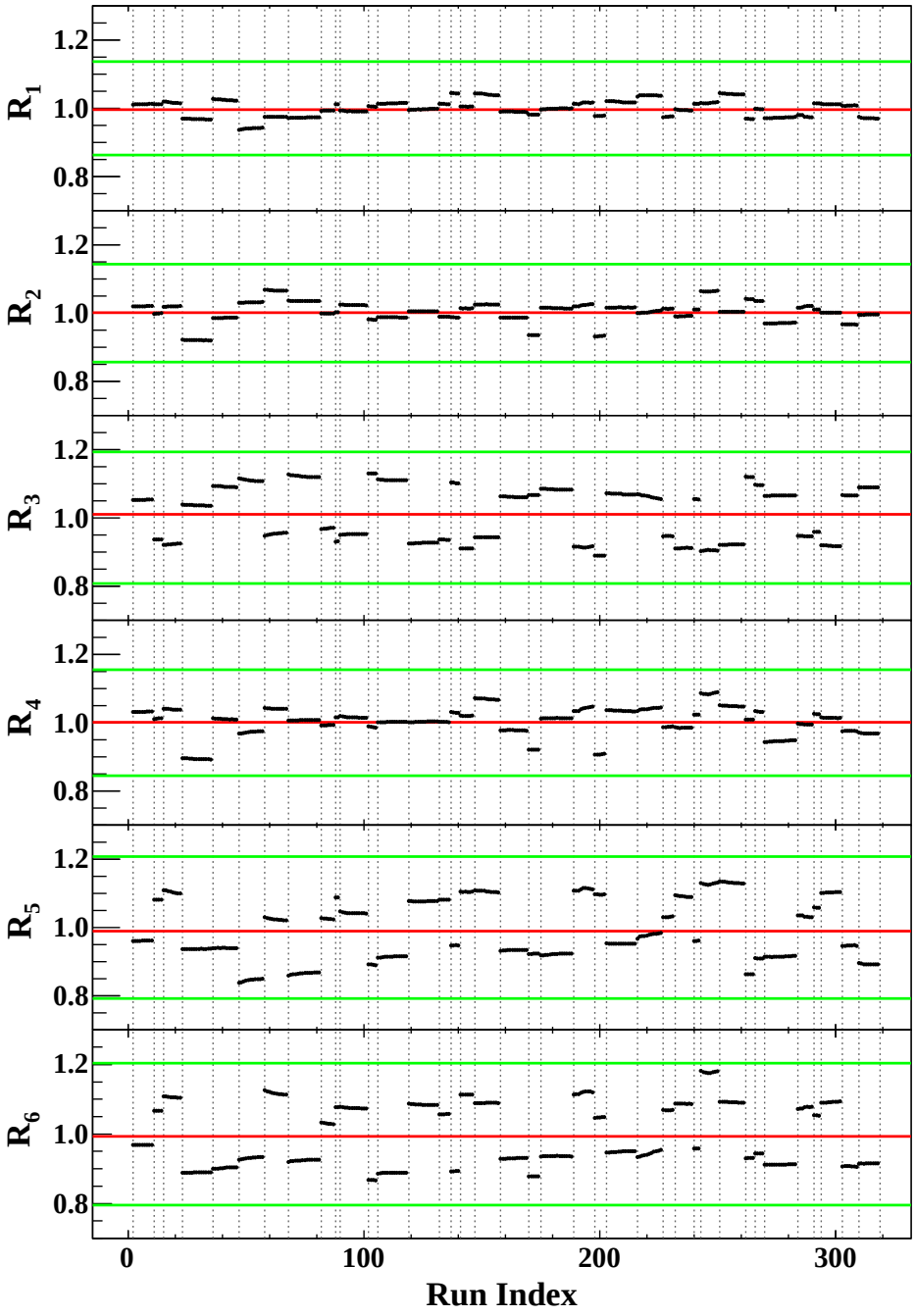

Figure 3.20: Relative luminosity values per run for run year 2006. The mean relative luminosity values are shown as red lines. The vertical dashed lines illustrate the separations between different fills. The horizontal green lines show the 2σ range. Runs with relative luminosity values outside the 2σ limit are removed from the list.

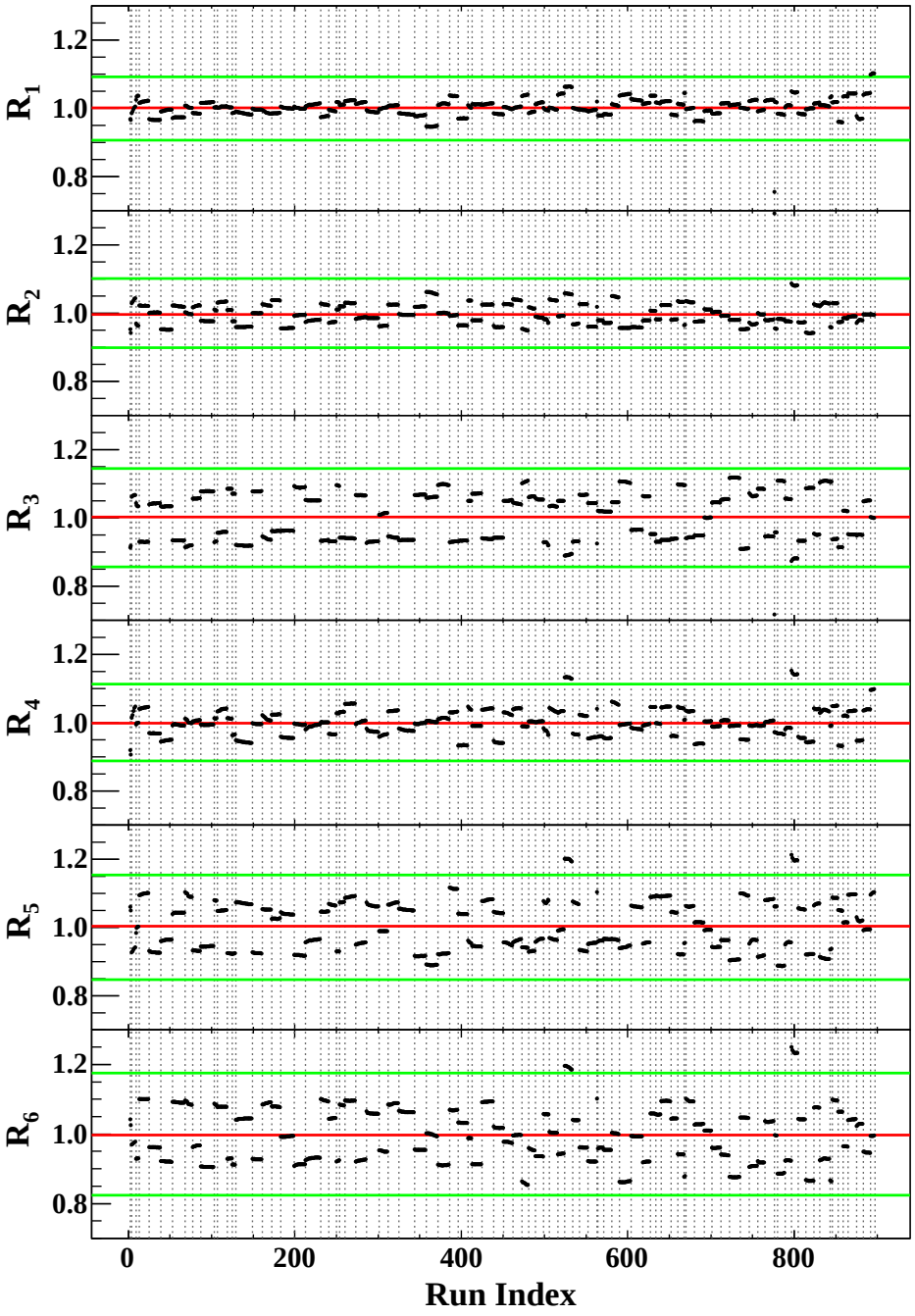

Figure 3.21: Relative luminosity values per run for run year 2009. The mean relative luminosity values are shown as red lines. The vertical dashed lines illustrate the separations between different fills. The horizontal green lines show the 2σ range. Runs with relative luminosity values outside the 2σ limit are removed from the list.

3.5 Data Selection

The analysis focuses on data collected during the longitudinally polarized proton-proton collisions at a center of mass energy of $\sqrt{s} = 200$ GeV for run year 2006 (May 11 - June 5) and 2009 (April 19 - July 4). The average beam polarization for the yellow beam, $\overline{P_Y}$, and for the blue beam, $\overline{P_B}$, for the fills used in the analysis are shown in Table 3.7 for run year 2006 and 2009 with their total absolute uncertainties. Three trigger conditions are used to record the data used in the analysis;

Run Year	$\overline{P_Y}$	$\overline{P_B}$
2006	$58 \pm 3\%$	$56 \pm 4\%$
2009	$57 \pm 4\%$	$57 \pm 3\%$

Table 3.7: Average beam polarization values

Jet Patch 1 (2006) (JP1–6), Jet Patch 1 (2009) (JP1–9), and L2 Jet High (2009) (L2JH–9). They require events to have at least one jet patch ($\Delta\eta \times \Delta\phi = 1 \times 1$) with minimum E_T threshold. Table 3.8 summarizes the different trigger configurations and recorded data. Trigger L2JH–9 is expected to have higher p_T $\Lambda(\overline{\Lambda})$s compared to JP1–9 as it requires a higher jet patch E_T threshold. In this section

Trigger Name	Trigger Id	E_T GeV	Recorded Runs	Recorded Events	Analyzed Runs	Analyzed Events
JP1–6	137221 137222	7.8/8.3	439	4.7M	302	164K
JP1–9	240410 240411	4.7-5.4	1263	139.6M	764	3M
L2JH–9	240650 240651 240652	6.4-7.3	1489	85.7M	824	2M

Table 3.8: Trigger configurations and data used in the analysis

we describe the procedure taken to determine the runs and events used for the analysis.

3.5.1 Event Selection

Events within a run can have different characteristics depending on which trigger conditions they satisfied. Global setup name is the name of a group of trigger conditions used for recording events. Table 3.9 lists the global setup names used in the analysis for both run years. An event can satisfy multiple trigger conditions.

Global Setup Name	
2006	2009
ppProductionLong	production2009_200GeV_Single production2009_200GeV_Hi production2009_200GeV_Lo production2009_200GeV_noendcap

Table 3.9: Global setup names for run year 2006 and 2009.

Events are required to have at least one jet patch above the minimum E_T threshold. A BBC coincidence requirement was also imposed in run year 2006. BBC coincidence is satisfied when particles produced in a beam collision at the STAR interaction region hit both the East and West BBC detectors. Events are rejected if it originates from a so-called abort gap and the bunch crossing does not contain one of the four double spin polarized states of interest. If a primary vertex cannot be reconstructed, the event is also rejected.

The BBC time bin was used when measuring the relative luminosity. Events with BBC time bins outside the interval [6,9] are rejected to match with the events used to measure the relative luminosity as shown in Figure 3.22a. The earlier/later BBC time bin events have their primary vertex spread farther away from the

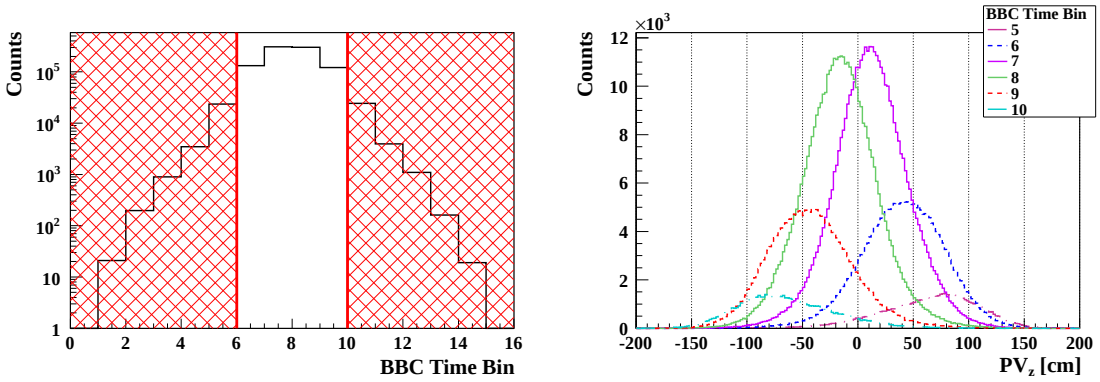

(a): Run year 2006 **(b):** Run year 2006

Figure 3.22: 2006 BBC timing and primary vertex distribution in $\hat{\mathbf{z}}$ direction for different BBC time bin values. The BBC time bins which lie within the hatched area are removed from the data set.

interaction point on the beam axis, $\hat{\mathbf{z}} = 0$ cm, as shown in Figure 3.22b. The primary vertex is required to be within $[-60,60]$ cm in the $\hat{\mathbf{z}}$ direction.

3.5.2 Run Selection

Runs are subjected to a quality assurance (QA) procedure. The QA process consists of checks on the integrity of the runs by validating the sub-detectors status and data recorded using the run logs and online plots. Any runs which fail to satisfy the QA requirements or are shorter than one minute in duration are removed from the run list. Runs with STAR-RTS status 'Junk' and shift leader status 'Bad' were removed. The remaining runs make up the priority run list for data production. Table 3.10 shows the number of runs which make up the priority run lists for run year 2006 and 2009 including all analyzed trigger configurations.

Runs from the run priority list are required to satisfy more conditions pertinent to the analysis. The minimum duration for each run is increased to two minutes. The BEMC and TPC detectors are required to be online and working for all runs. Runs for fills which have no beam polarization for either blue or yellow beam are

Run Year	Runs
2006	688
2009	1749

Table 3.10: Number of priority runs in run year 2006 and 2009 for all trigger conditions of interest

removed from the run list. Runs are also required to have relative luminosity measurements and a recorded spin pattern. The number of runs which satisfied the requirements are shown in Table 3.11 for all trigger configurations.

Run Year	Runs
2006	318
2009	877

Table 3.11: Number of priority runs in run year 2006 and 2009 which satisfy additional analysis-specific requirements.

Further checks are performed to the remaining runs by examining the stability of several observable distributions for both proton and π tracks, Reconstructed Jets, Initial Reconstructed V^0 particles, and Tuned Reconstructed V^0 particles for each trigger configuration. The observables distributions are expected to have a constant value throughout the entire run year unless the trigger or detector configurations change. Table 3.12 lists the observables that were examined. For each observable, the mean value is calculated throughout all runs. Examples of run versus observables plots are shown in Figures 3.23(a)–(f). The green horizontal lines illustrate the 5σ boundary. Runs which lie over 5σ away from the mean value are counted as potential problem runs for that specific observable set. Using a 5σ range limits the mis-identification of problem runs. Potential problem runs are tabulated to determine which runs to reject. If a run has more than two problem observables in a observable set or more than two observable sets with a problem

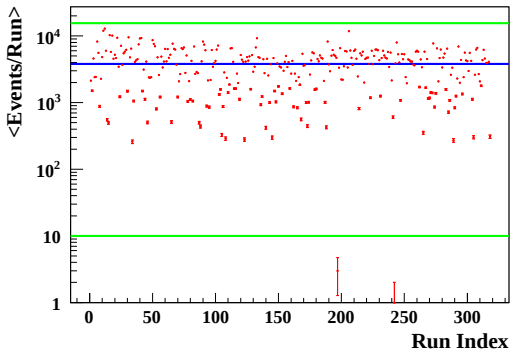

(a): ⟨Events⟩

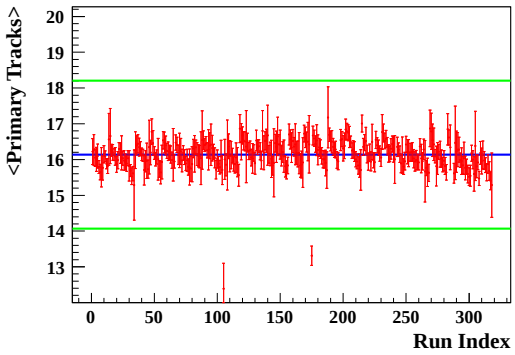

(b): ⟨Primary Tracks⟩

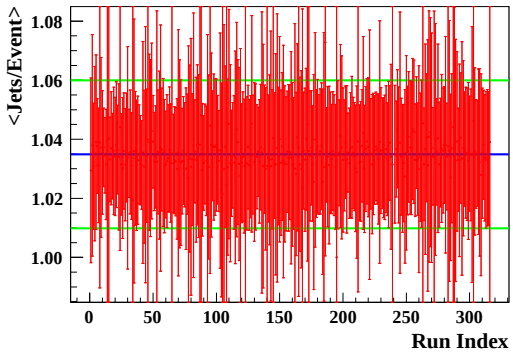

(c): ⟨Jets⟩

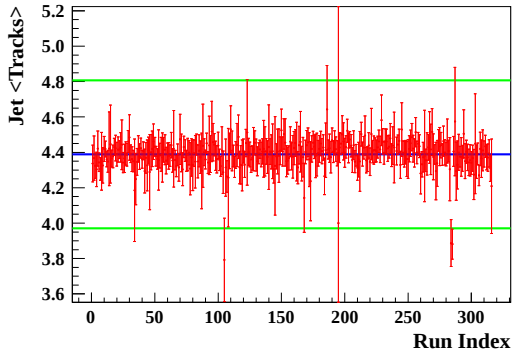

(d): ⟨Jet Tracks⟩

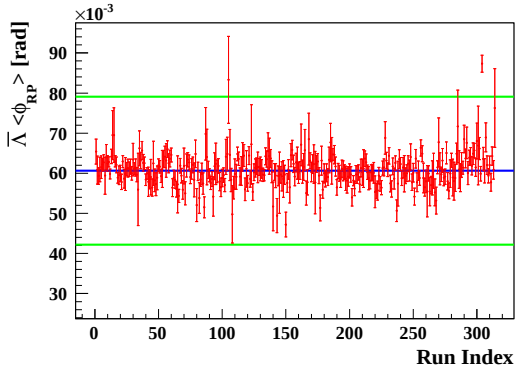

(e): Initial $\overline{\Lambda}$: $\langle\phi_{\mathrm{RP}}\rangle$

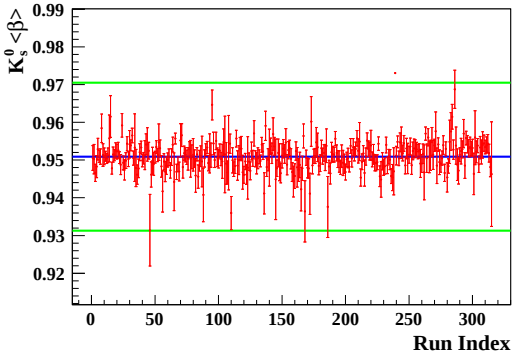

(f): Tuned $\mathrm{K}^0_{\mathrm{s}}$: $\langle\beta\rangle$

Figure 3.23: Observable distributions for run year 2006

Proton & π Tracks	Reconstructed Jets	Reconstructed V^0's
$\langle$Events$\rangle$	$\langle$Jets$\rangle$	$\langle V^0 \rangle$
$\langle$BBC Rates$\rangle$	$\langle p_T \rangle$ Jet	$\langle p_T \rangle$ V^0
$\langle$Primary Vertices$\rangle$	$\langle \eta \rangle$ Jet	$\langle$Decay Length$\rangle$ V^0
$\langle PV_Z \rangle$	$\langle$Jet Towers$\rangle$	$\langle$Opening Angle$\rangle$ V^0
$\langle$Primary Tracks$\rangle$	$\langle$Jet Tracks$\rangle$	$\langle \phi_{RP} \rangle$ V^0
$\langle$Global Tracks$\rangle$	$\langle p_T \rangle$ Jet Towers	$\langle \beta \rangle$ V^0
$\langle p_T \rangle$ Primary Tracks	$\langle p_T \rangle$ Jet Tracks	$\langle$DCA C^+-$C^-\rangle$ V^0
$\langle p_T \rangle$ Global Tracks	$\langle DCA_{XY} \rangle$ Jet Towers	$\langle \phi \rangle$ V^0
$\langle$TPC Hits$\rangle$ Primary Tracks	$\langle DCA_Z \rangle$ Jet Tracks	$\langle \eta \rangle$ V^0
$\langle$TPC Hits$\rangle$ Global Tracks		$\langle V^0/\Lambda \rangle$
		$\langle V^0/\overline{\Lambda} \rangle$
		$\langle V^0/K^0_s \rangle$

Table 3.12: Observables checked for stability throughout all runs. A column makes up a observable set. The reconstructed V^0 observable set is used for both the initial and the Tuned Reconstructed V^0 data.

observable, then the run is rejected. The rejected runs for run year 2006 and 2009 are shown in Tables 3.13–3.15.

The remaining runs containing hyperon-jet associated events make up the run list used for the analysis. Table 3.16 shows the number of runs used for each run year. A complete list of run numbers can be found in Appendix B.

Run Year 2006								
Run Number	(10) Proton & π Tracks	(9) Reconstructed Jets	(12) Initial Reconstructed Λ's	(12) Initial Reconstructed $\overline{\Lambda}$'s	(12) Initial Reconstructed K_s^0's	(12) Tuned Reconstructed Λ's	(12) Tuned Reconstructed $\overline{\Lambda}$'s	(12) Tuned Reconstructed K_s^0's
7133009						1	2	
7133053			2		1	1		
7139017	3	2	1	3		3		1
7139022			1	2		1		
7141034	1						1	
7141044			2	2		1		1
7142036	1							1
7143043	1			1	1	1		
7144009	8	4	13		11			
7148014	6	4	9		9			11
7154044		3						1
7154047	1	2						1
7155046			1	1				
7155053	1		1	1				
7156028				1				2

Table 3.13: Status for outlier runs for run year 2006. The number of observables checked per observable set is shown in parenthesis. For each run, the total number of outlier observable values for each observable set is used to determine whether to reject the run. If a run has more than two problem observables in a observable set or more than two observable sets with a problem observable, then the run is rejected.

Run Year 2009								
Run Number	(10) Proton & π Tracks	(9) Reconstructed Jets	(12) Initial Reconstructed Λ's	(12) Initial Reconstructed $\overline{\Lambda}$'s	(12) Initial Reconstructed K_s^{0}'s	(12) Tuned Reconstructed Λ's	(12) Tuned Reconstructed $\overline{\Lambda}$'s	(12) Tuned Reconstructed K_s^{0}'s
10142011	1		2	5	1	5	4	2
10142029				1		2		
10144038	4	1	1	5	1	2	8	4
10144086						2	3	
10144098			1		1		1	
10144099	1					1		
10146041				2			1	
10149001					1	2	2	1
10149036			1	2		3	3	
10150018						1	1	
10151041						6	1	
10154069	2					1		1
10156037				2		1	2	
10158046	2			1		7	1	
10158074	1	1				1	1	1

Table 3.14: Status for outlier runs for run year 2009. The number of observables checked per observable set is shown in parenthesis. For each run, the total number of outlier observable values for each observable set is used to determine whether to reject the run. If a run has more than two problem observables in a observable set or more than two observable sets with a problem observable, then the run is rejected.

Run Year 2009								
Run Number	(10) Proton & π Tracks	(9) Reconstructed Jets	(12) Initial Reconstructed Λ's	(12) Initial Reconstructed $\overline{\Lambda}$'s	(12) Initial Reconstructed K_s^0's	(12) Tuned Reconstructed Λ's	(12) Tuned Reconstructed $\overline{\Lambda}$'s	(12) Tuned Reconstructed K_s^0's
10160069	1					1		
10161014			1	3		6	2	2
10164018			2			4	1	1
10165042	1					2		
10165049						1	2	
10171009	1		1			2	2	
10172018	3	2	1	1	1	1	1	1
10172021	3	2			1		1	2
10172023	3	2	2	2	1	2	1	2
10172054	4	2	2	2	1	3	3	6
10172055	4	2	4	2	1	2	4	3
10172056	4	2	3	2	1	3	3	2
10172057	4	2	2	2	1	2	3	2
10172058	4	2	2	1		1	3	2
10172059	4	2	2		1	1	2	2
10177014	4	1	2	1	1			1
10179085	1		2					

Table 3.15: Status for outlier runs for run year 2009 (cont.). The number of observables checked per observable set is shown in parenthesis. For each run, the total number of outlier observable values for each observable set is used to determine whether to reject the run. If a run has more than two problem observables in a observable set or more than two observable sets with a problem observable, then the run is rejected.

Run Year	Runs
2006	303
2009	845

Table 3.16: Runs used in the analysis for run year 2006 and 2009

3.6 Hyperon and Jet Yields

3.6.1 $\Lambda(\overline{\Lambda})$ and K_s^0 Yields

The extraction of $\Lambda(\overline{\Lambda})$ and K_s^0 particles entailed iterating twice through particle selection parameter tuning and contamination reduction described in Section 3.1.1 and Section 3.1.4. The diagram in Figure 3.24 shows the workflow for extracting the V^0 particle yields. The second iteration imposes the contamination reduction

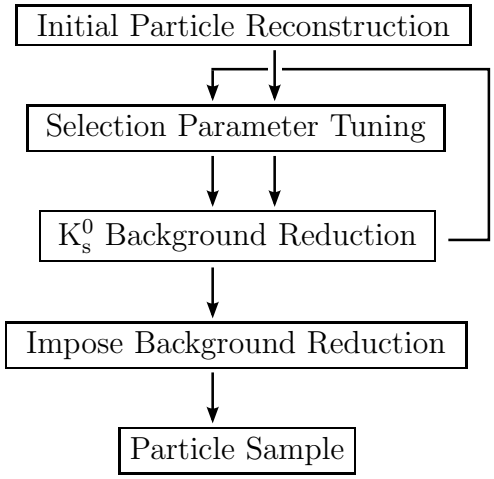

Figure 3.24: Particle extraction workflow.

condition by using the invariant mass signal regions and tuned selection cut parameters determined in the first iteration. The particles removed from contamination reduction condition allow the new selection cut parameter values to be relaxed, aiding in the retention of more V^0 particles. The selection parameter thresholds are

summarized on Tables 3.17–3.19 for both run years. Figures 3.25(a)–(d) show the trends for different selection parameter thresholds. The trends behave as expected, for example, ϕ_{RP} decreases as $\overline{\Lambda}$ $\mathrm{p_T}$ increases.

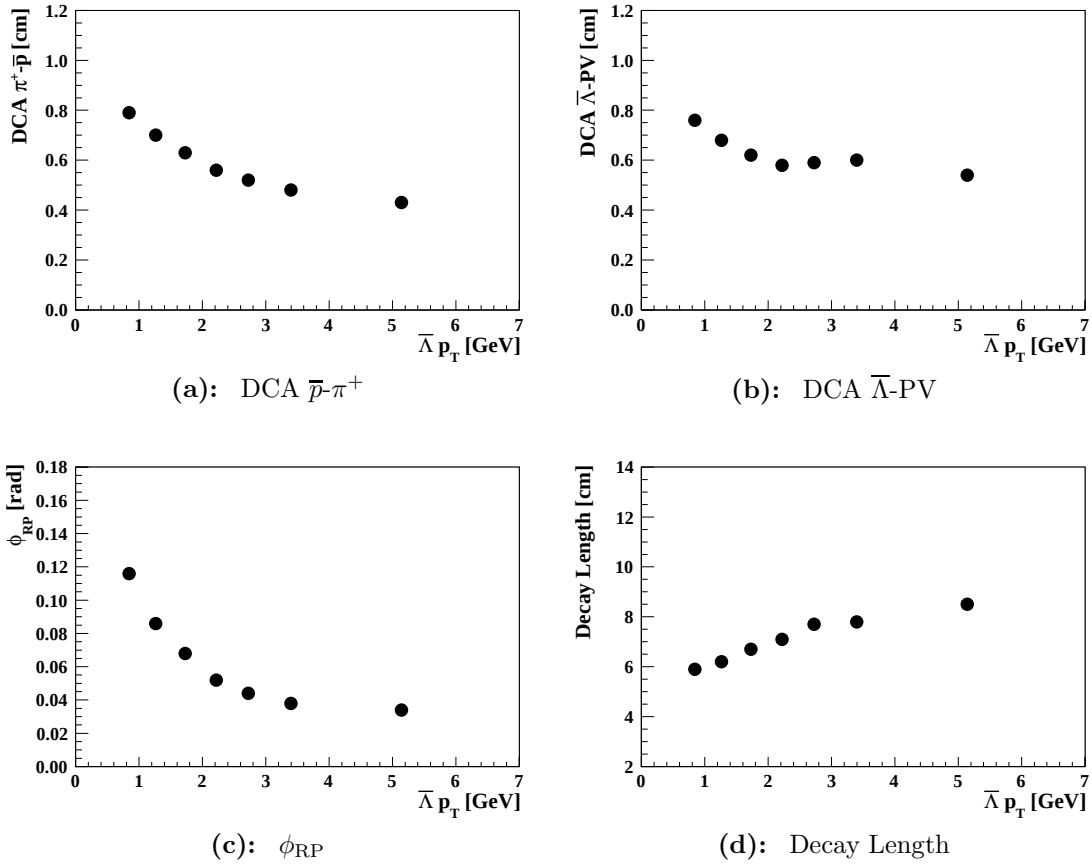

(a): DCA $\overline{p}$-π^+ **(b):** DCA $\overline{\Lambda}$-PV

(c): ϕ_{RP} **(d):** Decay Length

Figure 3.25: $\overline{\Lambda}$ selection parameter trends for JP1–9 triggered data. The angle between momentum vector and position vector is defined as ϕ_{RP}.

p_T GeV	DCA C^+-C^- cm	DCA V^0-PV cm	ϕ_{RP} rad	Decay Length cm	DCA C^--PV cm	DCA C^+-PV cm	Mixed Threshold Neg	Mixed Threshold Plus
				Λ				
$0.5 \leq p_T < 1.0$	0.82	0.80	0.12	6.2	0.87	0.33	1.3	1.1
$1.0 \leq p_T < 1.5$	0.73	0.79	0.09	6.2	0.99	0.45	1.5	0.9
$1.5 \leq p_T < 2.0$	0.67	0.67	0.07	7.1	0.99	0.43	1.4	0.8
$2.0 \leq p_T < 2.5$	0.62	0.65	0.06	7.1	1.05	0.39	1.8	0.8
$2.5 \leq p_T < 3.0$	0.59	0.58	0.05	8.7	0.87	0.39	1.5	1.1
$3.0 \leq p_T < 4.0$	0.61	0.43	0.04	8.2	0.81	0.35	1.8	1.2
$4.0 \leq p_T$	0.56	0.44	0.04	8.5	0.71	0.33	1.6	1.2
				$\overline{\Lambda}$				
$0.5 \leq p_T < 1.0$	0.84	0.87	0.12	6.2	0.71	0.91	0.6	1.2
$1.0 \leq p_T < 1.5$	0.80	0.73	0.09	6.6	0.45	1.01	0.8	1.4
$1.5 \leq p_T < 2.0$	0.69	0.68	0.08	6.8	0.41	1.01	0.8	1.6
$2.0 \leq p_T < 2.5$	0.64	0.57	0.06	6.9	0.39	1.07	0.8	1.5
$2.5 \leq p_T < 3.0$	0.60	0.53	0.05	7.5	0.39	0.85	1.1	1.7
$3.0 \leq p_T < 4.0$	0.71	0.52	0.04	9.1	0.35	0.83	1.2	1.7
$4.0 \leq p_T$	0.58	0.35	0.03	7.8	0.33	0.69	1.3	1.8
				K^0_s				
$0.5 \leq p_T < 1.0$	0.83	0.84	0.15	3.4	0.99	0.97	1.1	1.1
$1.0 \leq p_T < 1.5$	0.73	0.74	0.12	3.8	0.75	0.71	1.2	1.1
$1.5 \leq p_T < 2.0$	0.67	0.65	0.10	4.3	0.63	0.63	1.1	1.1
$2.0 \leq p_T < 2.5$	0.67	0.58	0.08	4.6	0.57	0.57	1.1	1.1
$2.5 \leq p_T < 3.0$	0.66	0.52	0.08	4.8	0.53	0.53	1.2	1.2
$3.0 \leq p_T < 4.0$	0.54	0.50	0.06	5.2	0.51	0.53	1.2	1.1
$4.0 \leq p_T$	0.52	0.36	0.05	5.6	0.47	0.45	1.3	1.3

Table 3.17: Selection parameter thresholds for JP1-6 data

p_T GeV	DCA C^+-C^- cm	DCA V^0-PV cm	ϕ_{RP} rad	Decay Length cm	DCA C^--PV cm	DCA C^+-PV cm	Mixed Threshold Neg	Mixed Threshold Plus
				Λ				
$0.5 \leq p_T < 1.0$	0.78	0.80	0.12	6.0	0.83	0.37	1.3	1.0
$1.0 \leq p_T < 1.5$	0.70	0.71	0.09	6.3	0.89	0.41	1.5	0.9
$1.5 \leq p_T < 2.0$	0.64	0.64	0.07	6.6	0.91	0.37	1.6	0.9
$2.0 \leq p_T < 2.5$	0.59	0.57	0.05	7.1	0.87	0.35	1.7	0.9
$2.5 \leq p_T < 3.0$	0.58	0.53	0.04	7.6	0.85	0.35	1.7	1.2
$3.0 \leq p_T < 4.0$	0.57	0.50	0.04	7.7	0.77	0.33	1.8	1.3
$4.0 \leq p_T$	0.55	0.43	0.03	8.0	0.73	0.29	1.9	1.4
				$\overline{\Lambda}$				
$0.5 \leq p_T < 1.0$	0.76	0.79	0.12	5.9	0.43	0.85	1.0	1.2
$1.0 \leq p_T < 1.5$	0.68	0.70	0.09	6.2	0.39	0.89	0.9	1.4
$1.5 \leq p_T < 2.0$	0.62	0.63	0.07	6.7	0.37	0.89	0.9	1.5
$2.0 \leq p_T < 2.5$	0.58	0.56	0.05	7.1	0.35	0.85	0.9	1.6
$2.5 \leq p_T < 3.0$	0.59	0.52	0.04	7.7	0.33	0.75	1.2	1.8
$3.0 \leq p_T < 4.0$	0.60	0.48	0.04	7.8	0.33	0.75	1.3	1.8
$4.0 \leq p_T$	0.54	0.43	0.03	8.5	0.29	0.73	1.4	1.7
				K^0_s				
$0.5 \leq p_T < 1.0$	0.70	0.76	0.15	3.4	0.91	0.89	1.2	1.1
$1.0 \leq p_T < 1.5$	0.65	0.67	0.12	3.9	0.69	0.67	1.1	1.1
$1.5 \leq p_T < 2.0$	0.61	0.61	0.10	4.4	0.61	0.61	1.1	1.0
$2.0 \leq p_T < 2.5$	0.58	0.56	0.08	4.7	0.55	0.55	1.0	1.0
$2.5 \leq p_T < 3.0$	0.54	0.52	0.07	4.9	0.51	0.51	1.1	1.1
$3.0 \leq p_T < 4.0$	0.51	0.46	0.06	5.1	0.49	0.49	1.2	1.2
$4.0 \leq p_T$	0.47	0.37	0.05	5.7	0.45	0.45	1.3	1.2

Table 3.18: Selection parameter thresholds for JP1-9 data

p_T GeV	DCA C^+-C^- cm	DCA V^0-PV cm	ϕ_{RP} rad	Decay Length cm	DCA C^--PV cm	DCA C^+-PV cm	Mixed Threshold Neg	Mixed Threshold Plus
				Λ				
$0.5 \leq p_T < 1.0$	0.79	0.80	0.12	6.0	0.81	0.33	1.3	1.1
$1.0 \leq p_T < 1.5$	0.71	0.73	0.09	6.3	0.91	0.41	1.5	0.9
$1.5 \leq p_T < 2.0$	0.63	0.66	0.07	6.6	0.91	0.39	1.5	0.8
$2.0 \leq p_T < 2.5$	0.58	0.60	0.06	7.2	0.89	0.37	1.6	0.8
$2.5 \leq p_T < 3.0$	0.58	0.56	0.04	7.8	0.87	0.35	1.7	1.2
$3.0 \leq p_T < 4.0$	0.57	0.52	0.04	8.0	0.77	0.33	1.7	1.2
$4.0 \leq p_T$	0.55	0.44	0.03	7.6	0.69	0.31	1.8	1.4
				$\overline{\Lambda}$				
$0.5 \leq p_T < 1.0$	0.76	0.83	0.12	5.9	0.41	0.81	1.0	1.2
$1.0 \leq p_T < 1.5$	0.69	0.72	0.09	6.4	0.39	0.91	0.9	1.4
$1.5 \leq p_T < 2.0$	0.64	0.65	0.07	6.6	0.37	0.89	0.9	1.6
$2.0 \leq p_T < 2.5$	0.58	0.57	0.06	7.2	0.37	0.87	0.8	1.6
$2.5 \leq p_T < 3.0$	0.56	0.52	0.05	7.5	0.35	0.77	1.1	1.7
$3.0 \leq p_T < 4.0$	0.55	0.49	0.04	7.6	0.33	0.77	1.2	1.7
$4.0 \leq p_T$	0.53	0.43	0.03	7.7	0.31	0.73	1.3	1.7
				K_s^0				
$0.5 \leq p_T < 1.0$	0.71	0.77	0.15	3.4	0.89	0.87	1.2	1.1
$1.0 \leq p_T < 1.5$	0.66	0.69	0.12	4.0	0.69	0.67	1.1	1.1
$1.5 \leq p_T < 2.0$	0.62	0.62	0.10	4.4	0.61	0.61	1.1	1.1
$2.0 \leq p_T < 2.5$	0.58	0.57	0.08	4.8	0.55	0.55	1.0	1.0
$2.5 \leq p_T < 3.0$	0.54	0.54	0.07	4.8	0.51	0.51	1.2	1.1
$3.0 \leq p_T < 4.0$	0.52	0.48	0.06	5.1	0.49	0.49	1.2	1.2
$4.0 \leq p_T$	0.47	0.38	0.05	5.6	0.45	0.45	1.3	1.2

Table 3.19: Selection parameter thresholds for L2JH-9 data

The invariant mass spectra for $\Lambda(\overline{\Lambda})$ and K^0_s particles for run year 2006 and 2009 are shown in Figures 3.26(a)–(c) and Figures 3.27(a)–(f). The green area defines the signal region. The dark blue areas define the background regions while the light blue area at the bottom of the signal region is the residual background.

The background and mass widths are well behaved for each V^0 p_T interval are

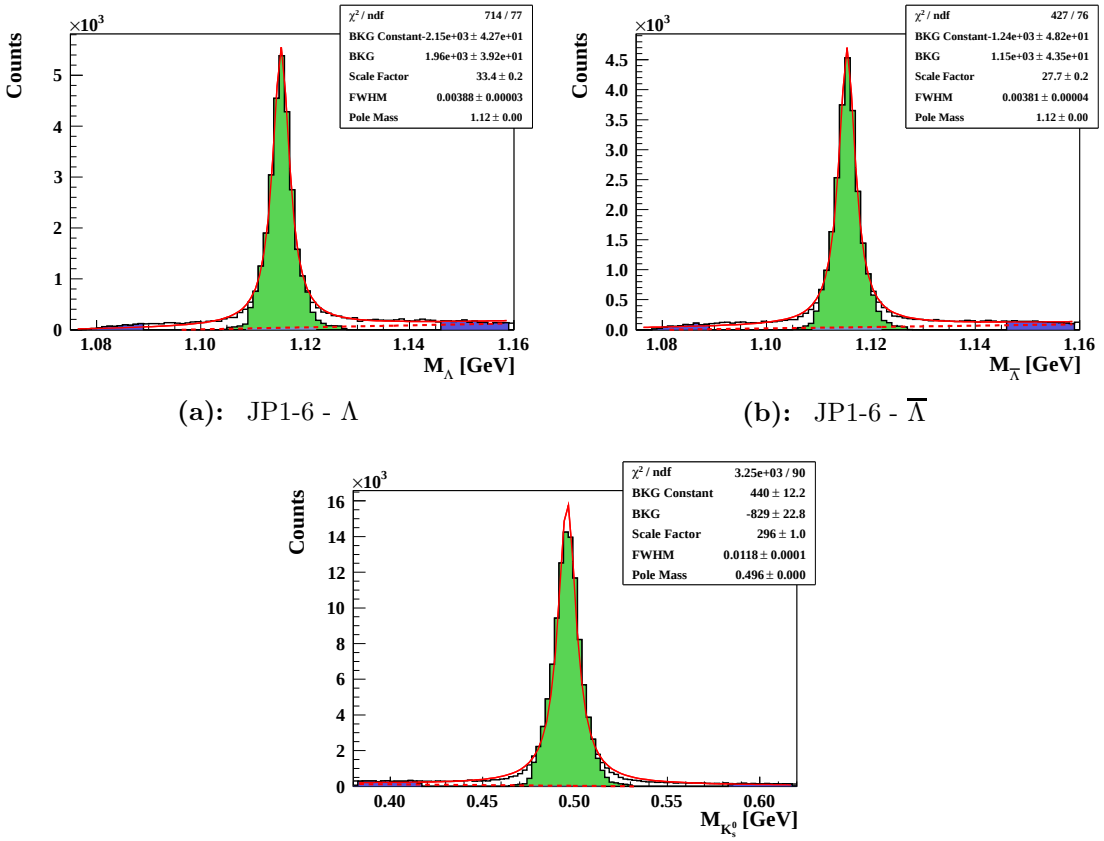

(a): JP1-6 - Λ

(b): JP1-6 - $\overline{\Lambda}$

(c): JP1-6 - K^0_s

Figure 3.26: Invariant mass spectra for JP1–6 triggered data

illustrated in Figures 3.28(a)–(g) for JP1-6 $\overline{\Lambda}$'s.

The central values for the invariant masses and FWHM for $\Lambda(\overline{\Lambda})$ and K^0_s at different p_T intervals for both run years are shown in Figures 3.29–3.31. The TPC resolution decreases as particles p_T increases, resulting in a broadening of the invariant mass peak seen for $p_T > 4$ GeV. The amount of V^0 particles within

either the signal or background regions are given in Table 3.20 for both run years. The residual background is defined as the area within the signal region from the linear component of the fitted Lorentzian function. The residual background is expected to be mostly unpolarized, diluting the extracted D_{LL} values.

	Λ	$\overline{\Lambda}$	K^0_s
		JP1–6	
Signal Range	29K	24K	105K
Background Range	3K	2K	6K
Residual Background (%)	1.5	1.6	0.9
		JP1–9	
Signal Range	628K	621K	2025K
Background Range	46K	42K	96K
Residual Background (%)	0.4	0.3	0.2
		L2JH–9	
Signal Range	356K	350K	1329K
Background Range	33K	29K	70K
Residual Background (%)	1.1	0.8	0.5

Table 3.20: Particle yield summary for run year 2006 and 2009

To check if tuning the selection parameters might result in artificially shaping the invariant mass spectrum a check was made by applying the tuned selection parameters to a background sample to see if any noticeable signal shaping took place. A sample of V^0 particles was created using the same jet triggered data set but by rotating all positively charged decay particles by 180° around the azimuth. The rotation of positively charged particles destroys the real V^0 particle decays, so that only combinatorial background is reconstructed. As mentioned in Section 3.1.1, a positively and a negatively charged particle are required when reconstructing $\Lambda(\overline{\Lambda})$ or K^0_s particles. Signal combinations of a rotated positively charged track with its corresponding negatively track partner at the new secondary decay position are

all rejected for containing an opening angle above threshold. Figures 3.32(a)–(f) show the initial and tuned invariant mass yields from the combinatorial background sample of $\Lambda(\overline{\Lambda})$ and K_s^0 particles for JP1–6 triggered data. Similar plots for JP1–9 triggered combinatorial background set are shown in Figures 3.33(a)–(f). There is no artificial signal generated by the analysis procedure throughout the p_T intervals for all V^0 species. The dip seen in the lower mass region for $\Lambda(\overline{\Lambda})$ yields is due to the removal of electron pairs with low reconstructed invariant mass from the samples.

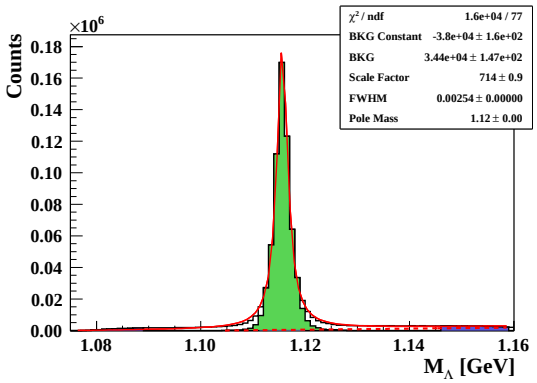

(a): JP1-9 - Λ

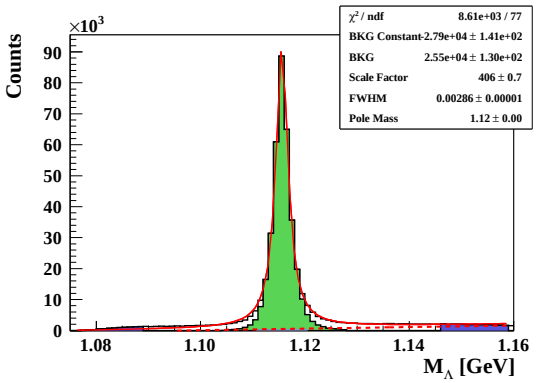

(b): L2JH-9 - Λ

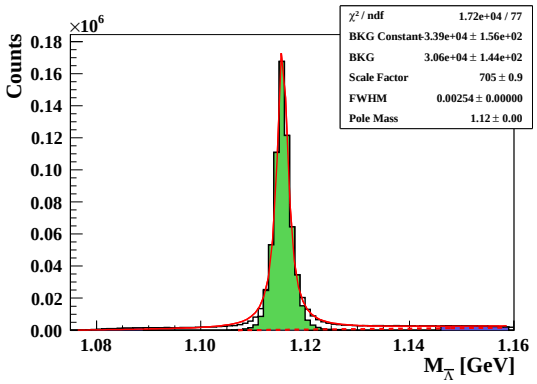

(c): JP1-9 - $\overline{\Lambda}$

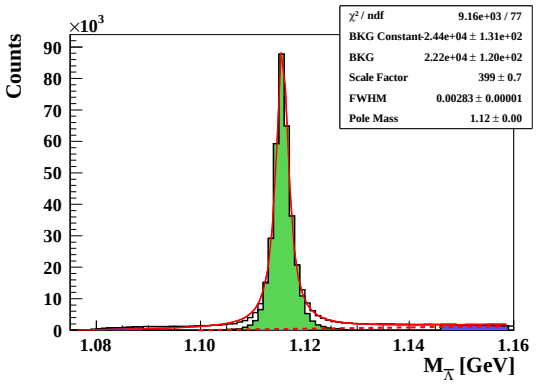

(d): L2JH-9 - $\overline{\Lambda}$

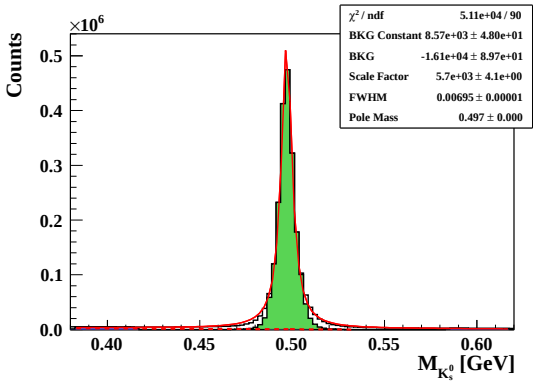

(e): JP1-9 - K^0_s

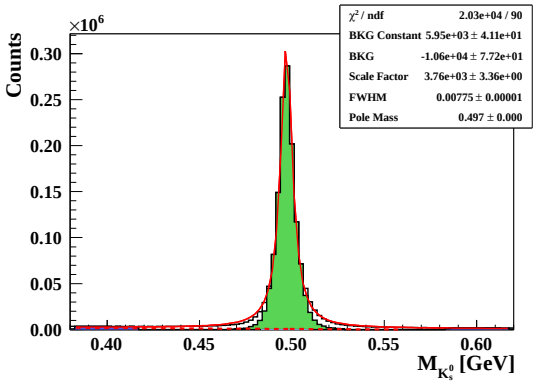

(f): L2JH-9 - K^0_s

Figure 3.27: Invariant mass spectra for JP1–9 and L2JH–9 triggered data

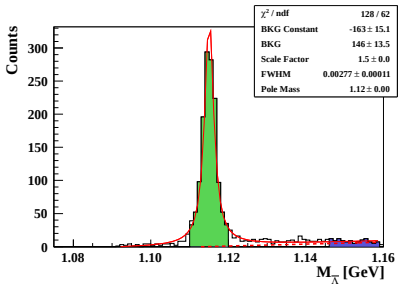

(a): $0.5 \leq p_T < 1.0$ GeV

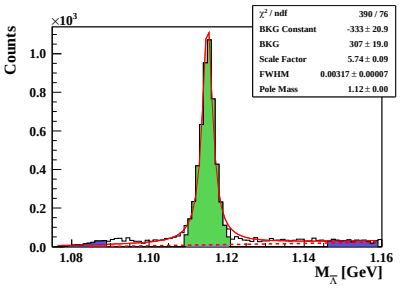

(b): $1.0 \leq p_T < 1.5$ GeV

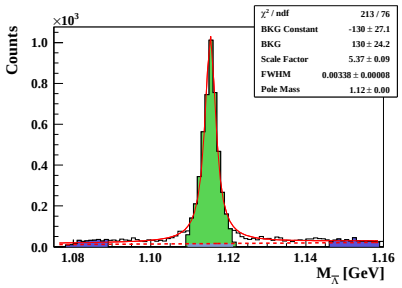

(c): $1.5 \leq p_T < 1.0$ GeV

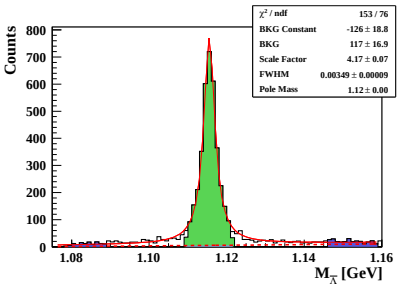

(d): $2.0 \leq p_T < 2.5$ GeV

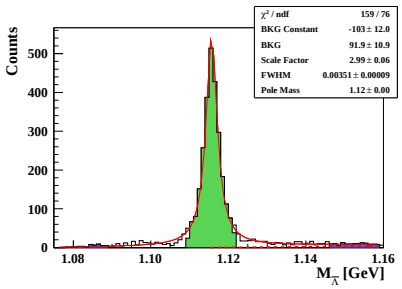

(e): $2.5 \leq p_T < 2.0$ GeV

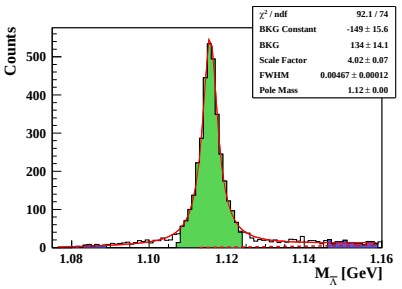

(f): $3.0 \leq p_T < 4.0$ GeV

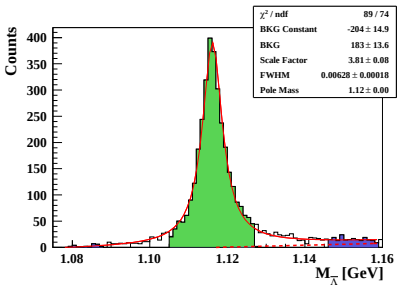

(g): $4.0 \leq p_T$ GeV

Figure 3.28: $\overline{\Lambda}$ invariant mass yields for JP1-6 trigger for different p_T intervals. The invariant mass peak is well behaved for all p_T intervals. Similar behavior is found for Λ and K^0_s in JP1–6, JP1–9, and L2JH–9 triggered data.

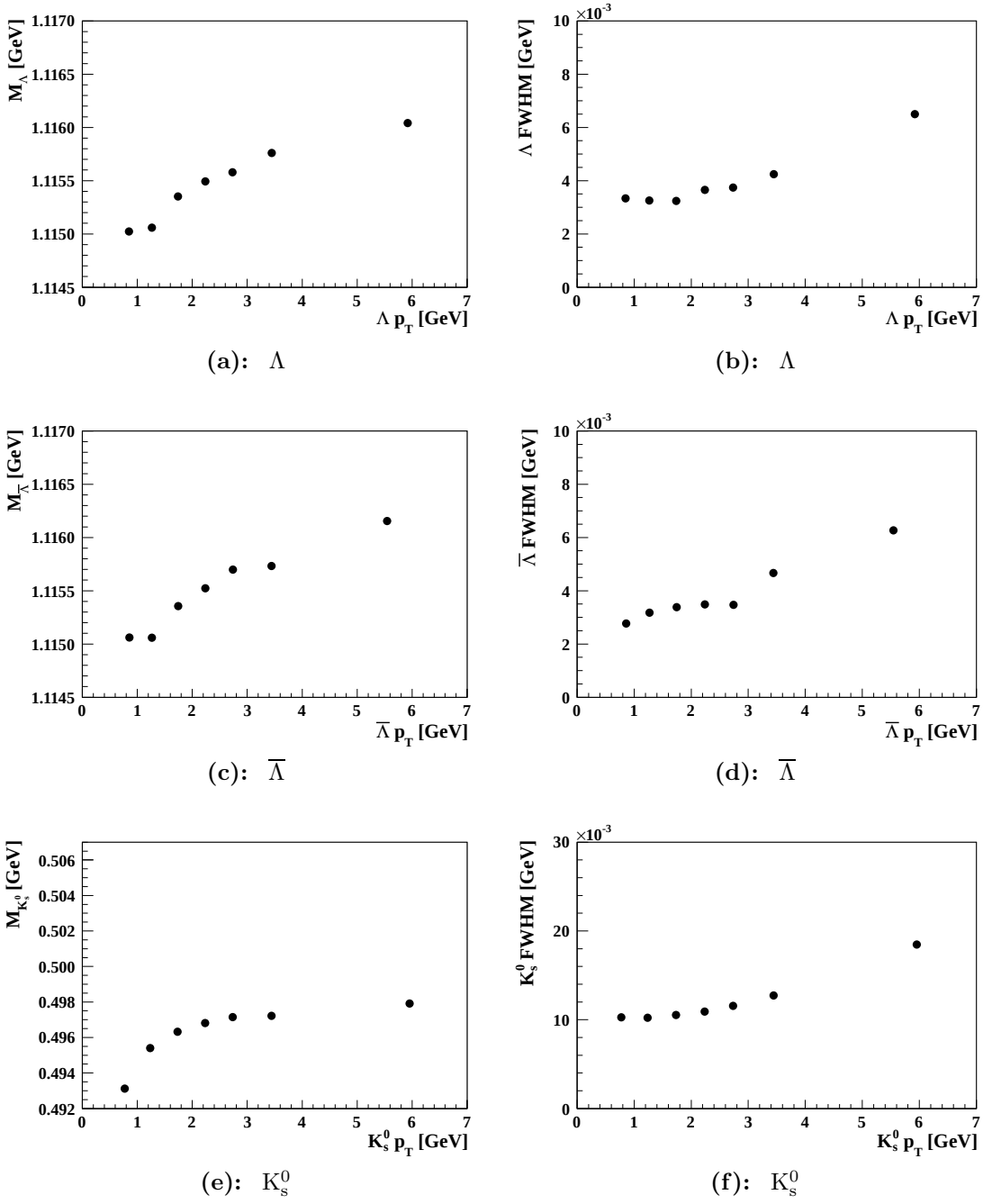

(a): Λ **(b):** Λ

(c): $\overline{\Lambda}$ **(d):** $\overline{\Lambda}$

(e): K^0_s **(f):** K^0_s

Figure 3.29: Central invariant mass and FWHM trends for JP1–6 data. Lower K^0_s p_T intervals exhibit lower central invariant mass values because of differences in combinatorial background. The FWHM increases for higher p_T intervals as expected.

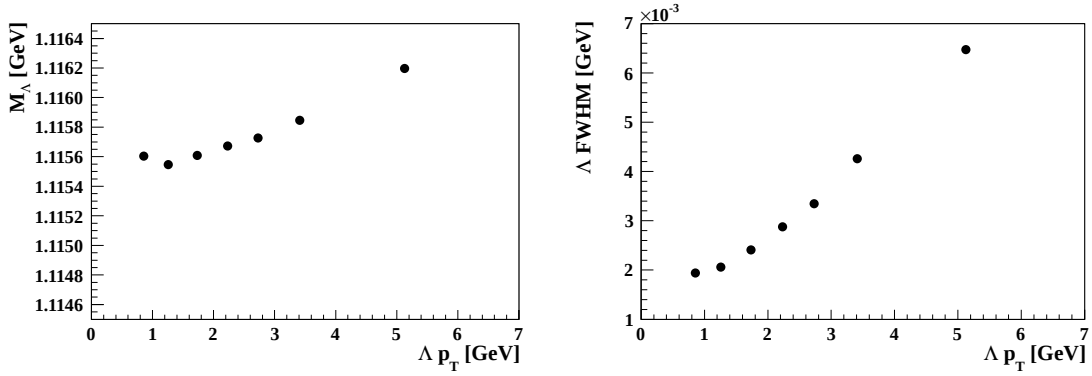

(a): Λ **(b):** Λ

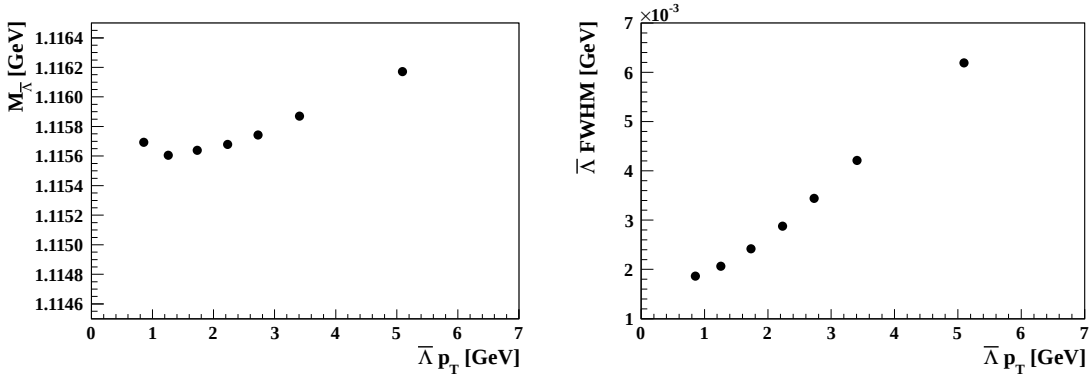

(c): $\overline{\Lambda}$ **(d):** $\overline{\Lambda}$

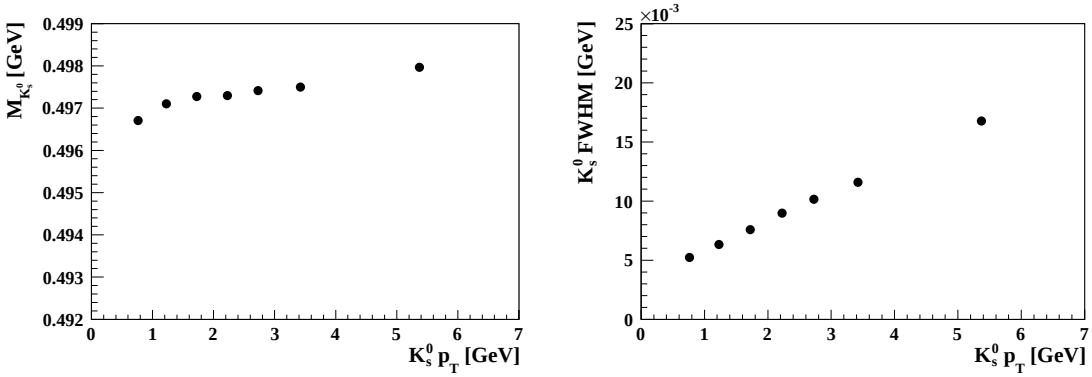

(e): K^0_S **(f):** K^0_S

Figure 3.30: Central invariant mass and FWHM trends for JP1–9 data. The FWHM increases for higher p_T intervals as expected.

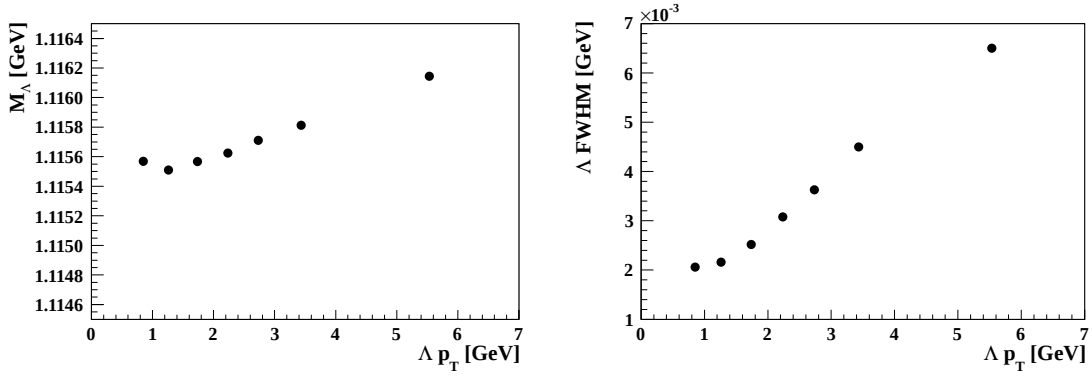

(a): Λ **(b):** Λ

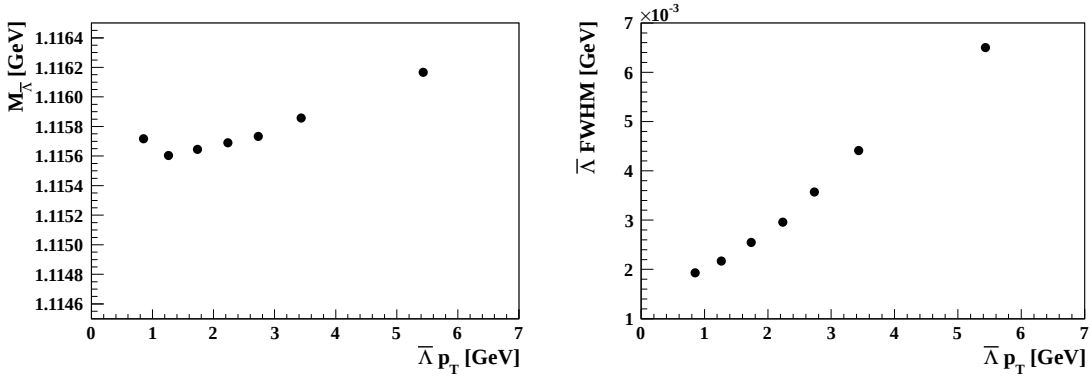

(c): $\overline{\Lambda}$ **(d):** $\overline{\Lambda}$

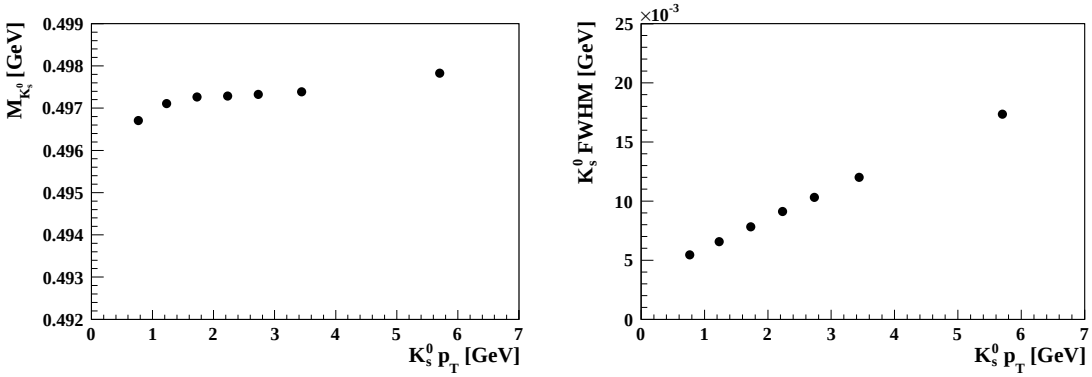

(e): K_s^0 **(f):** K_s^0

Figure 3.31: Central invariant mass and FWHM trends for L2JH–9 data. The FWHM increases for higher p_T intervals as expected.

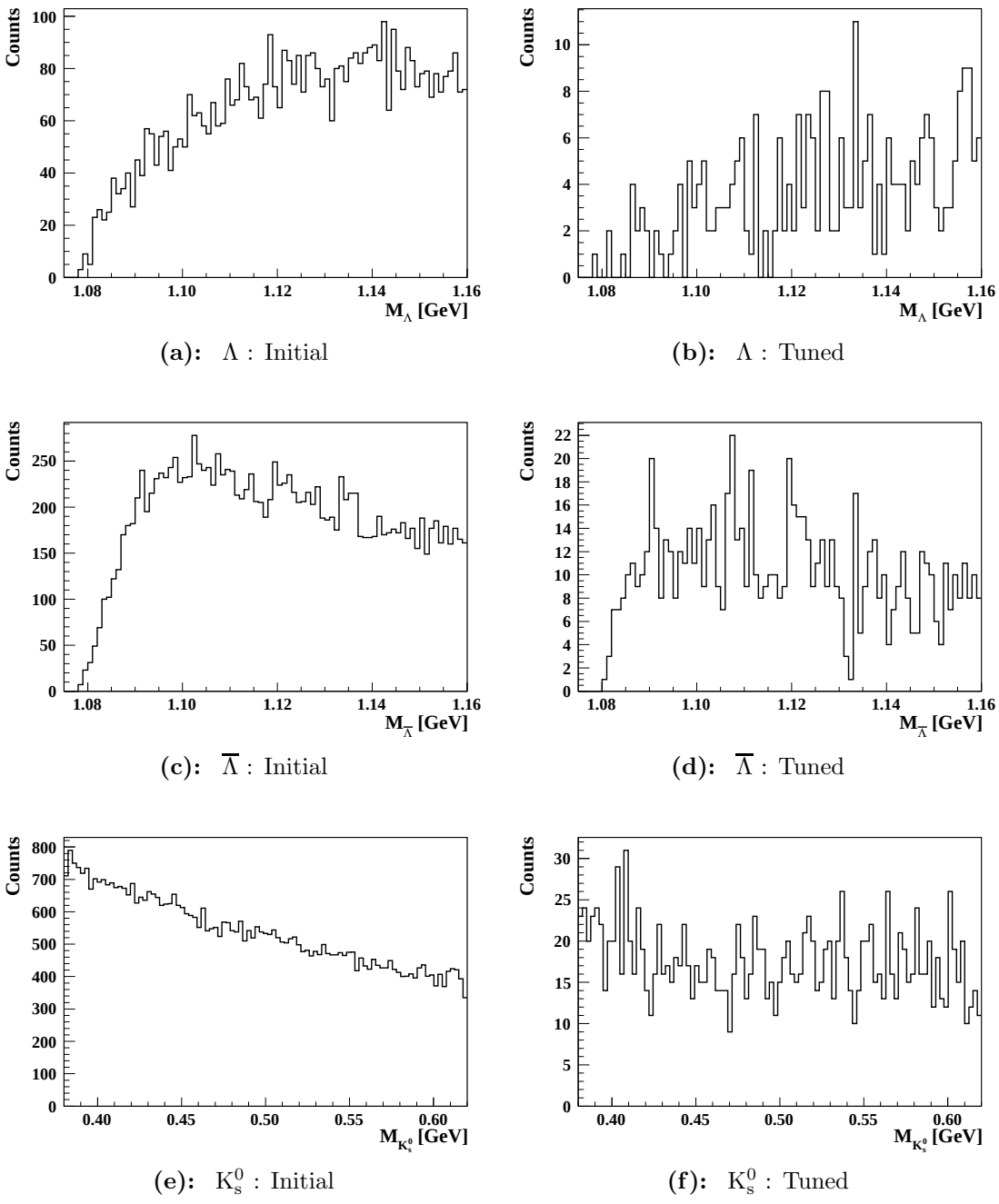

(a): Λ : Initial

(b): Λ : Tuned

(c): $\overline{\Lambda}$: Initial

(d): $\overline{\Lambda}$: Tuned

(e): K^0_s : Initial

(f): K^0_s : Tuned

Figure 3.32: JP1–6 triggered $\Lambda(\overline{\Lambda})$ and K^0_s invariant mass yields for $p_T > 0.5$ GeV for the rotated track data sample. Positively charged tracks were rotated by 180° azimuthally. The left column shows the invariant mass yields with the initial selection parameters while the right column shows the invariant mass yields with the tuned selection parameters. No evidence for any artificial signal due to tuned selection parameters is found.

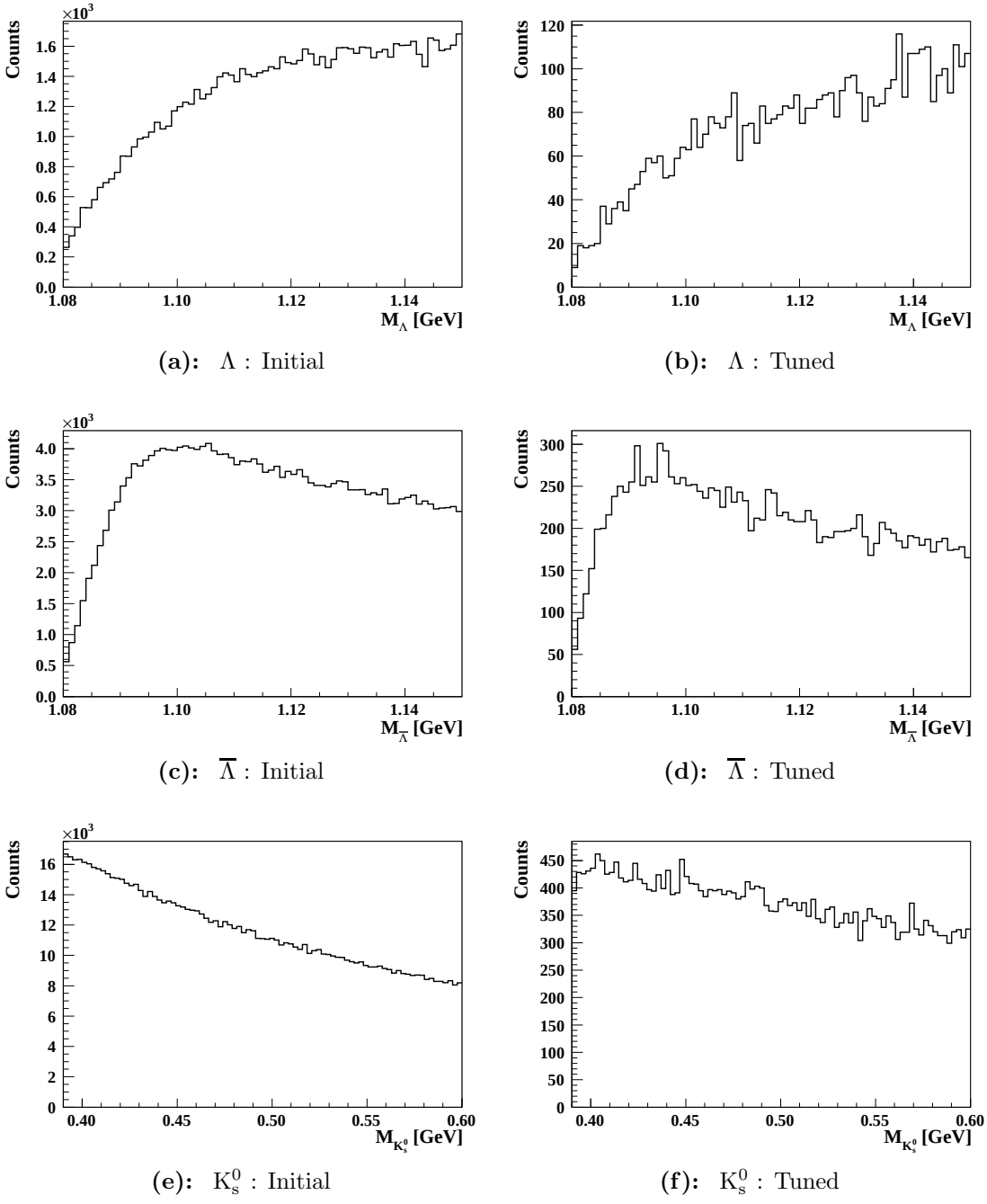

(a): Λ : Initial

(b): Λ : Tuned

(c): $\overline{\Lambda}$: Initial

(d): $\overline{\Lambda}$: Tuned

(e): K^0_s : Initial

(f): K^0_s : Tuned

Figure 3.33: JP1–9 triggered $\Lambda(\overline{\Lambda})$ and K^0_s invariant mass yields for $p_T > 0.5$ GeV for the rotated track data sample. The positively charged tracks were rotated by 180° azimuthally. The left column shows the invariant mass yields with initial selection parameters while the right column shows the invariant mass yields with the tuned selection parameters. No evidence for any artificial signal due to tuned selection parameters is found. Similar results are arrived at for L2JH–9 triggered combinatorial background data set.

3.6.2 Jet Yields

For run year 2006 and 2009, jets were reconstructed for each trigger of interest using the STAR jet reconstruction algorithm described in Section 3.2.1. Events which had no jets matching at least one of the triggered jet patches were rejected. Conditions were imposed on the neutral energy ratio,

$$R_T = \frac{E_T^{Neutral}}{E_T^{Jet}}, \tag{3.34}$$

where $E_T^{Neutral}$ is the energy reconstructed on the BEMC and E_T^{Jet} is the total energy deposited from charged tracks and neutral particles to further reduce the contribution from beam gas background [Abe08]. Figures 3.34(a)–(f) show the neutral energy ratio and multiplicity distributions for reconstructed jets from both run years. Jets residing in the cross-hatched regions were rejected from the jet sample since they contain a large beam gas background contribution. For run year 2009, six additional jet patches were implemented which contain towers in both the East and West halves of the BEMC. The additional jet patches resulted in a more uniform jet acceptance. Mid-rapidity jets reside between jet patches covering the East and West halves of the BEMC and would otherwise have deposited their energy in two jet patches, not necessarily satisfying the minimum trigger E_T threshold for either jet patch. The $\eta_{\rm jet}$ distributions are shown for both run year 2006 and 2009 in Figures 3.35(a)–(b). The extra six jet patches in run year 2009 are responsible for the more uniform acceptance near $\eta = 0$ compared to run year 2006. Figure 3.36 shows the jet p_T distributions for the three triggers of interest. The jet p_T range extends further for L2JH–9, which is expected since L2JH–9 requires a higher jet E_T threshold than JP1–9. The $p_T^{\rm Jet}$ distributions for JP1–6 and L2JH–9 have similar shape compared to JP1–6 where its deviates for $p_T^{\rm Jet} < 25$ GeV. The JP1–6 trigger has lower E_T threshold values, resulting in an increase acceptance of lower $p_T^{\rm Jet}$ jets.

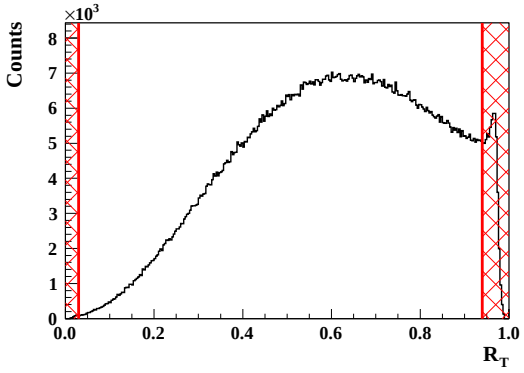

(a): JP1–6: R_T

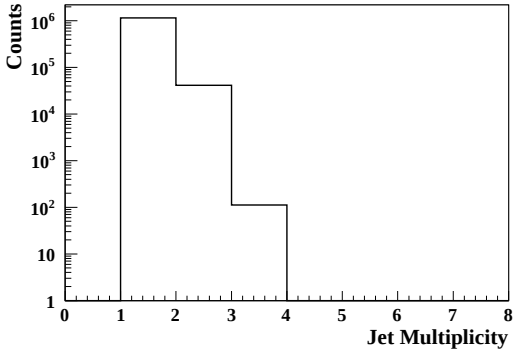

(b): JP1–6: Jet Multiplicities

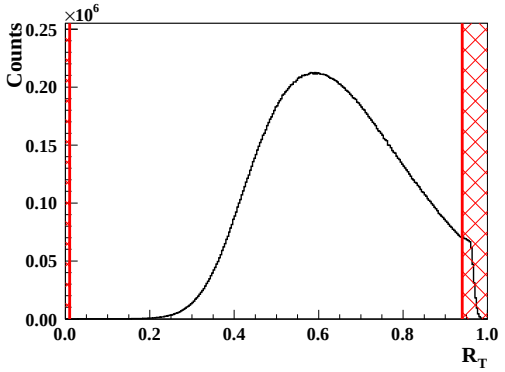

(c): JP1–9: R_T

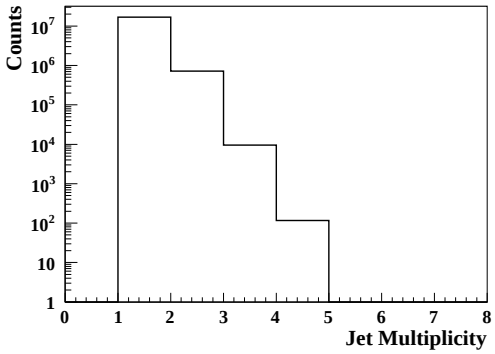

(d): JP1–9: Jet Multiplicities

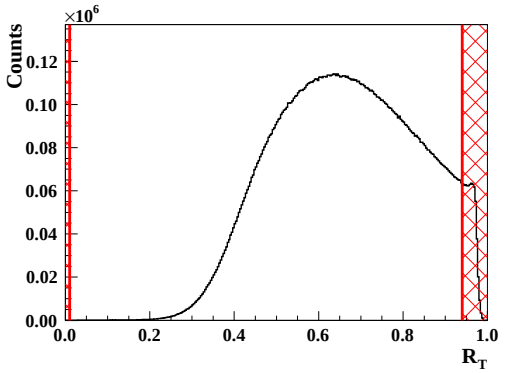

(e): L2JH–9: R_T

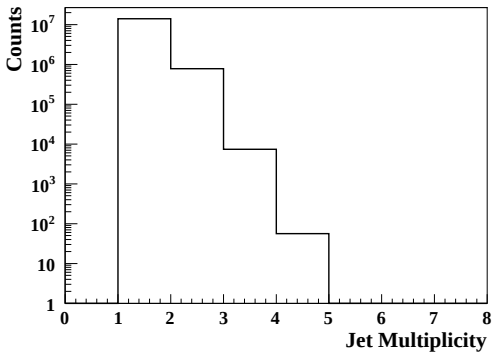

(f): L2JH–9: Jet Multiplicities

Figure 3.34: Jet neutral energy ratio and jet multiplicity distributions for both run years. Jets residing in the red cross-hatched region are rejected in order to reduce the contribution from beam gas background. Jets are required to match a triggered jet patch.

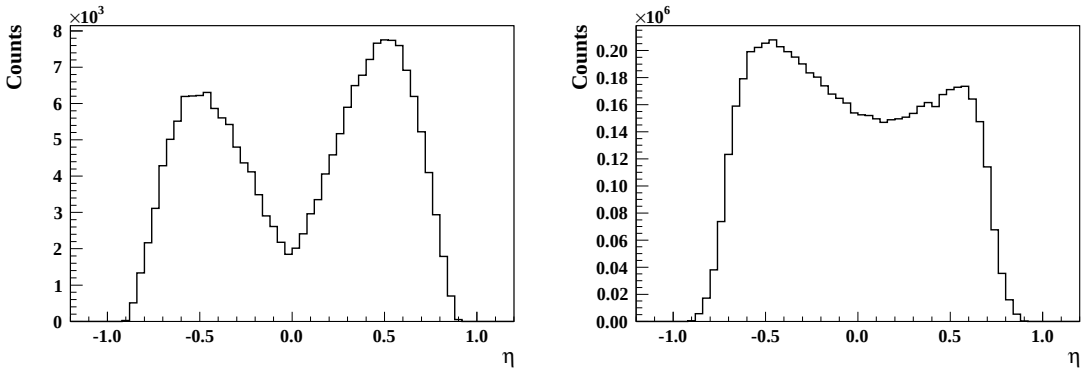

(a): 2006 **(b):** 2009

Figure 3.35: Jet η distributions for run year 2006 and 2009. The additional six jet patches in run year 2009 allowed for a more uniform acceptance compared to run year 2006 as described in the text.

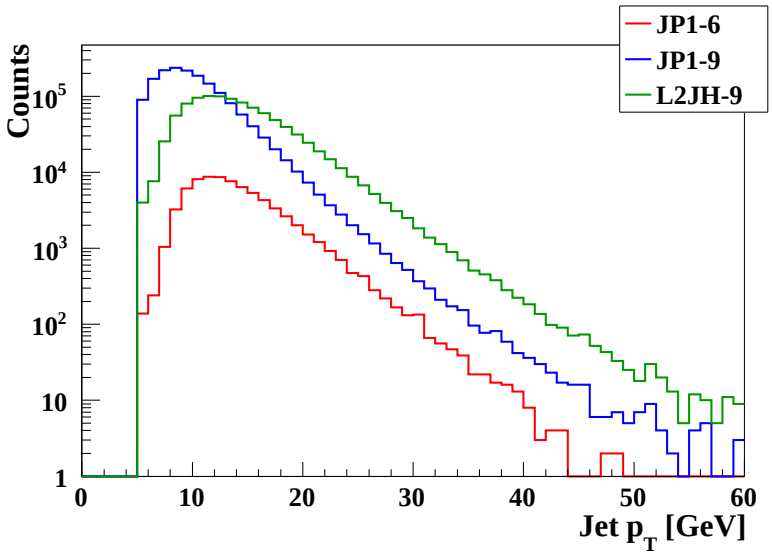

Figure 3.36: Jet p_T distributions for both run years. L2JH–9 contains more events containing higher jet p_T than other triggered data sets. The three jet p_T distributions have similar shape for $p_T^{Jet} > 25$ GeV. JP1–9 has lower E_T threshold values resulting in an increase acceptance of lower p_T^{Jet} jets.

3.6.3 Hyperon-Jet Association

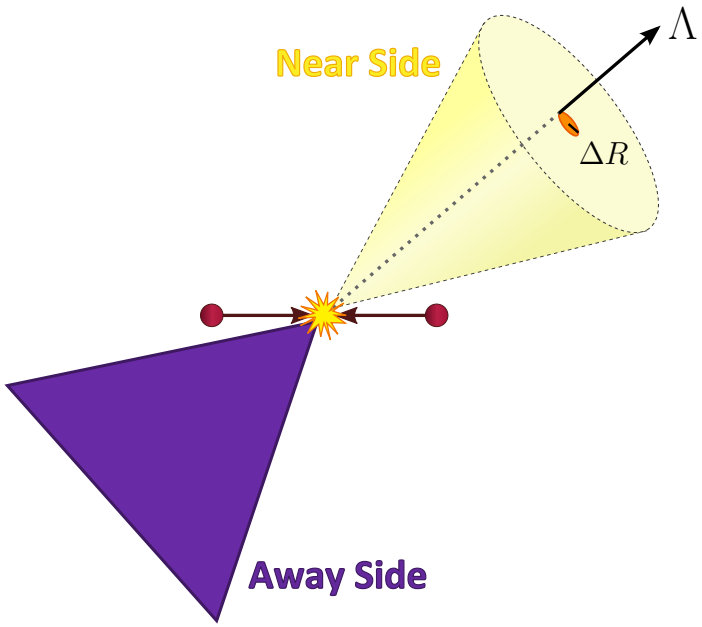

Figure 3.37: Diagram of hyperon-jet association. Near-side Λs reside within the triggered jet cone radius while away-side Λs reside within the ϕ range away from the triggered jet.

Run year 2006 and 2009 used trigger conditions to record events with high p_T jets. The association of $\Lambda(\overline{\Lambda})$s to triggered jets increases the likelihood that the $\Lambda(\overline{\Lambda})$s originated from hard 2→2 scattering collisions. The associated $\Lambda(\overline{\Lambda})$s are categorized as near-side and away-side $\Lambda(\overline{\Lambda})$s as shown in Figure 3.37. Near-side $\Lambda(\overline{\Lambda})$s are defined as $\Lambda(\overline{\Lambda})$s residing within the jet cone radius of 0.7,

$$R = \sqrt{(\Delta\eta)^2 + (\Delta\phi)^2} = 0.7, \tag{3.35}$$

from a triggered jet as shown in Figures 3.38(a)–(f) while $\Lambda(\overline{\Lambda})$s residing between $\Delta\phi$ [1.7, 4.6] rad on the transverse plane from a triggered jet are defined as away-side $\Lambda(\overline{\Lambda})$s. The $\Delta\phi$ range is chosen so as to discriminate signal from underlying event background as seen in Figures 3.39(a)–(f). In categorizing the $\Lambda(\overline{\Lambda})$s,

the near-side takes priority if the $\Lambda(\overline{\Lambda})$ association satisfies both near-side and away-side conditions for events with multiple trigger jets. The K^0_s particles were associated to jets and categorized in the same way.

Jets are comprised of a collection of particles, each contributing to the jet's total momentum. The momentum fraction, z, can be calculated for each constituent particle as

$$z = \frac{\mathbf{p}_f \cdot \mathbf{P}_j}{P^2}, \tag{3.36}$$

where $\mathbf{p}_f$ and $\mathbf{P}_j$ are the momentum for the constituent particle and jet, respectively. Using the p_T component for the associated $\Lambda(\overline{\Lambda})$ and triggered jet, the jet p_T fragmentation distribution for different $p_T^{\Lambda(\overline{\Lambda})}$ intervals are shown in Figures 3.40–3.42. There is a positive trend of the average z values with $p_T^{\Lambda(\overline{\Lambda})}$, as expected. With increasing $p_T^{\Lambda(\overline{\Lambda})}$ the $\Lambda(\overline{\Lambda})$s are increasingly likely to be the leading particle in the jet, contributing most of the jet momentum. In calculating z, no corrections were performed for detector acceptance, resolution, or efficiency on the jet energy scale. Table 3.21 shows the hyperon-jet associated yields of $\Lambda(\overline{\Lambda})$ and K^0_s particles within the invariant mass signal region for run year 2006 and 2009. The residual background contribution was recalculated for the hyperon-jet associated yields which are summarized in Table 3.22. There is an overall increase of the residual background contribution for all trigger sets after imposing hyperon-jet association. The highest p_T interval contains the largest residual background contribution for all particle species and trigger sets. This is expected since the observed invariant mass peak widens as a p_T increases because of resolution effects, thus increasing the underlying background counts. Figures 3.43(a)–(f) show the p_T distributions of near-side and away-side $\Lambda(\overline{\Lambda})$s which reside within the invariant mass signal region for run year 2006 and 2009 triggers. The near-side $\Lambda(\overline{\Lambda})$s contain higher p_T $\Lambda(\overline{\Lambda})$s compared to the away-side sample for both run years.

Jets are reconstructed using TPC charged tracks and BEMC neutral energy deposits. The reconstruction therefore does not explicitly consider the hyperons of interest. Although a reconstructed hyperon resides within the triggered jet cone after association, the decay daughters may not. This is expected to happen more to the $\pi^+(\pi^-)$ daughters, which tend to carry a smaller portion of the hyperon's momentum and be produced at larger angles. Furthermore, the jet reconstruction uses only tracks classified as primary tracks. Primary tracks are particle tracks that point back to the primary vertex and are used to determine to the primary vertex. The hyperon decay daughter tracks originate from a secondary vertex, and may not be classified as primary tracks. Figures 3.44–3.45 show the number distributions when neither, either, or both of the decay daughters are part of the jet finding and reconstruction for $\Lambda(\overline{\Lambda})$ hyperons associated with jets from jet triggered data for run year 2006 and 2009 (continuous lines). For each of the four entries in these distributions, the colored entries indicate if the decay daughters were primary or global tracks. Most of the daughters are identified as global tracks when neither of the daughters contribute to the associated jet's reconstruction as expected. The $p(\overline{p})$ from $\Lambda(\overline{\Lambda})$ hyperon decay contributed 70-79% to the associated jet's reconstruction for run year 2006 and 2009. This is expected as $p(\overline{p})$ carries more of the $\Lambda(\overline{\Lambda})$'s momentum. Daughter particles identified as primary tracks contributed 72-79% to the associated jet's reconstruction for run year 2006 and 2009.

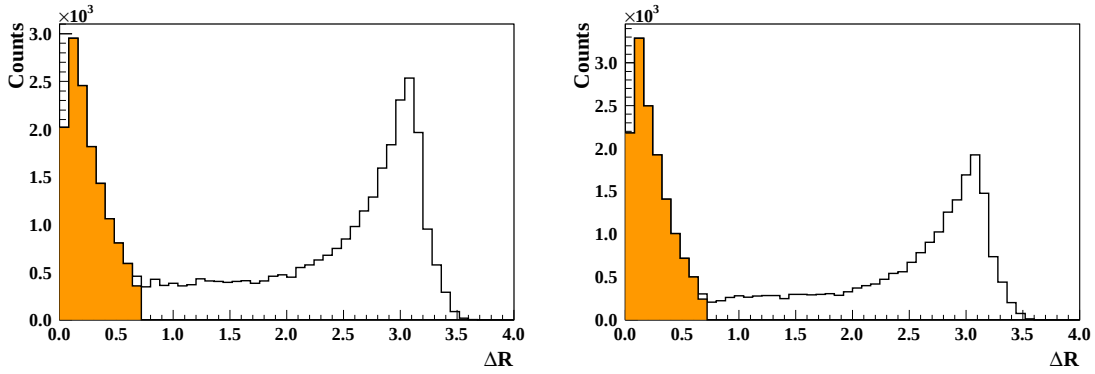

(a): JP1–6: Λ **(b):** JP1–6: $\overline{\Lambda}$

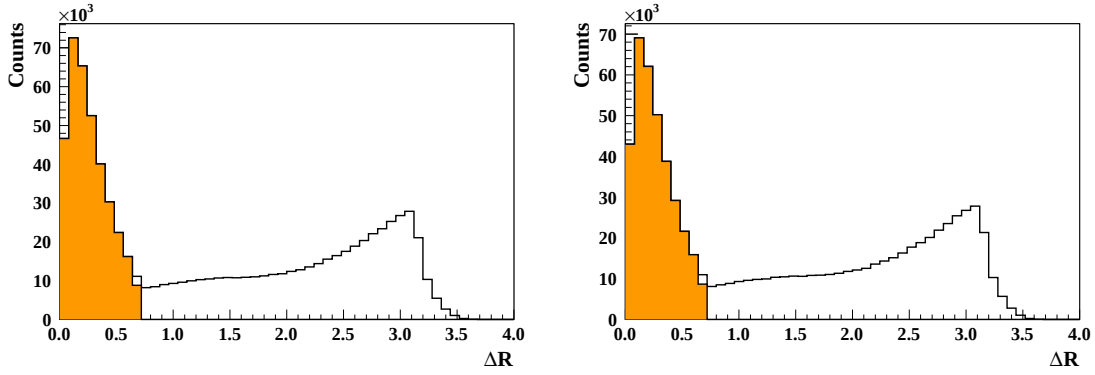

(c): JP1–9: Λ **(d):** JP1–9: $\overline{\Lambda}$

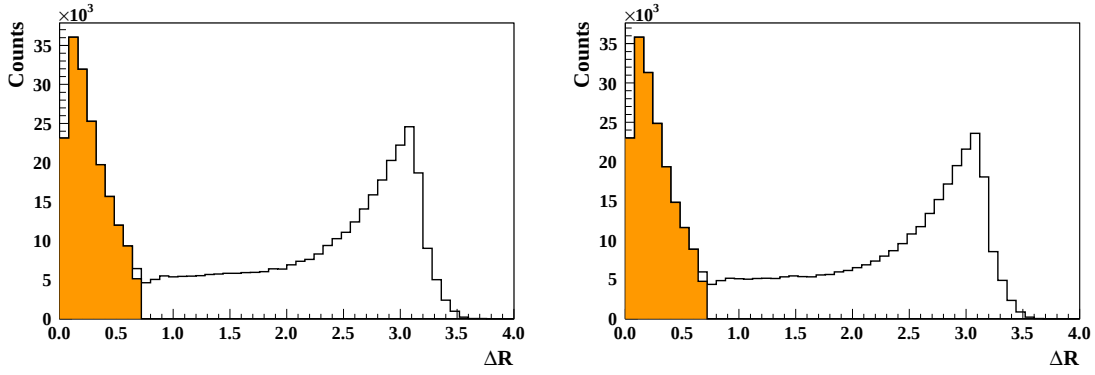

(e): L2JH–9: Λ **(f):** L2JH–9: $\overline{\Lambda}$

Figure 3.38: ΔR between $\Lambda(\overline{\Lambda})$ and jets for both run years. The orange shaded region contains the near-side $\Lambda(\overline{\Lambda})$s.

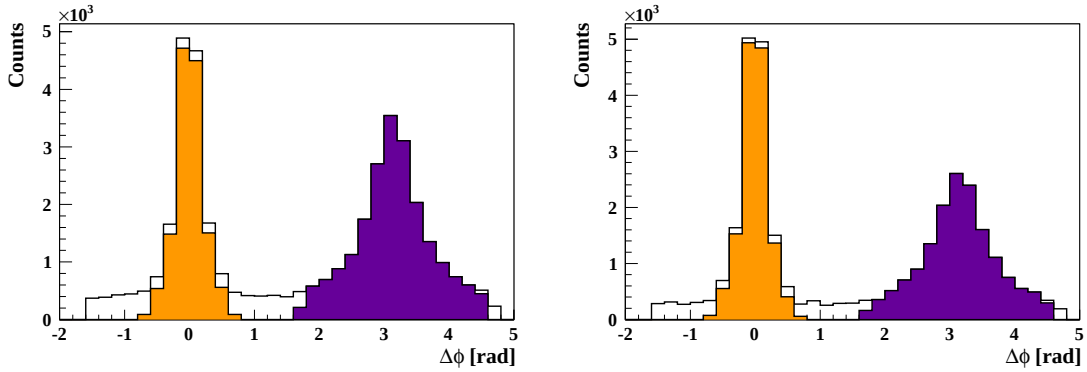

(a): JP1–6: Λ **(b):** JP1–6: $\overline{\Lambda}$

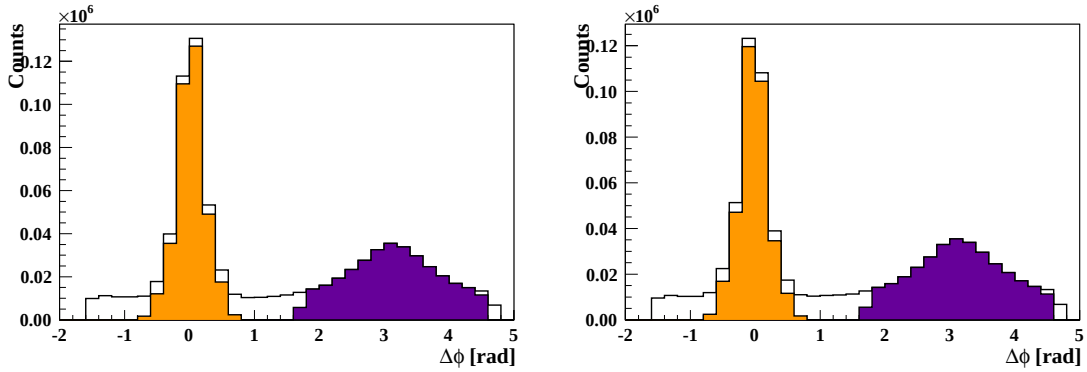

(c): JP1–9: Λ **(d):** JP1–9: $\overline{\Lambda}$

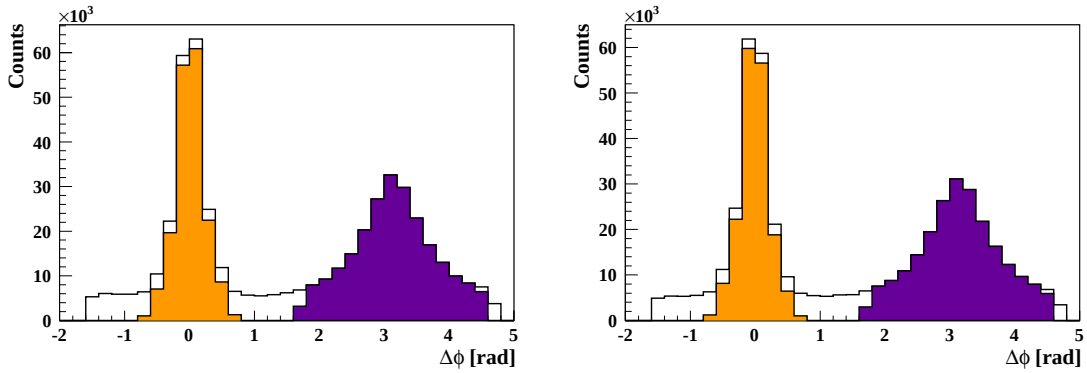

(e): L2JH–9: Λ **(f):** L2JH–9: $\overline{\Lambda}$

Figure 3.39: $\Delta\phi$ between $\Lambda(\overline{\Lambda})$ and jets for both run years. The orange shaded region contains the near-side $\Lambda(\overline{\Lambda})$s. Away-side $\Lambda(\overline{\Lambda})$s reside in the purple shaded region.

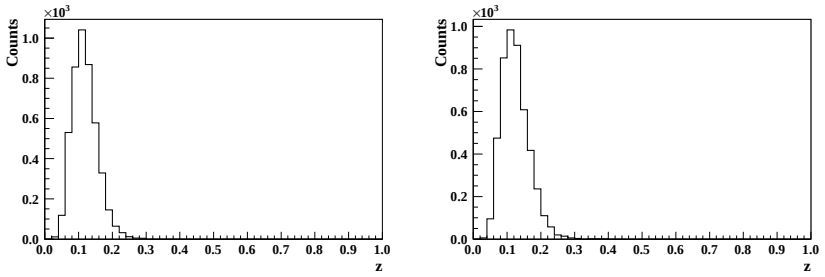

(a): Λ : $1.0 \leq p_T < 2.0$ GeV

(b): $\overline{\Lambda}$: $1.0 \leq p_T < 2.0$ GeV

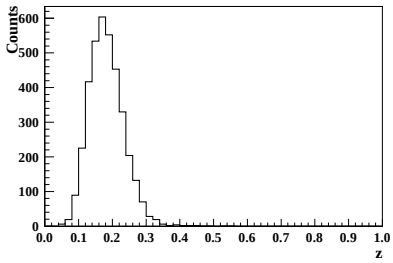

(c): Λ : $2.0 \leq p_T < 3.0$ GeV

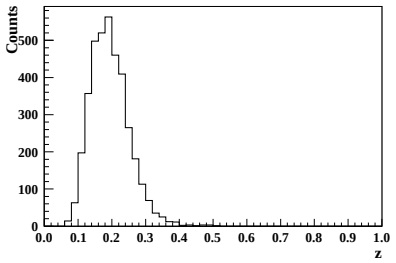

(d): $\overline{\Lambda}$: $2.0 \leq p_T < 3.0$ GeV

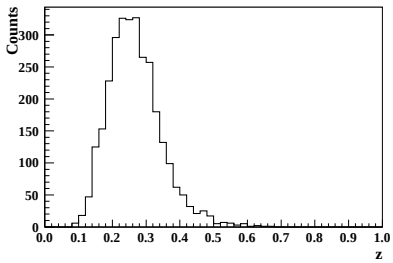

(e): Λ : $3.0 \leq p_T < 5.0$ GeV

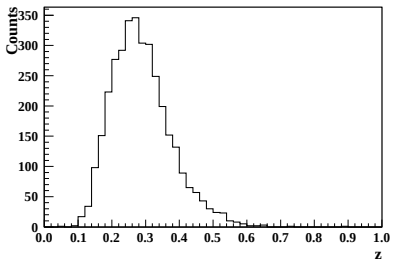

(f): $\overline{\Lambda}$: $3.0 \leq p_T < 5.0$ GeV

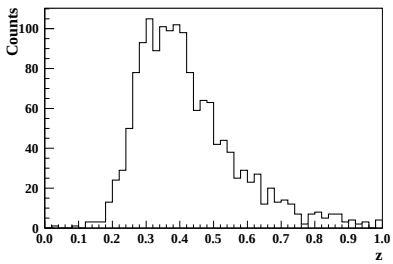

(g): Λ : $5.0 \leq p_T$ GeV

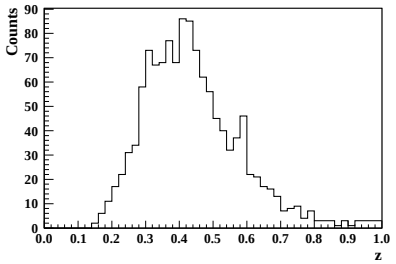

(h): $\overline{\Lambda}$: $5.0 \leq p_T$ GeV

Figure 3.40: Raw z distributions for JP1–6 for different $p_T^{\Lambda(\overline{\Lambda})}$ intervals. No corrections have been applied to the jet energy scale or for resolution effects.

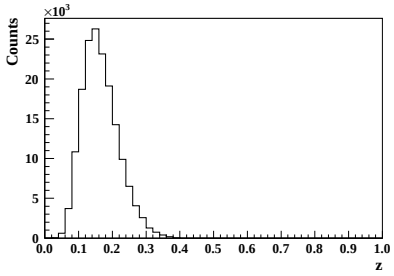

(a): Λ : $1.0 \leq p_T < 2.0$ GeV

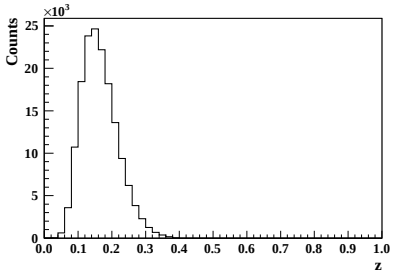

(b): $\overline{\Lambda}$: $1.0 \leq p_T < 2.0$ GeV

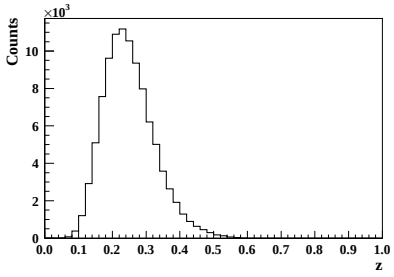

(c): Λ : $2.0 \leq p_T < 3.0$ GeV

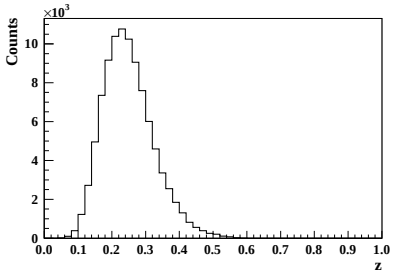

(d): $\overline{\Lambda}$: $2.0 \leq p_T < 3.0$ GeV

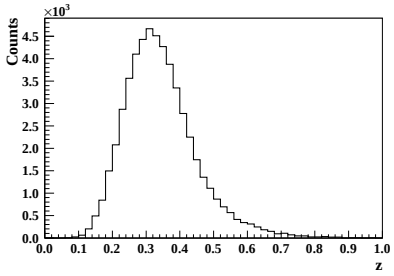

(e): Λ : $3.0 \leq p_T < 5.0$ GeV

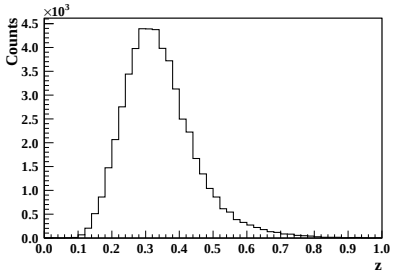

(f): $\overline{\Lambda}$: $3.0 \leq p_T < 5.0$ GeV

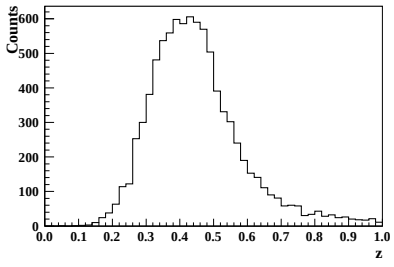

(g): Λ : $5.0 \leq p_T$ GeV

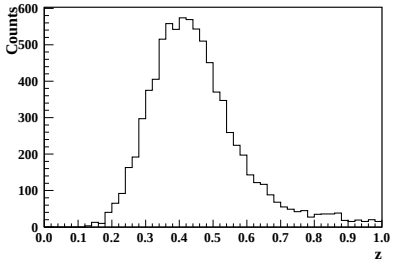

(h): $\overline{\Lambda}$: $5.0 \leq p_T$ GeV

Figure 3.41: Raw z distributions for JP1–9 for different $p_T^{\Lambda(\overline{\Lambda})}$ intervals. No corrections have been applied to the jet energy scale or for resolution effects.

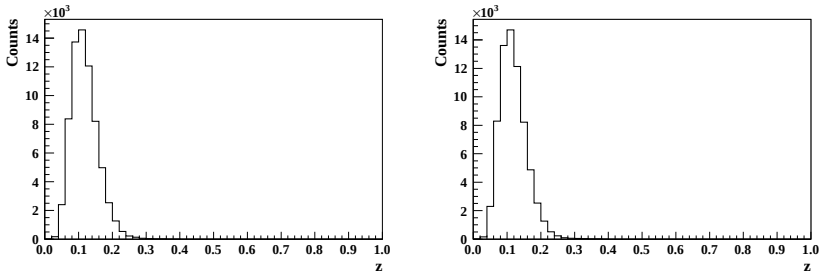

(a): Λ : $1.0 \leq p_T < 2.0$ GeV

(b): $\overline{\Lambda}$: $1.0 \leq p_T < 2.0$ GeV

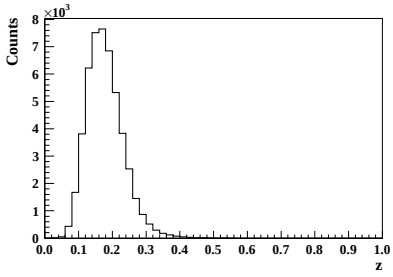

(c): Λ : $2.0 \leq p_T < 3.0$ GeV

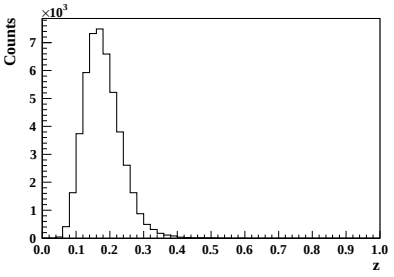

(d): $\overline{\Lambda}$: $2.0 \leq p_T < 3.0$ GeV

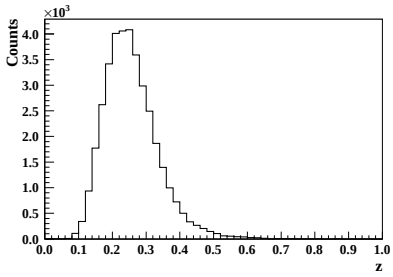

(e): Λ : $3.0 \leq p_T < 5.0$ GeV

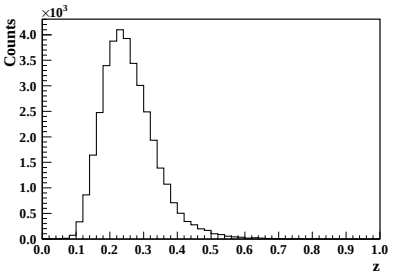

(f): $\overline{\Lambda}$: $3.0 \leq p_T < 5.0$ GeV

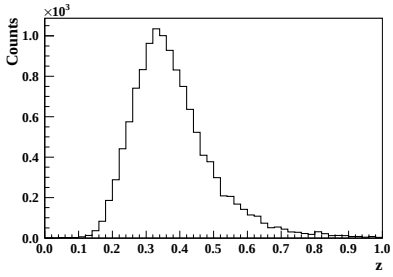

(g): Λ : $5.0 \leq p_T$ GeV

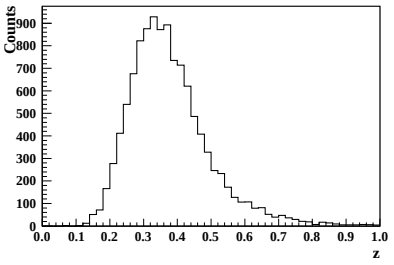

(h): $\overline{\Lambda}$: $5.0 \leq p_T$ GeV

Figure 3.42: Raw z distributions for L2JH–9 for different $p_T^{\Lambda(\overline{\Lambda})}$ intervals. No corrections have been applied to the jet energy scale or for resolution effects.

p_T GeV	Near-Side Λ	Near-Side $\overline{\Lambda}$	Near-Side K^0_s	Away-Side Λ	Away-Side $\overline{\Lambda}$	Away-Side K^0_s
			JP1–6			
$0.5 \leq p_T < 1.0$	436	324	4271	1250	648	10935
$1.0 \leq p_T < 2.0$	2989	3213	12752	6282	4859	21896
$2.0 \leq p_T < 3.0$	2625	2828	8603	3861	2922	10354
$3.0 \leq p_T < 5.0$	2385	2798	7283	2801	2221	7207
$5.0 \leq p_T$	1141	987	3940	1043	622	3418
$0.5 \leq p_T$	9576	10150	36849	15237	11272	53810
			JP1–9			
$0.5 \leq p_T < 1.0$	19331	17648	135091	32461	30986	306654
$1.0 \leq p_T < 2.0$	128951	123268	296324	132814	137395	419686
$2.0 \leq p_T < 3.0$	79390	75344	133417	52233	53234	120353
$3.0 \leq p_T < 5.0$	44645	42673	78325	20370	20307	53292
$5.0 \leq p_T$	7139	6621	23006	2865	2711	12002
$0.5 \leq p_T$	279456	265554	666163	240743	244633	911987
			L2JH–9			
$0.5 \leq p_T < 1.0$	7188	6733	68023	17789	16322	170917
$1.0 \leq p_T < 2.0$	48100	48950	171330	79411	79670	278803
$2.0 \leq p_T < 3.0$	36231	36064	97669	41612	40174	109745
$3.0 \leq p_T < 5.0$	29032	28907	75708	24043	23305	67952
$5.0 \leq p_T$	9642	8698	33887	5839	5035	24268
$0.5 \leq p_T$	130193	129352	446617	168694	164506	651685

Table 3.21: Hyperon-jet associated yields within the invariant mass signal region for jet triggered data from run year 2006 and 2009

p_T GeV	Near-Side Λ	Near-Side $\overline{\Lambda}$	Near-Side K^0_s	Away-Side Λ	Away-Side $\overline{\Lambda}$	Away-Side K^0_s
			JP1–6			
$0.5 \leq p_T < 1.0$	2.8	3.1	1.8	1.9	0.2	2.8
$1.0 \leq p_T < 2.0$	3.4	2.8	0.1	1.8	3.2	0.1
$2.0 \leq p_T < 3.0$	1.7	0.8	0.2	0.5	1.2	0.2
$3.0 \leq p_T < 5.0$	0.7	0.1	0.3	0.6	0.8	0.3
$5.0 \leq p_T$	5.5	1.1	0.8	1.0	4.2	0.9
			JP1–9			
$0.5 \leq p_T < 1.0$	0.1	$<10^{-1}$	0.5	0.8	0.4	0.7
$1.0 \leq p_T < 2.0$	0.2	0.1	$<10^{-1}$	0.7	0.7	$<10^{-1}$
$2.0 \leq p_T < 3.0$	$<10^{-1}$	$<10^{-1}$	$<10^{-1}$	0.2	$<10^{-1}$	$<10^{-1}$
$3.0 \leq p_T < 5.0$	$<10^{-1}$	$<10^{-1}$	$<10^{-1}$	0.1	0.1	$<10^{-1}$
$5.0 \leq p_T$	2.3	0.6	0.1	5.8	2.1	0.2
			L2JH–9			
$0.5 \leq p_T < 1.0$	0.7	0.2	1.2	1.4	0.7	1.4
$1.0 \leq p_T < 2.0$	1.3	1.2	$<10^{-1}$	1.6	1.2	$<10^{-1}$
$2.0 \leq p_T < 3.0$	0.7	0.9	$<10^{-1}$	0.3	0.2	$<10^{-1}$
$3.0 \leq p_T < 5.0$	0.1	$<10^{-1}$	$<10^{-1}$	0.1	0.1	$<10^{-1}$
$5.0 \leq p_T$	4.1	2.2	0.1	3.9	2.1	0.1

Table 3.22: Fractional hyperon-jet associated residual background contribution for jet triggered data from run year 2006 and 2009. Values are given in percentages.

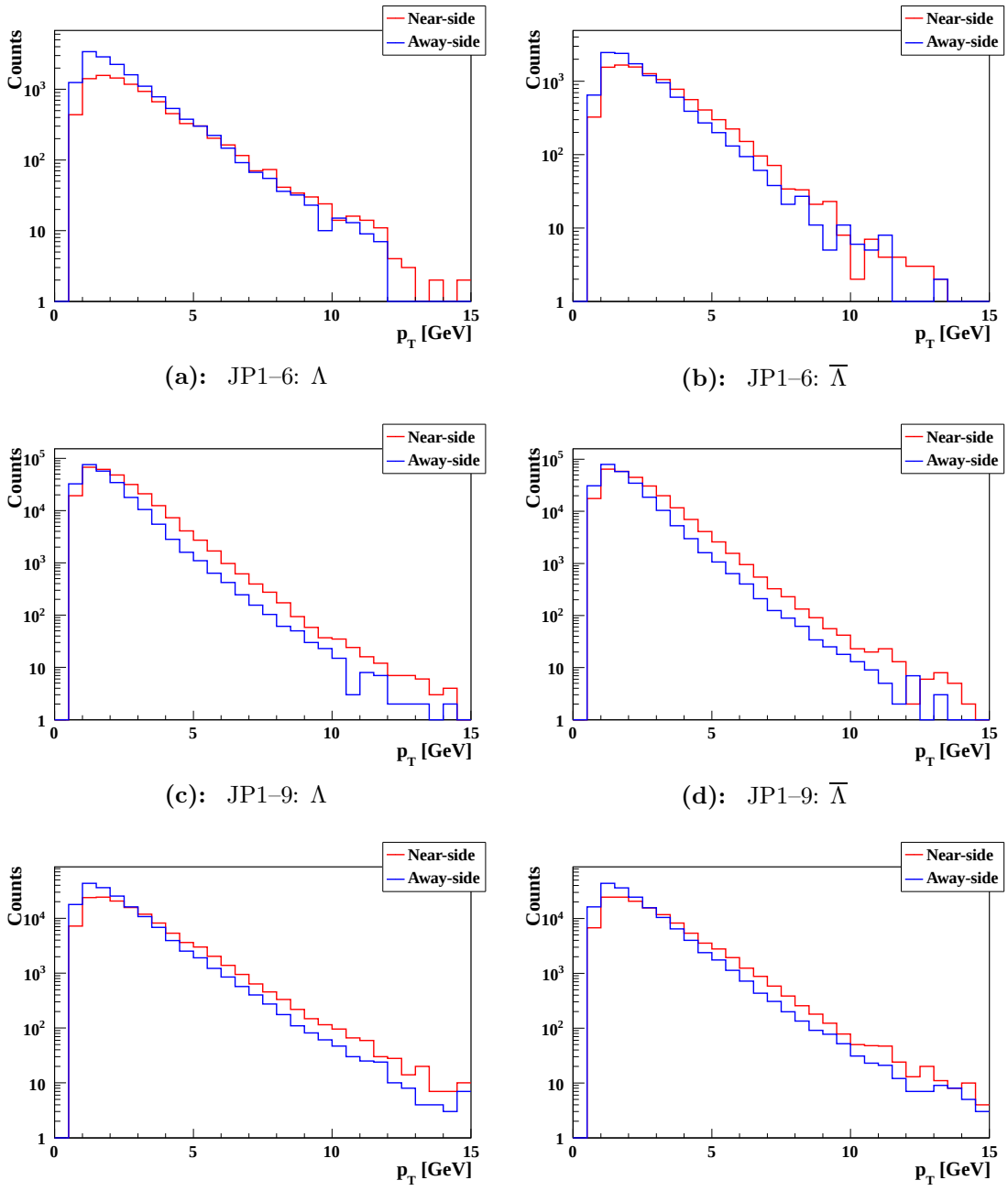

(a): JP1–6: Λ **(b):** JP1–6: $\overline{\Lambda}$

(c): JP1–9: Λ **(d):** JP1–9: $\overline{\Lambda}$

(e): L2JH–9: Λ **(f):** L2JH–9: $\overline{\Lambda}$

Figure 3.43: Near-side and away-side $\Lambda(\overline{\Lambda})$ raw p_T distributions.

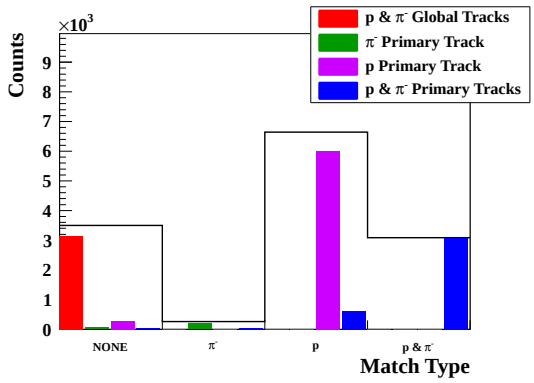

(a): JP1–6: Λ

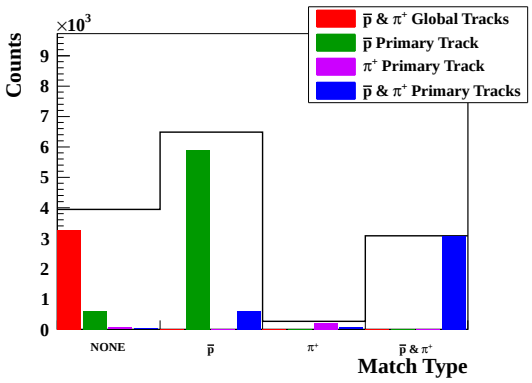

(b): JP1–6: $\overline{\Lambda}$

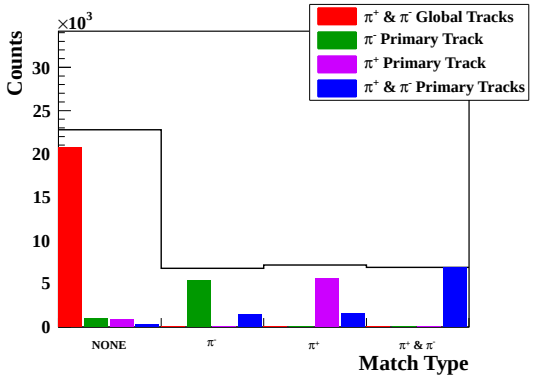

(c): JP1–6: K^0_s

Figure 3.44: Contribution to the reconstructed jet for associated hyperon-jets in run year 2006. The contributions are shown as continuous lines in four columns, when both daughters contribute, only one daughter contributes, and neither daughter contributes to the jet reconstruction. For each column, the entries are further classified, using color, as primary or global tracks.

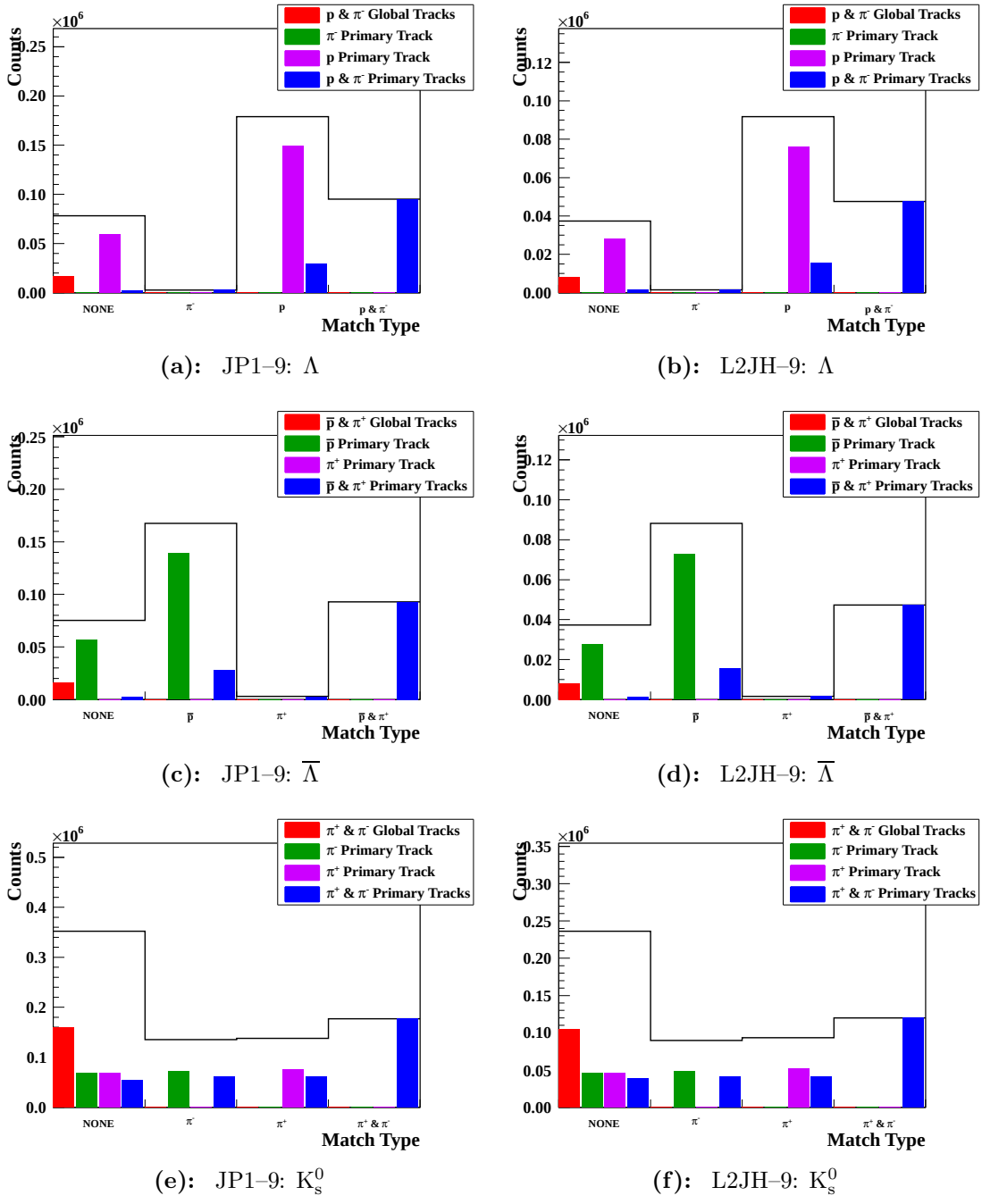

(a): JP1–9: Λ **(b):** L2JH–9: Λ

(c): JP1–9: $\overline{\Lambda}$ **(d):** L2JH–9: $\overline{\Lambda}$

(e): JP1–9: K^0_s **(f):** L2JH–9: K^0_s

Figure 3.45: Contribution to the reconstructed jet for associated hyperon-jets in run year 2009. The contributions are shown as continuous lines in four columns, when both daughters contribute, only one daughter contributes, and neither daughter contributes to the jet reconstruction. For each column, the entries are further classified, using color, as primary or global tracks.

3.7 D_{LL} Extraction

The longitudinal spin transfer, D_{LL}, to $\Lambda(\overline{\Lambda})$ from longitudinally polarized proton-proton collisions is defined as the ratio of the difference of the inclusive cross section for $\Lambda(\overline{\Lambda})$ with positive and negative helicity to the sum in singly polarized proton collisions,

$$D_{LL} \equiv \frac{\sigma_{p^+p\to\Lambda(\overline{\Lambda})^+X} - \sigma_{p^+p\to\Lambda(\overline{\Lambda})^-X}}{\sigma_{p^+p\to\Lambda(\overline{\Lambda})^+X} + \sigma_{p^+p\to\Lambda(\overline{\Lambda})^-X}}, \tag{3.37}$$

where the $+(-)$ signs denote particle helicity. At STAR both beams are polarized and the data samples recorded for opposite spin directions of one of the beams are therefore first summed. Corrections are included for differences in beam polarization and relative luminosity. In the description below, the D_{LL} extraction method for Λ particles is described. The same D_{LL} extraction method can then be used for $\overline{\Lambda}$ and K^0_s particles.

Weak Λ decay is self-analyzing and the angular distribution of the detected decayed proton at Λ's rest frame [Ack98] is given by

$$\frac{dN'_\Lambda}{d\cos(\theta^*)} = \frac{N^{tot}_\Lambda}{2}\left[1 + \alpha_w P_\Lambda \cos(\theta^*)\right] A(\cos(\theta^*)), \tag{3.38}$$

where

$$\begin{aligned}
\frac{dN'_\Lambda}{d\cos(\theta^*)} &: \text{Differential polarized } \Lambda \text{ counts,}\\
N^{tot}_\Lambda &: \text{Total } \Lambda \text{ counts,}\\
\alpha_w &: \Lambda \text{ weak decay parameter,}\\
P_\Lambda &: \Lambda \text{ polarization,}\\
\theta^* &: \text{Angle between } \mathbf{p}_\Lambda \text{ and } \hat{\mathbf{p}}_\Lambda \text{ in } \Lambda \text{ rest frame,}\\
A(\cos(\theta^*)) &: \text{Detector acceptance function.}
\end{aligned}$$

The Λ polarization observed in experiment is smaller than the beam polarization,

$$P_\Lambda = P_{beam} D_{LL}, \tag{3.39}$$

where the D_{LL} is the amount of beam polarization transferred to the Λ polarization. The integration of Equation 3.38 over an interval [cos (θ_1^*),cos (θ_2^*)] and substitution in Equation 3.39 gives

$$\begin{aligned}\frac{2N_\Lambda^{'}}{N_\Lambda^{tot}} = & \quad [\cos(\theta_2^*) - \cos(\theta_1^*)]\, A(\cos(\theta_2^*)) \\ & - \int_{\cos(\theta_1^*)}^{\cos(\theta_2^*)} \cos(\theta^*) \frac{\partial A(\cos(\theta^*))}{\partial \cos(\theta^*)} d\cos(\theta^*) \\ & + \frac{\alpha_w P_{beam} D_{LL}}{2} \left[\cos^2(\theta_2^*) - \cos^2(\theta_1^*)\right] A(\cos(\theta_2^*)) \\ & - \frac{\alpha_w P_{beam} D_{LL}}{2} \int_{\cos(\theta_1^*)}^{\cos(\theta_2^*)} \cos^2(\theta^*) \frac{\partial A(\cos(\theta^*))}{\partial \cos(\theta^*)} d\cos(\theta^*).\end{aligned} \tag{3.40}$$

For a small cos (θ^*) interval, the detector acceptance function behaves as a constant function

$$\frac{\partial A(\cos(\theta^*))}{\partial \cos(\theta^*)} = 0, \tag{3.41}$$

which gives an initial expression for D_{LL} in terms of experimental observables,

$$\begin{aligned}D_{LL} = & \frac{2}{P_{beam}\alpha_w \left[\cos^2(\theta_2^*) - \cos^2(\theta_1^*)\right]} \\ & \times \left[\frac{2N_\Lambda^{'}}{N_\Lambda^{tot} A(\cos(\theta_2^*))} - (\cos(\theta_2^*) - \cos(\theta_1^*))\right].\end{aligned} \tag{3.42}$$

STAR's geometry allows to exploit parity conservation in Λ production as shown in Figure 3.46, giving the following relation

$$D_{LL} \equiv {D_{LL}}^{+} = -{D_{LL}}^{-}, \tag{3.43}$$

where ${D_{LL}}^{+}$ and ${D_{LL}}^{-}$ contain positive and negative helicity Λ counts respectively. Using Equation 3.43, the following relations,

$$0 = {D_{LL}}^{+} + {D_{LL}}^{-}, \tag{3.44}$$

$$2D_{LL} = {D_{LL}}^{+} - {D_{LL}}^{-}, \tag{3.45}$$

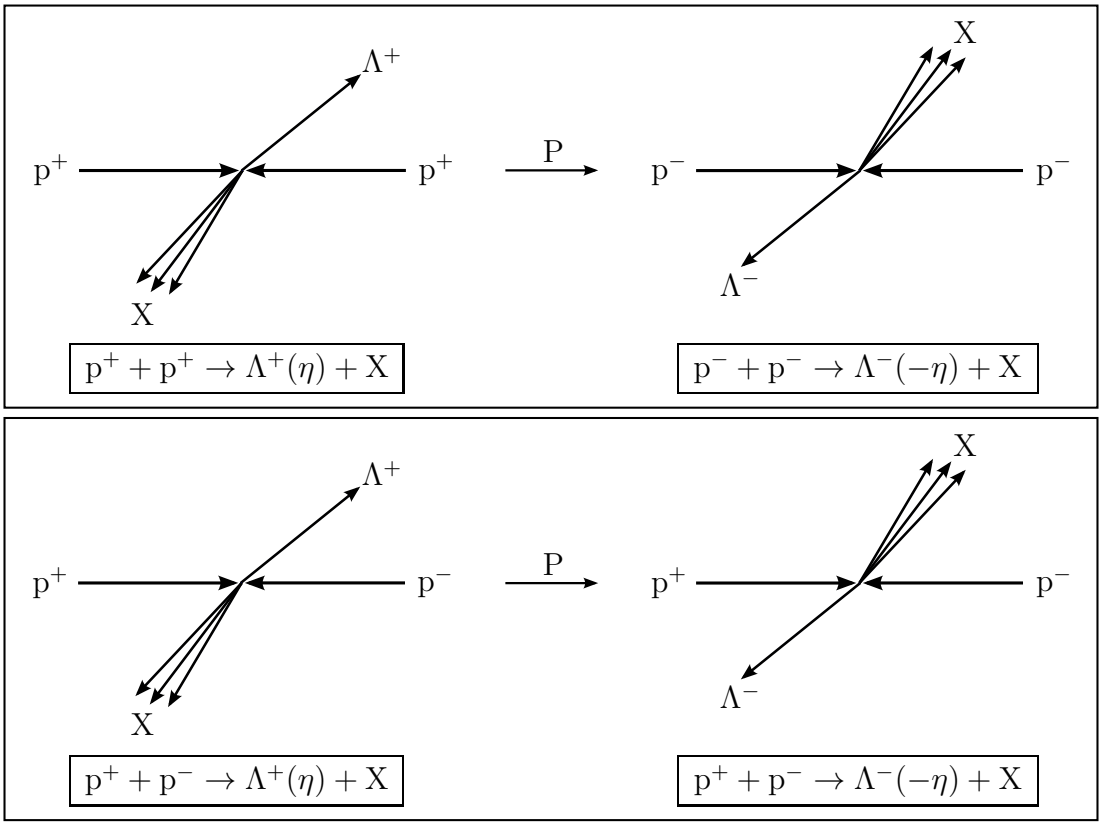

Figure 3.46: $\Lambda(\overline{\Lambda})$ parity conservation diagrams for the STAR detector geometry

are used to express D_{LL} in terms of spin sorted Λ counts. The detector acceptance function is canceled out in the extracted D_{LL} relation. The mean $\cos(\theta^*)$ interval value is defined as

$$\langle \cos(\theta^*) \rangle = \frac{\cos(\theta_2^*) + \cos(\theta_1^*)}{2}. \tag{3.46}$$

The D_{LL} for Λ is extracted using

$$D_{LL}^{\Lambda} = \frac{1}{P_{beam}\alpha_w \langle \cos(\theta^*) \rangle} \frac{N_{\Lambda}^{+} - N_{\Lambda}^{-}}{N_{\Lambda}^{+} + N_{\Lambda}^{-}}, \tag{3.47}$$

where $N_{\Lambda}^{+(-)}$ define the helicity sorted luminosity corrected $\Lambda(\overline{\Lambda})$ counts. The superscript $+(-)$ denotes the helicity state. Both proton beams are longitudinally polarized in the recorded events. Samples with different spin states are combined to

spin average one of the polarized proton beams. A separate D_{LL} measurement can be made for each polarized beam. The raw spin sorted Λ counts are luminosity corrected using the relative luminosity ratios to compensate for different beam intensities at each spin bit state. The longitudinally polarized blue beam D_{LL} can be extracted using

$$D^{\Lambda}_{LL,B} = \frac{1}{P_B \alpha_w \langle \cos(\theta^*) \rangle} \frac{\left(\frac{n^{++}_{\Lambda,B}}{R_4} + \frac{n^{-+}_{\Lambda,B}}{R_6}\right) - \left(n^{--}_{\Lambda,B} + \frac{n^{+-}_{\Lambda,B}}{R_5}\right)}{\left(\frac{n^{++}_{\Lambda,B}}{R_4} + \frac{n^{-+}_{\Lambda,B}}{R_6}\right) + \left(n^{--}_{\Lambda,B} + \frac{n^{+-}_{\Lambda,B}}{R_5}\right)} \tag{3.48}$$

and the longitudinally polarized yellow beam using

$$D^{\Lambda}_{LL,Y} = \frac{1}{P_Y \alpha_w \langle \cos(\theta^*) \rangle} \frac{\left(\frac{n^{++}_{\Lambda,Y}}{R_4} + \frac{n^{+-}_{\Lambda,Y}}{R_5}\right) - \left(n^{--}_{\Lambda,Y} + \frac{n^{-+}_{\Lambda,Y}}{R_6}\right)}{\left(\frac{n^{++}_{\Lambda,Y}}{R_4} + \frac{n^{+-}_{\Lambda,Y}}{R_5}\right) + \left(n^{--}_{\Lambda,Y} + \frac{n^{-+}_{\Lambda,Y}}{R_6}\right)}, \tag{3.49}$$

where

$$\begin{aligned} R_4\,,\ R_5\,,\ R_6 \quad &: \quad \text{Relative luminosity ratios for polarized} \\ & \quad\ \ \text{proton-proton spin states,} \\ n^{++}_{\Lambda,B(Y)}\,,\ n^{-+}_{\Lambda,B(Y)}\,, & \\ n^{+-}_{\Lambda,B(Y)}\,,\ n^{--}_{\Lambda,B(Y)} & \quad : \quad \Lambda \text{ counts for polarized} \\ & \quad\ \ \text{blue(yellow) beam proton-proton spin states.} \end{aligned}$$

The relative luminosities, $R_{1\text{-}6}$, were previously defined in Section 2.2.6. Using detector symmetry relations shown in Figure 3.47 and the parity conservation relations from Equation 3.43, the blue and yellow longitudinally polarized beam Λ counts can be merged to extract one D_{LL} measurement in the forward, $\eta_{physics} > 0$, and one in the backward, $\eta_{physics} < 0$, direction. This increases the statistics used for the extracted D_{LL} measurements. For the forward direction, the D_{LL} measure-

ment for $\Lambda(\overline{\Lambda})$ can be extracted using

$$D_{LL} = \frac{1}{\overline{P}_{beam}\alpha_w\langle\cos(\theta^*)\rangle} \times \frac{\left(\frac{n_B^{++}}{R_4} + \frac{n_B^{-+}}{R_6}\right) + \left(\frac{n_Y^{++}}{R_4} + \frac{n_Y^{+-}}{R_5}\right) - \left(n_B^{--} + \frac{n_B^{+-}}{R_5}\right) - \left(n_Y^{--} + \frac{n_Y^{-+}}{R_6}\right)}{\left(\frac{n_B^{++}}{R_4} + \frac{n_B^{-+}}{R_6}\right) + \left(\frac{n_Y^{++}}{R_4} + \frac{n_Y^{+-}}{R_5}\right) + \left(n_B^{--} + \frac{n_B^{+-}}{R_5}\right) + \left(n_Y^{--} + \frac{n_Y^{-+}}{R_6}\right)}, \tag{3.50}$$

where $\overline{P}_{beam}$ is the mean polarization value for the blue and yellow beam.

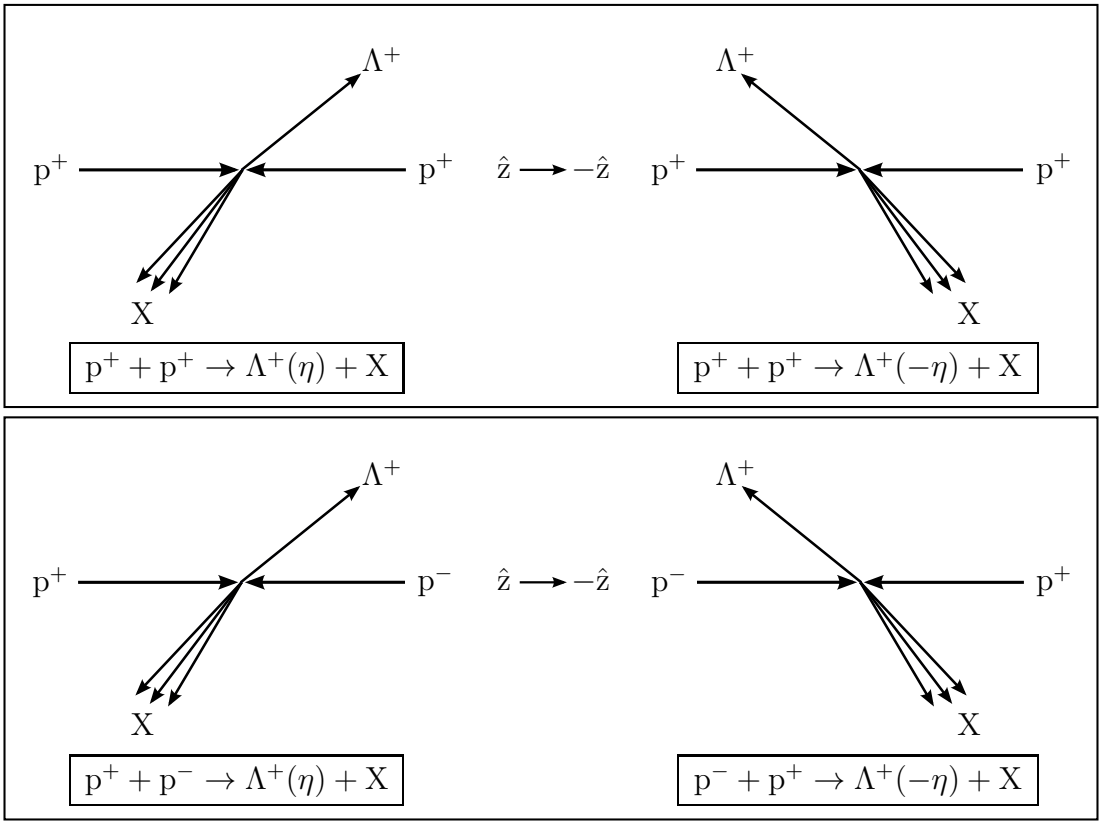

Figure 3.47: $\Lambda(\overline{\Lambda})$ STAR detector symmetry diagrams

The D_{LL} measurement is performed in equally spaced $\cos(\theta^*)$ intervals for the $\cos(\theta^*)$ range of [−1,1]. Twenty $\cos(\theta^*)$ intervals are used to cancel the acceptance function in the extracted D_{LL}. For each $\cos(\theta^*)$ interval, the D_{LL} is extracted using Equation 3.50. The weak decay parameter value from PDG [Ams08],

$\alpha_{\rm w} = 0.642(-0.642) \pm 0.013$, was used for $\Lambda(\overline{\Lambda})$s. For the $\rm K^0_s$ sample, an artificial weak parameter, $\alpha^{'}{}_{\rm w} = 1$, was used when extracting the $\rm D_{LL}$. The mean $\cos(\theta^*)$ value is calculated using the relation,

$$\langle \cos(\theta^*) \rangle = \frac{\sum_{i}^{N} \cos(\theta^*)}{N}, \tag{3.51}$$

where the $\cos(\theta^*)$ values are obtained from all the spin sorted counts, N, extracted from all fills. The polarization values for each beam have been calculated for each fill. The duration of each fill varies and the trigger conditions may vary for each run, making the effective data recording time different per fill. Using the number of events which satisfy the trigger conditions of interest for each fill, an overall weighted mean beam polarization was calculated for all fills, F, using,

$$P_{beam} = \frac{\sum_{j}^{F} m_j \overline{P}_j}{\sum_{j}^{F} m_j}, \tag{3.52}$$

where m_j is the number of events satisfying the trigger conditions in each fill. The beam polarization value per fill, $\overline{P}_j$, is the mean between the blue and yellow beam polarizations with no additional weights because the number of events recorded is the same for both blue and yellow beams. The spin sorted $\Lambda(\overline{\Lambda})$ yields counts for all runs, G, are defined as

$$\begin{aligned} N^+ &= \sum_{k}^{G} \left[N^+_{B,k} + N^+_{Y,k} \right] \\ &= \sum_{B,k}^{G} \left[\left(\frac{n^{++}_{B,k}}{R_{4,k}} + \frac{n^{-+}_{B,k}}{R_{6,k}} \right) + \left(\frac{n^{++}_{Y,k}}{R_{4,k}} + \frac{n^{+-}_{Y,k}}{R_{5,k}} \right) \right] \end{aligned} \tag{3.53}$$

and

$$N^{-} = \sum_{k}^{G} \left[N_{B,k}^{-} + N_{Y,k}^{-} \right] \tag{3.54}$$
$$= \sum_{B,k}^{G} \left[\left(n_{B,k}^{--} + \frac{n_{B,k}^{+-}}{R_{5,k}} \right) + \left(n_{Y,k}^{--} + \frac{n_{Y,k}^{-+}}{R_{6,k}} \right) \right].$$

The relative beam luminosity values are used to correct the difference between the beam intensities. The mean $\mathrm{D_{LL}}$ value between all $\cos(\theta^*)$ intervals are calculated. Near-side $\mathrm{D_{LL}}$ values within $2.0 \leq \mathrm{p_T} < 3.0$ GeV and $\eta_{physics} > 0$ are shown for $\Lambda(\overline{\Lambda})$ and $\mathrm{K_s^0}$ particles which reside in the signal range in Figures 3.48(a)–(c). The $\langle \cos(\theta^*) \rangle$ value in the denominator increases the $\mathrm{D_{LL}}$ values and their uncertainties for $\cos(\theta^*)$ intervals near $\cos(\theta^*) = 0$.

The extracted $\mathrm{D_{LL}}$ values residing within the particle candidate invariant mass range still contain a residual background contribution. The background consists of combinatorial background and $\mathrm{K_s^0}$ contamination. They are expected to be comprised of mostly unpolarized particles and their primary effect is thus to dilute the extracted $\mathrm{D_{LL}}$. A background $\mathrm{D_{LL}^{Bkg}}$ is extracted using the particles which reside within the invariant mass range for background. The background $\mathrm{D_{LL}}$ measurement is subtracted as

$$D_{LL}^{physics} = \frac{D_{LL}^{Sig} - r D_{LL}^{Bkg}}{1 - r}, \tag{3.55}$$

where r is the average fractional residual background contained within the signal range. The corrected $\mathrm{D_{LL}}$ is defined as $\mathrm{D_{LL}^{physics}}$ and has a statistical uncertainty of

$$\delta D_{LL}^{physics} = \frac{\sqrt{\left(\delta D_{LL}^{Sig}\right)^2 + \left(r \delta D_{LL}^{Bkg}\right)^2}}{1 - r}. \tag{3.56}$$

The residual backgrounds for JP1–6 and JP1–9(L2JH–9) are 1.7% and 0.3(1.0)%, respectively, and therefore increase the $\mathrm{D_{LL}}$ uncertainty by more than 1.8% and

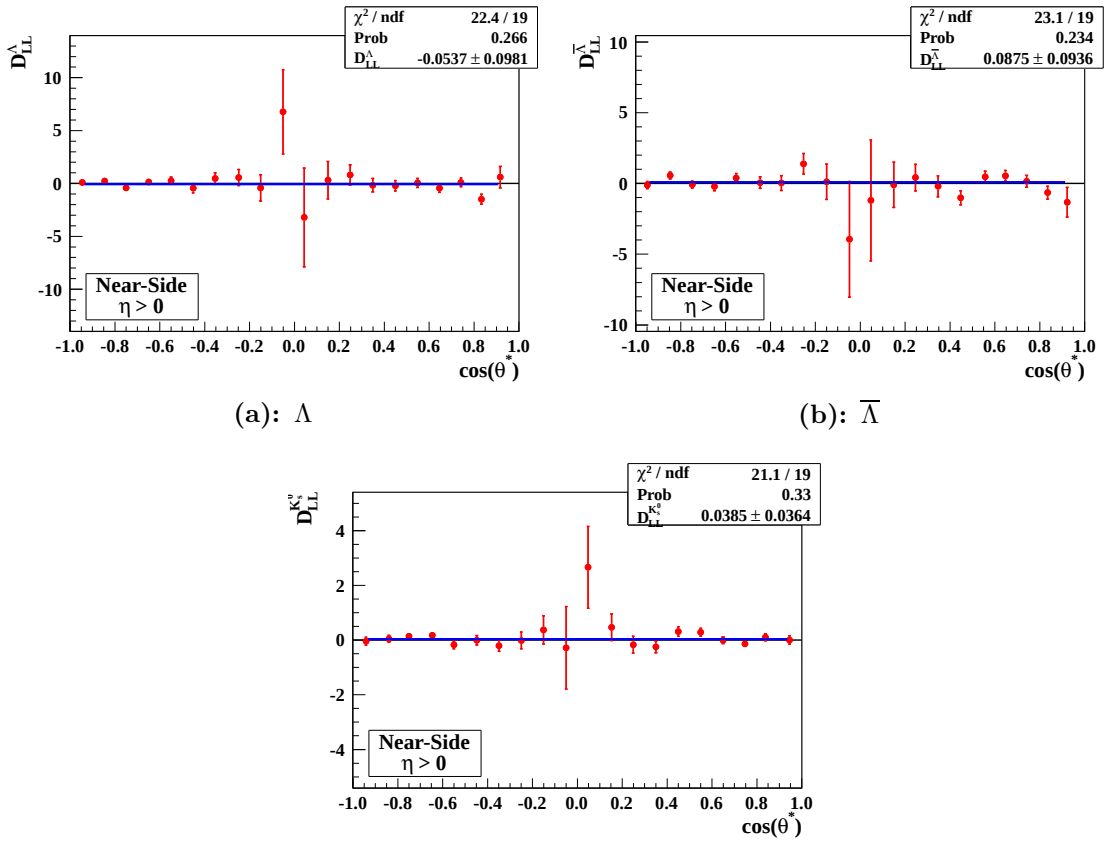

(a): Λ **(b):** $\overline{\Lambda}$

(c): K_s^0

Figure 3.48: Near-side D_{LL} values for candidates particles as a function of $\cos(\theta^*)$ at $2.0 \leq p_T < 3.0$ GeV in the forward direction for JP1–6. The mean D_{LL} is shown as a blue line. For the plots shown, the fitted mean D_{LL} had a good quality fit to the data.

0.3(1.0)%. In run year 2005, the D_{LL} uncertainty increases because of background was more than 10% and the average residual background value was 11%.

3.8 Monte Carlo Simulations

Monte Carlo (MC) simulated samples were created and the observable distributions were compared with the jet triggered data to study the QCD processes selected after imposing trigger conditions and quantify trigger bias in the measurement. Figure 3.49 shows the workflow for creating the simulated data set. PYTHIA

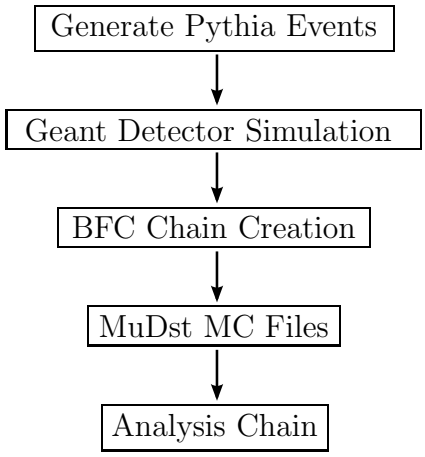

Figure 3.49: MC simulation workflow. The BFC chain generates the simulated MuDst event files used in the analysis.

6.4.23 [Sj06] with CDF Tune A [Fie05] parameters and default parton distributions, CTEQ5L [Lai00], were used to generate 9M(17.6M) $p + p$ collision events with a primary vertex within [−100,100] cm and 40 cm spread in the $\hat{\mathbf{z}}$ direction for run year 2006(2009). The generated events were defined to originate from the following hard collision sub-processes,

$$
\begin{aligned}
q + q' &\rightarrow q + q' \ , \\
q + \overline{q} &\rightarrow q' + \overline{q}' \ , \\
q + \overline{q} &\rightarrow g + g \ , \\
q + g &\rightarrow q + g \ , \\
g + g &\rightarrow q + \overline{q} \ , \\
g + g &\rightarrow g + g \ ,
\end{aligned}
$$

where q and g describe a quark and gluon, respectively. The CDF Tune A parameters were determined to describe the underlying event for CDF Run II. The underlying event is the set of particles generated in the collision which did not come from hard scattering. STAR detector models are implemented in GEANT 3.2.1 [Goo93], containing the description of the magnetic field and various materials for different detector configurations. GEANT processes the PYTHIA generated events by simulating the behavior of the generated particles as they traverse the STAR detector model. The BFC Chain creates MuDst files using the trigger conditions from the data taking sessions. The MC simulated MuDst files were then analyzed in the same way as the data MuDst files.

A modified version of PYTHIA was used to save only generated events that contain at least one $\Lambda(\overline{\Lambda})$ with $p_T \geq 0.5$ GeV and $|\eta| \leq 1.6$ rad [Xu09]. The $\Lambda(\overline{\Lambda})$ cross section is small and it would have taken significantly more computing resources to process all events, including those which would have been rejected at the late stage of the $\Lambda(\overline{\Lambda})$ reconstruction chain because they contain no $\Lambda(\overline{\Lambda})$ particles. The large cross section for lower hard transverse momentum, $\hat{p}_T$, collisions overwhelm the events generated throughout the entire $\hat{p}_T$ range. Time and resource constraints does not allow generation of events over the entire $\hat{p}_T$ collision range in an unweighted way. Instead, PYTHIA events are generated in 0.5 GeV $\hat{p}_T$ collision intervals to build a sample of events which spans the entire $\hat{p}_T$ collision

range. The $\hat{p}_T$ intervals are weighted by

$$w_i = \frac{\sigma_i}{\sigma_0 N_i}, \tag{3.57}$$

which uses a normalizing cross section value, σ_0, as well as the cross section value and the number of events generated for the $\hat{p}_T$ interval, N_i. Figures 3.50(a)–(b) shows the generated weighted $\hat{p}_T$ spectrum for run year 2006 and 2009.

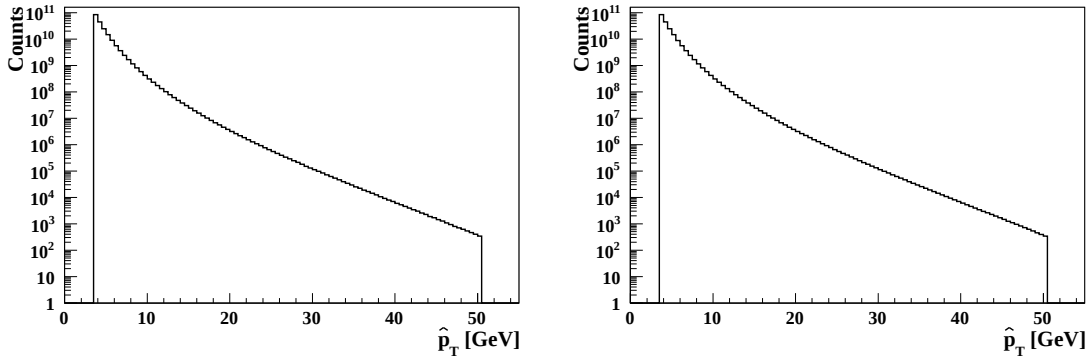

(a): 2006 **(b):** 2009

Figure 3.50: Monte Carlo events weighted at each $\hat{p}_T$ interval for run year 2006 and 2009.

The 2006h(2009b) STAR detector geometry model was used in GEANT for run year 2006(2009). When the events were processed through the BFC Chain, the MC dE/dx values were found to not correctly match the values from both run year 2006 and 2009 triggered data sets due to a normalization factor. An ADC scale factor of 2.55 was used to improve the description of the data. Figure 3.51 show the MC and data dE/dx vs. momentum plots for tracks with $|n\sigma| < 3$ for both the proton and the π from run year 2006. The spread of $n\sigma$ distributions are narrower in the simulated data than those in the jet triggered data set as seen in Figure 3.52. No correction was made to the simulation for this effect. However, the selection criteria applied to the $n\sigma$ distributions were scaled to reflect the narrower spread seen in the MC simulated sample. The scale factor was taken to be the ratio of

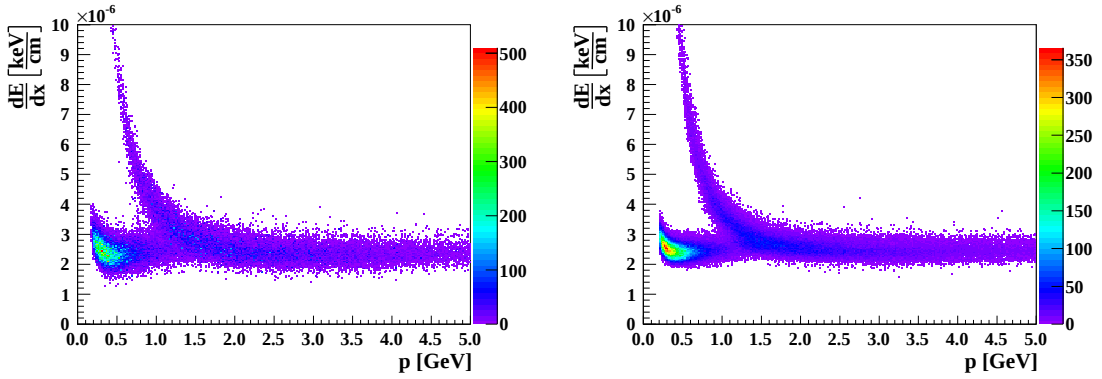

(a): 2006: Monte Carlo

(b): 2006: Data

Figure 3.51: Monte Carlo and data particle ionization energy loss in the TPC gas versus particle momentum for run year 2006 after ADC scale factor normalization correction.

the nσ widths seen in the MC simulated and in the jet triggered data samples.

The generated events are processed using the V^0 particle and jet reconstruction chains described in Section 3.1 and Section 3.2.1. The simulated data were analyzed in the same p_T intervals as the data, using the same selection criteria except for nσ as described above. The same jet patch trigger conditions from the jet triggers are imposed on the MC generated samples to create MC jet triggered samples. The MC triggered samples, mcJP1–6, mcJP1–9, and mcL2JH–9 are created and compared with the jet triggered data sets. Table 3.23 summarizes the simulated trigger configurations.

The reconstructed V^0 particles and jets are weighted by their corresponding $\hat{p}_T$ intervals. The statistical uncertainties are evaluated per bin for each parameter distribution using

$$(\delta b)^2 = \sum_i (\sqrt{n_i} w_i)^2, \tag{3.58}$$

where

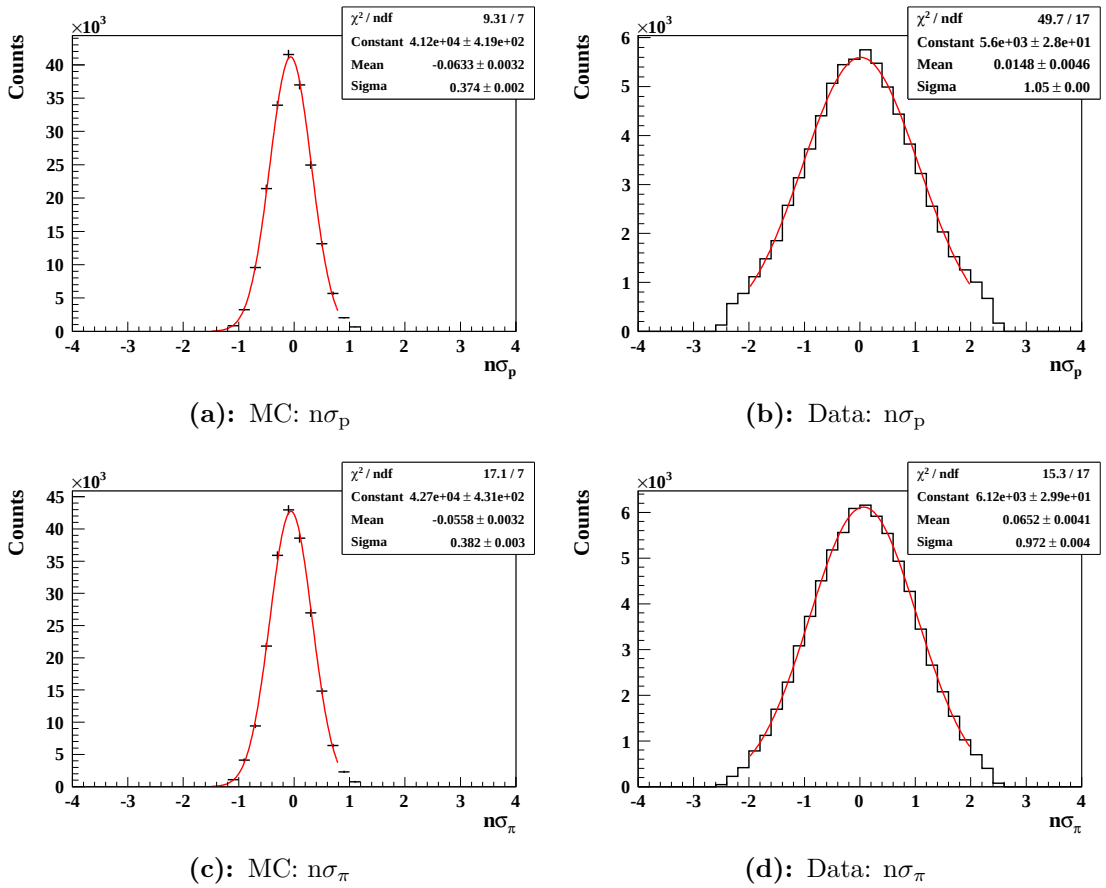

(a): MC: $n\sigma_{\mathrm{p}}$ **(b):** Data: $n\sigma_{\mathrm{p}}$

(c): MC: $n\sigma_{\pi}$ **(d):** Data: $n\sigma_{\pi}$

Figure 3.52: MC and jet triggered data $n\sigma$ distributions for run year 2006 after MC cross section scaling.

δb : Statistical uncertainty for the bin,

n_i : Number of counts in bin for $\hat{\mathrm{p}}_{\mathrm{T}}$ interval i,

w_i : Weight of $\hat{\mathrm{p}}_{\mathrm{T}}$ interval i.

The statistical uncertainty values were taken into account when determining the number of events to generate per $\hat{\mathrm{p}}_{\mathrm{T}}$ interval. The $\hat{\mathrm{p}}_{\mathrm{T}}$ interval weight decreases as the number of generated events increases. Generating more events reduces the $\hat{\mathrm{p}}_{\mathrm{T}}$ interval weight linearly while $\sqrt{n_i}$ increases much slower, giving an effective reduction on the statistical uncertainty at the expense of more computation time.

MC Trigger Name	Trigger Id	E_T GeV	Generated Events
		2006	
mcJP1–6	137221 137222	7.8/8.3	138K
mcMB–6	117001	–	1206K
		2009	
mcJP1–9	240410 240410	4.7/5.4	1552K
mcL2JH–9	240650 240651 240652	6.4/7.3	958K
mcMB–9	240025	–	3825K

Table 3.23: Simulated trigger configurations used for the analysis. The generated event counts are listed prior to scaling with weight per $\hat{p}_T$ interval.

3.8.1 Data and Monte Carlo Comparison

Before the simulated triggered samples can be used to study trigger bias and hard scattering sub-process contributions, the simulated triggered samples were compared with the jet triggered data. Basic kinematic observables from protons, pions, jets, and $\Lambda(\overline{\Lambda})$ particles are compared to study agreement between MC and data. The observed agreement between MC and data justifies the use of mcJP1–6, mcJP1–9, and mcL2JH–9 to study quantities that are not accessible in the data, such as the sub-process contributions. Three methods were used to normalize the MC distributions to the jet triggered data. The MC invariant mass distributions were normalized such that largest bins from both MC and data match. The hyperon-jet $\Delta\phi$ distributions were normalized to best match all bins from MC and data. All other MC distributions were normalized to have equal counts as the data distributions.

The primary vertex distributions in the $\hat{\mathbf{z}}$ direction are compared between the MC and data samples. The distributions should be in agreement in order to avoid acceptance differences and allow the comparisons between other kinematic observables. The mcJP1–6 triggered sample has a 10% smaller fitted spread compared to JP1–6 while mcJP1–9(mcL2JH–9) triggered sample has a 11%(8%) smaller fitted spread compared to JP1–9(L2JH–9). Figure 3.53(c) shows mcJP1–6 distribution is in agreement with the JP1–6 primary vertex distribution in the $\hat{\mathbf{z}}$ direction. A similar conclusion can be drawn for mcJP1–9(mcL2JH–9) as seen in Figure 3.54(e)(Figure 3.54(f)).

Kinematic observable distributions for each decay particle were compared between MC and data. Figures 3.55–3.56 show the p_T, η, and ϕ distributions for each daughter particle from $\Lambda(\overline{\Lambda})$ decay for run year 2006. The agreement between MC and data is better for $p(\overline{p})$ than that for $\pi^+(\pi^-)$. In addition, the opening angle distributions are compared for $\Lambda(\overline{\Lambda})$ particles in Figures 3.57–3.58. The MC samples are seen to form a good description of the jet triggered data samples.

The invariant mass distributions for $\Lambda(\overline{\Lambda})$ for MC and data are compared in Figures 3.59–3.60. The MC distributions contain lower residual background compared to MC distributions before and after the selection optimization and reduction of contamination from misidentified decay daughters. A narrower mass peak is also seen for MC distributions compared to the data. This is expected as the decay particles in the MC samples used more fit points when determining the decay particle's track. Having a more precise track fit increases the accuracy of the measured position and momentum for the decay particle.

Lorentz distributions were fitted to the MC and data to study trends with p_T. Care was taken to remove the background bins with low statistical uncertainty from the simulated data, since these would otherwise have large weights in the

fit compared to the bins within the signal range. The MC and data have similar trends for the central value of the reconstructed $\Lambda(\overline{\Lambda})$ invariant mass versus $\Lambda(\overline{\Lambda})$ p_T as shown in Figure 3.61.

The MC kinematic observable distributions for triggered jets are also compared against the data distributions. Figure 3.62 show the jet transverse momentum p_T^{Jet}, neutral energy fraction R_T, jet η, and jet ϕ distributions for MC and data for run year 2006. The disagreement in the R_T distributions is well-known from other STAR jet analyses and is attributed to beam gas background. The MC simulation does not incorporate beam gas background contributions. In Figure 3.63, the data R_T distributions show a decrease of jets with high R_T as jet p_T increases. Beam gas background is expected to have a different p_T distribution than jet signals produced in hard collisions. The η and ϕ distributions at various jet p_T intervals are shown in Figures 3.64–3.65 for MC and data for run year 2006. The agreement is satisfactory. Figure 3.66 shows the simulated jet p_T distributions for both run years. Similar to the data jet p_T distributions shown in Figure 3.36, the distributions show similar shape for $p_T^{Jet} > 25$ GeV.

The distributions of ΔR and $\Delta\phi$ between $\Lambda(\overline{\Lambda})$ and triggered jets for MC and data are shown in Figure 3.67. The mcJP1–6 sample is in better agreement with JP1–6 data for $\overline{\Lambda}$ than for Λ. An enhancement is seen in the near-side region in the mcJP1–6 data for both Λ and $\overline{\Lambda}$. The enhancement can be attributed to differences in the BEMC hadronic response in the MC sample and in the data.

The role of the jet-associated $\Lambda(\overline{\Lambda})$ decay $p(\overline{p})$ and $\pi^+(\pi^-)$ in the jet reconstruction were studied as well (cf. Section 3.6.3). The contributions for data in both run years are shown in Figure 3.44 while Figure 3.68 show the contributions for the simulated data sets. An increase in the number of daughter particles identified as primary tracks in MC compared to data contribute to the slight decrease

in associated hyperon-jets containing no daughter particles. The $p(\overline{p})$ from $\Lambda(\overline{\Lambda})$ hyperon decay contributed 76(73)% while the daughter particles identified as primary tracks contributed 74(77)% to the associated jet's reconstruction from MC. This is on average a 4%(3%) increase compared to 2006(2009) data. The principal primary/global track contribution to the associated hyperon-jets is similar for both MC and jet triggered data samples.

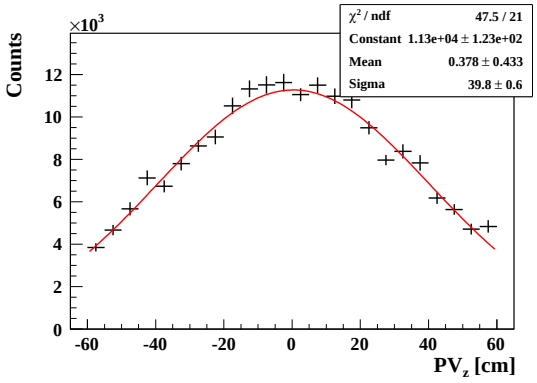

(a): mcJP1–6

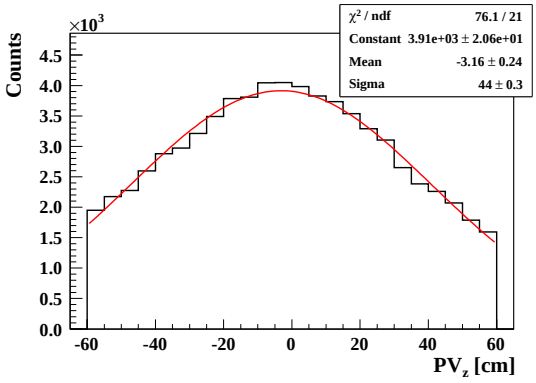

(b): JP1–6

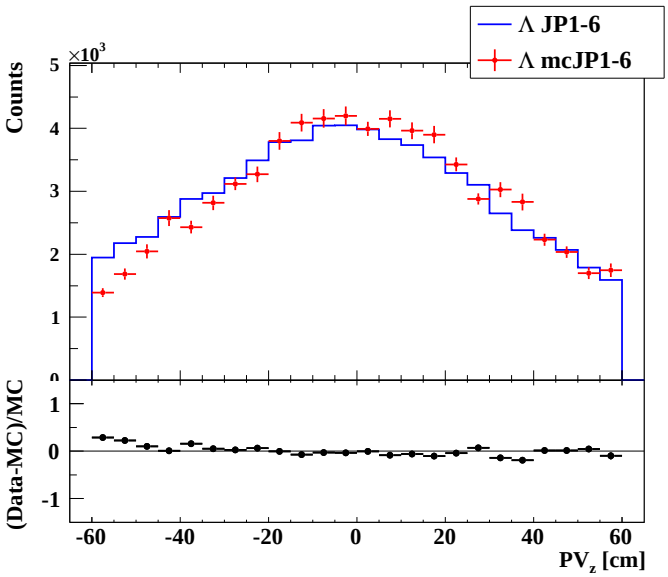

(c): mcJP1–6 and JP1–6 comparison

Figure 3.53: MC and data primary vertex distributions in $\hat{\mathbf{z}}$ direction for run year 2006.

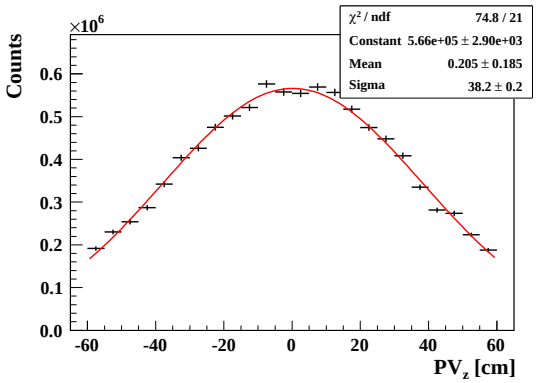

(a): mcJP1–9

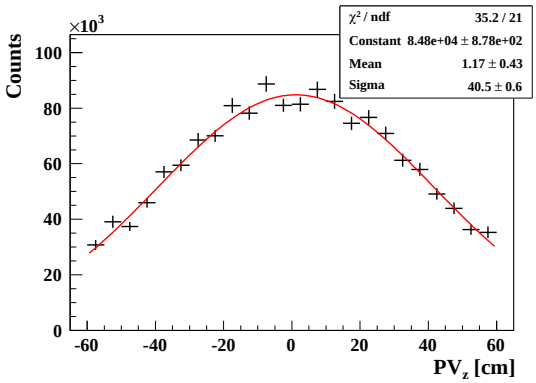

(b): mcL2JH–9

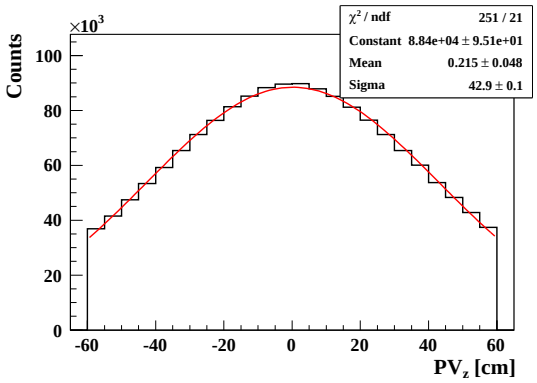

(c): JP1–9

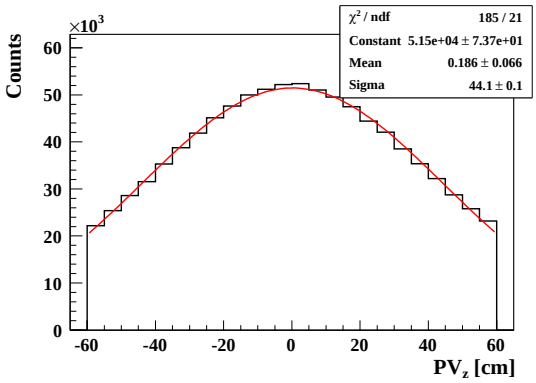

(d): L2JH–9

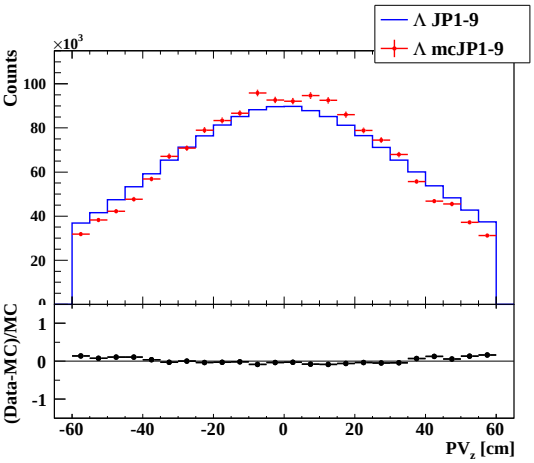

(e): mcJP1–6 and JP1–9 comparison

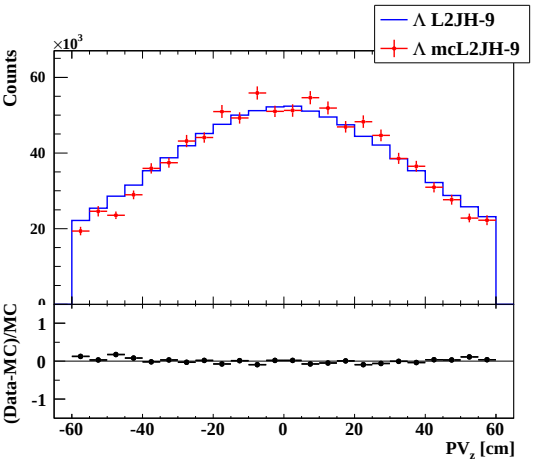

(f): mcL2JH–9 and L2JH–9 comparison

Figure 3.54: MC and data primary vertex distributions in $\hat{\mathbf{z}}$ direction for run year 2009.

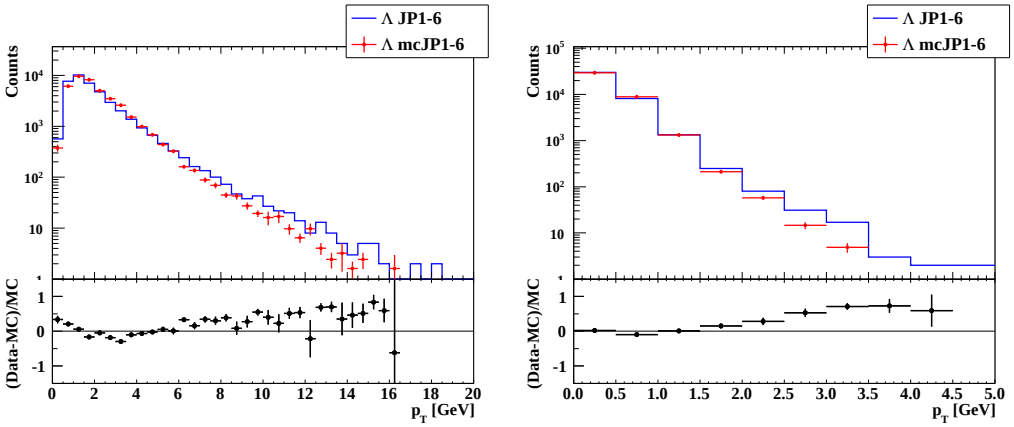

(a): p: p_T

(b): π^-: p_T

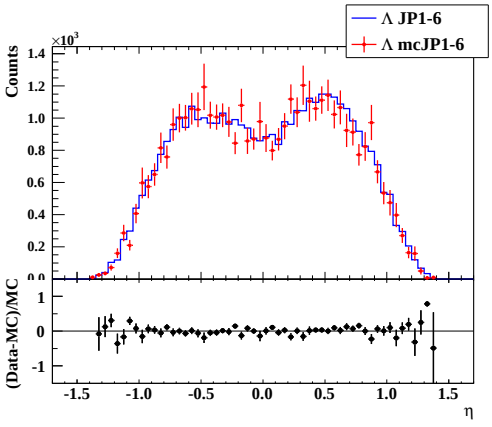

(c): p: η

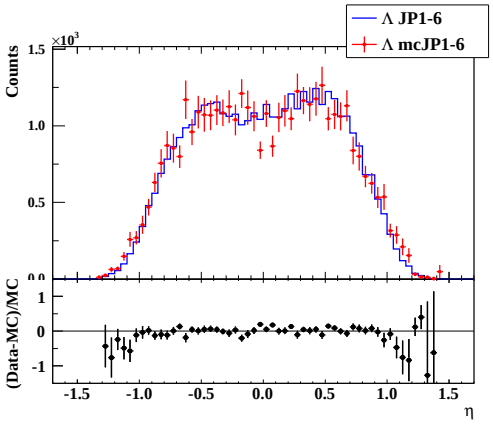

(d): π^-: η

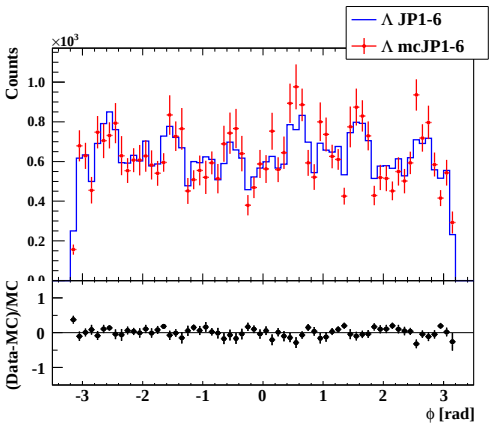

(e): p: ϕ

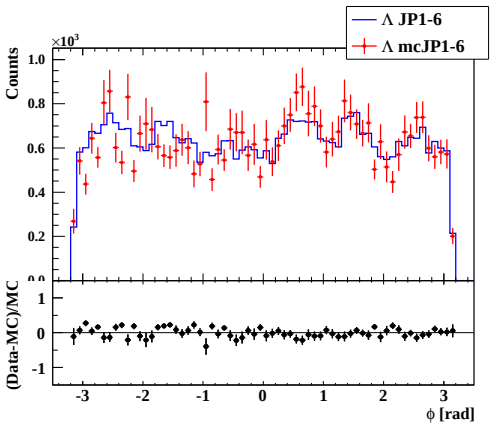

(f): π^-: ϕ

Figure 3.55: Transverse momentum, pseudo-rapidity, and azimuthal angle distributions for the p and π^- originating from Λ decay for the JP1–6 (blue) and mcJP1–6 (red) triggered samples, and their ratio. Similar agreement found between MC and data in run year 2009.

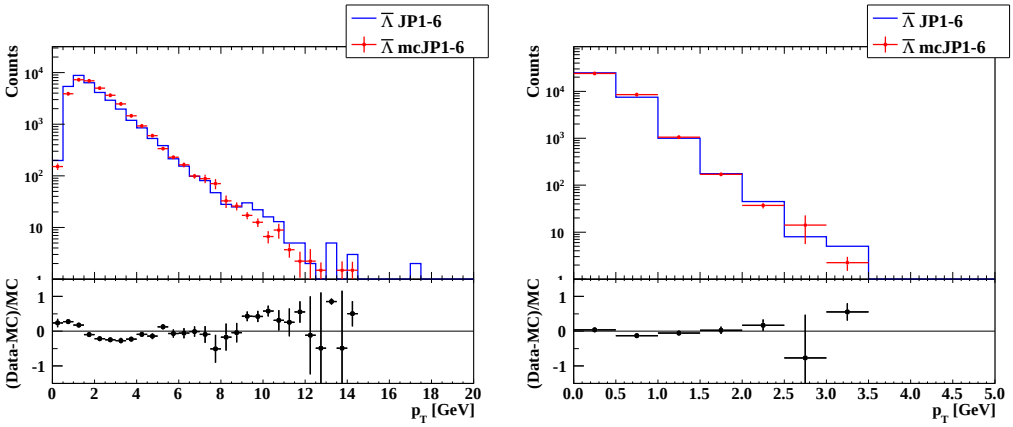

(a): $\overline{p}$: p_T **(b):** π^+: p_T

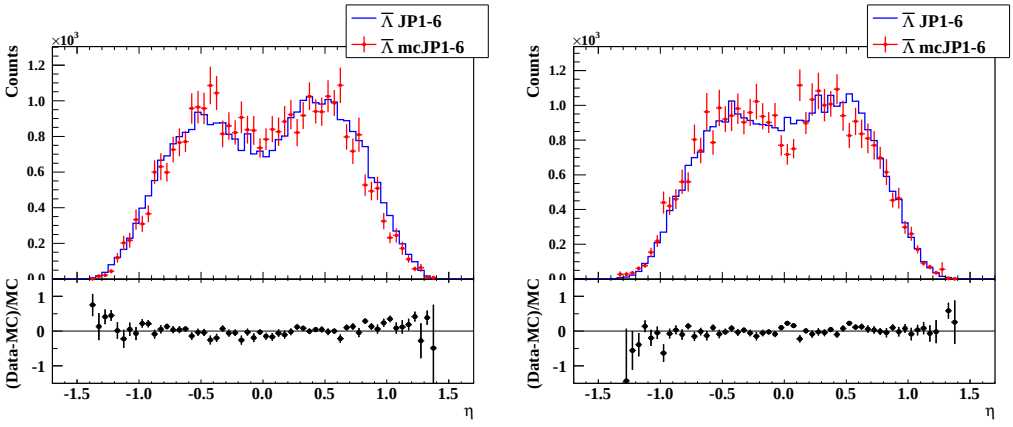

(c): $\overline{p}$: η **(d):** π^+: η

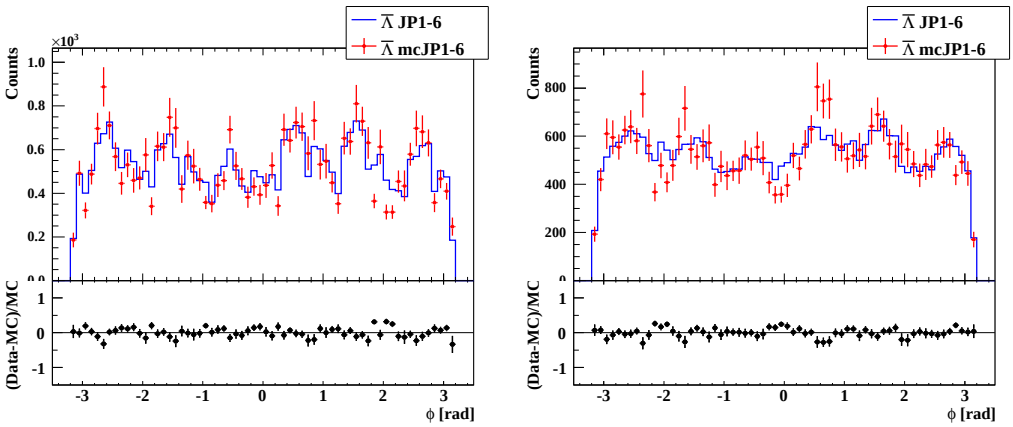

(e): $\overline{p}$: ϕ **(f):** π^+: ϕ

Figure 3.56: Transverse momentum, pseudo-rapidity, and azimuthal angle distributions for the $\overline{p}$ and π^+ originating from Λ decay for the JP1–6 (blue) and mcJP1–6 (red) triggered samples, and their ratio. Similar agreement found between MC and data in run year 2009.

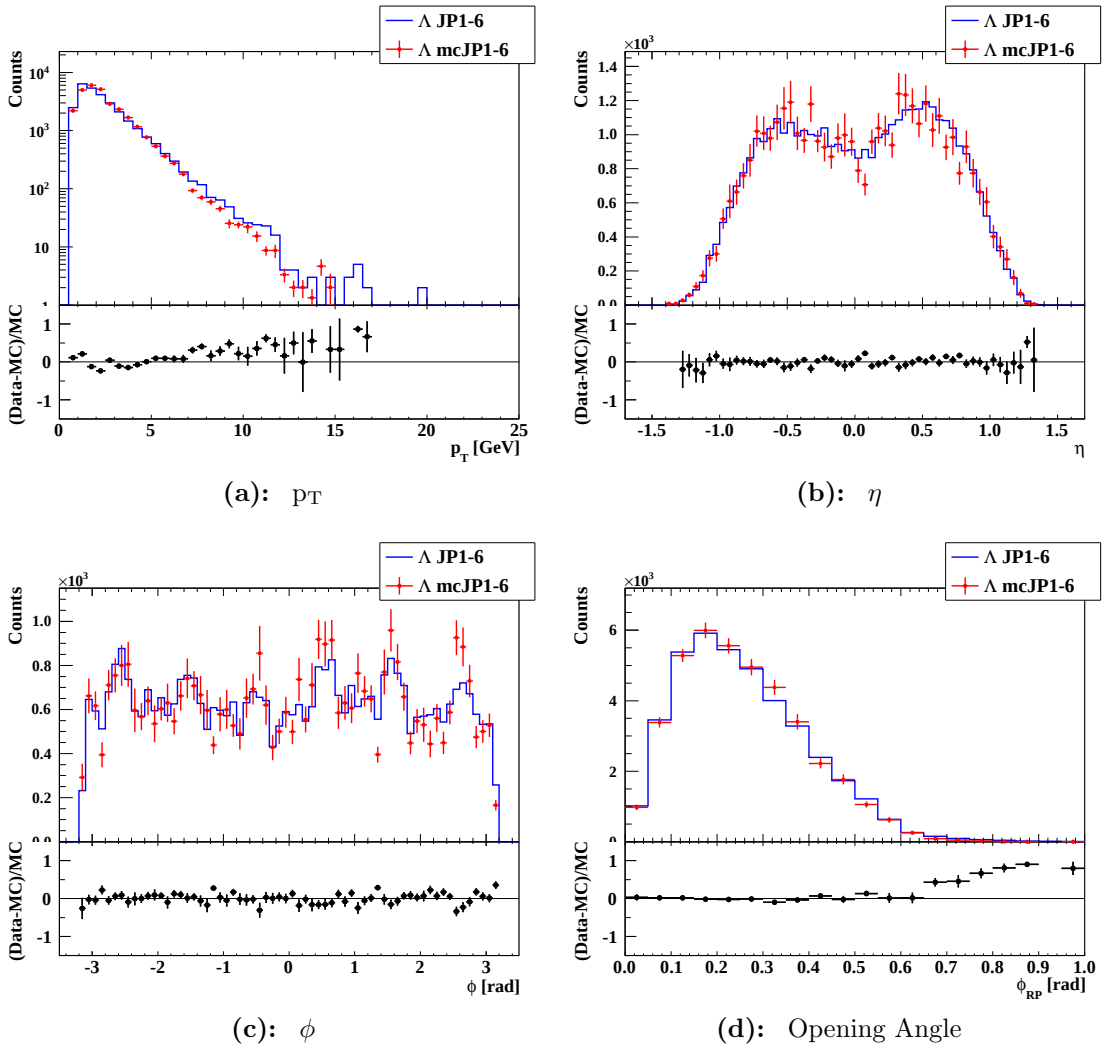

(a): p_T **(b):** η

(c): ϕ **(d):** Opening Angle

Figure 3.57: Transverse momentum, pseudo-rapidity, azimuthal angle, and opening angle distributions from Λ candidates for the JP1–6 (blue) and mcJP1–6 (red) triggered samples, and their ratio. Similar agreement found between MC and data in run year 2009.

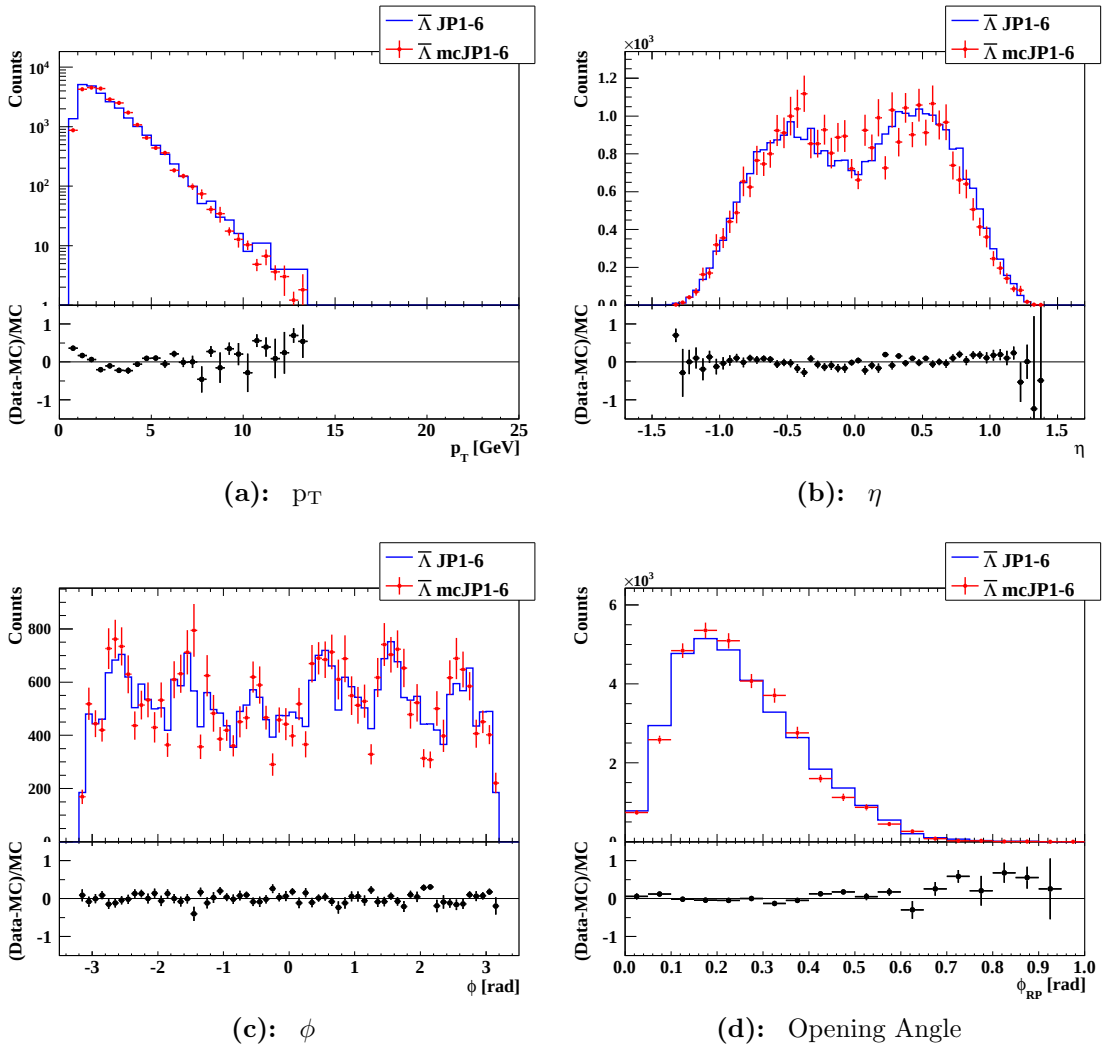

(a): p_T **(b):** η

(c): ϕ **(d):** Opening Angle

Figure 3.58: Transverse momentum, pseudo-rapidity, azimuthal angle, and opening angle distributions from $\overline{\Lambda}$ candidates for the JP1–6 (blue) and mcJP1–6 (red) triggered samples, and their ratio. Similar agreement found between MC and data in run year 2009.

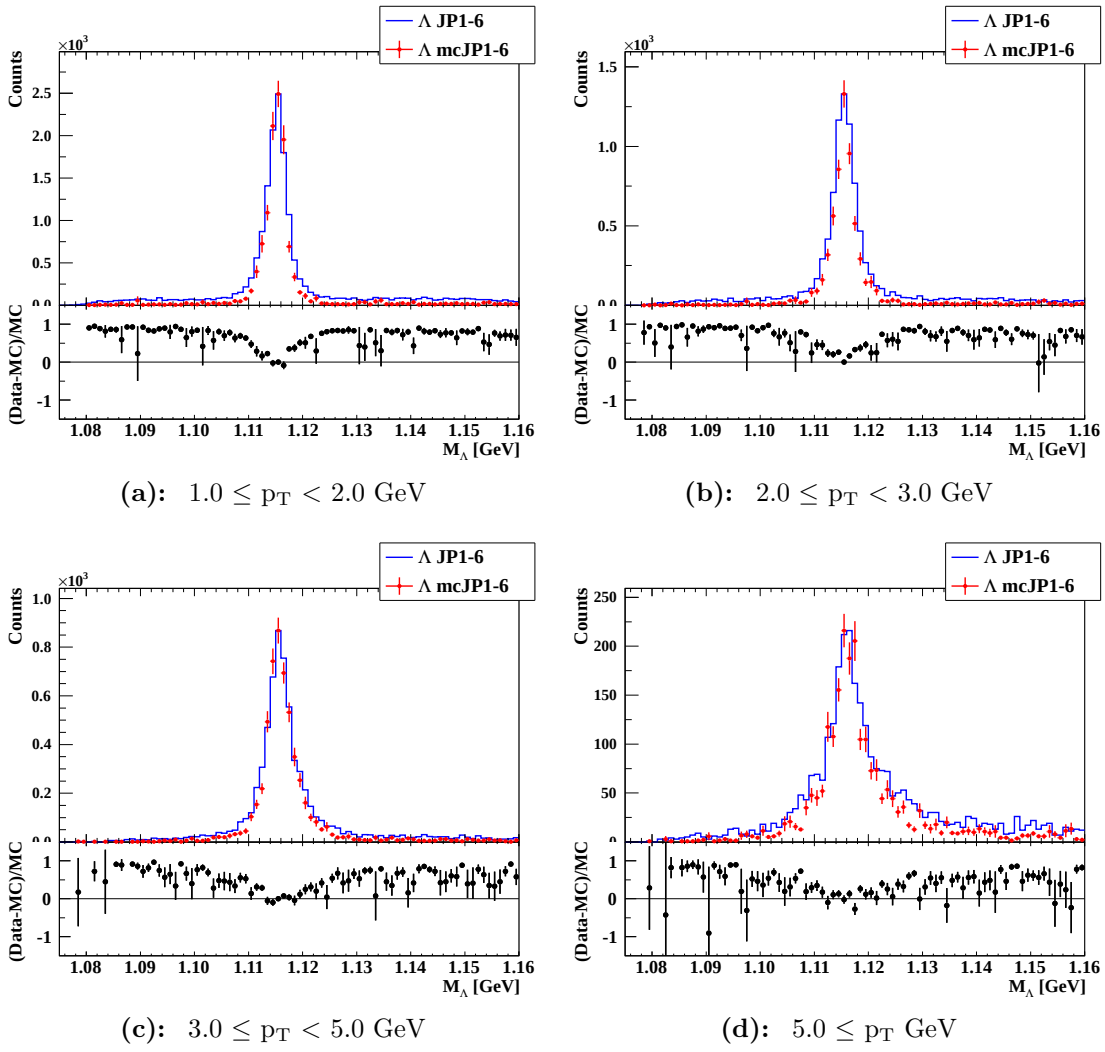

(a): $1.0 \leq p_T < 2.0$ GeV

(b): $2.0 \leq p_T < 3.0$ GeV

(c): $3.0 \leq p_T < 5.0$ GeV

(d): $5.0 \leq p_T$ GeV

Figure 3.59: Comparison of Λ invariant mass distributions between mcJP1–6 and JP1–6 triggered samples. Similar agreement found between MC and data in run year 2009.

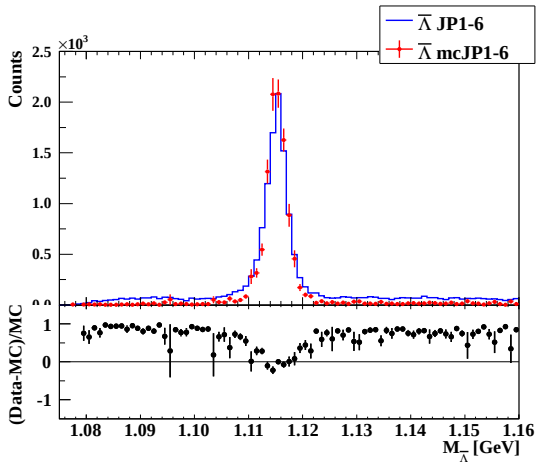

(a): $1.0 \leq p_T < 2.0$ GeV

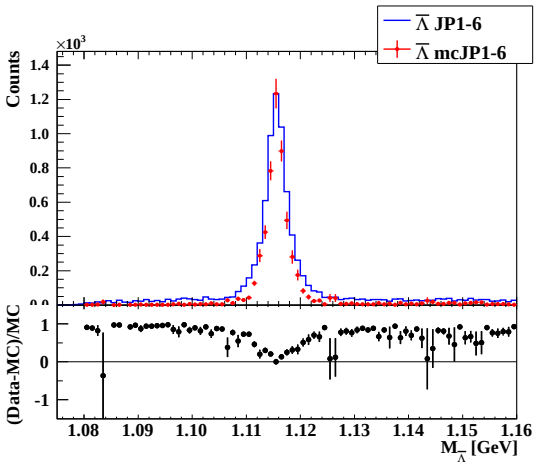

(b): $2.0 \leq p_T < 3.0$ GeV

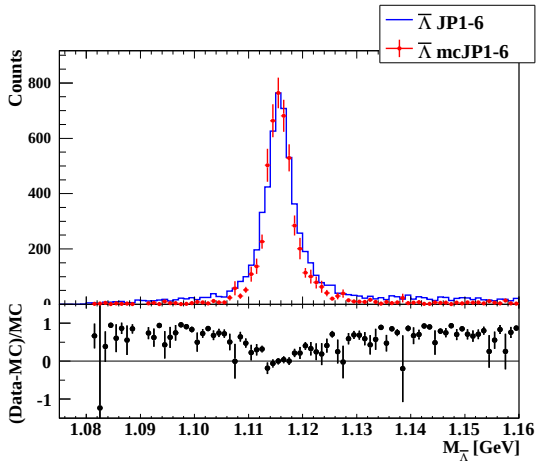

(c): $3.0 \leq p_T < 5.0$ GeV

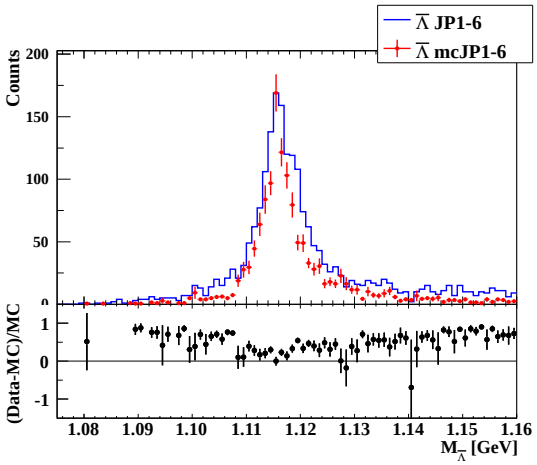

(d): $5.0 \leq p_T$ GeV

Figure 3.60: Comparison of $\overline{\Lambda}$ invariant mass distributions between mcJP1–6 and JP1–6 triggered samples. Similar agreement found between MC and data in run year 2009.

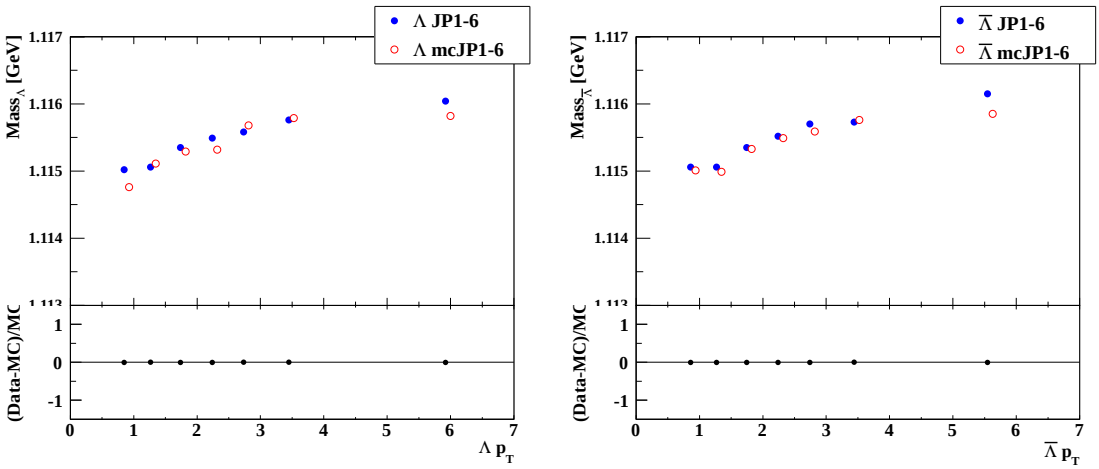

(a): Λ: Central Mass Value

(b): $\overline{\Lambda}$: Central Mass Value

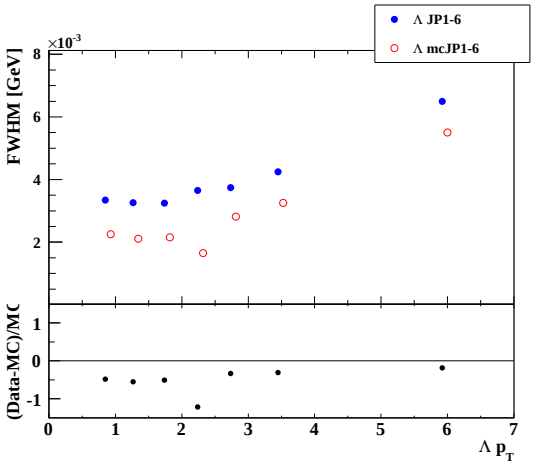

(c): Λ: Central FWHM Value

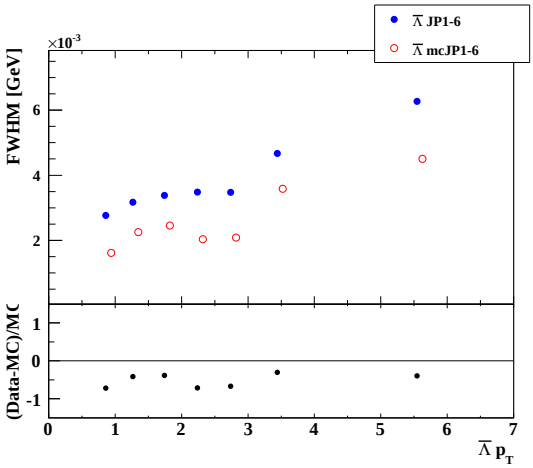

(d): $\overline{\Lambda}$: Central FWHM Value

Figure 3.61: Central values for invariant mass distributions and FWHM at different $\Lambda(\overline{\Lambda})$ p_T intervals between mcJP1–6 and JP1–6 triggered samples, and their ratio. The mcJP1–6 points are shifted to the right for viewing purposes. Lower statistical uncertainties in the bins near the base of the invariant mass peak are responsible for a narrower fit resulting in smaller FWHM values obtained from the fit for mcJP1–6. Similar agreement found between MC and data in run year 2009.

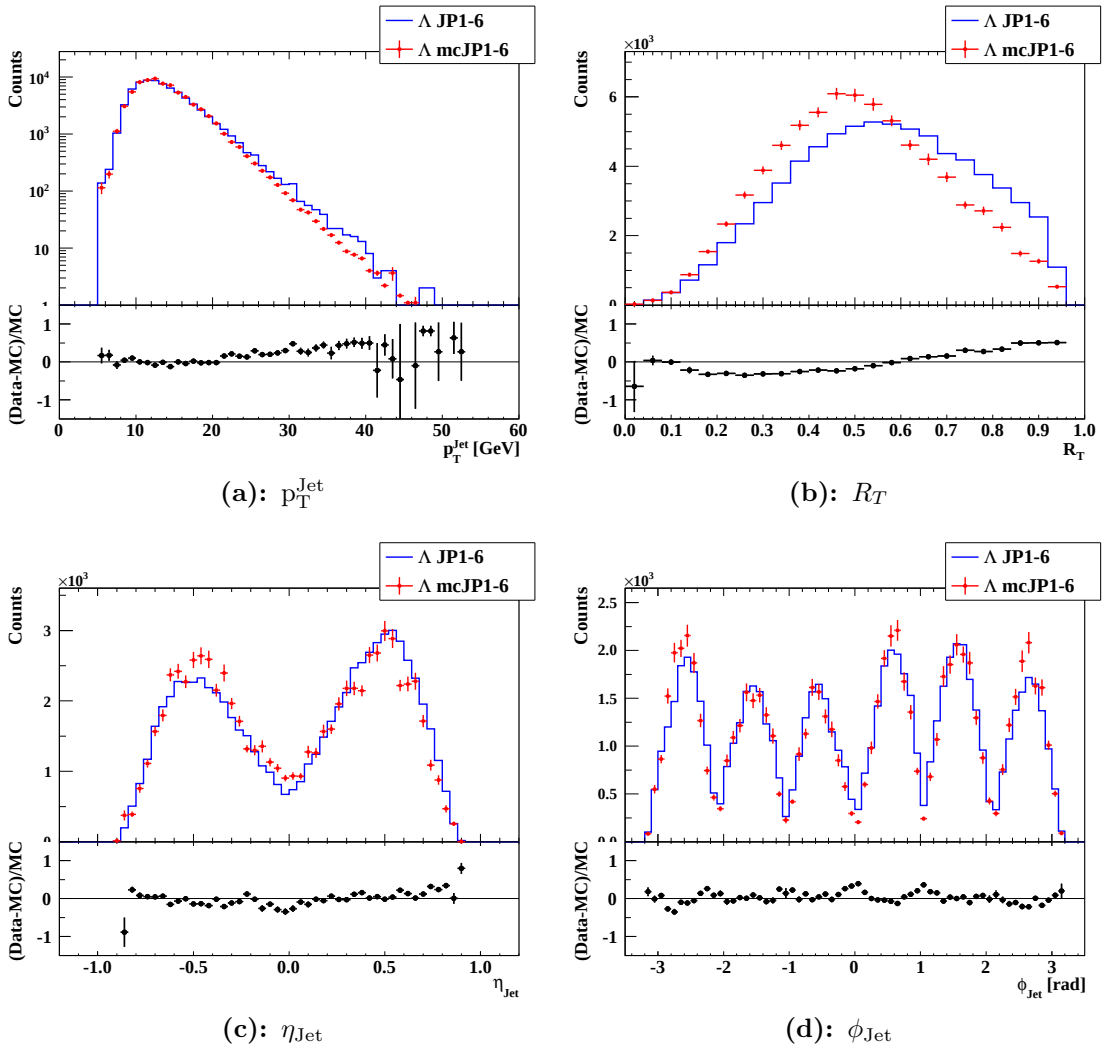

(a): p_T^{Jet} **(b):** R_T

(c): η_{Jet} **(d):** ϕ_{Jet}

Figure 3.62: Transverse jet momentum, neutral energy fraction R_T, pseudo-rapidity, and azimuthal angle distributions for the mcJP1–6 and JP1–6 triggered samples, and their ratio. Similar agreement found between MC and data in run year 2009.

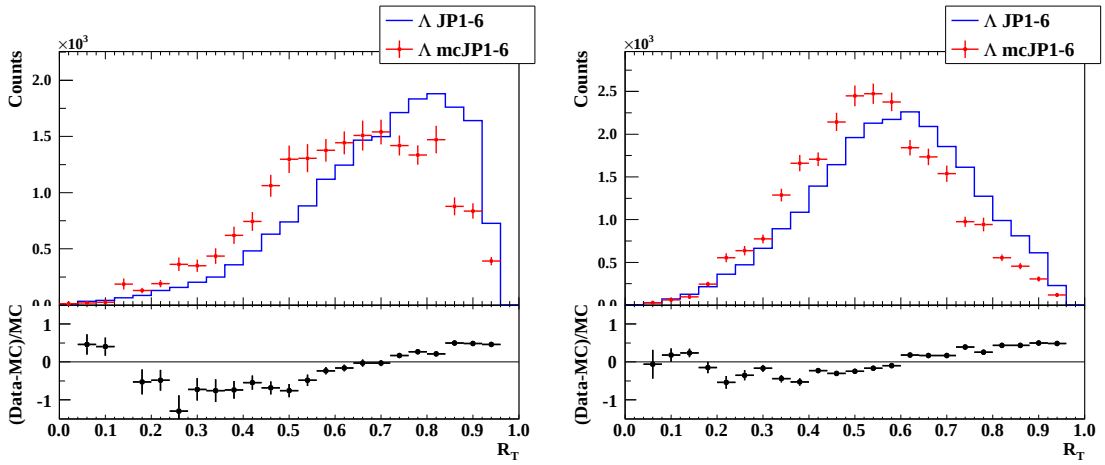

(a): R_T: $5 \leq \mathrm{p_T^{Jet}} < 11$ GeV

(b): R_T: $11 \leq \mathrm{p_T^{Jet}} < 14$ GeV

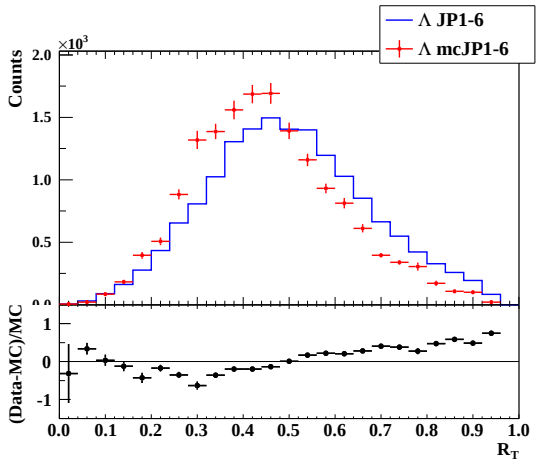

(c): R_T: $14 \leq \mathrm{p_T^{Jet}} < 17$ GeV

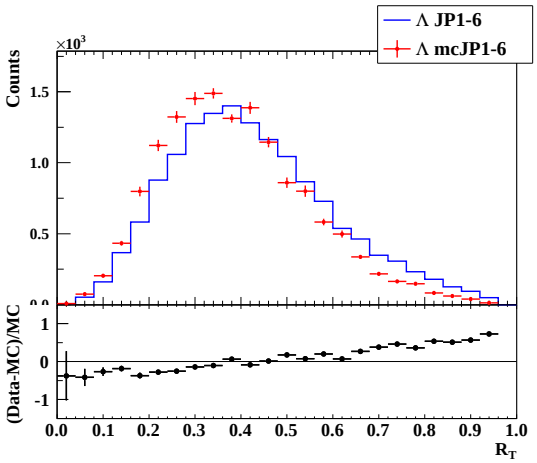

(d): R_T: $17 \leq \mathrm{p_T^{Jet}}$ GeV

Figure 3.63: Neutral energy fraction distributions for the mcJP1–6 and JP1–6 triggered samples, and their ratio at different $\mathrm{p_T^{Jet}}$ intervals. Lower $\mathrm{p_T^{Jet}}$ jets have more contributions from beam gas background compared to high $\mathrm{p_T^{Jet}}$ jets. Similar agreement found between MC and data in run year 2009.

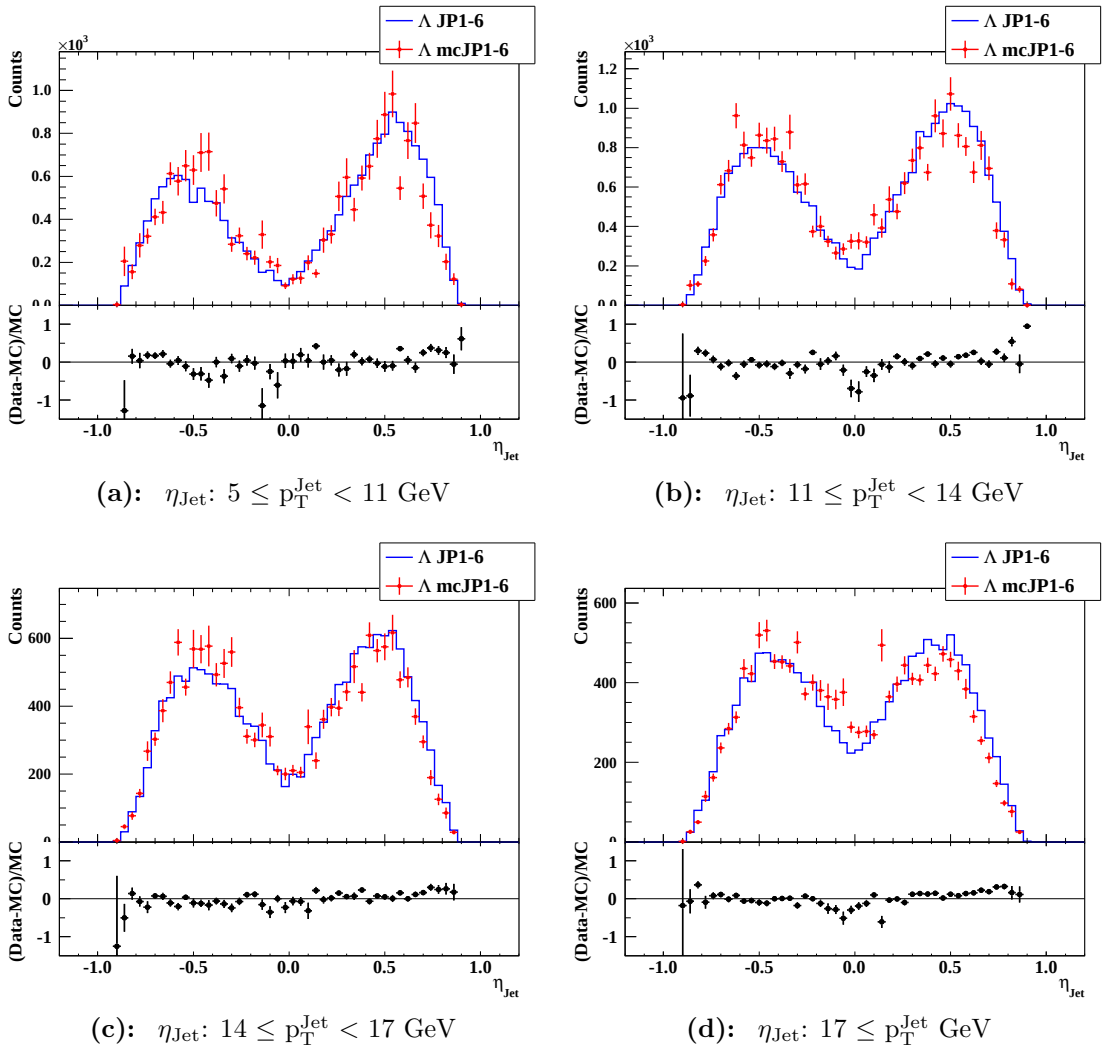

(a): η_{Jet}: $5 \leq \mathrm{p_T^{Jet}} < 11$ GeV

(b): η_{Jet}: $11 \leq \mathrm{p_T^{Jet}} < 14$ GeV

(c): η_{Jet}: $14 \leq \mathrm{p_T^{Jet}} < 17$ GeV

(d): η_{Jet}: $17 \leq \mathrm{p_T^{Jet}}$ GeV

Figure 3.64: Jet pseudo-rapidity distributions for the mcJP1–6 and JP1–6 triggered samples, and their ratio at different $\mathrm{p_T^{Jet}}$ intervals. Similar agreement found between MC and data in run year 2009.

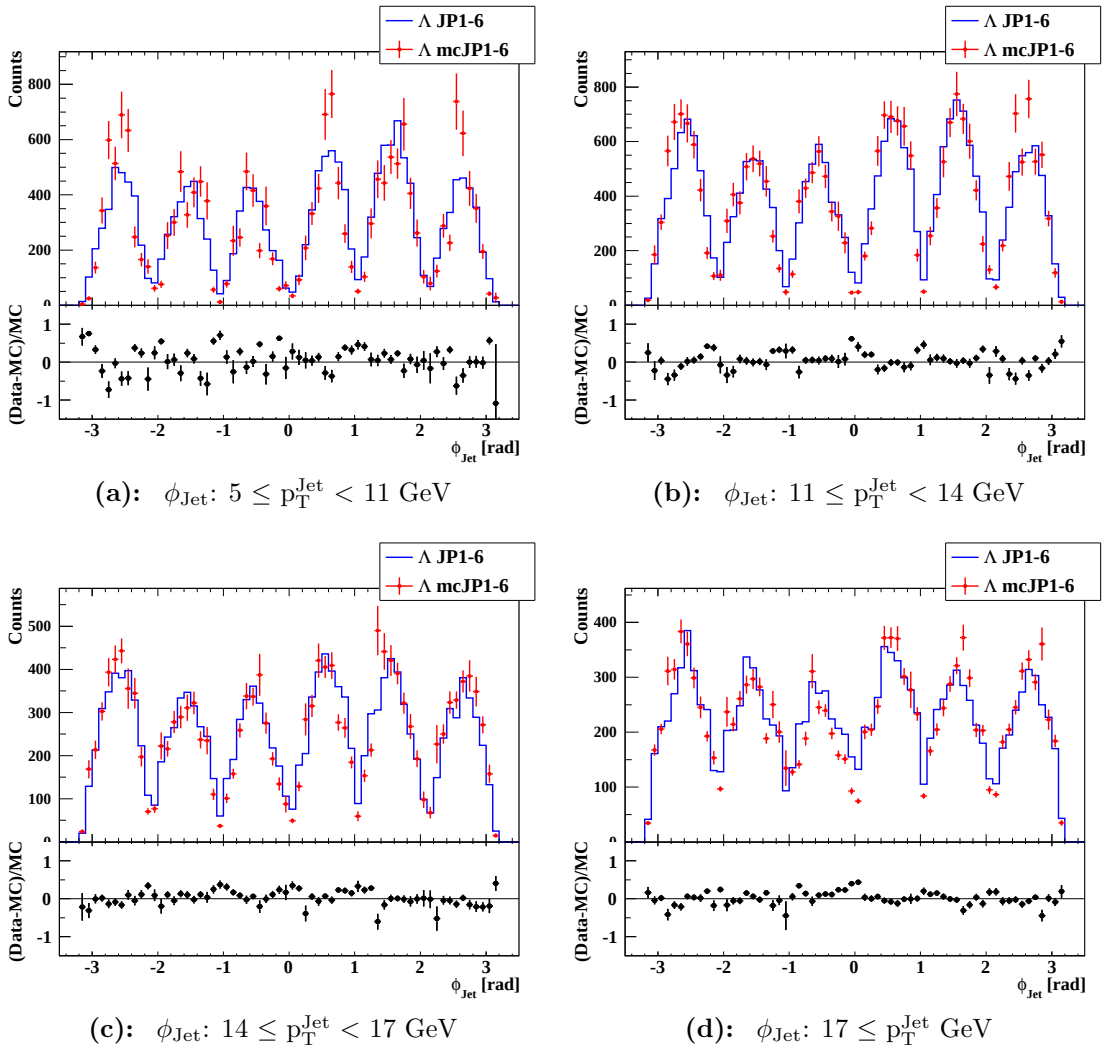

(a): ϕ_{Jet}: $5 \leq \mathrm{p_T^{Jet}} < 11$ GeV

(b): ϕ_{Jet}: $11 \leq \mathrm{p_T^{Jet}} < 14$ GeV

(c): ϕ_{Jet}: $14 \leq \mathrm{p_T^{Jet}} < 17$ GeV

(d): ϕ_{Jet}: $17 \leq \mathrm{p_T^{Jet}}$ GeV

Figure 3.65: Jet azimuthal angle distributions for the mcJP1–6 and JP1–6 triggered samples, and their ratio at different $\mathrm{p_T^{Jet}}$ intervals. Similar agreement found between MC and data in run year 2009.

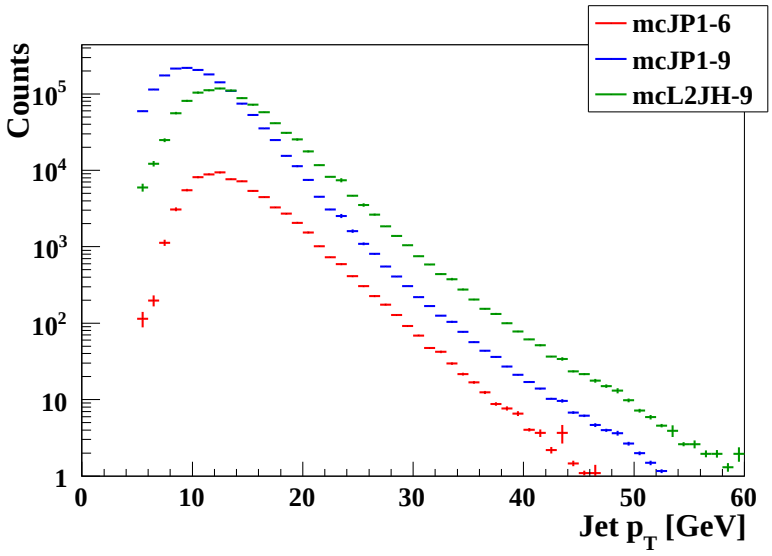

Figure 3.66: MC jet p_T distributions for both run years. All distributions have similar shape for $p_T^{Jet} > 25$ GeV as seen in data.

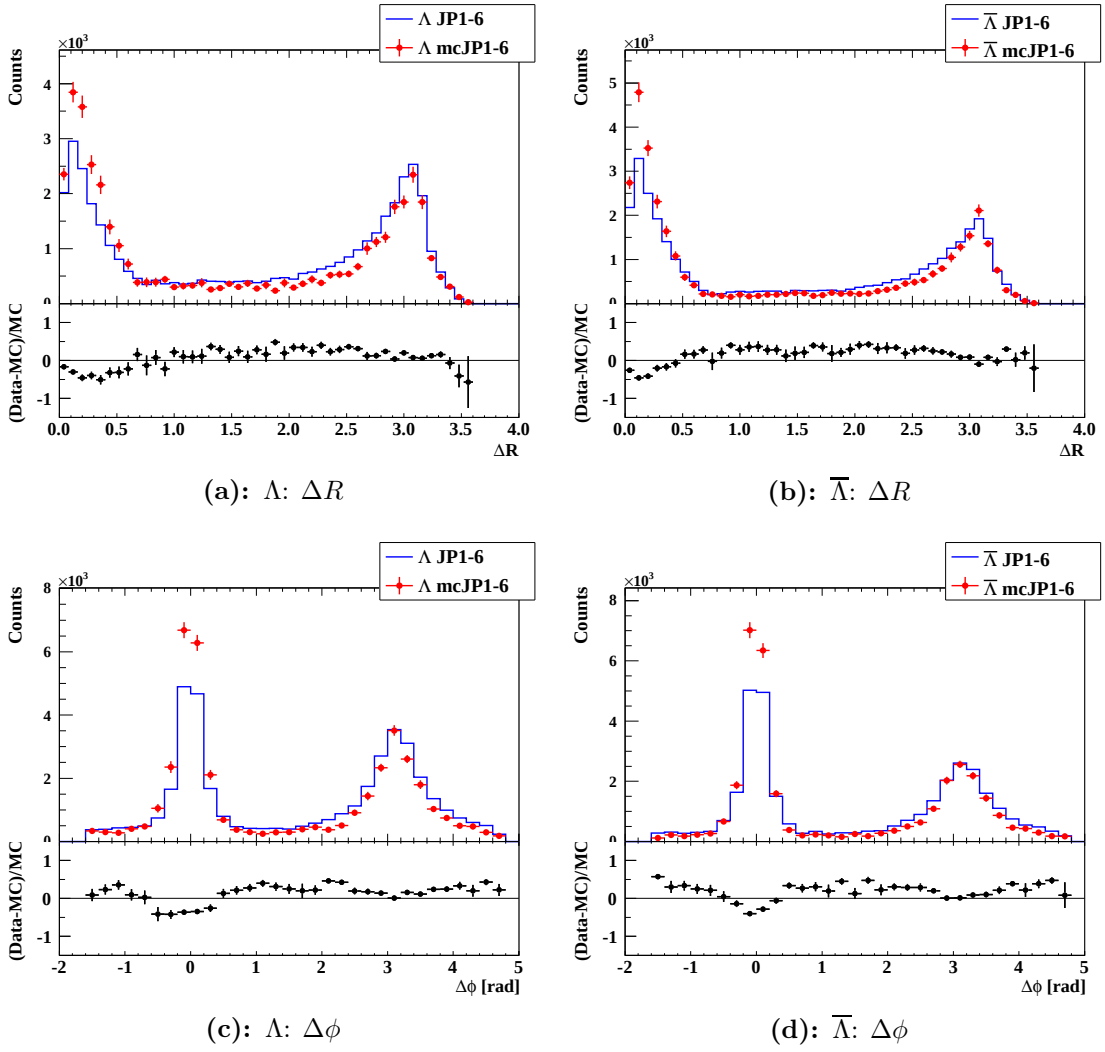

(a): Λ: ΔR **(b):** $\overline{\Lambda}$: ΔR

(c): Λ: $\Delta\phi$ **(d):** $\overline{\Lambda}$: $\Delta\phi$

Figure 3.67: Hyperon-jet ΔR and $\Delta\phi$ distributions for the mcJP1–6 and JP1–6 triggered samples, and their ratio. An enhancement on the near-side $\Lambda(\overline{\Lambda})$s for mcJP1–6 can be attributed to the difference in BEMC detector efficiency for mcJP1–6 and JP1–6. Similar agreement found between MC and data in run year 2009.

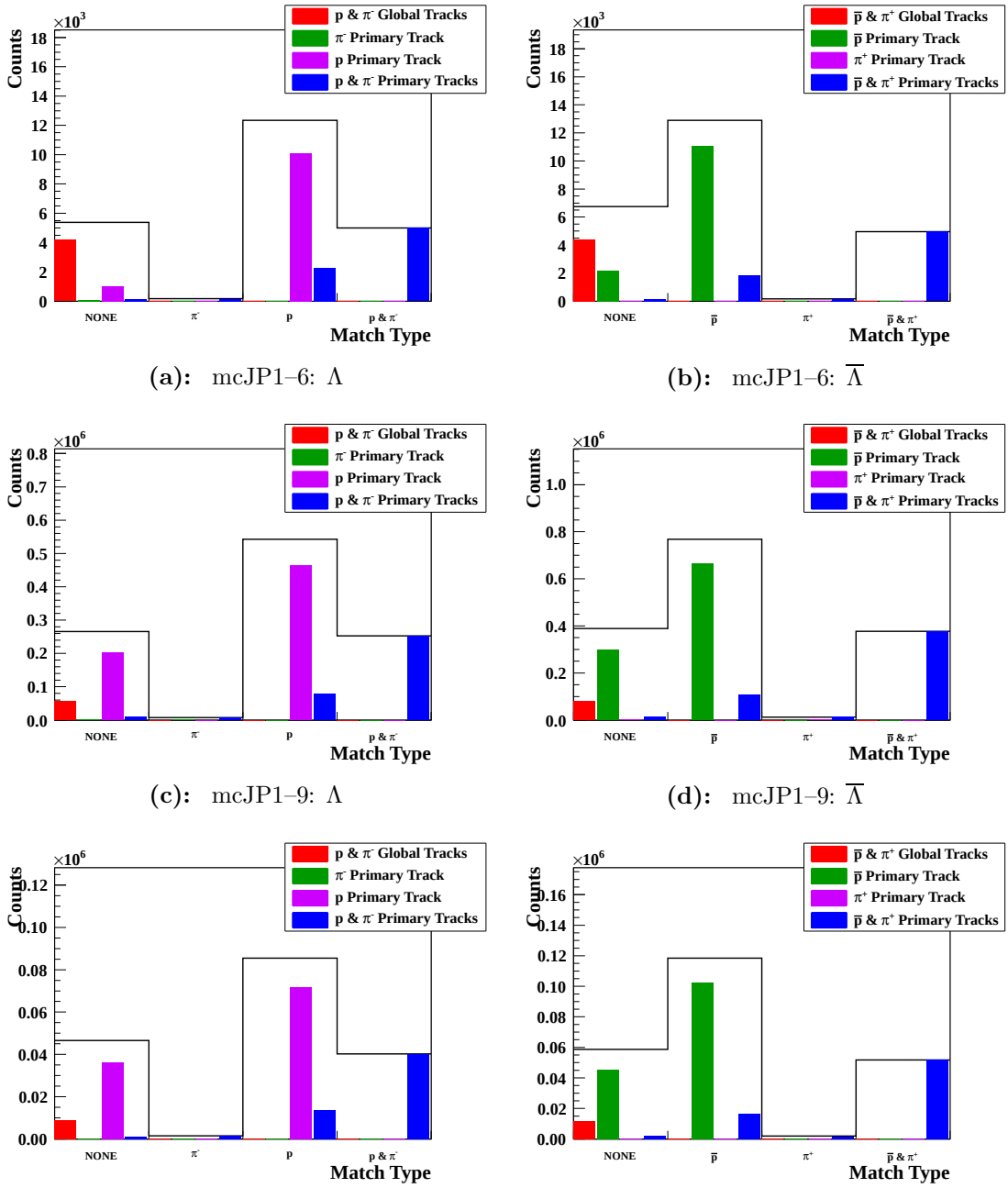

(a): mcJP1–6: Λ **(b):** mcJP1–6: $\overline{\Lambda}$

(c): mcJP1–9: Λ **(d):** mcJP1–9: $\overline{\Lambda}$

(e): mcL2JH–9: Λ **(f):** mcL2JH–9: $\overline{\Lambda}$

Figure 3.68: Contribution to the simulated reconstructed jet for associated hyperon-jets. The contributions are shown in four columns, when both daughters contribute, only one daughter contributes, and neither daughter contributes to the associated jet's reconstruction. For each column, the individual daughters are further separated as primary or global tracks. Primary tracks are particle tracks which are used to determine the primary vertex. Global tracks are tracks from secondary decays.

3.9 Study of Biases and Uncertainties

3.9.1 Beam Polarization

The beam polarization values used contain statistical and systematic uncertainty contribution from the measurement. The principal systematic uncertainty contributions come from the molecular contamination in the polarized atomic hydrogen during the hydrogen-jet measurement, the energy correction of the deposited energy from the recoiled carbon, and the vertical polarization profile [Oka06a, Gro11a, Gro11b]. The D_{LL} systematic uncertainty due to beam polarization, $\delta D_{LL}{}^{sys.pol.}$, is defined as

$$\delta D_{LL}{}^{sys.pol.} = |D_{LL}(P_{beam}) - D_{LL}(P_{beam} + \delta P_{beam}^{sys.})|, \tag{3.59}$$

which reduces to a scaling factor of D_{LL},

$$\delta D_{LL}{}^{sys.pol.} = \left[\frac{\delta P_{beam}^{sys.}}{P_{beam} + \delta P_{beam}^{sys.}}\right] D_{LL}(P_{beam}). \tag{3.60}$$

The $\delta D_{LL}{}^{sys.pol.}$ contributions for D_{LL}^{Sig} were calculated using Equation 3.60. The upper limit from $\delta D_{LL}{}^{sys.pol.}$ contribution is 0.001 for $\Lambda(\overline{\Lambda})$ particles.

3.9.2 Relative Luminosity

The systematic uncertainty from the relative luminosity $R_{1\cdot6}$ ratios, $\delta R_{1\cdot6}{}^{sys.}$, are calculated by determining the difference between the relative luminosity values from the BBC and ZDC scaler boards [Sak11, See11]. The $\delta R_3{}^{sys.}$ value was determined to be 5.5×10^{-4} [Sas07] for run year 2006 while $\delta R_4{}^{sys.}$, $\delta R_5{}^{sys.}$, and $\delta R_6{}^{sys.}$ were determined to be 1.7×10^{-3}, 2.7×10^{-4}, and 1.7×10^{-3} [Hay11] for run year 2009. The relative luminosity R_3 ratio can be defined as a linear combination of R_4, R_5, and R_6 ratios as

$$R_3 = \frac{R_4 + 1}{R_5 + R_6}. \tag{3.61}$$

The sum of systematic uncertainties for R_4, R_5, and R_6 ratios are therefore related to $\delta R_3{}^{\text{sys.}}$. The value of 5.5×10^{-4} was used for $\delta R_4{}^{\text{sys.}}$, $\delta R_5{}^{\text{sys.}}$, and $\delta R_6{}^{\text{sys.}}$ as an upper limit for run year 2006. The D_{LL} systematic uncertainty from relative luminosity, $\delta D_{LL}{}^{\text{sys.rel.lum.}}$, is defined as

$$\delta D_{LL}{}^{sys.rel.lum.} = |D_{LL}(R_4, R_5, R_6) - D_{LL}(R_4 + \delta R_4^{sys}, R_5 + \delta R_5^{sys}, R_6 + \delta R_6^{sys})|. \tag{3.62}$$

Different $\delta D_{LL}{}^{\text{sys.rel.lum.}}$ were calculated with $\delta R_4{}^{\text{sys.}}$, $\delta R_5{}^{\text{sys.}}$, and $\delta R_6{}^{\text{sys.}}$ values positively and negatively correlated. The maximal $\delta D_{LL}{}^{\text{sys.rel.lum.}}$ value was chosen as the upper limit. The upper limit from $\delta D_{LL}{}^{\text{sys.rel.lum.}}$ contribution is 0.006 for $\Lambda(\overline{\Lambda})$ particles.

3.9.3 Residual Background

The systematic uncertainty contribution from residual background is quantified by performing a second independent method for determining the residual background. The background counts from the invariant mass background sideband regions are summed and scaled as

$$\text{Scaled Bkg. Counts} = \text{Bkg. Counts} \times \frac{\text{Sig. Range}}{\text{Bkg. Range}}, \tag{3.63}$$

such that both signal and background regions are of equal range. Assuming the background is linear and uniform throughout the invariant mass range, the scaled background counts describe the background within the signal region and are then used to calculate the residual background. The systematic uncertainty contribution from residual background, $\delta D_{LL}{}^{\text{sys.res.bkg.}}$, is defined as

$$\delta D_{LL}{}^{sys.res.bkg.} = |D_{LL}{}^{method\,1} - D_{LL}{}^{method\,2}|.$$

where $D_{LL}{}^{method\,1}$ measurement is calculated using the residual background method described in Section 3.6.1 and the residual background determined in this section

is used to calculate $D_{LL}{}^{method\,2}$. The upper limit from $\delta \mathrm{D_{LL}}^{\mathrm{sys.res.bkg.}}$ contribution is 0.037 for $\Lambda(\overline{\Lambda})$ particles.

3.9.4 Residual Transverse Polarized Component

The polarized beams travel in RHIC with their polarization vectors transverse to the horizontal plane of the accelerator rings to minimize depolarization effects. To achieve a longitudinally polarized beam, the beams are rotated longitudinally by the spin rotators before they reach the detector at the interaction point. The longitudinally polarized beams still contain a residual transverse polarization component. In this section, the propagation of the systematic uncertainty contribution from the residual transverse component is presented.

Beam		θ rad	ϕ rad
		2006	
Yellow	($<$ 7138034)	0.176 $\pm$ 0.003	0.60 $\pm$ 0.02
Yellow	($>$ 7138034)	0.068 $\pm$ 0.002	$-$0.84 $\pm$ 0.03
Blue	($<$ 7138034)	0.121 $\pm$ 0.003	1.53 $\pm$ 0.03
Blue	($>$ 7138034)	0.015 $\pm$ 0.002	1.21 $\pm$ 0.02
		2009	
Yellow	($<$ 10173048)	0.15 $\pm$ 0.02	$-$0.5 $\pm$ 0.1
Yellow	($>$ 10173048)	0.13 $\pm$ 0.02	$-$0.5 $\pm$ 0.1
Blue	($<$ 10173048)	0.25 $\pm$ 0.02	$-$1.5 $\pm$ 0.1
Blue	($>$ 10173048)	0.10 $\pm$ 0.03	$-$1.4 $\pm$ 0.1

Table 3.24: Residual transverse and radial polarization angles for run year 2006 and 2009.

The residual transverse and radial polarization components are determined using the local polarimetry measurements as described in Section 2.2.5. Table 3.24 show the residual transverse angle, θ, and the angle from the residual radial component given by ϕ for both run year 2006 and 2009. The measured beam polarization

can be decomposed to its longitudinal and transverse components as

$$P_{beam}^2 = P_{beam,L}^2 + P_{beam,T}^2, \tag{3.64}$$

where $P_{beam,L}$ is the longitudinal and $P_{beam,T}$ is the transverse polarized beam component. The D_{LL} systematic uncertainty from the residual transverse beam polarization, $\delta D_{LL}^{\text{sys.res.trans.}}$, is defined as

$$\delta {D_{LL}}^{sys.res.trans.} = |D_{LL}(P_{beam}) - D_{LL}(P_{beam}\cos(\theta))|, \tag{3.65}$$

which reduces to a scaling factor of D_{LL},

$$\delta {D_{LL}}^{sys.res.trans.} = \left[\frac{\cos(\theta) - 1}{\cos(\theta)}\right] D_{LL}(P_{beam}). \tag{3.66}$$

The scaling factor is 0.006 and 0.01 for run year 2006 and 2009, respectively. The upper limit from $\delta D_{LL}^{\text{sys.res.trans.}}$ contribution is 0.003 for $\Lambda(\overline{\Lambda})$ particles.

The residual transverse polarization component allows the transverse spin transfer, D_{NN}, to contribute to the measured longitudinal spin transfer, D_{LL}. The systematic contribution from D_{NN} can be expressed as

$$\delta {D_{LL}}^{sys.\,d_{nn}} = \frac{P_{beam,T}}{P_{Beam}} D_{NN}. \tag{3.67}$$

Assuming the D_{NN} measurements are of similar amplitude as D_{LL} measurements for each individual interval, the largest D_{LL} amplitude from all triggers is used as a conservative value for D_{NN} for each particular interval which reduces the systematic contribution to a scaling factor of D_{LL},

$$\delta {D_{LL}}^{sys.\,d_{nn}} = \sin(\theta) D_{LL}. \tag{3.68}$$

The scaling factor is 0.10 and 0.15 for run year 2006 and 2009, respectively.

3.9.5 Pileup

Pileup occurs when particles from preceding or succeeding collisions are included in the data that is read out for the analyzed event and originates, primarily, from the slow readout time of the TPC compared to the RHIC beam bunch crossing period. The TPC takes a maximum of 38.4 μs for an electron to drift from the central membrane to the end cap [And03], however the average bunch crossing timing is 107 ns. When the L0 trigger starts an event acquisition, the TPC is likely to contain tracks from multiple bunch crossing collisions. Pileup can also occur when multiple collisions occur in a single beam bunch crossing. An event with multiple collisions contains more tracks which may result in not correctly reconstructing the primary vertex and an increase in the reconstructed number of particles per event. The probability for this to occur is small for the luminosities in run year 2006 and 2009.

The $\Lambda(\overline{\Lambda})$ and K^0_s production rate per event is used run-by-run to estimate the contribution from pileup. A constant rate per event is expected if each collision is recorded within all the sub-detector readout times regardless of the collision rate in each run. To determine the pileup contribution, the production rates of $\Lambda(\overline{\Lambda})$ and K^0_s particles were extracted per run and the mean BBC coincidence rate for each run was calculated. The production rate of Λ and $\overline{\Lambda}$ are comparable and therefore were combined to increase statistics. Runs with less than 1000 events, 20 $\Lambda + \overline{\Lambda}$, or 20 K^0_s particles are removed when determining the pileup contribution. The production rates were plotted for each run versus the corresponding BBC coincidence rate. The scatter plots are fitted with a constant and a linear function. The constant function describes constant hyperons production, the case of negligible pile-up. The linear function describes the recorded hyperons production rate at different BBC coincidence rates. The fitted lines were extrapolated to low BBC co-

incidence rates of 10 kHz, which is below the rate at which the TPC will complete its readout cycle before the next bunch crossing occurs. The contribution from pileup is taken to be the percentage ratio between the fitted lines at 10 kHz BBC coincidence rate. Figures 3.69(a)–(f) show the fitted scatter plots used to determine the pileup contribution for $\Lambda + \overline{\Lambda}$ and K^0_s particles. The blue line shows the constant hyperons production rate while the green line fits the scatter points. The pileup contribution for $\Lambda + \overline{\Lambda}$ and K^0_s are summarized on Table 3.25. The negative contributions can be attributed the average number of hit points per event used for reconstructing the particle tracks. At higher BBC rates, the average number of hit points decreases, resulting in more fragmented tracks.

	Pileup Contribution (%)		
	JP1–6	JP1–9	L2JH–9
$\Lambda + \overline{\Lambda}$	3.47 ± 2.75	-2.92 ± 0.26	-1.07 ± 0.30
K^0_s	1.36 ± 2.16	-4.42 ± 0.22	-3.42 ± 0.23

Table 3.25: Pileup contribution of $\Lambda + \overline{\Lambda}$ and K^0_s

The JP1–6 trigger requirement reduces pileup by requiring the triggered jet to have a minimum E_T. The BEMC active time is much smaller, 20 ns, lowering the contribution to pileup from the energy deposited on the BEMC compared to the TPC reconstructed tracks from pileup particles. Without the jet triggered condition, the pileup tracks reconstructed in the TPC are more likely to satisfy the track quality conditions.

The spin configuration for each bunch is different from its neighboring bunches. Pileup from neighboring bunch crossing collisions will effectively create a spin average pileup contribution throughout the recorded events, diluting the extracted D_{LL} measurements. The pileup contribution for each spin 4-bit configuration was calculated. In addition to requiring at least 1000 events and 20 hyperons par-

	Pileup Contribution (%)			
	spin 4-bit 5	spin 4-bit 6	spin 4-bit 9	spin 4-bit 10
		JP1–6		
$\Lambda + \overline{\Lambda}$	4.63 ± 5.21	1.18 ± 5.24	8.17 ± 5.21	-1.30 ± 5.22
K^0_s	-3.41 ± 4.03	3.83 ± 4.08	-0.81 ± 4.08	4.68 ± 4.11
		JP1–9		
$\Lambda + \overline{\Lambda}$	-3.10 ± 0.51	-4.39 ± 0.51	-2.61 ± 0.51	-2.51 ± 0.51
K^0_s	-3.84 ± 0.42	-5.58 ± 0.42	-4.30 ± 0.42	-4.23 ± 0.42
		L2JH–9		
$\Lambda + \overline{\Lambda}$	-1.39 ± 0.58	-2.02 ± 0.57	-0.02 ± 0.58	-0.42 ± 0.57
K^0_s	-3.10 ± 0.45	-4.29 ± 0.45	-3.37 ± 0.45	-3.03 ± 0.45

Table 3.26: Pileup contribution of $\Lambda + \overline{\Lambda}$ and K^0_s at different spin 4-bit states

ticles for all spin 4-bit configurations, each spin 4-bit configuration subset also required to have at least 250 events and 5 hyperons particles for each spin 4-bit subset. Figures 3.70–3.72 show the scatter plots of $\Lambda + \overline{\Lambda}$ for different spin 4-bit configurations. The different spin 4-bit pileup contributions for $\Lambda + \overline{\Lambda}$ and K^0_s are summarized in Table 3.26. The pileup contribution is subtracted from each spin 4-bit configuration counts when extracting the pileup corrected D_{LL} measurements.

The correlation between the hyperons production rates for different spin 4-bit configurations were studied to check the importance of the covariant terms which make up the systematic uncertainty. Figures 3.73–3.75 show the scatter plots between the $\Lambda + \overline{\Lambda}$ production rates for different spin 4-bit configurations. The green lines describe the calculated correlation coefficient. The correlation coefficients for both $\Lambda + \overline{\Lambda}$ and K^0_s at different spin 4-bit configurations are summarized in Table 3.27. The correlation coefficient values for the $\Lambda + \overline{\Lambda}$ and K^0_s production rates at different spin 4-bit configuration show no strong correlation for JP1–6. The systematic uncertainty contribution for pileup can then be calculated separately

Spin 4-Bit Comparison	Correlation Coefficient					
	JP1–6		JP1–9		L2JH–9	
	$\Lambda+\overline{\Lambda}$	K^0_s	$\Lambda+\overline{\Lambda}$	K^0_s	$\Lambda+\overline{\Lambda}$	K^0_s
5 vs. 6	0.08	0.05	0.08	0.05	0.04	0.29
5 vs. 9	−0.10	−0.06	$<10^{-2}$	−0.08	0.04	0.28
5 vs. 10	−0.06	−0.03	0.39	−0.03	0.28	0.55
6 vs. 9	$<10^{-2}$	0.05	0.52	0.05	0.37	0.56
6 vs. 10	−0.13	−0.17	0.09	−0.17	0.05	0.27
9 vs. 10	−0.09	−0.15	0.11	−0.19	0.06	0.26

Table 3.27: Correlation coefficient between different spin 4-bit configurations of $\Lambda+\overline{\Lambda}$ and K^0_s mean production rates per run

for each spin 4-bit configuration state. In the case for JP1–9 and L2JH–9, the spin 4-bit configurations 5-10 and 6-9 show a significant correlation for both $\Lambda+\overline{\Lambda}$ and K^0_s. The systematic uncertainty contribution for pileup is changed to reflect the correlation between the various spin 4-bit configurations. The systematic uncertainty propagation on D_{LL} due to pileup is calculated by determining the difference between the extracted D_{LL} sample and the pileup corrected D_{LL} for each spin 4-bit configuration,

$$\left(\delta {D_{LL}}^{sys.pileup}\right)^2 = \sum_{\substack{k=++,-+,\\ +-,--}} \left[D_{LL}(n^k) - D_{LL}\left((1-u^k)n^k\right)\right]^2, \qquad (3.69)$$

where n^{++}, n^{-+}, n^{+-}, and n^{--} are the spin 4-bit sorted hyperons counts and u^{++}, u^{-+}, u^{+-}, and u^{--} the spin 4-bit sorted pileup contributions. If the uncertainty of the pileup contribution is larger than the calculated value, the uncertainty value is used instead. Tables 3.28–3.30 summarizes the D_{LL} systematic uncertainty values from pileup for $\Lambda(\overline{\Lambda})$ and K^0_s particles in both forward and backward direction. The increased statistics in run year 2009 and detector configuration result in smaller systematic contribution from pileup compared to run year 2006.

	$\delta D_{LL}^{sys.pileup}$					
	Λ	$\overline{\Lambda}$	K_s^0	Λ	$\overline{\Lambda}$	K_s^0
	Near-Side ($\eta_{physics} < 0$)			Near-Side ($\eta_{physics} > 0$)		
$0.5 \leq p_T < 1.0$	0.0679	0.0699	0.0022	0.0669	0.0695	0.0032
$1.0 \leq p_T < 2.0$	0.0696	0.0680	0.0017	0.0695	0.0673	0.0016
$2.0 \leq p_T < 3.0$	0.0321	0.0325	0.0013	0.0301	0.0323	0.0012
$3.0 \leq p_T < 5.0$	0.0083	0.0045	0.0013	0.0081	0.0038	0.0011
$5.0 \leq p_T$	0.0142	0.0117	0.0012	0.0088	0.0075	0.0008
	Away-Side ($\eta_{physics} < 0$)			Away-Side ($\eta_{physics} > 0$)		
$0.5 \leq p_T < 1.0$	0.0670	0.0703	0.0015	0.0668	0.0701	0.0015
$1.0 \leq p_T < 2.0$	0.0702	0.0673	0.0009	0.0700	0.0670	0.0009
$2.0 \leq p_T < 3.0$	0.0317	0.0326	0.0009	0.0322	0.0331	0.0011
$3.0 \leq p_T < 5.0$	0.0073	0.0133	0.0010	0.0073	0.0124	0.0013
$5.0 \leq p_T$	0.0070	0.0187	0.0024	0.0089	0.0195	0.0012

Table 3.28: Systematic uncertainty propagation from pileup to D_{LL} for JP1–6.

	$\delta D_{LL}^{sys.pileup}$					
	Λ	$\overline{\Lambda}$	K_s^0	Λ	$\overline{\Lambda}$	K_s^0
	Near-Side ($\eta_{physics} < 0$)			Near-Side ($\eta_{physics} > 0$)		
$0.5 \leq p_T < 1.0$	0.0387	0.0379	0.0007	0.0387	0.0379	0.0008
$1.0 \leq p_T < 2.0$	0.0381	0.0382	0.0001	0.0381	0.0382	0.0001
$2.0 \leq p_T < 3.0$	0.0183	0.0184	0.0006	0.0182	0.0184	0.0007
$3.0 \leq p_T < 5.0$	0.0021	0.0024	0.0008	0.0023	0.0022	0.0009
$5.0 \leq p_T$	0.0071	0.0077	0.0018	0.0068	0.0064	0.0018
	Away-Side ($\eta_{physics} < 0$)			Away-Side ($\eta_{physics} > 0$)		
$0.5 \leq p_T < 1.0$	0.0381	0.0379	0.0006	0.0381	0.0379	0.0006
$1.0 \leq p_T < 2.0$	0.0373	0.0371	0.0004	0.0374	0.0370	0.0004
$2.0 \leq p_T < 3.0$	0.0166	0.0166	0.0006	0.0166	0.0167	0.0006
$3.0 \leq p_T < 5.0$	0.0017	0.0018	0.0008	0.0021	0.0015	0.0010
$5.0 \leq p_T$	0.0093	0.0044	0.0024	0.0081	0.0049	0.0029

Table 3.29: Systematic uncertainty propagation from pileup to D_{LL} for JP1–9.

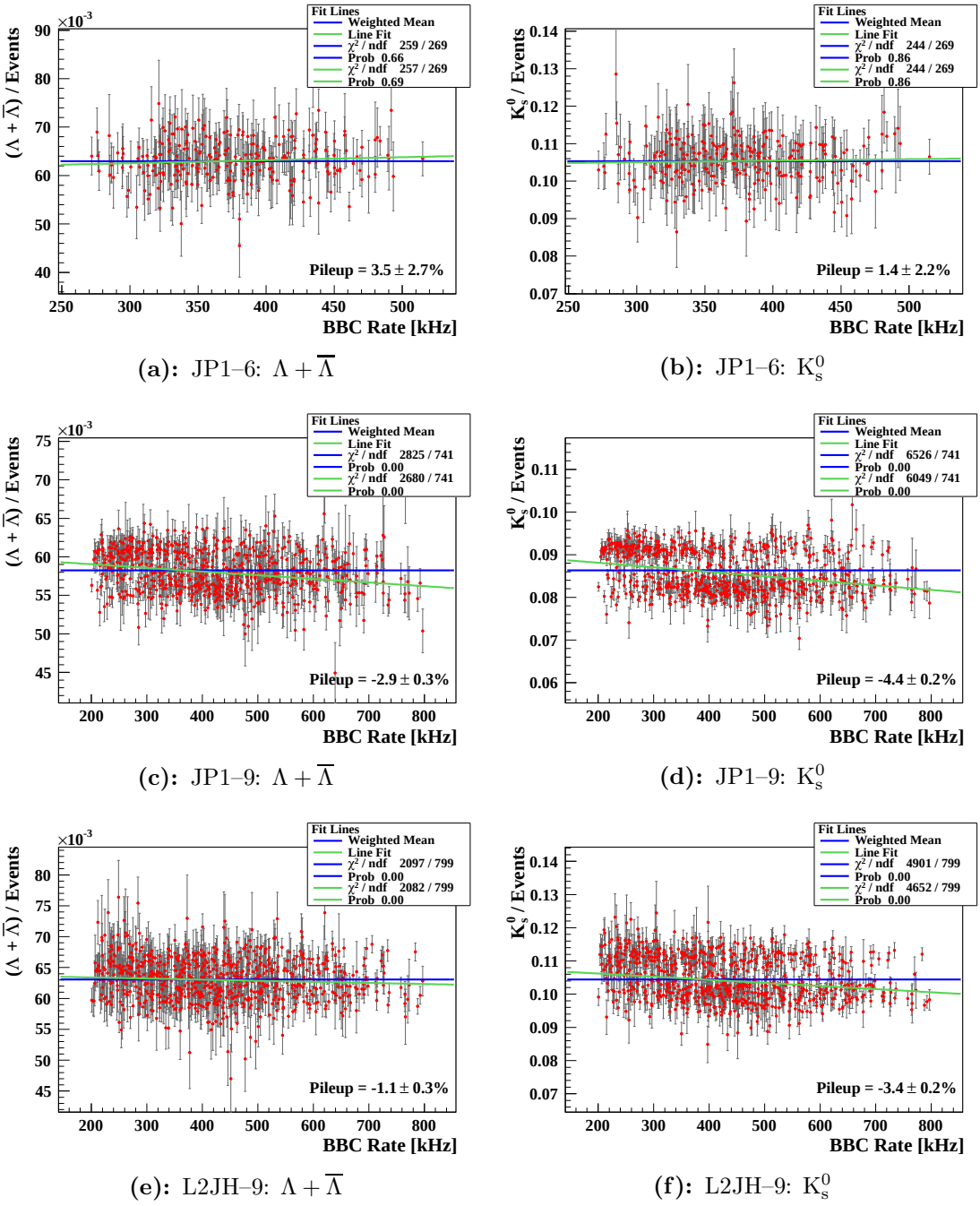

(a): JP1–6: $\Lambda + \overline{\Lambda}$ **(b):** JP1–6: K^0_s

(c): JP1–9: $\Lambda + \overline{\Lambda}$ **(d):** JP1–9: K^0_s

(e): L2JH–9: $\Lambda + \overline{\Lambda}$ **(f):** L2JH–9: K^0_s

Figure 3.69: The scatter plots for $\Lambda + \overline{\Lambda}$ and K^0_s production rates for each mean BBC rate per run are used for determining the pileup contribution. The blue line is constant and fitted to the scatter points. The green line describes a linear fit to the scatter points. The percentage difference ratio between the constant and linear fitted lines at 10 kHz give the pileup contribution.

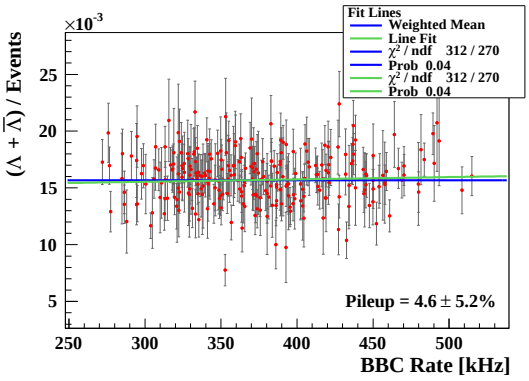

(a): spin 4-bit 5

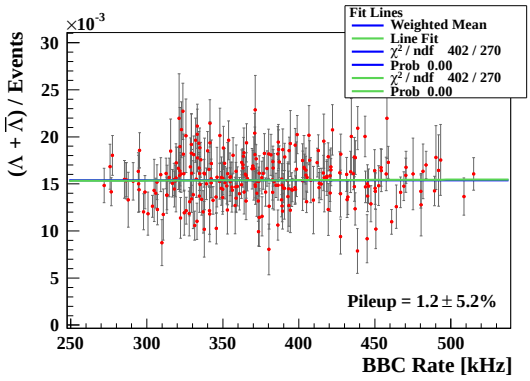

(b): spin 4-bit 6

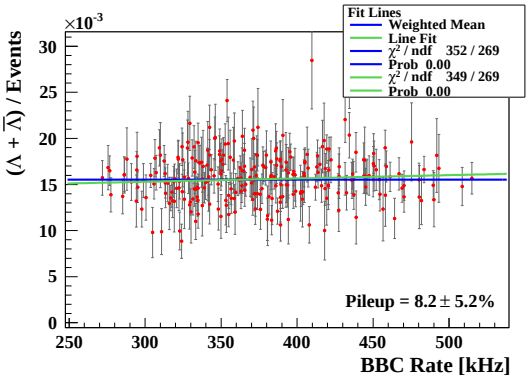

(c): spin 4-bit 9

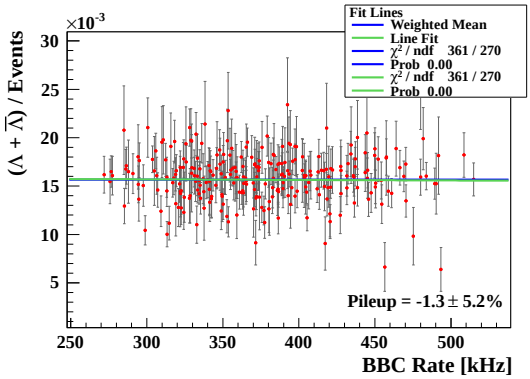

(d): spin 4-bit 10

Figure 3.70: Determination of pileup contribution for $\Lambda + \overline{\Lambda}$ particles with different spin 4-bit configuration from JP1–6 triggered events.

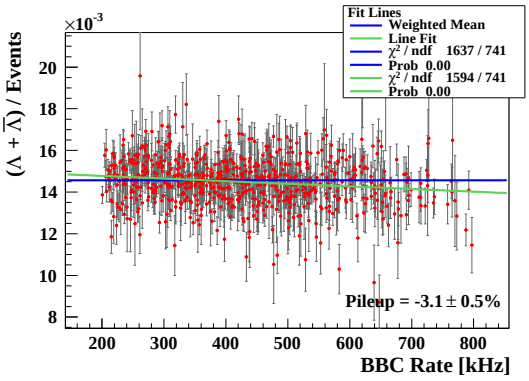

(a): JP1–6: spin 4-bit 5

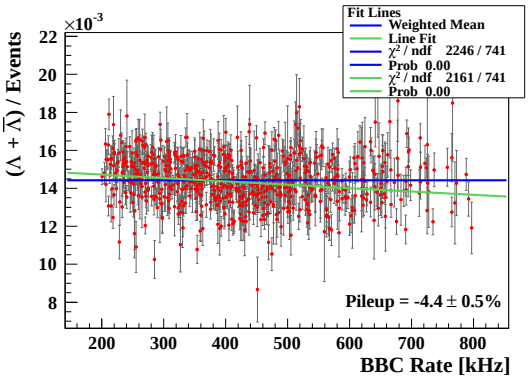

(b): JP1–6: spin 4-bit 6

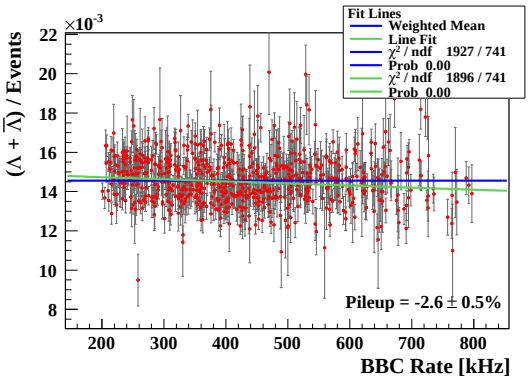

(c): JP1–6: spin 4-bit 9

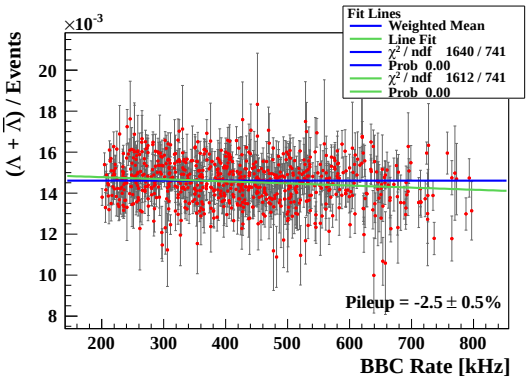

(d): JP1–6: spin 4-bit 10

Figure 3.71: Determination of pileup contribution for $\Lambda + \overline{\Lambda}$ particles with different spin 4-bit configuration from JP1–9 triggered events.

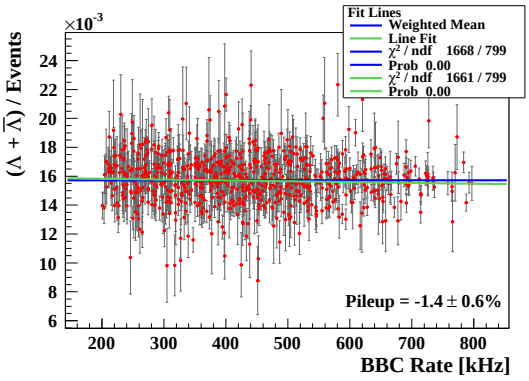

(a): L2JH–9: spin 4-bit 5

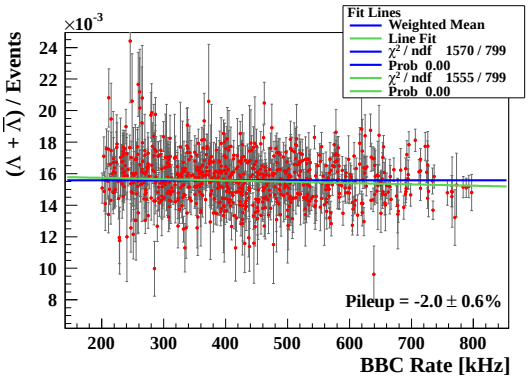

(b): L2JH–9: spin 4-bit 6

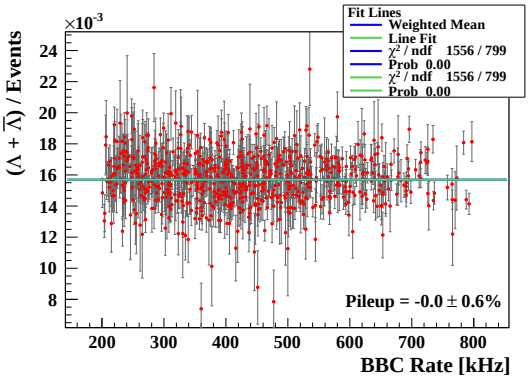

(c): L2JH–9: spin 4-bit 9

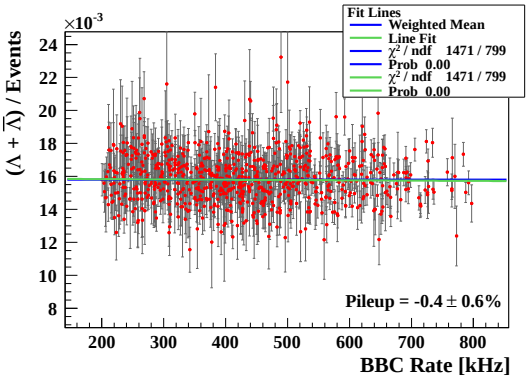

(d): L2JH–9: spin 4-bit 10

Figure 3.72: Determination of pileup contribution for $\Lambda + \overline{\Lambda}$ particles with different spin 4-bit configuration from L2JH–9 triggered events.

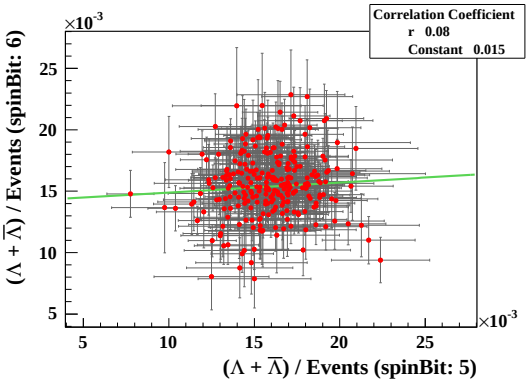

(a): spin 4-bit 5 vs. spin 4-bit 6

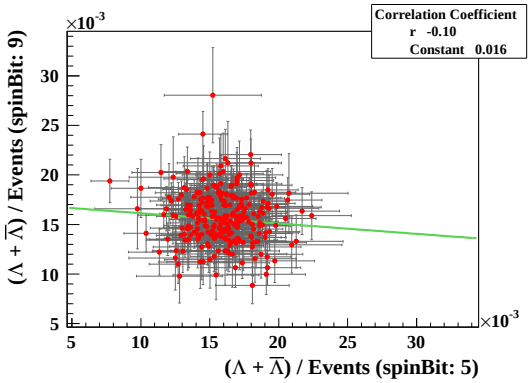

(b): spin 4-bit 5 vs. spin 4-bit 9

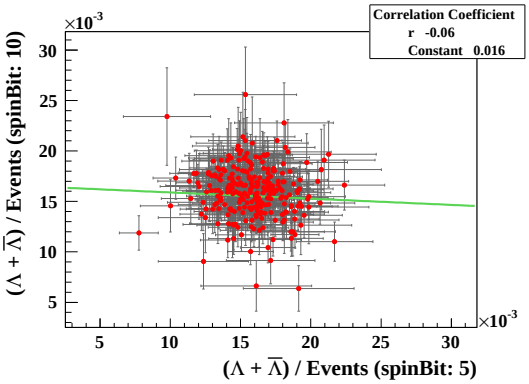

(c): spin 4-bit 5 vs. spin 4-bit 10

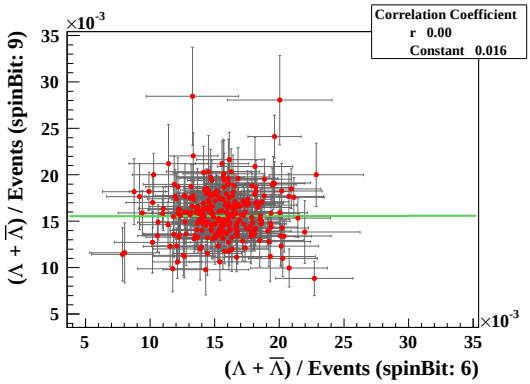

(d): spin 4-bit 6 vs. spin 4-bit 9

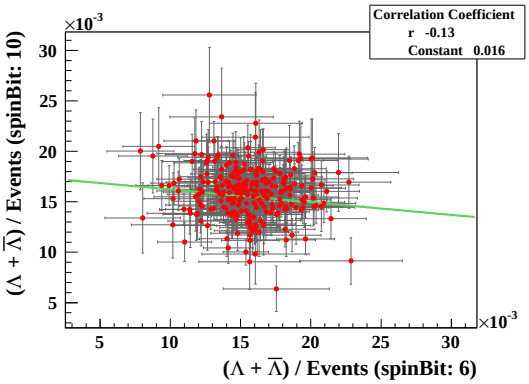

(e): spin 4-bit 6 vs. spin 4-bit 10

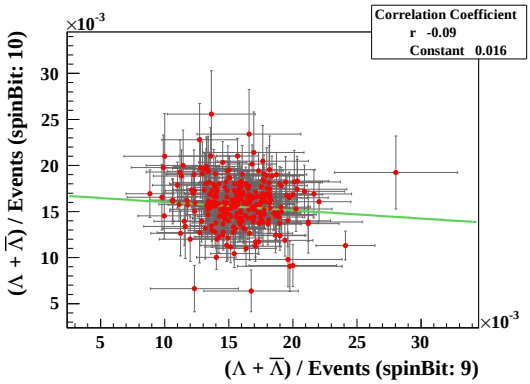

(f): spin 4-bit 9 vs. spin 4-bit 10

Figure 3.73: Correlation coefficient between different spin 4-bit configurations of mean $\Lambda + \overline{\Lambda}$ production rates per run for JP1–6

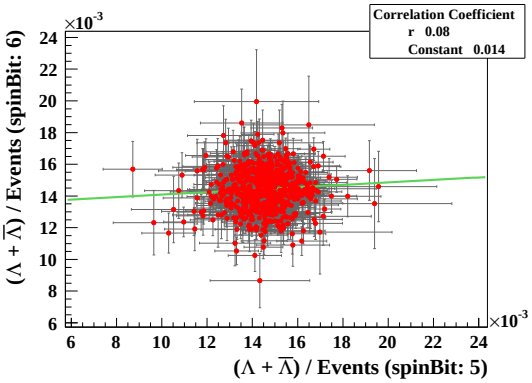

(a): spin 4-bit 5 vs. spin 4-bit 6

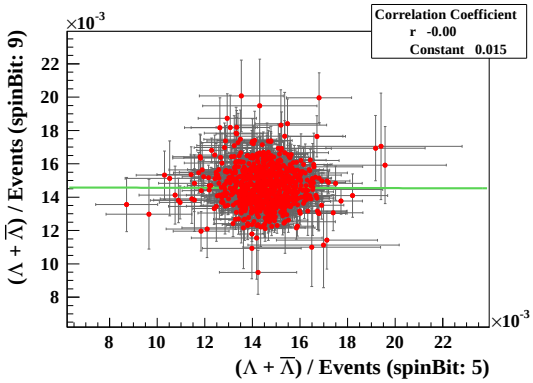

(b): spin 4-bit 5 vs. spin 4-bit 9

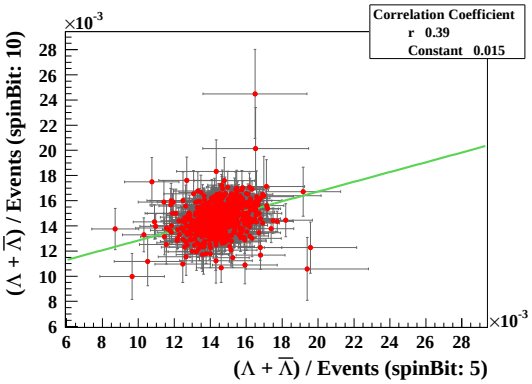

(c): spin 4-bit 5 vs. spin 4-bit 10

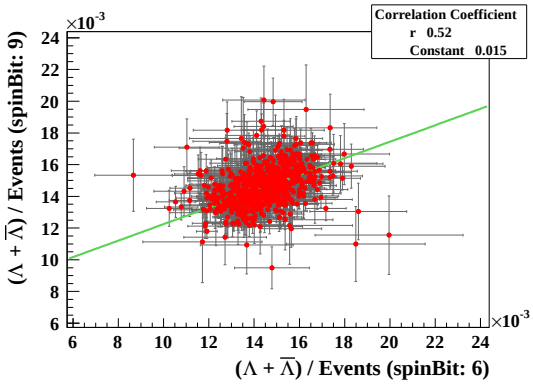

(d): spin 4-bit 6 vs. spin 4-bit 9

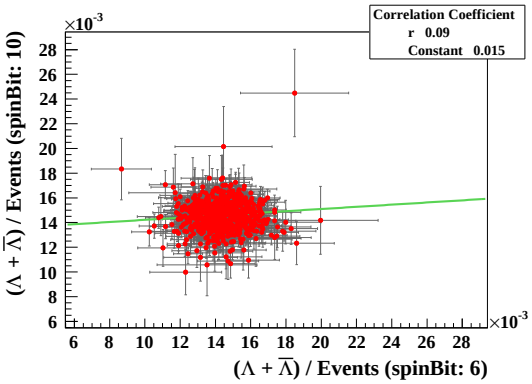

(e): spin 4-bit 6 vs. spin 4-bit 10

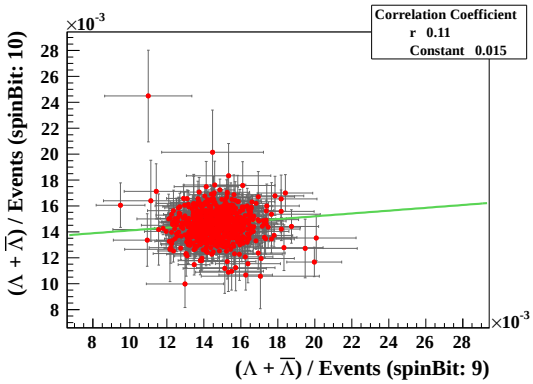

(f): spin 4-bit 9 vs. spin 4-bit 10

Figure 3.74: Correlation coefficient between different spin 4-bit configurations of mean $\Lambda + \overline{\Lambda}$ production rates per run for JP1–9

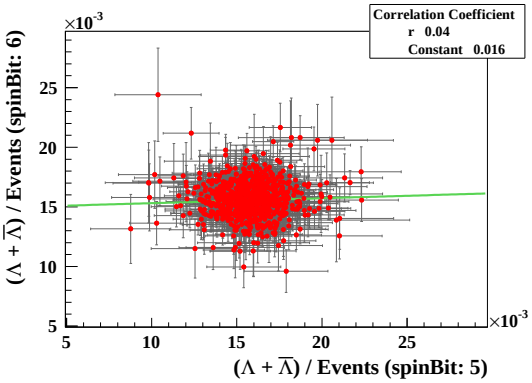

(a): spin 4-bit 5 vs. spin 4-bit 6

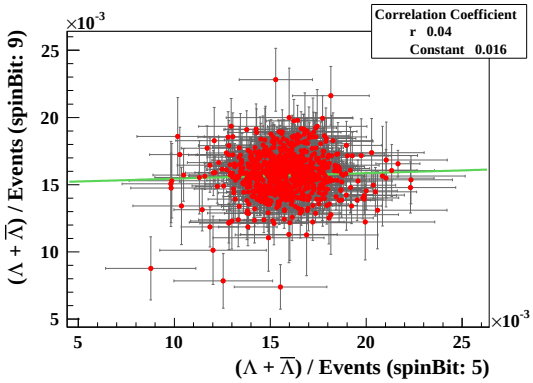

(b): spin 4-bit 5 vs. spin 4-bit 9

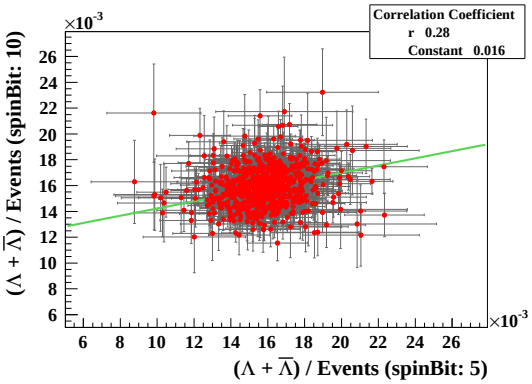

(c): spin 4-bit 5 vs. spin 4-bit 10

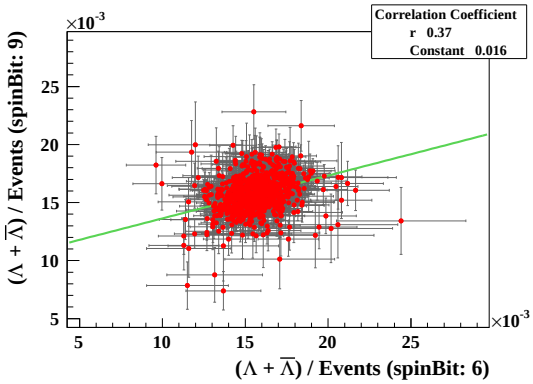

(d): spin 4-bit 6 vs. spin 4-bit 9

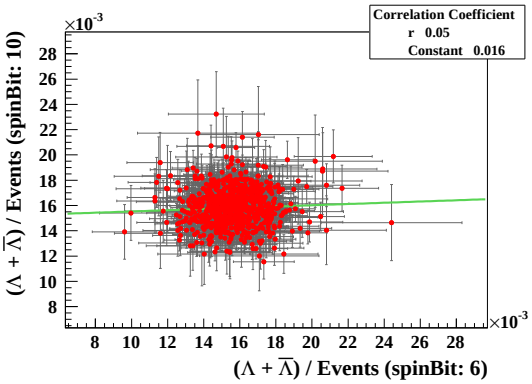

(e): spin 4-bit 6 vs. spin 4-bit 10

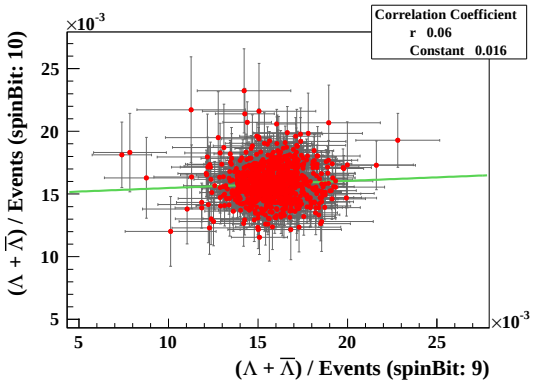

(f): spin 4-bit 9 vs. spin 4-bit 10

Figure 3.75: Correlation coefficient between different spin 4-bit configurations of mean $\Lambda + \overline{\Lambda}$ production rates per run for L2JH–9

	$\delta D_{LL}^{sys.pileup}$					
	Λ	$\overline{\Lambda}$	K_s^0	Λ	$\overline{\Lambda}$	K_s^0
	Near-Side ($\eta_{physics} < 0$)			Near-Side ($\eta_{physics} > 0$)		
$0.5 \leq p_T < 1.0$	0.0142	0.0143	0.0006	0.0141	0.0141	0.0006
$1.0 \leq p_T < 2.0$	0.0144	0.0147	0.0005	0.0146	0.0143	0.0004
$2.0 \leq p_T < 3.0$	0.0057	0.0062	0.0002	0.0057	0.0063	0.0002
$3.0 \leq p_T < 5.0$	0.0006	0.0008	0.0003	0.0007	0.0010	0.0003
$5.0 \leq p_T$	0.0023	0.0026	0.0012	0.0023	0.0023	0.0015
	Away-Side ($\eta_{physics} < 0$)			Away-Side ($\eta_{physics} > 0$)		
$0.5 \leq p_T < 1.0$	0.0140	0.0141	0.0004	0.0140	0.0141	0.0004
$1.0 \leq p_T < 2.0$	0.0139	0.0140	0.0001	0.0139	0.0140	0.0001
$2.0 \leq p_T < 3.0$	0.0060	0.0061	0.0002	0.0059	0.0064	$<10^{-5}$
$3.0 \leq p_T < 5.0$	0.0007	0.0012	0.0005	0.0006	0.0013	0.0005
$5.0 \leq p_T$	0.0027	0.0015	0.0017	0.0028	0.0019	0.0017

Table 3.30: Systematic uncertainty propagation from pileup to D_{LL} for L2JH–9.

3.9.6 Trigger Bias

To study the trigger bias contribution from jet triggered data, simulated minimum bias triggers, mcMB–6 and mcMB–9, were generated. The MC simulated samples described in Section 3.8 were used to create mcMB–6 and mcMB–9 triggered samples. The tuned selection parameters determined from data were imposed on the simulated minimum bias triggers. The systematic uncertainty from flavor separated sub-processes ratios and raw z shift between the triggers make up the systematic uncertainty from trigger bias.

The raw z distributions are shown in Figures 3.76–3.81 for $\Lambda(\overline{\Lambda})$. The central value for each z distribution is determined and used to calculate the relative shift MC jet triggered z distributions have with respect to the MC minimum bias triggered z distributions. The central z values and percentage ratios are shown in Tables 3.31–3.33 for both MC simulated minimum bias and jet triggered samples. The mcJP1–6 triggered jets are shifted by 0.09 and 0.07 to a lower z with respect to mcMB–6 triggered jets for Λ and $\overline{\Lambda}$, respectively. The jet trigger requirement places a minimum E_T limit, removing lower p_T jets. The lack of minimum jet patch threshold for minimum bias trigger allows events to satisfy the trigger condition which contains softer jets. The softer triggered jets create higher z values when associated with the $\Lambda(\overline{\Lambda})$ particles.

The minimum bias and jet triggered samples z distributions for $\Lambda(\overline{\Lambda})$ at different p_T^{Jet} intervals are shown in Figures 3.82–3.84 for both run years. For higher p_T^{Jet} intervals, the central z values for minimum bias and jet triggered samples are comparable which is expected since the jet triggers are a subset of the minimum bias triggers. The lowest p_T^{Jet} interval is the largest contributor of lower jet trigger simulated z values compared to the minimum bias sample.

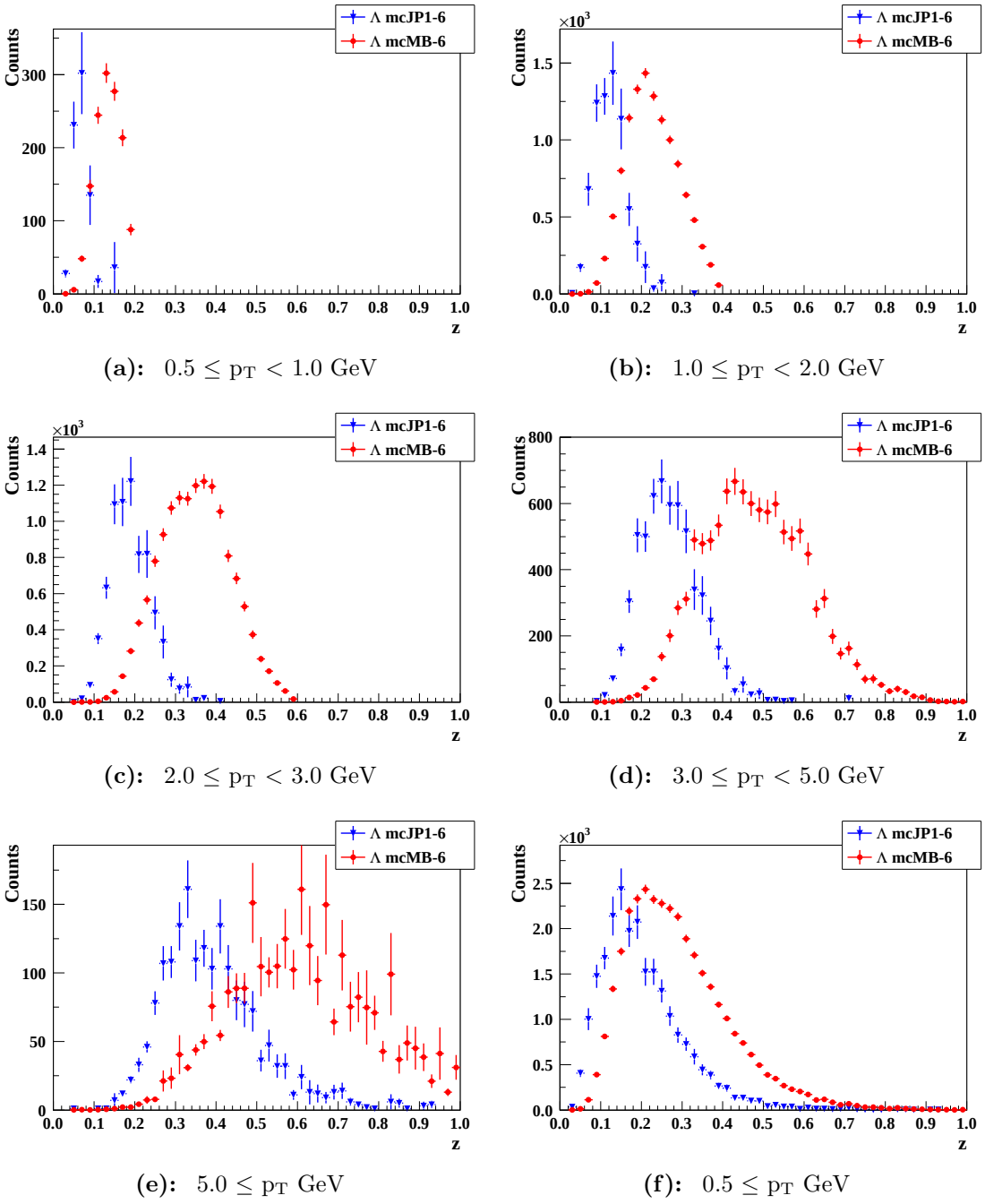

(a): $0.5 \leq p_T < 1.0$ GeV

(b): $1.0 \leq p_T < 2.0$ GeV

(c): $2.0 \leq p_T < 3.0$ GeV

(d): $3.0 \leq p_T < 5.0$ GeV

(e): $5.0 \leq p_T$ GeV

(f): $0.5 \leq p_T$ GeV

Figure 3.76: Comparison of raw z for Λs from mcMB–6 and mcJP1–6 triggered events. mcJP1–6 trigger imposes mcMB–6 trigger conditions plus additional triggered jet conditions. The mean z for mcMB–6 are higher for all Λ p_T intervals compared to mcJP1–6 which is expected as the mcMB–6 triggered sample contains lower p_T jets, resulting in higher z values.

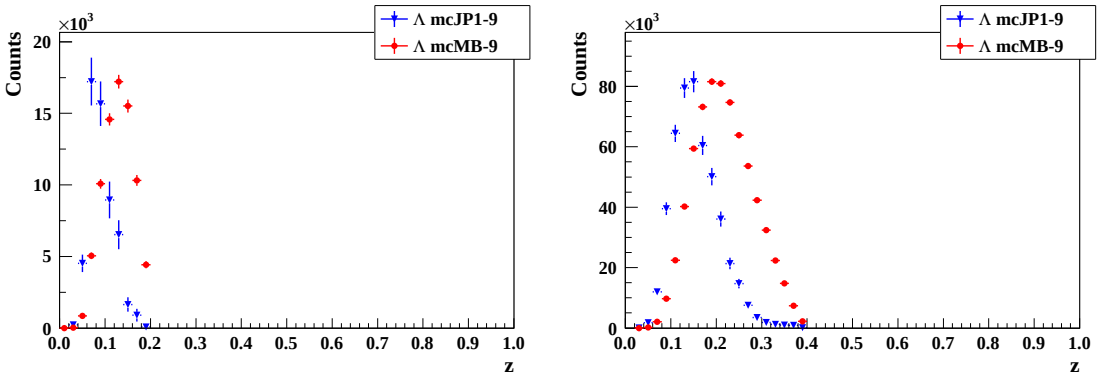

(a): $0.5 \leq p_T < 1.0$ GeV

(b): $1.0 \leq p_T < 2.0$ GeV

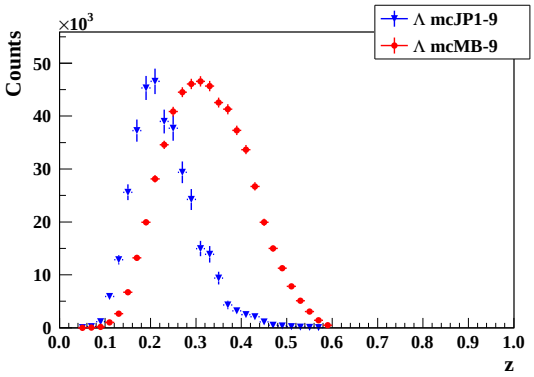

(c): $2.0 \leq p_T < 3.0$ GeV

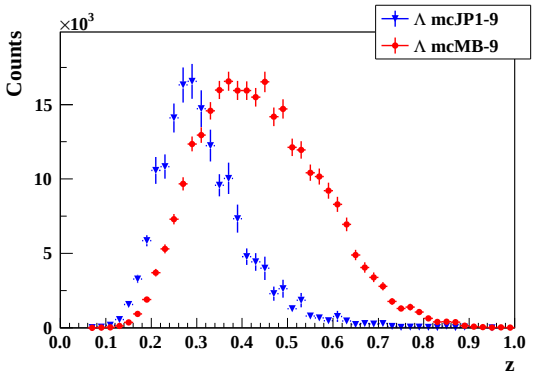

(d): $3.0 \leq p_T < 5.0$ GeV

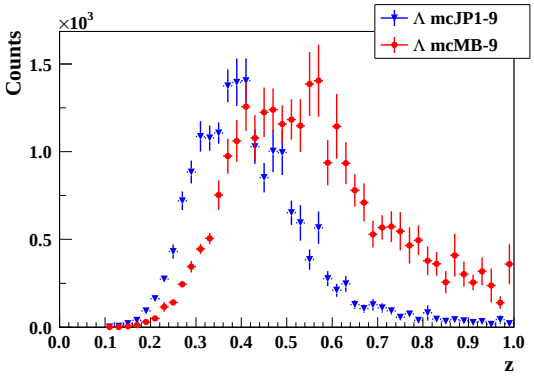

(e): $5.0 \leq p_T$ GeV

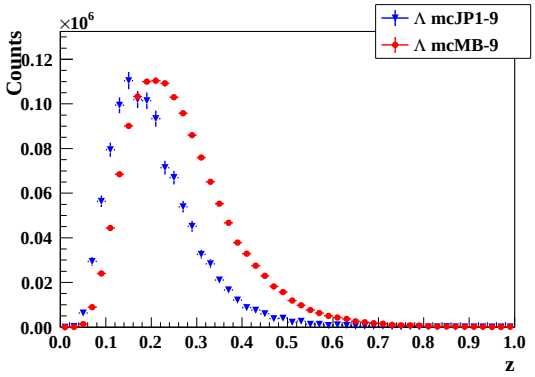

(f): $0.5 \leq p_T$ GeV

Figure 3.77: Comparison of raw z for Λs from mcMB–9 and mcJP1–9 triggered events. mcJP1–9 trigger imposes mcMB–9 trigger conditions plus additional triggered jet conditions. The mean z for mcMB–9 are higher for all Λ p_T intervals compared to mcJP1–9 which is expected as the mcMB–9 triggered sample contains lower p_T jets, resulting in higher z values.

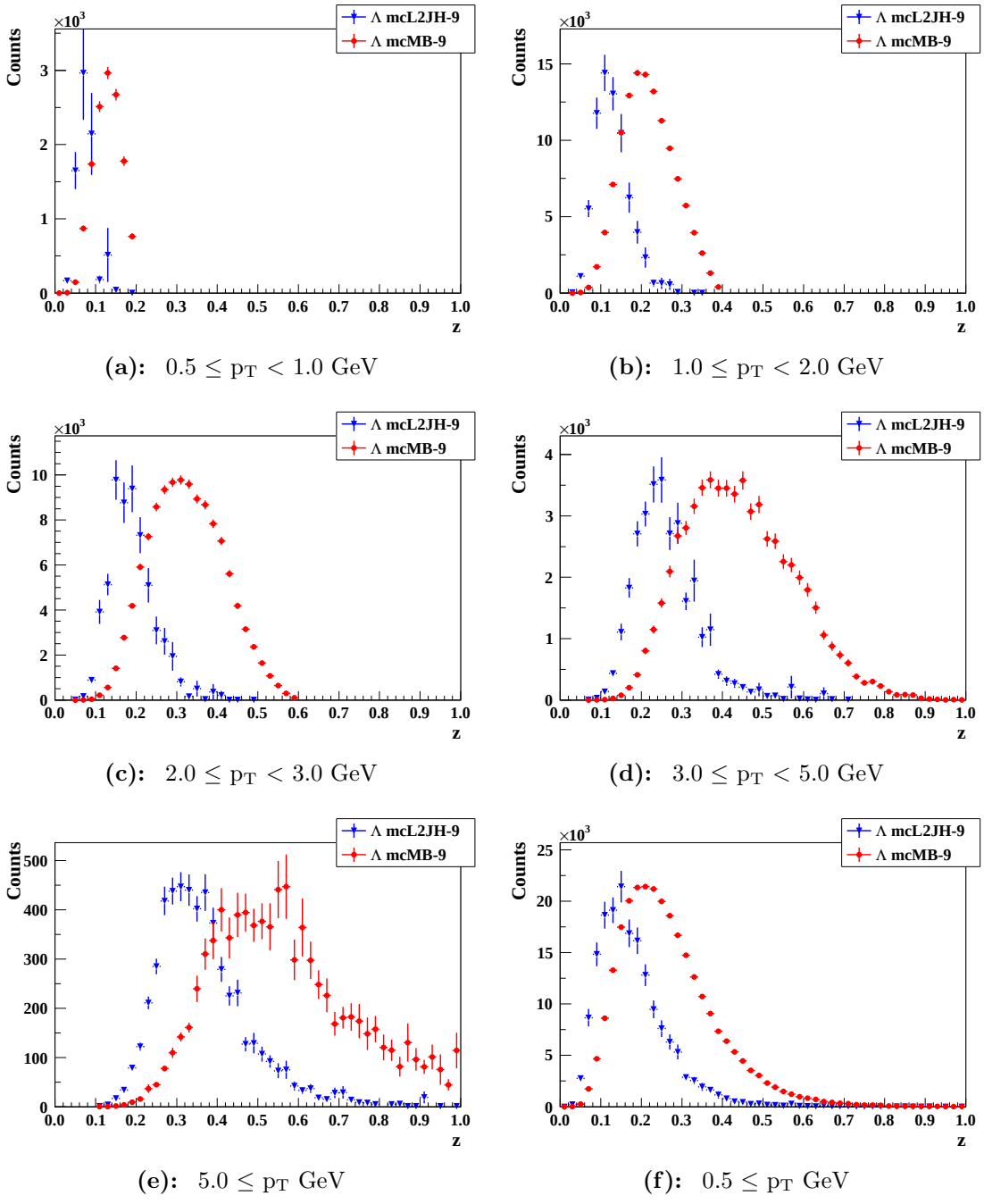

(a): $0.5 \leq p_T < 1.0$ GeV

(b): $1.0 \leq p_T < 2.0$ GeV

(c): $2.0 \leq p_T < 3.0$ GeV

(d): $3.0 \leq p_T < 5.0$ GeV

(e): $5.0 \leq p_T$ GeV

(f): $0.5 \leq p_T$ GeV

Figure 3.78: Comparison of raw z for Λs from mcMB–9 and mcL2JH–9 triggered events. mcL2JH–9 trigger imposes mcMB–9 trigger conditions plus additional triggered jet conditions. The mean z for mcMB–9 are higher for all Λ p_T intervals compared to mcL2JH–9 which is expected as the mcMB–9 triggered sample contains lower p_T jets, resulting in higher z values.

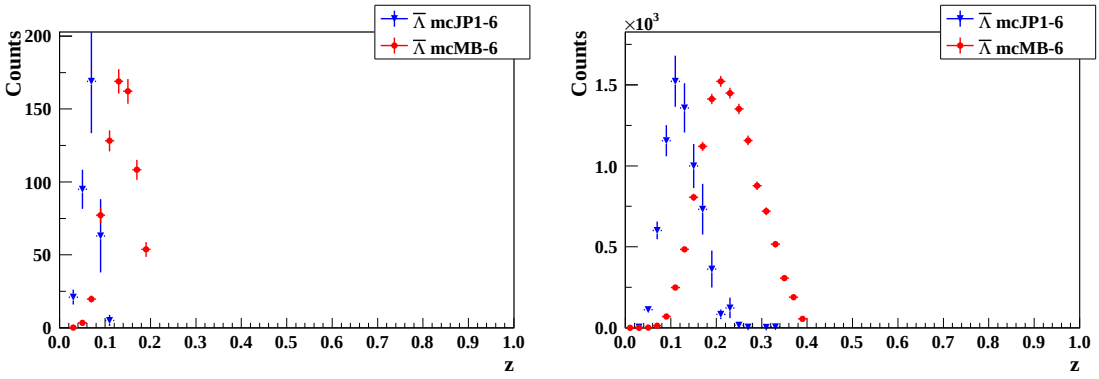

(a): $0.5 \leq p_T < 1.0$ GeV

(b): $1.0 \leq p_T < 2.0$ GeV

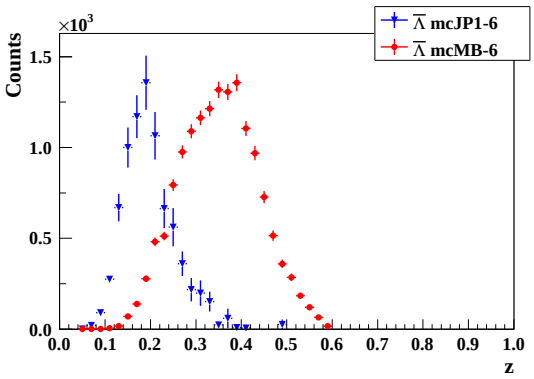

(c): $2.0 \leq p_T < 3.0$ GeV

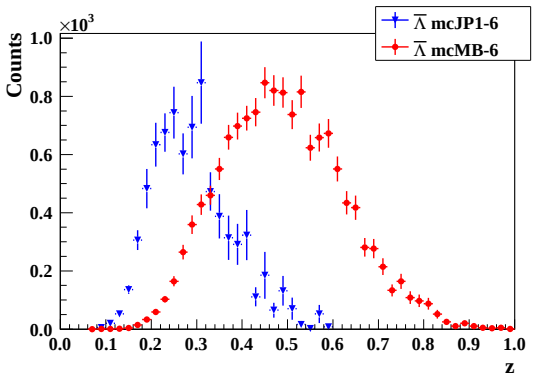

(d): $3.0 \leq p_T < 5.0$ GeV

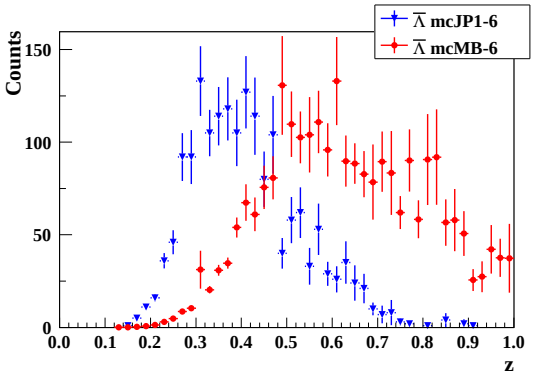

(e): $5.0 \leq p_T$ GeV

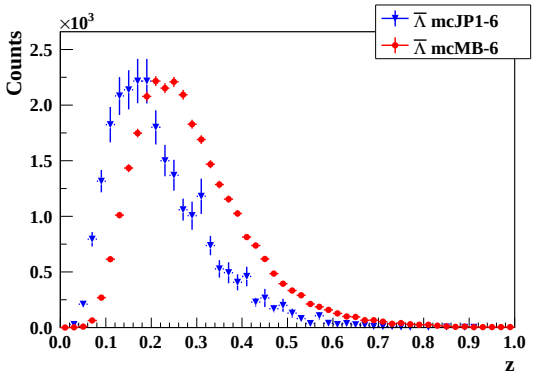

(f): $0.5 \leq p_T$ GeV

Figure 3.79: Comparison of z for $\overline{\Lambda}$s from mcMB–6 and mcJP1–6 triggered events. mcJP1–6 trigger imposes mcMB–6 trigger conditions plus additional triggered jet conditions. The mean z for mcMB–6 are higher for all $\overline{\Lambda}$ p_T intervals compared to JP1–6 which is expected as the mcMB–6 triggered sample contains lower p_T jets, resulting in higher z values.

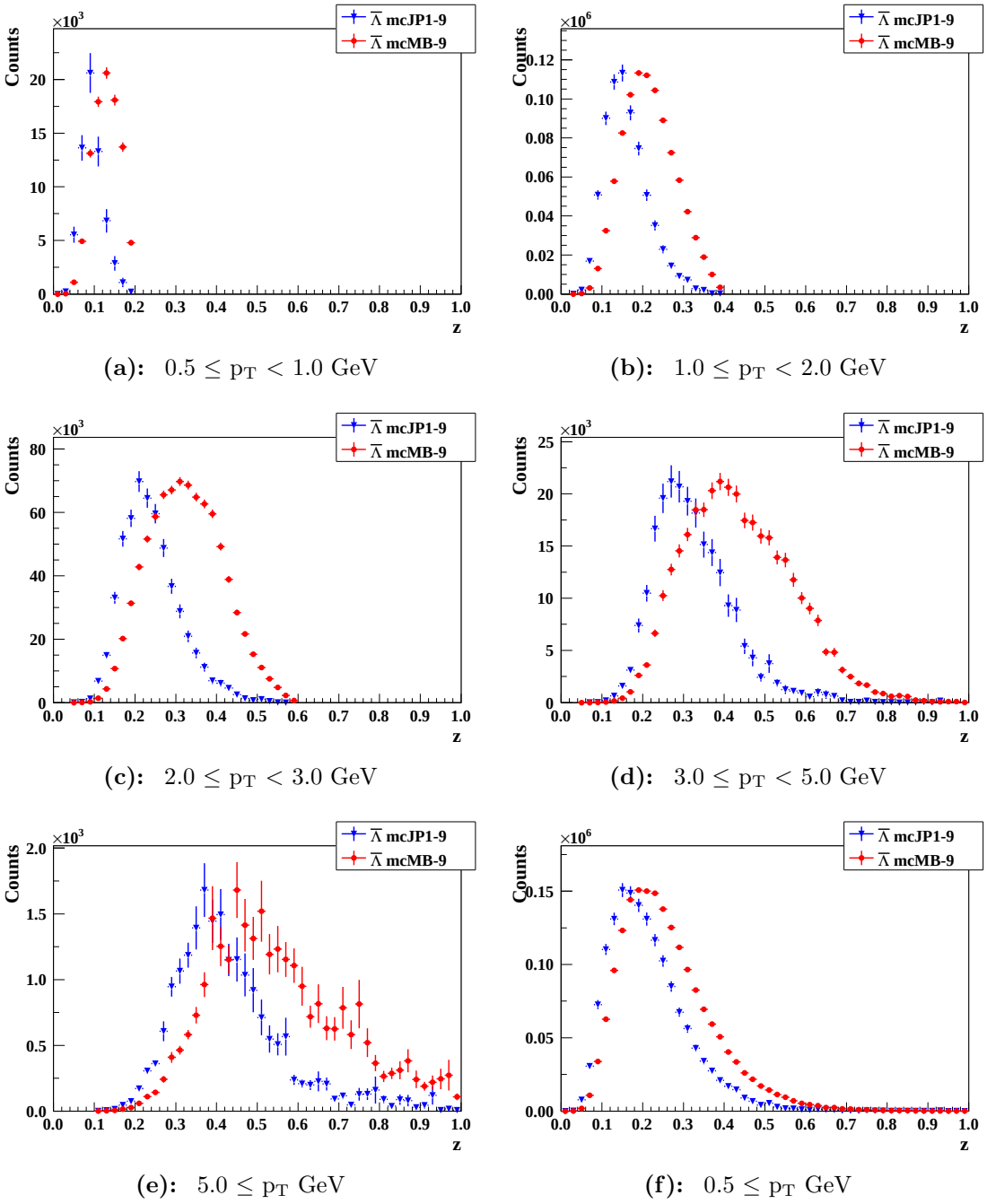

(a): $0.5 \leq p_T < 1.0$ GeV

(b): $1.0 \leq p_T < 2.0$ GeV

(c): $2.0 \leq p_T < 3.0$ GeV

(d): $3.0 \leq p_T < 5.0$ GeV

(e): $5.0 \leq p_T$ GeV

(f): $0.5 \leq p_T$ GeV

Figure 3.80: Comparison of z for $\overline{\Lambda}$s from mcMB–9 and mcJP1–9 triggered events. mcJP1–9 trigger imposes mcMB–9 trigger conditions plus additional triggered jet conditions. The mean z for mcMB–9 are higher for all $\overline{\Lambda}$ p_T intervals compared to JP1–9 which is expected as the mcMB–9 triggered sample contains lower p_T jets, resulting in higher z values.

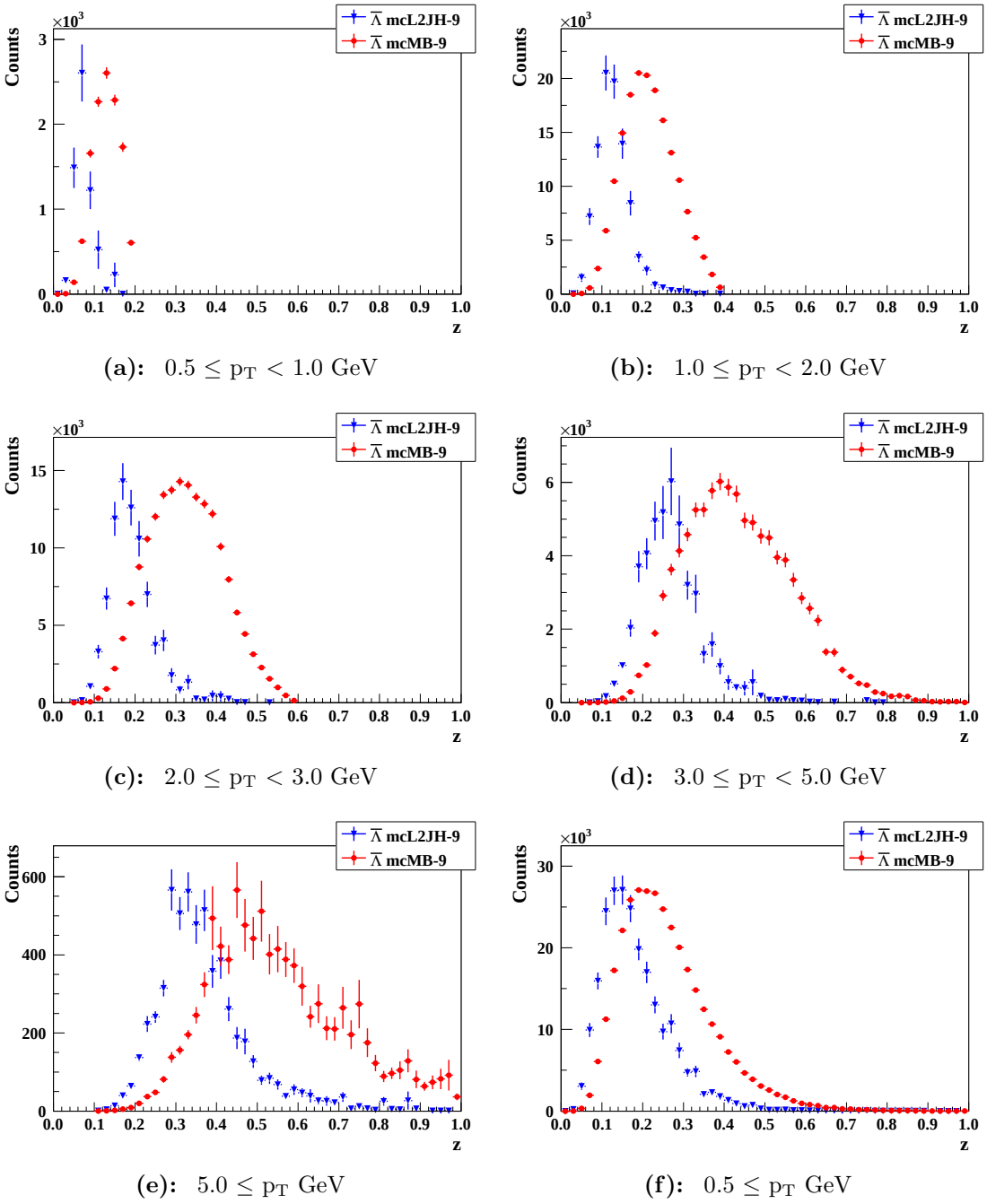

(a): $0.5 \leq p_T < 1.0$ GeV

(b): $1.0 \leq p_T < 2.0$ GeV

(c): $2.0 \leq p_T < 3.0$ GeV

(d): $3.0 \leq p_T < 5.0$ GeV

(e): $5.0 \leq p_T$ GeV

(f): $0.5 \leq p_T$ GeV

Figure 3.81: Comparison of z for $\overline{\Lambda}$s from mcMB–9 and mcL2JH–9 triggered events. mcL2JH–9 trigger imposes mcMB–9 trigger conditions plus additional triggered jet conditions. The mean z for mcMB–9 are higher for all $\overline{\Lambda}$ p_T intervals compared to L2JH–9 which is expected as the mcMB–9 triggered sample contains lower p_T jets, resulting in higher z values.

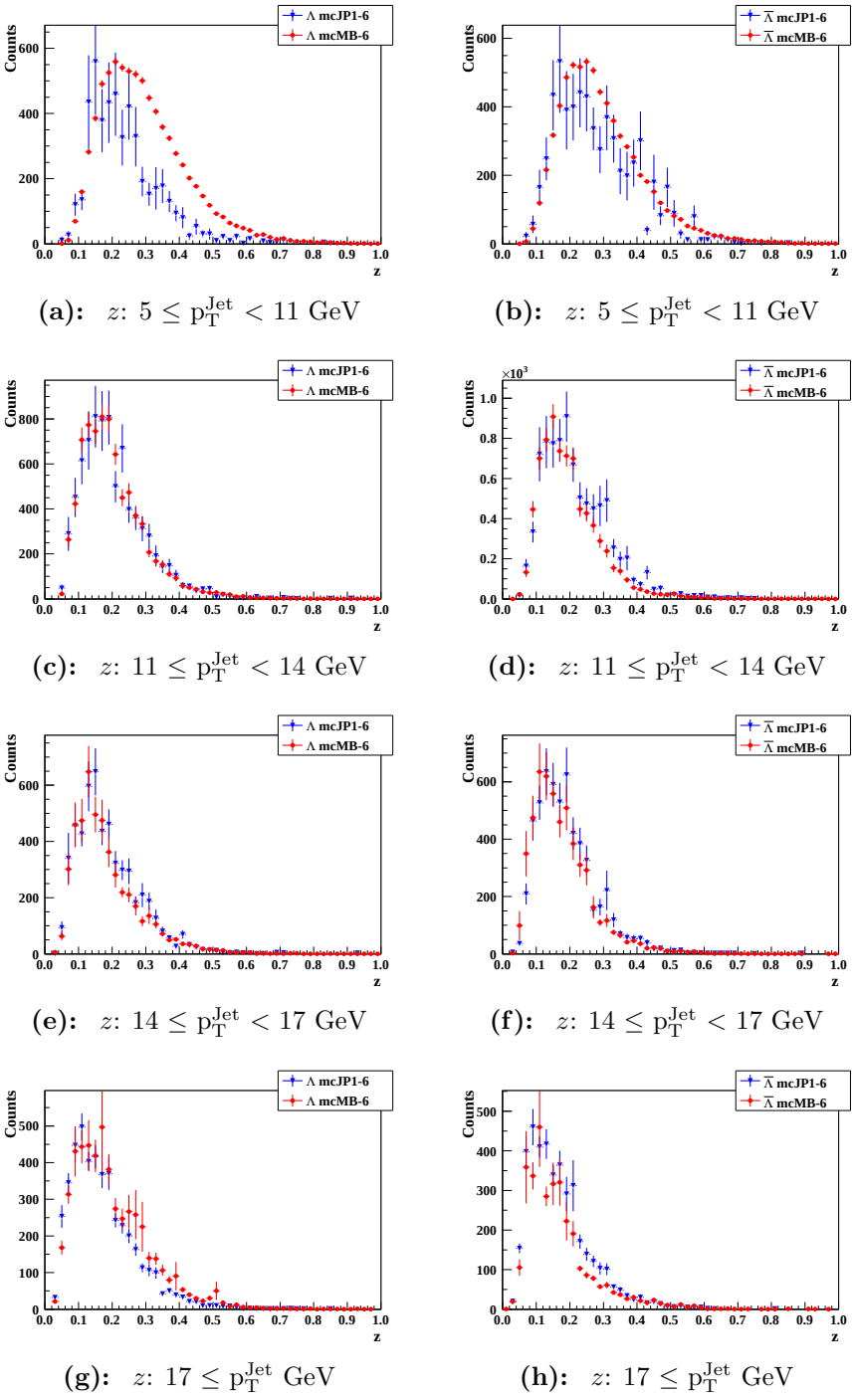

(a): z: $5 \leq p_T^{Jet} < 11$ GeV

(b): z: $5 \leq p_T^{Jet} < 11$ GeV

(c): z: $11 \leq p_T^{Jet} < 14$ GeV

(d): z: $11 \leq p_T^{Jet} < 14$ GeV

(e): z: $14 \leq p_T^{Jet} < 17$ GeV

(f): z: $14 \leq p_T^{Jet} < 17$ GeV

(g): z: $17 \leq p_T^{Jet}$ GeV

(h): z: $17 \leq p_T^{Jet}$ GeV

Figure 3.82: Comparison of z distribution for various p_T^{Jet} intervals between mcJP1–6 and mcMB–6 triggered events. The distributions are comparable for jets with $p_T^{Jet} > 11$ GeV. At lower p_T^{Jet}, mcJP1–6 contains less softer jets, shifting the z distribution to lower values with respect to mcMB–6 z distributions.

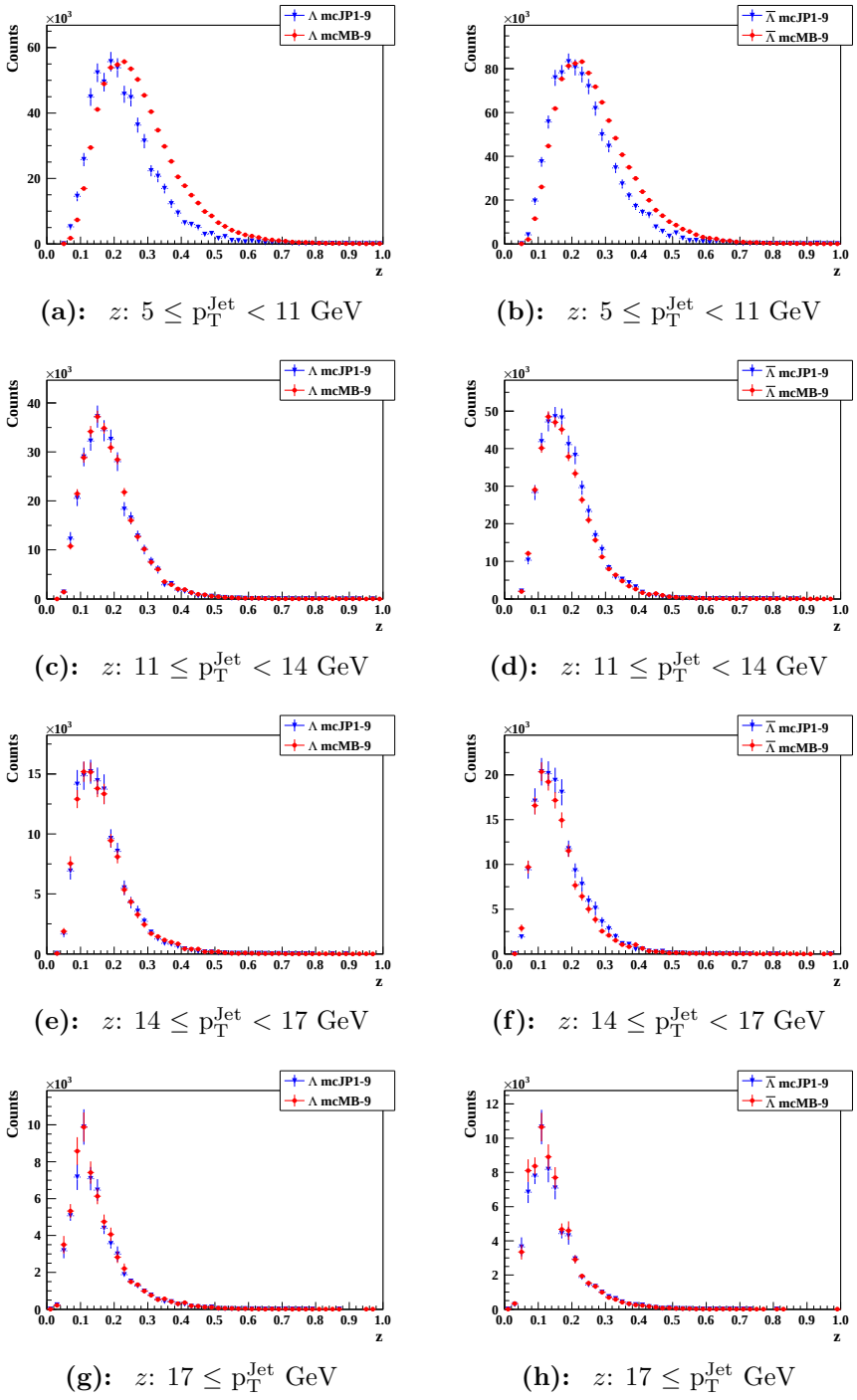

(a): z: $5 \leq p_T^{Jet} < 11$ GeV

(b): z: $5 \leq p_T^{Jet} < 11$ GeV

(c): z: $11 \leq p_T^{Jet} < 14$ GeV

(d): z: $11 \leq p_T^{Jet} < 14$ GeV

(e): z: $14 \leq p_T^{Jet} < 17$ GeV

(f): z: $14 \leq p_T^{Jet} < 17$ GeV

(g): z: $17 \leq p_T^{Jet}$ GeV

(h): z: $17 \leq p_T^{Jet}$ GeV

Figure 3.83: Comparison of z distribution for various p_T^{Jet} intervals between mcJP1–9 and mcMB–9 triggered events. The distributions are comparable for jets with $p_T^{Jet} > 11$ GeV. At lower p_T^{Jet}, mcJP1–9 contains less softer jets, shifting the z distribution to lower values with respect to mcMB–9 z distributions.

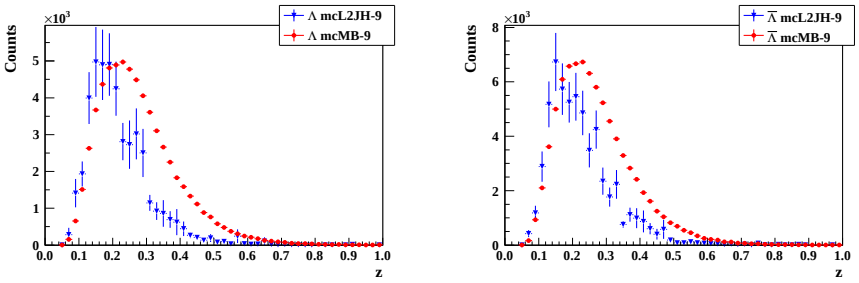

(a): z: $5 \leq p_T^{Jet} < 11$ GeV

(b): z: $5 \leq p_T^{Jet} < 11$ GeV

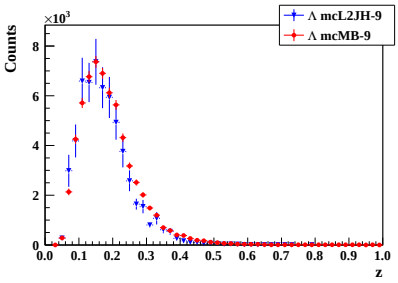

(c): z: $11 \leq p_T^{Jet} < 14$ GeV

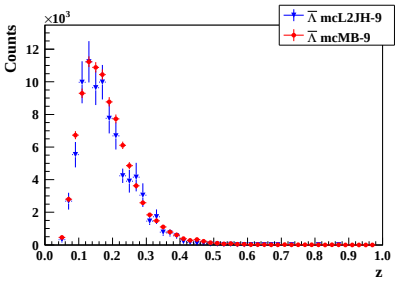

(d): z: $11 \leq p_T^{Jet} < 14$ GeV

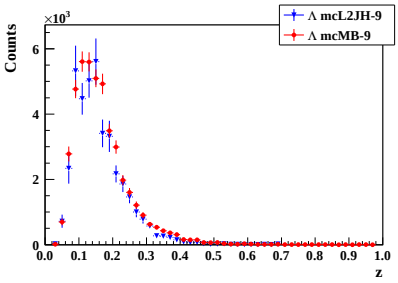

(e): z: $14 \leq p_T^{Jet} < 17$ GeV

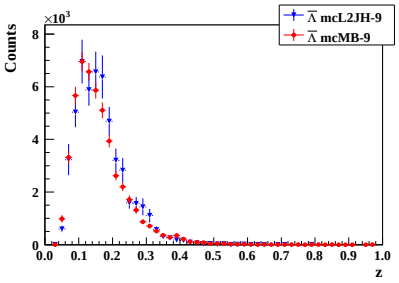

(f): z: $14 \leq p_T^{Jet} < 17$ GeV

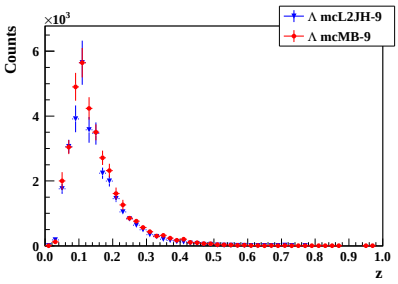

(g): z: $17 \leq p_T^{Jet}$ GeV

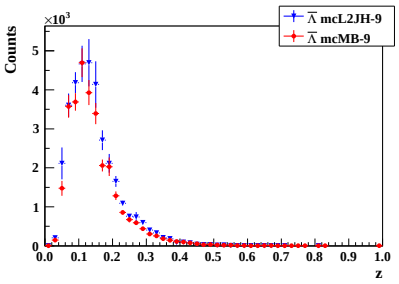

(h): z: $17 \leq p_T^{Jet}$ GeV

Figure 3.84: Comparison of z distribution for various p_T^{Jet} intervals between mcL2JH–9 and mcMB–9 triggered events. The distributions are comparable for jets with $p_T^{Jet} > 11$ GeV. At lower p_T^{Jet}, mcL2JH–9 contains less softer jets, shifting the z distribution to lower values with respect to mcMB–9 z distributions.

		Λ	
$\Lambda(\overline{\Lambda})$ p_T GeV	z (mcMB–6)	z (mcJP1–6)	Diff. Ratio
$0.5 \leq p_T < 1.0$	0.13	0.07	0.47
$1.0 \leq p_T < 2.0$	0.23	0.12	0.46
$2.0 \leq p_T < 3.0$	0.35	0.19	0.46
$3.0 \leq p_T < 5.0$	0.48	0.27	0.44
$5.0 \leq p_T$	0.61	0.39	0.36
$0.5 \leq p_T$	0.29	0.20	0.30
		$\overline{\Lambda}$	
$0.5 \leq p_T < 1.0$	0.14	0.07	0.51
$1.0 \leq p_T < 2.0$	0.23	0.13	0.45
$2.0 \leq p_T < 3.0$	0.35	0.20	0.44
$3.0 \leq p_T < 5.0$	0.49	0.29	0.40
$5.0 \leq p_T$	0.63	0.41	0.35
$0.5 \leq p_T$	0.29	0.22	0.24

Table 3.31: Central z values for mcMB–6 and mcJP1–6 triggered events. Fractional difference of z values from mcJP1–6 with respect to mcMB–6 are shown on the last column.

		Λ	
$\Lambda(\overline{\Lambda})$ p_T GeV	z (mcMB–9)	z (mcJP1–9)	Diff. Ratio
$0.5 \leq p_T < 1.0$	0.13	0.09	0.29
$1.0 \leq p_T < 2.0$	0.22	0.16	0.28
$2.0 \leq p_T < 3.0$	0.33	0.23	0.29
$3.0 \leq p_T < 5.0$	0.44	0.32	0.29
$5.0 \leq p_T$	0.56	0.43	0.25
$0.5 \leq p_T$	0.27	0.21	0.23
		$\overline{\Lambda}$	
$0.5 \leq p_T < 1.0$	0.13	0.09	0.27
$1.0 \leq p_T < 2.0$	0.22	0.16	0.25
$2.0 \leq p_T < 3.0$	0.32	0.24	0.26
$3.0 \leq p_T < 5.0$	0.44	0.33	0.26
$5.0 \leq p_T$	0.55	0.43	0.22
$0.5 \leq p_T$	0.26	0.21	0.18

Table 3.32: Central z values for mcMB–9 and mcJP1–9 triggered events. Fractional difference of z values from mcJP1–9 with respect to mcMB–9 are shown on the last column.

		Λ	
$\Lambda(\overline{\Lambda})$ p_T GeV	z (mcMB–9)	z (mcL2JH–9)	Diff. Ratio
$0.5 \leq p_T < 1.0$	0.13	0.08	0.41
$1.0 \leq p_T < 2.0$	0.22	0.13	0.41
$2.0 \leq p_T < 3.0$	0.33	0.19	0.42
$3.0 \leq p_T < 5.0$	0.44	0.26	0.40
$5.0 \leq p_T$	0.56	0.37	0.35
$0.5 \leq p_T$	0.27	0.18	0.33
		$\overline{\Lambda}$	
$0.5 \leq p_T < 1.0$	0.13	0.07	0.42
$1.0 \leq p_T < 2.0$	0.22	0.13	0.41
$2.0 \leq p_T < 3.0$	0.32	0.19	0.41
$3.0 \leq p_T < 5.0$	0.44	0.27	0.38
$5.0 \leq p_T$	0.55	0.37	0.33
$0.5 \leq p_T$	0.26	0.18	0.30

Table 3.33: Central z values for mcMB–9 and mcL2JH–9 triggered events. Fractional difference of z values from mcL2JH–9 with respect to mcMB–9 are shown on the last column.

		Λ	
p_T^{Jet} GeV	z (mcMB–6)	z (mcJP1–6)	Diff. Ratio
$5.0 \leq p_T^{Jet} < 11.0$	0.29	0.24	0.20
$11.0 \leq p_T^{Jet} < 14.0$	0.20	0.20	−0.00
$14.0 \leq p_T^{Jet} < 17.0$	0.18	0.19	−0.02
$17.0 \leq p_T^{Jet}$	0.20	0.17	0.13
		$\overline{\Lambda}$	
$5.0 \leq p_T^{Jet} < 11.0$	0.30	0.28	0.05
$11.0 \leq p_T^{Jet} < 14.0$	0.20	0.22	−0.09
$14.0 \leq p_T^{Jet} < 17.0$	0.18	0.19	−0.07
$17.0 \leq p_T^{Jet}$	0.17	0.17	−0.01

Table 3.34: Central z values of mcMB–6 and mcJP1–6 triggered events at different p_T^{Jet} intervals. Fractional difference of z values between the two triggers are shown.

		Λ	
p_T^{Jet} GeV	z (mcMB–9)	z (mcJP1–9)	Diff. Ratio
$5.0 \leq p_T^{Jet} < 11.0$	0.28	0.23	0.16
$11.0 \leq p_T^{Jet} < 14.0$	0.19	0.19	0.01
$14.0 \leq p_T^{Jet} < 17.0$	0.17	0.17	0.01
$17.0 \leq p_T^{Jet}$	0.15	0.15	0.00
		$\overline{\Lambda}$	
$5.0 \leq p_T^{Jet} < 11.0$	0.27	0.24	0.11
$11.0 \leq p_T^{Jet} < 14.0$	0.18	0.19	−0.01
$14.0 \leq p_T^{Jet} < 17.0$	0.16	0.17	−0.02
$17.0 \leq p_T^{Jet}$	0.14	0.15	−0.00

Table 3.35: Central z values of mcMB–9 and mcJP1–9 triggered events at different p_T^{Jet} intervals. Fractional difference of z values between the two triggers are shown.

		Λ	
p_T^{Jet} GeV	z (mcMB–9)	z (mcL2JH–9)	Diff. Ratio
$5.0 \leq p_T^{Jet} < 11.0$	0.28	0.22	0.17
$11.0 \leq p_T^{Jet} < 14.0$	0.19	0.18	0.02
$14.0 \leq p_T^{Jet} < 17.0$	0.17	0.16	−0.03
$17.0 \leq p_T^{Jet}$	0.15	0.15	−0.01
		$\overline{\Lambda}$	
$5.0 \leq p_T^{Jet} < 11.0$	0.27	0.22	0.05
$11.0 \leq p_T^{Jet} < 14.0$	0.18	0.18	−0.10
$14.0 \leq p_T^{Jet} < 17.0$	0.16	0.17	−0.07
$17.0 \leq p_T^{Jet}$	0.14	0.15	−0.01

Table 3.36: Central z values of mcMB–9 and mcL2JH–9 triggered events at different p_T^{Jet} intervals. Fractional difference of z values between the two triggers are shown.

The relative contributions for flavor-separated sub-processes contributing to hard scattering collision can be extracted for the minimum bias and jet triggered samples. Figures 3.85–3.90 show the sub-process contributions at various $\Lambda(\overline{\Lambda})$ p_T intervals. The sub-process $q + g \rightarrow q + g$ is the dominant contribution for both mcJP1–6 and mcMB–6 triggers. A larger contribution of $g + g \rightarrow g + g$ is seen for the minimum bias triggered simulated samples. This is expected as $q + q \rightarrow q + q$ and $q + g \rightarrow q + g$ sub-processes are enhanced when the high jet p_T requirement for the jet triggered samples is imposed.

The relative contribution for different partons were also extracted for the minimum bias and jet triggered samples. The simulated sample includes initial and final state radiation. Partons coming from initial and final state radiation, initial and final partons from the proton collisions are considered. Figures 3.91–3.96 show the parton contributions at various $\Lambda(\overline{\Lambda})$ p_T intervals for both run years. The gluon contribution is dominant for $4.0 < p_T$ GeV $\Lambda(\overline{\Lambda})$s in the minimum bias sample. There is a higher strange quark contribution in the minimum bias triggered samples for higher p_T compared to jet triggered samples.

The production of $\Lambda(\overline{\Lambda})$ particles originates from hard scattering collisions and feed-down decays from heavier hyperons. The principal feed-down decay modes to $\Lambda(\overline{\Lambda})$ come from Σ^0, $\Sigma^{*0,+,-}$, and $\Xi^{0,+,-}$ decays. Contributions from feed-down $\Lambda(\overline{\Lambda})$ can dilute the extracted D_{LL} measurement [Bor00]. The relative $\Lambda(\overline{\Lambda})$ production contribution are shown in Figures 3.97–3.99 for both minimum bias and jet triggered sets. Direct $\Lambda(\overline{\Lambda})$ production increases for higher p_T $\Lambda(\overline{\Lambda})$s in the minimum bias sample while direct $\Lambda(\overline{\Lambda})$ production is constant for the jet triggered sample.

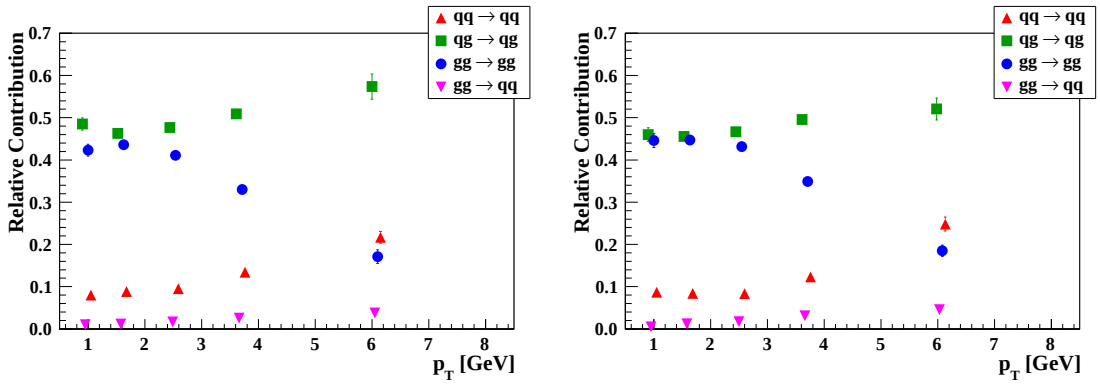

(a): mcMB–6: Λ Near-Side

(b): mcMB–6: $\overline{\Lambda}$ Near-Side

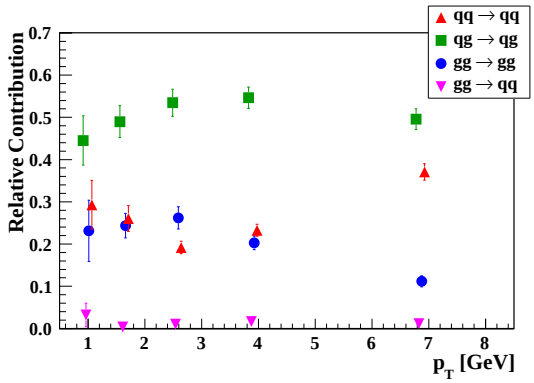

(c): mcJP1–6: Λ Near-Side

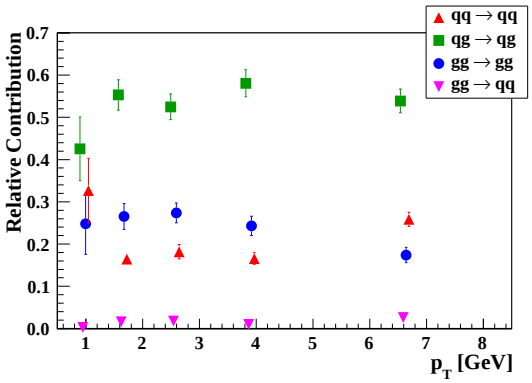

(d): mcJP1–6: $\overline{\Lambda}$ Near-Side

Figure 3.85: Comparison of collision sub-processes at various $\Lambda(\overline{\Lambda})$ p_T intervals between near-side mcMB–6 and mcJP1–6 triggered events.

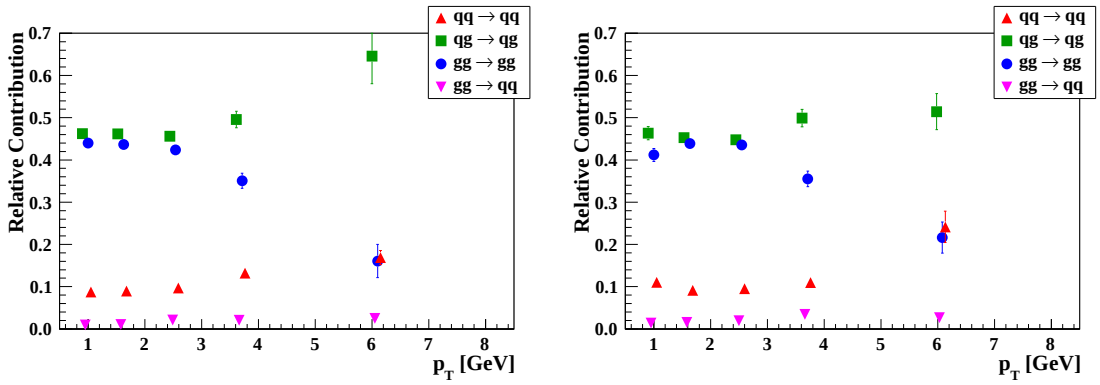

(a): mcMB–6: Λ Away-Side

(b): mcMB–6: $\overline{\Lambda}$ Away-Side

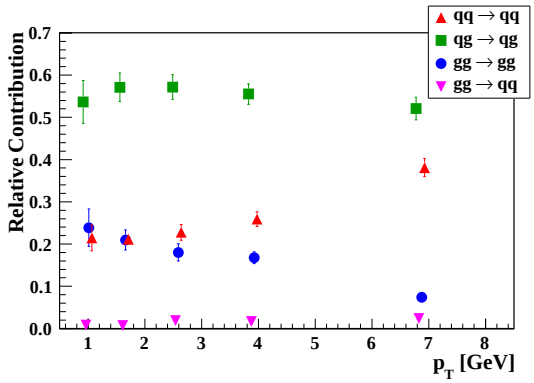

(c): mcJP1–6: Λ Away-Side

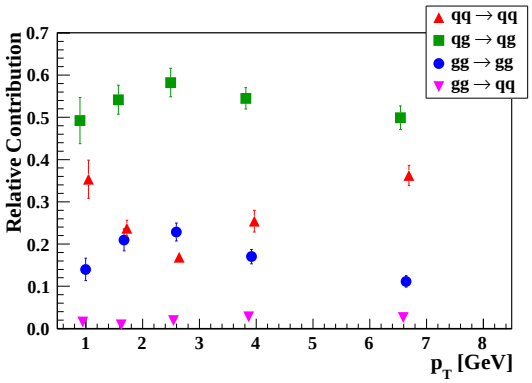

(d): mcJP1–6: $\overline{\Lambda}$ Away-Side

Figure 3.86: Comparison of collision sub-processes at various $\Lambda(\overline{\Lambda})$ p_T intervals between away-side mcMB–6 and mcJP1–6 triggered events.

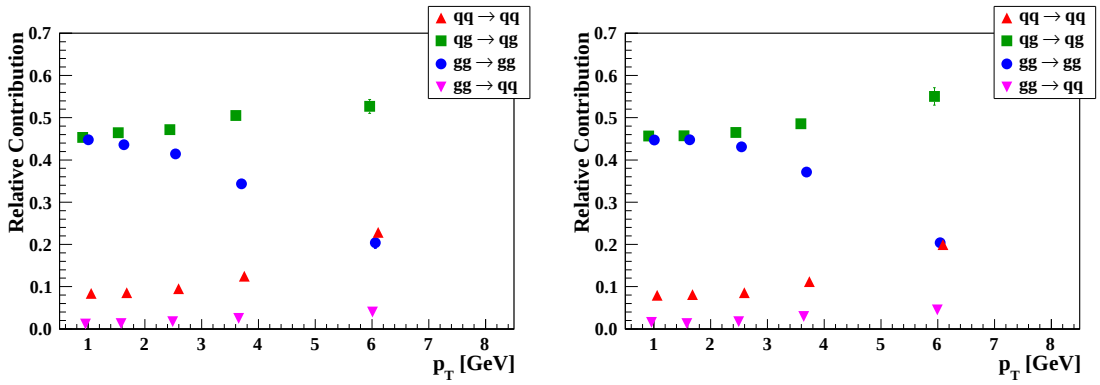

(a): mcMB–9: Λ Near-Side

(b): mcMB–9: $\overline{\Lambda}$ Near-Side

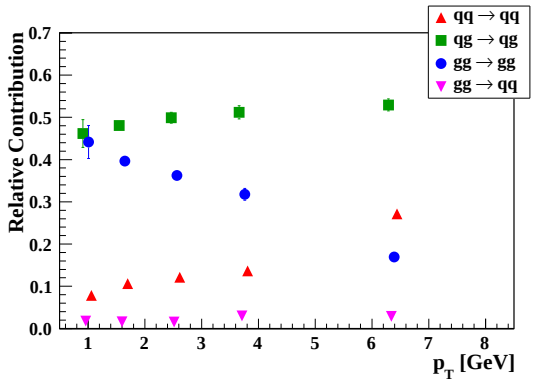

(c): mcJP1–9: Λ Near-Side

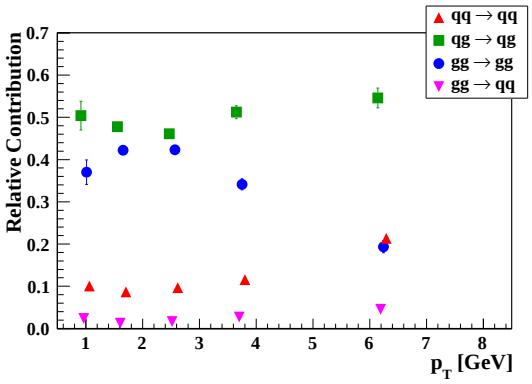

(d): mcJP1–9: $\overline{\Lambda}$ Near-Side

Figure 3.87: Comparison of collision sub-processes at various $\Lambda(\overline{\Lambda})$ p_T intervals between near-side mcMB–9 and mcJP1–9 triggered events.

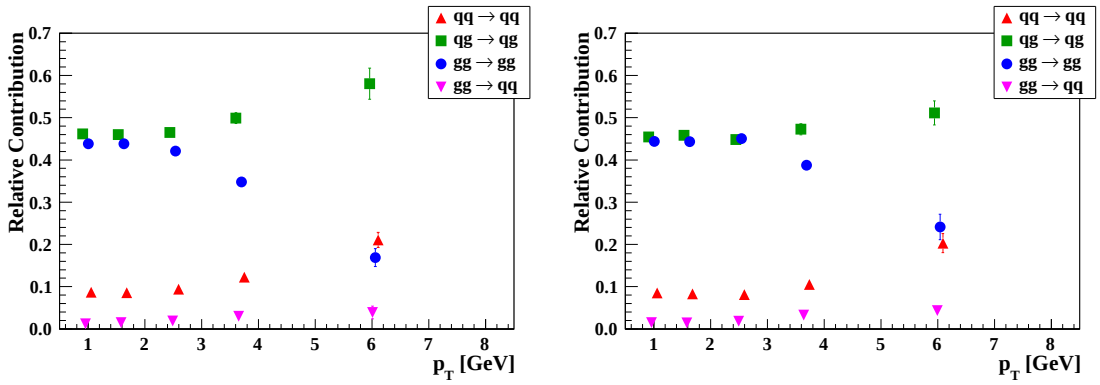

(a): mcMB–9: Λ Away-Side

(b): mcMB–9: $\overline{\Lambda}$ Away-Side

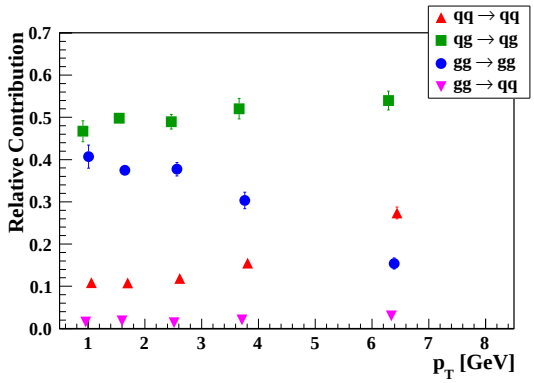

(c): mcJP1–9: Λ Away-Side

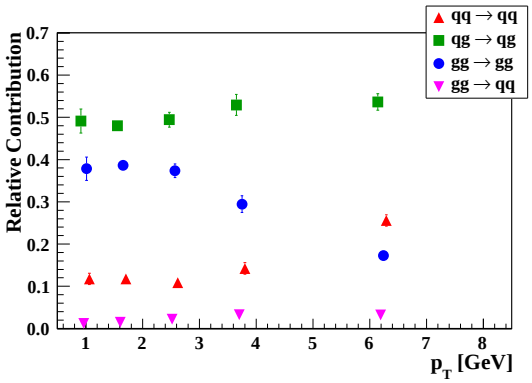

(d): mcJP1–9: $\overline{\Lambda}$ Away-Side

Figure 3.88: Comparison of collision sub-processes at various $\Lambda(\overline{\Lambda})$ p_T intervals between away-side mcMB–9 and mcJP1–9 triggered events.

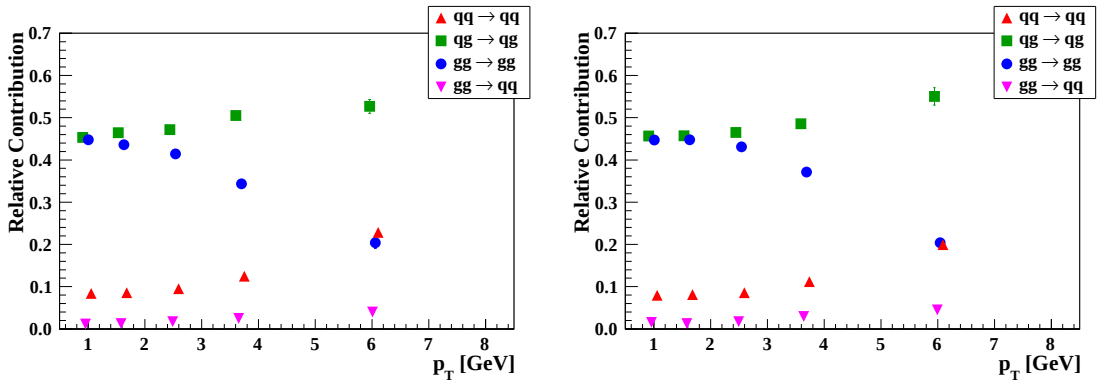

(a): mcMB–9: Λ Near-Side

(b): mcMB–9: $\overline{\Lambda}$ Near-Side

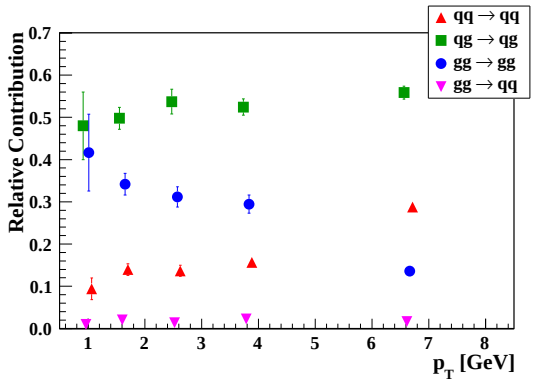

(c): mcL2JH–9: Λ Near-Side

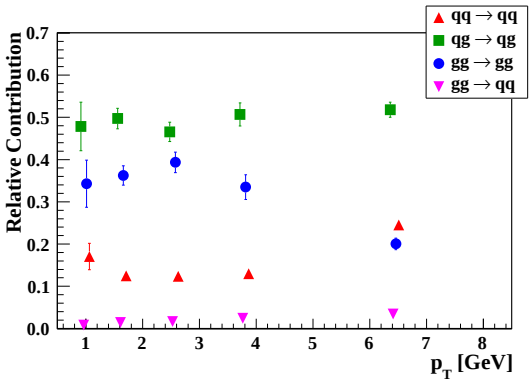

(d): mcL2JH–9: $\overline{\Lambda}$ Near-Side

Figure 3.89: Comparison of collision sub-processes at various $\Lambda(\overline{\Lambda})$ p_T intervals between near-side mcMB–9 and mcL2JH–9 triggered events.

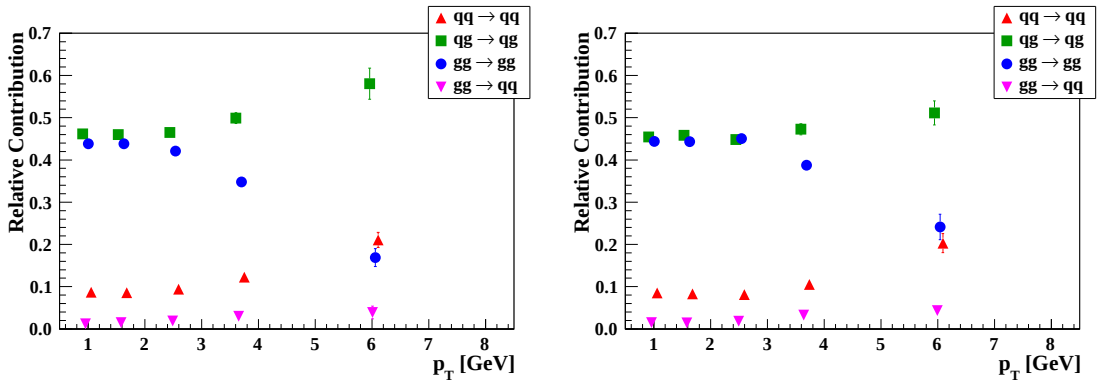

(a): mcMB–9: Λ Away-Side

(b): mcMB–9: $\overline{\Lambda}$ Away-Side

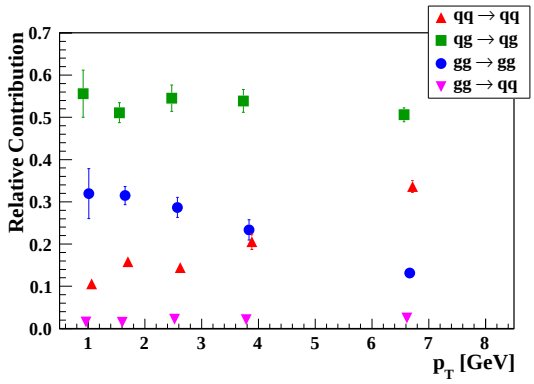

(c): mcL2JH–9: Λ Away-Side

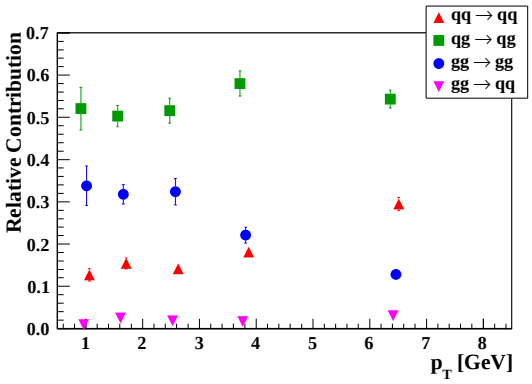

(d): mcL2JH–9: $\overline{\Lambda}$ Away-Side

Figure 3.90: Comparison of collision sub-processes at various $\Lambda(\overline{\Lambda})$ p_T intervals between away-side mcMB–9 and mcL2JH–9 triggered events.

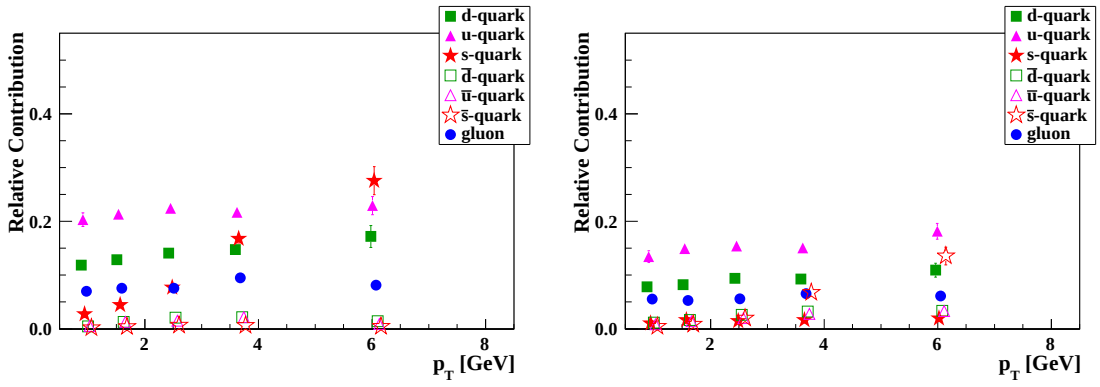

(a): mcMB–6: Λ Near-Side

(b): mcMB–6: $\overline{\Lambda}$ Near-Side

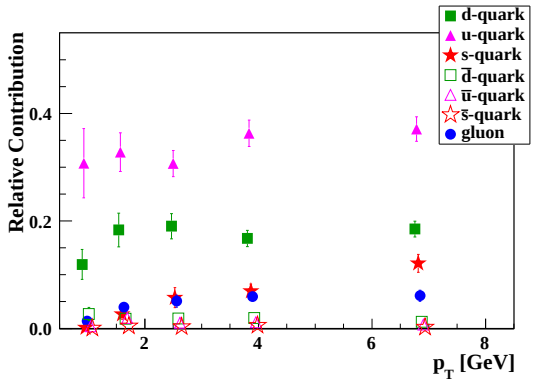

(c): mcJP1–6: Λ Near-Side

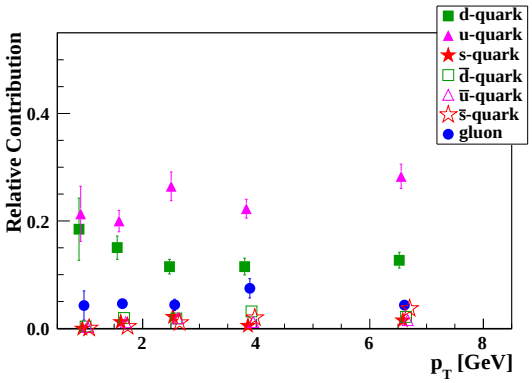

(d): mcJP1–6: $\overline{\Lambda}$ Near-Side

Figure 3.91: Comparison of outgoing parton at various $\Lambda(\overline{\Lambda})$ p_T intervals between near-side mcMB–6 and mcJP1–6 triggered events.

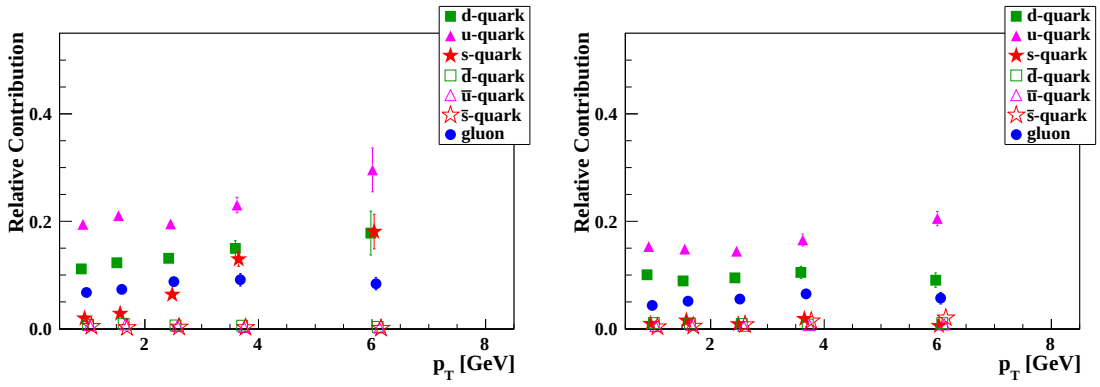

(a): mcMB–6: Λ Away-Side

(b): mcMB–6: $\overline{\Lambda}$ Away-Side

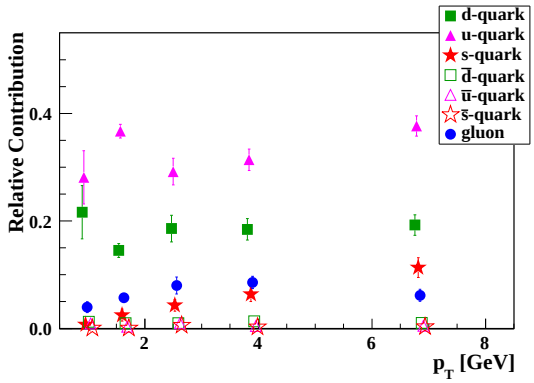

(c): mcJP1–6: Λ Away-Side

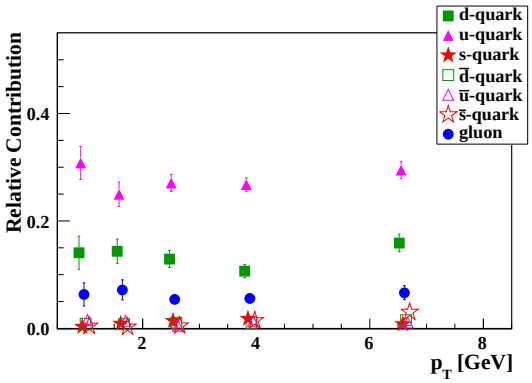

(d): mcJP1–6: $\overline{\Lambda}$ Away-Side

Figure 3.92: Comparison of outgoing parton at various $\Lambda(\overline{\Lambda})$ p_T intervals between away-side mcMB–6 and mcJP1–6 triggered events.

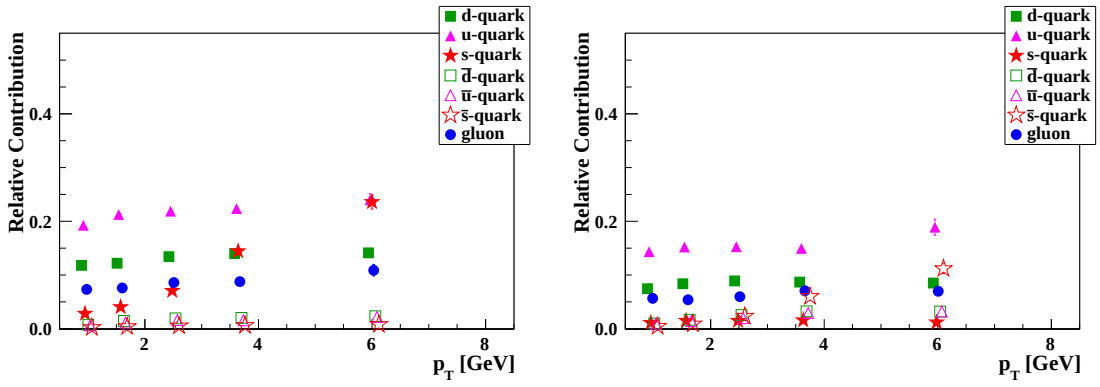

(a): mcMB–9: Λ Near-Side

(b): mcMB–9: $\overline{\Lambda}$ Near-Side

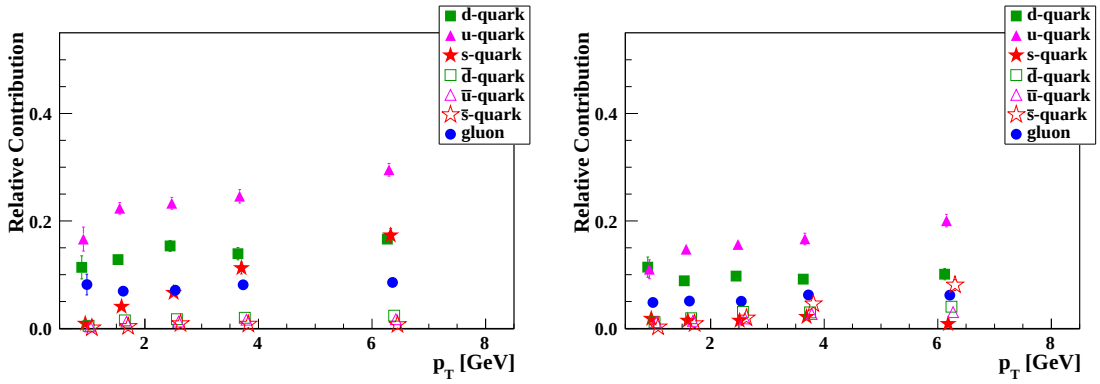

(c): mcJP1–9: Λ Near-Side

(d): mcJP1–9: $\overline{\Lambda}$ Near-Side

Figure 3.93: Comparison of outgoing parton at various $\Lambda(\overline{\Lambda})$ p_T intervals between near-side mcMB–9 and mcJP1–9 triggered events.

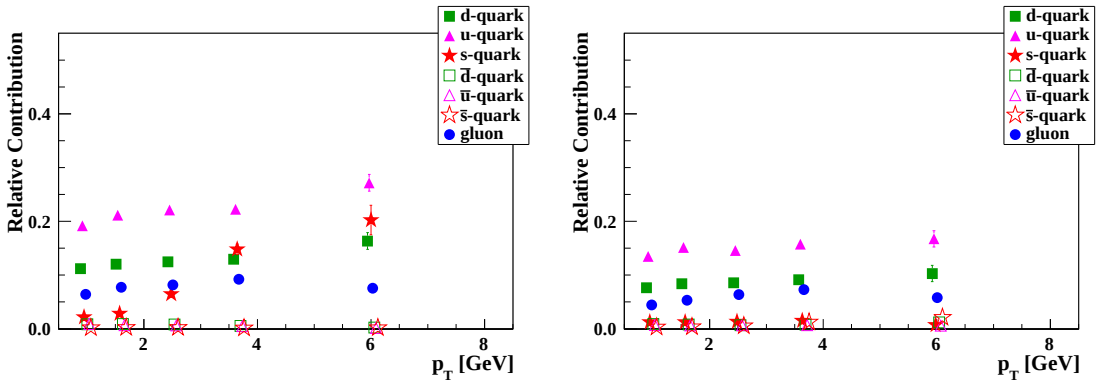

(a): mcMB–9: Λ Away-Side

(b): mcMB–9: $\overline{\Lambda}$ Away-Side

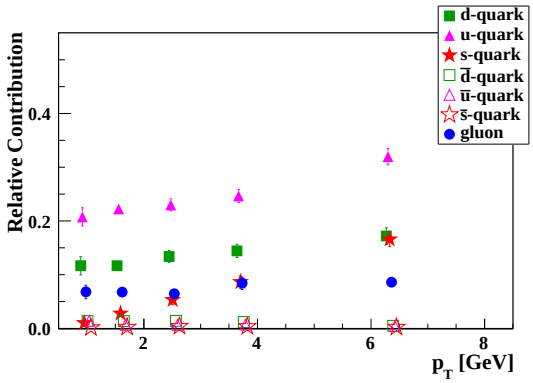

(c): mcJP1–9: Λ Away-Side

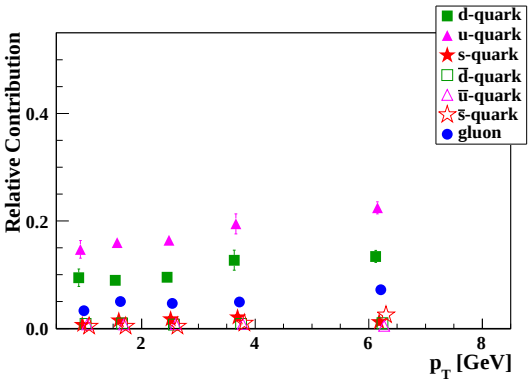

(d): mcJP1–9: $\overline{\Lambda}$ Away-Side

Figure 3.94: Comparison of outgoing parton at various $\Lambda(\overline{\Lambda})$ p_T intervals between away-side mcMB–9 and mcJP1–9 triggered events.

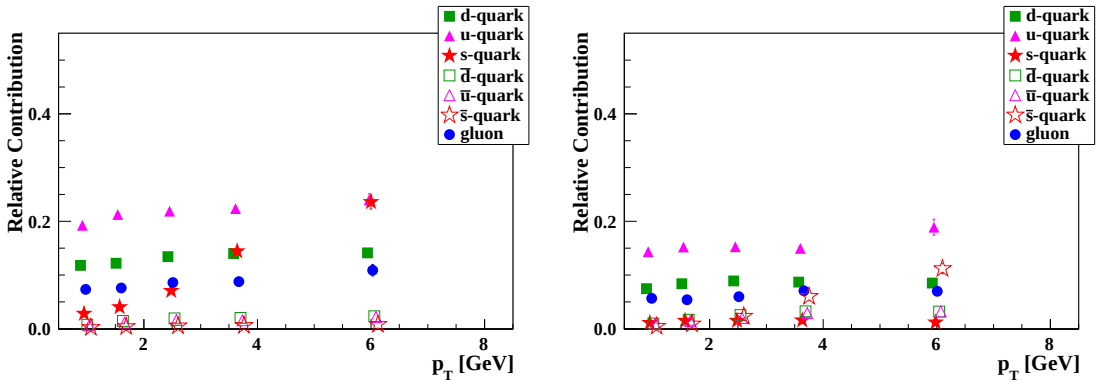

(a): mcMB–9: Λ Near-Side

(b): mcMB–9: $\overline{\Lambda}$ Near-Side

(c): mcL2JH–9: Λ Near-Side

(d): mcL2JH–9: $\overline{\Lambda}$ Near-Side

Figure 3.95: Comparison of outgoing parton at various $\Lambda(\overline{\Lambda})$ p_T intervals between near-side mcMB–9 and mcL2JH–9 triggered events.

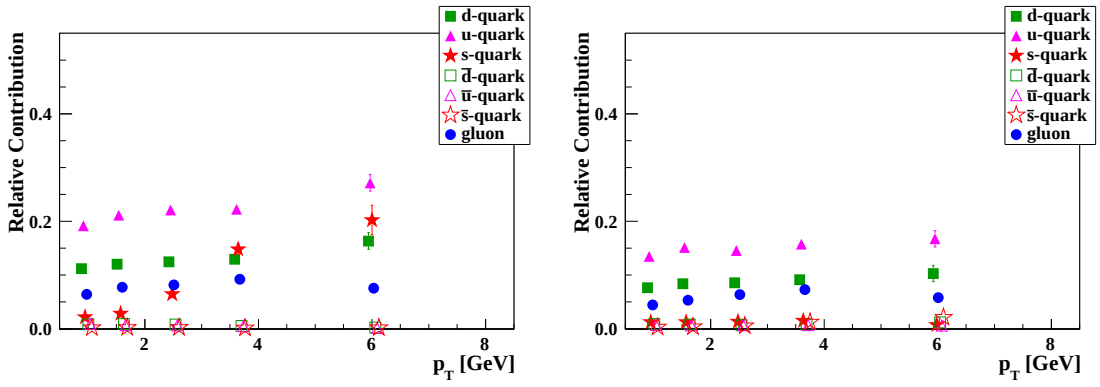

(a): mcMB–9: Λ Away-Side

(b): mcMB–9: $\overline{\Lambda}$ Away-Side

(c): mcL2JH–9: Λ Away-Side

(d): mcL2JH–9: $\overline{\Lambda}$ Away-Side

Figure 3.96: Comparison of outgoing parton at various $\Lambda(\overline{\Lambda})$ p_T intervals between away-side mcMB–9 and mcL2JH–9 triggered events.

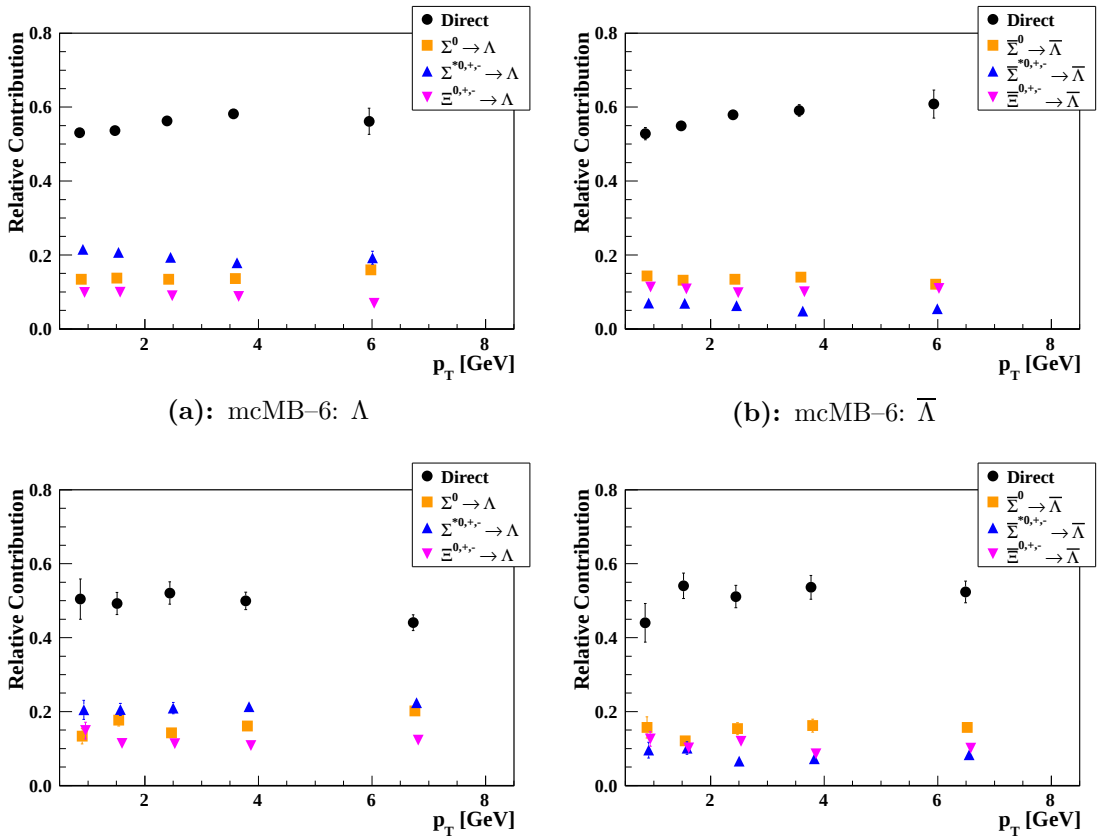

(a): mcMB–6: Λ

(b): mcMB–6: $\overline{\Lambda}$

(c): mcJP1–6: Λ

(d): mcJP1–6: $\overline{\Lambda}$

Figure 3.97: Comparison of feed-down contributions at various $\Lambda(\overline{\Lambda})$ p_T intervals between mcMB–6 and mcJP1–6 triggered events.

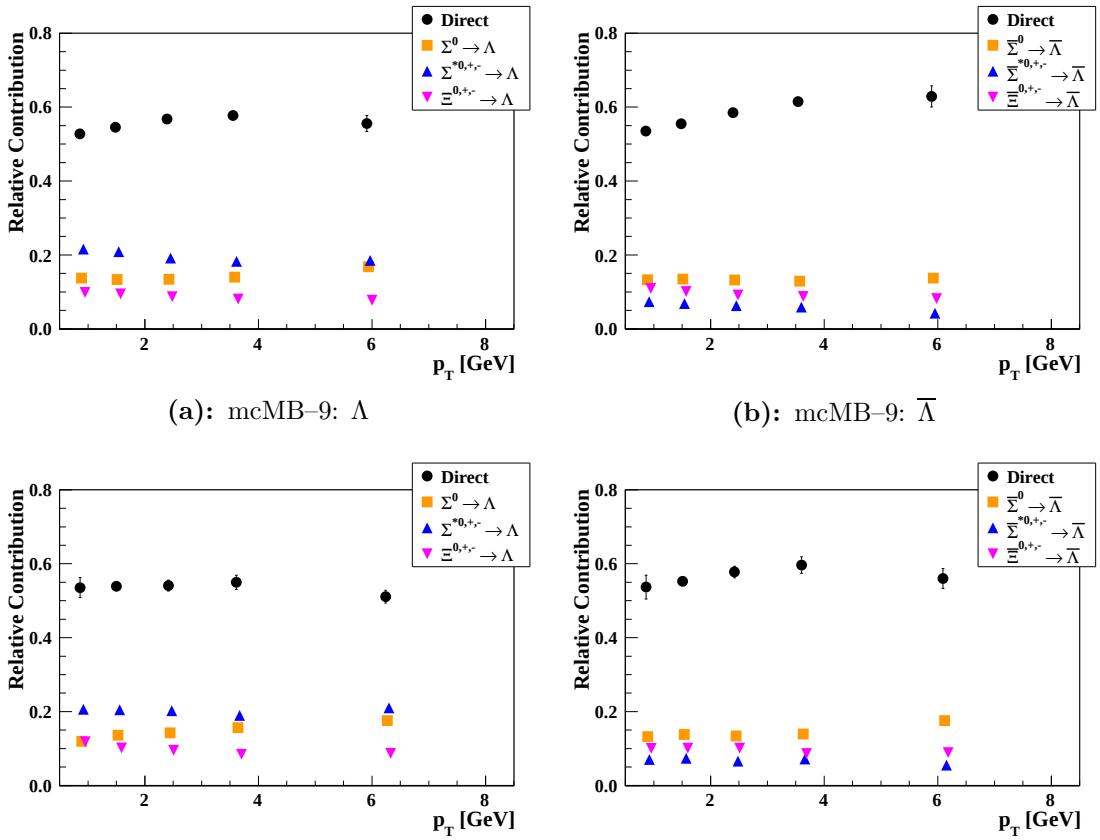

(a): mcMB–9: Λ **(b):** mcMB–9: $\overline{\Lambda}$

(c): mcJP1–9: Λ **(d):** mcJP1–9: $\overline{\Lambda}$

Figure 3.98: Comparison of feed-down contributions at various $\Lambda(\overline{\Lambda})$ p_T intervals between mcMB–9 and mcJP1–9 triggered events.

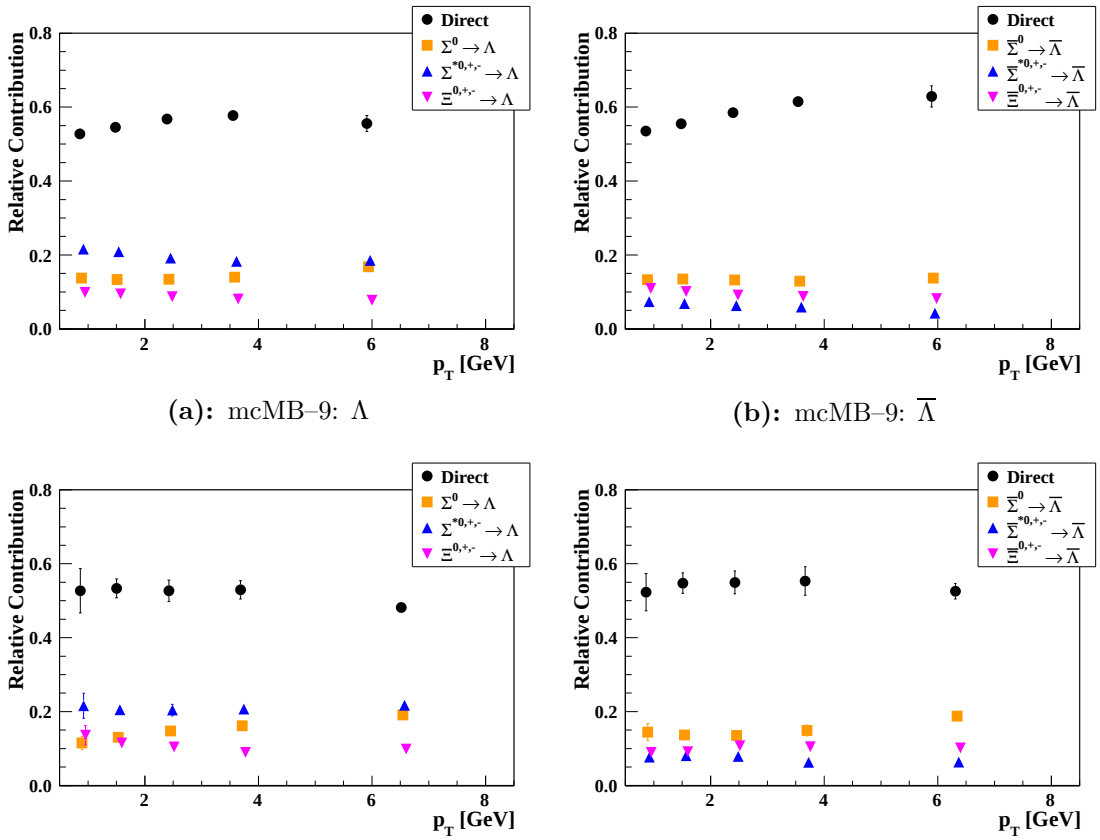

(a): mcMB–9: Λ

(b): mcMB–9: $\overline{\Lambda}$

(c): mcJP1–9: Λ

(d): mcJP1–9: $\overline{\Lambda}$

Figure 3.99: Comparison of feed-down contributions at various $\Lambda(\overline{\Lambda})$ p_T intervals between mcMB–9 and mcJP1–9 triggered events.

The systematic uncertainty from trigger bias is quantified by calculating the systematic contribution from the flavor-separated outgoing parton relative contributions and the shift in z. Changes to the ratio of the outgoing partons due to trigger conditions are calculated using the flavor-separated sub-process contributions. The fragmentation function is dependent on z. Studying the shift in z due to trigger conditions allow to calculate the systematic uncertainty from fragmentation.

The relative flavor-separated sub-process contributions are compared to the expected outgoing partons given by the different model scenarios from Ref. [Xu06]. For the SU(6) model scenario, the strange quark is the only contributor to the fragmentation while the DIS model scenario describes contributions from strange quarks and a negative contribution from the up and down quarks. The up and down quark ratios are expected to be in the order of -0.17 while 0.62 for the strange quark in the DIS model scenario [Bor98a]. The percentage difference between the sub-process partons from the minimum bias and jet triggers are utilized to determine the systematic uncertainty to the model scenario curve value. The model curves for SU(6) and DIS for GRSV2000 standard were used to determine the systematic uncertainty. The percentage difference between the relative sub-process contributions for the two triggers is used to determine the error within each model scenario as shown in Table 3.37.

The raw z values from the minimum bias and jet triggered samples at different p_T^{Jet} intervals are used to quantify the systematic effect from trigger bias to the extracted D_{LL} values. To determine the relative z shift, the data is separated into sectors of hyperon p_T vs. jet p_T. Figures 3.100–3.101 show the hyperon p_T vs. jet p_T scatter plots for the different minimum bias and jet triggers for both run years. The horizontal and vertical red lines define the edges of the sectors. Using

	$\delta D_{LL}^{\text{sys. sub-proc.}}$					
	JP1–6		JP1–9		L2JH–9	
	SU(6)	DIS	SU(6)	DIS	SU(6)	DIS
			Λ			
$0.5 \leq p_T < 1.0$	0.0007	0.0004	0.0005	0.0003	0.0004	0.0002
$1.0 \leq p_T < 2.0$	0.0006	0.0004	$<10^{-4}$	$<10^{-4}$	0.0004	0.0002
$2.0 \leq p_T < 3.0$	0.0007	0.0007	0.0002	0.0002	0.0004	0.0005
$3.0 \leq p_T < 5.0$	0.0038	0.0036	0.0015	0.0013	0.0031	0.0028
$5.0 \leq p_T$	0.0126	0.0118	0.0060	0.0056	0.0104	0.0097
			$\overline{\Lambda}$			
$0.5 \leq p_T < 1.0$	$<10^{-4}$	$<10^{-4}$	$<10^{-4}$	$<10^{-4}$	$<10^{-4}$	$<10^{-4}$
$1.0 \leq p_T < 2.0$	0.0008	0.0002	0.0010	0.0003	0.0009	0.0003
$2.0 \leq p_T < 3.0$	0.0017	0.0006	0.0025	0.0010	0.0028	0.0011
$3.0 \leq p_T < 5.0$	0.0066	0.0029	0.0065	0.0031	0.0078	0.0036
$5.0 \leq p_T$	0.0263	0.0114	0.0218	0.0104	0.0264	0.0123

Table 3.37: Flavor-separated sub-process systematic uncertainty contributions, $\delta D_{LL}^{\text{sys. sub-proc.}}$, for run year 2006 and 2009. The systematic uncertainties were calculated using the SU(6) and DIS model curves for GRSV2000 standard from Ref. [Xu06].

the relation,

$$p_T^{\Lambda} = z p_T^{Jet}, \tag{3.70}$$

a corresponding p_T^{Λ} value is calculated for each sector. The D_{LL} values from the DIS GRSV2000 standard model curve in Ref. [Xu06] are calculated for the mapped p_T^{Λ} values. The difference between the model D_{LL} values for the mapped p_T^{Λ} values are defined as the systematic uncertainty from the shift in z for the purposes of the analysis. The systematic uncertainty values for the sectors residing within each $\Lambda(\overline{\Lambda})$ p_T interval are summed in quadrature. Table 3.38 summarizes the systematic contributions $\delta D_{LL}^{\text{sys. z-shift.}}$.

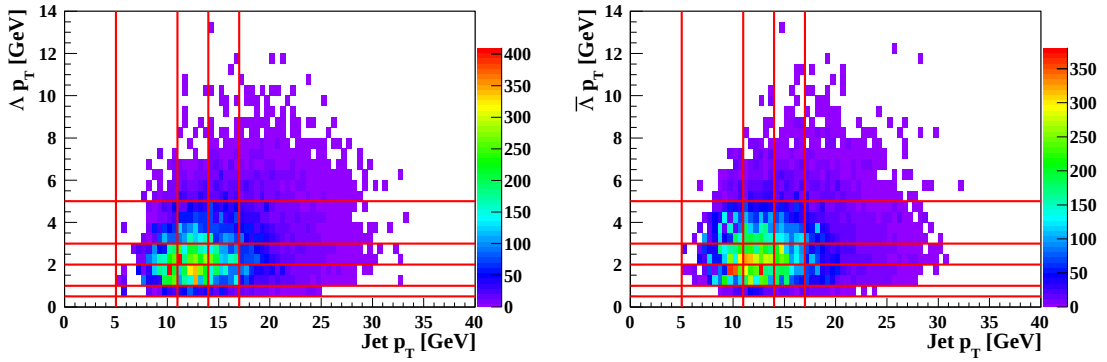

(a): mcJP1–6: Λ **(b):** mcJP1–6: $\overline{\Lambda}$

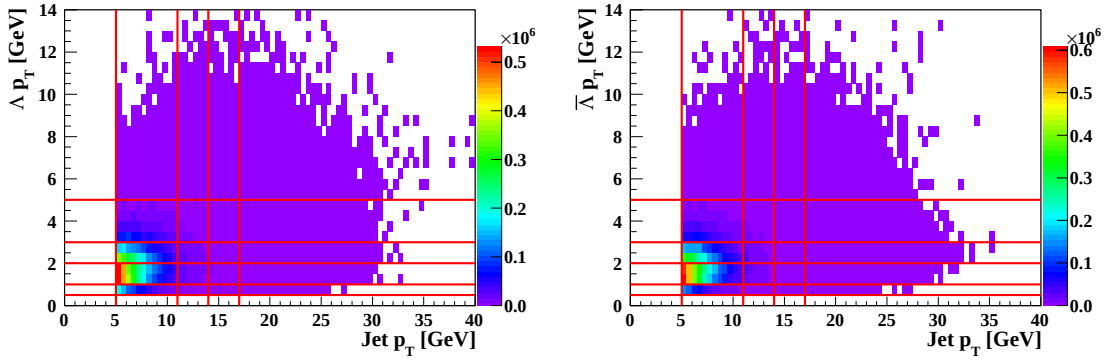

(c): mcMB–6: Λ **(d):** mcMB–6: $\overline{\Lambda}$

Figure 3.100: $\Lambda(\overline{\Lambda})$ p_T vs. jet p_T sectors for run year 2006. The horizontal and vertical red lines define the sector boundaries.

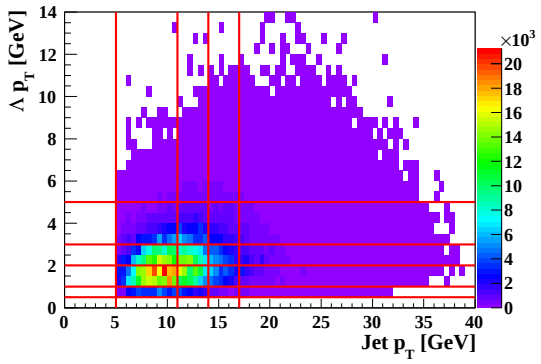

(a): mcJP1–9: Λ

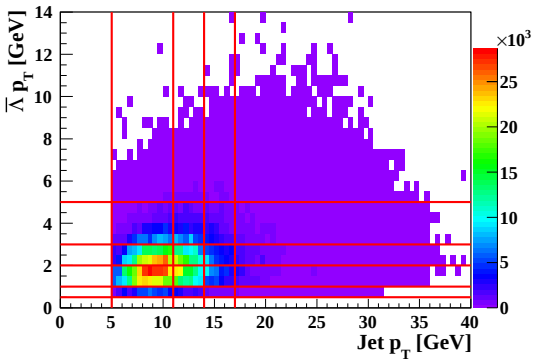

(b): mcJP1–9: $\overline{\Lambda}$

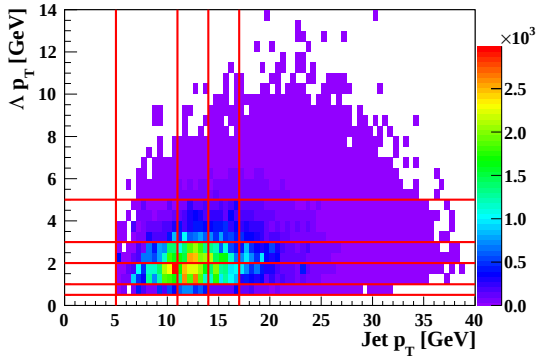

(c): mcL2JH–9: Λ

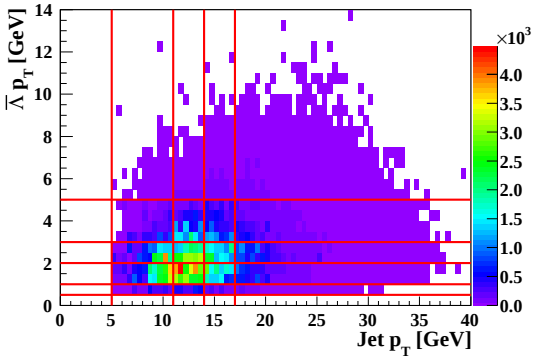

(d): mcL2JH–9: $\overline{\Lambda}$

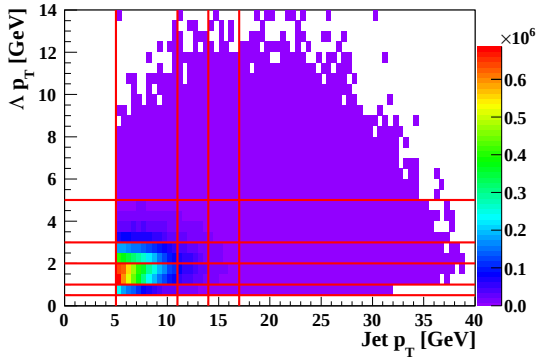

(e): mcMB–9: Λ

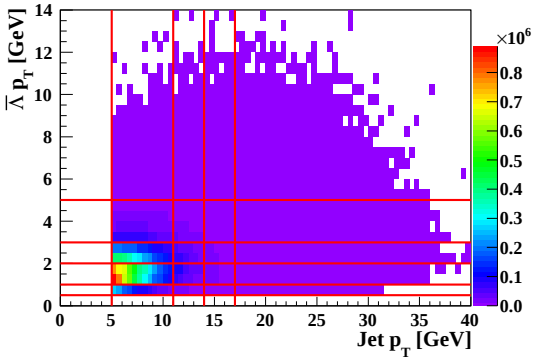

(f): mcMB–9: $\overline{\Lambda}$

Figure 3.101: $\Lambda(\overline{\Lambda})$ p_T vs. jet p_T sectors for run year 2009. The horizontal and vertical red lines define the sector boundaries.

	$\delta D_{LL}{}^{\text{sys. z-shift}}$		
	JP1–6	JP1–9	L2JH–9
		Λ	
$0.5 \leq p_T < 1.0$	0.0001	$<10^{-4}$	0.0001
$1.0 \leq p_T < 2.0$	0.0001	0.0001	0.0001
$2.0 \leq p_T < 3.0$	0.0001	0.0001	0.0001
$3.0 \leq p_T < 5.0$	0.0004	0.0003	0.0004
$5.0 \leq p_T$	0.0010	0.0001	0.0022
		Λ	
$0.5 \leq p_T < 1.0$	0.0001	$<10^{-4}$	$<10^{-4}$
$1.0 \leq p_T < 2.0$	0.0002	0.0002	0.0001
$2.0 \leq p_T < 3.0$	0.0003	0.0002	0.0003
$3.0 \leq p_T < 5.0$	0.0020	0.0004	0.0006
$5.0 \leq p_T$	0.0018	0.0009	0.0031

Table 3.38: Systematic uncertainty contributions from z shift

CHAPTER 4

Results

Measurements of the spin transfer D_{LL} and double-longitudinal spin asymmetry A_{LL} are presented for $\Lambda(\overline{\Lambda})$ hyperon production in jet-patch triggered data obtained during run year 2006 and 2009. Separate values are extracted for hyperons on the near-side and on the away-side of the jet that triggered the event. For D_{LL}, the results are further separated to positive and negative physics pseudo-rapidity $\eta_{physics}$. The direction of motion of the polarized beam defines positive $\eta_{physics}$. The D_{LL} values are extracted using

$$D_{LL} = \frac{1}{\bar{P}_{beam}\alpha_w\langle\cos(\theta^*)\rangle} \times \frac{\left(\frac{n_B^{++}}{R_4}+\frac{n_B^{-+}}{R_6}\right)+\left(\frac{n_Y^{++}}{R_4}+\frac{n_Y^{+-}}{R_9}\right)-\left(\frac{n_B^{+-}}{R_9}+n_B^{--}\right)-\left(\frac{n_Y^{-+}}{R_6}+n_Y^{--}\right)}{\left(\frac{n_B^{++}}{R_4}+\frac{n_B^{-+}}{R_6}\right)+\left(\frac{n_Y^{++}}{R_4}+\frac{n_Y^{+-}}{R_9}\right)+\left(\frac{n_B^{+-}}{R_9}+n_B^{--}\right)+\left(\frac{n_Y^{-+}}{R_6}+n_Y^{--}\right)} \tag{4.1}$$

where

$$\begin{aligned}
\alpha_w &: \Lambda(\overline{\Lambda}) \text{ weak decay parameter,}\\
\bar{P}_{beam} &: \text{Average blue and yellow beam polarization,}\\
\theta^* &: \text{Angle between } \mathbf{p}_{\Lambda(\overline{\Lambda})} \text{ and } \hat{\mathbf{p}}_{\Lambda(\overline{\Lambda})} \text{ in } \Lambda(\overline{\Lambda}) \text{ rest frame,}\\
R_4,\, R_5,\, R_6 &: \text{Relative luminosity ratios,}\\
\left.\begin{matrix} n_{B(Y)}^{++},\, n_{B(Y)}^{-+},\\ n_{B(Y)}^{+-},\, n_{B(Y)}^{--} \end{matrix}\right\} &: \begin{matrix}\Lambda(\overline{\Lambda}) \text{ counts for polarized}\\ \text{blue(yellow) beam proton-proton spin states.}\end{matrix}
\end{aligned}$$

The A_{LL} values are extracted using

$$A_{LL} = \frac{1}{P_B P_Y} \frac{(n^{++} + n^{--}) - R_3 (n^{+-} + n^{-+})}{(n^{++} + n^{--}) + R_3 (n^{+-} + n^{-+})} \tag{4.2}$$

where

$$\begin{aligned} P_B,\, P_Y &: \text{Blue and yellow beam polarization,} \\ R_3 &: \text{Relative luminosity ratio,} \\ \left.\begin{matrix} n^{++}\,,\, n^{-+}\,, \\ n^{+-}\,,\, n^{--} \end{matrix}\right\} &: \Lambda(\overline{\Lambda}) \text{ counts for proton-proton spin states.} \end{aligned}$$

The mean blue and yellow beam polarization values were determined by weighing the measured polarizations by the number of hyperon-jet associated triggered events for each fill. The mean weighted blue and yellow beam polarization values were then combined and used as the mean beam polarization for the D_{LL} extraction measurements.

The asymmetries presented in this chapter have been corrected for dilution from residual background using a very similar procedure described for D_{LL} in Section 3.7. The corrected asymmetry,

$$A^{physics} = \frac{A^{sig.} - rA^{bg.}}{1 - r}, \tag{4.3}$$

where r is the residual background fraction, $A^{sig.}$ is the asymmetry from the invariant mass signal region hyperons and $A^{bg.}$ is the asymmetry from the invariant mass background region candidates. The statistical uncertainty is

$$\delta A^{physics} = \frac{\sqrt{(\delta A^{sig.})^2 + (r\delta A^{bg.})^2}}{1 - r}, \tag{4.4}$$

where $\delta A^{sig.}$ and $\delta A^{bg.}$ are the statistical uncertainties for the asymmetries.

The statistical uncertainty contributions from the weak decay parameter, beam polarization, relative luminosity, and spin sorted hyperon yields are summed in

quadrature to obtain the statistical uncertainty in the extracted D_{LL} and A_{LL} values. The largest statistical uncertainty contribution comes from the spin sorted $\Lambda(\overline{\Lambda})$ yields. The systematic uncertainties are determined by evaluating the possible effects from the various causes of systematic uncertainty described in Section 3.9. Pileup is the dominant source of systematic uncertainty. For each individual data point, the error bars indicate the size of the statistical uncertainty whereas colored areas are used to indicate the size of the systematic uncertainties. The average value spanning all interval points is shown as a colored solid line and its weighted averaged statistical uncertainty placed on the right edge of the plot.

4.1 Cross Checks

Several cross checks were made for $\Lambda(\overline{\Lambda})$ in JP1–6, JP1–9, and L2JH–9 triggered data to search for possible unaccounted systematics. These checks and their results are described below

4.1.1 Null measurement of D_{LL} with Kaons

K^0_s particles are spin-zero particles and are therefore expected to have null D_{LL} values across all p_T intervals. The near-side and away-side $D_{LL}^{K^0_s}$ values were extracted for positive and negative $\eta_{physics}$. The extracted $D_{LL}^{K^0_s}$ at different p_T intervals are shown in Figure 4.1 for run year 2006 and 2009. The numerical values are summarized in Tables 4.1–4.3 for run year 2006 and 2009 jet-patch triggered $D_{LL}^{K^0_s}$. The extracted mean $D_{LL}^{K^0_s}$ values are consistent with zero across the measured p_T intervals, as expected. The largest deviation is 1.2σ away from zero and occurs for the near-side $\eta_{physics} > 0$ in JP1–9. No evidence is found for any difference in the away-side and the near-side samples. The $D_{LL}^{K^0_s}$ measurements have a higher statis-

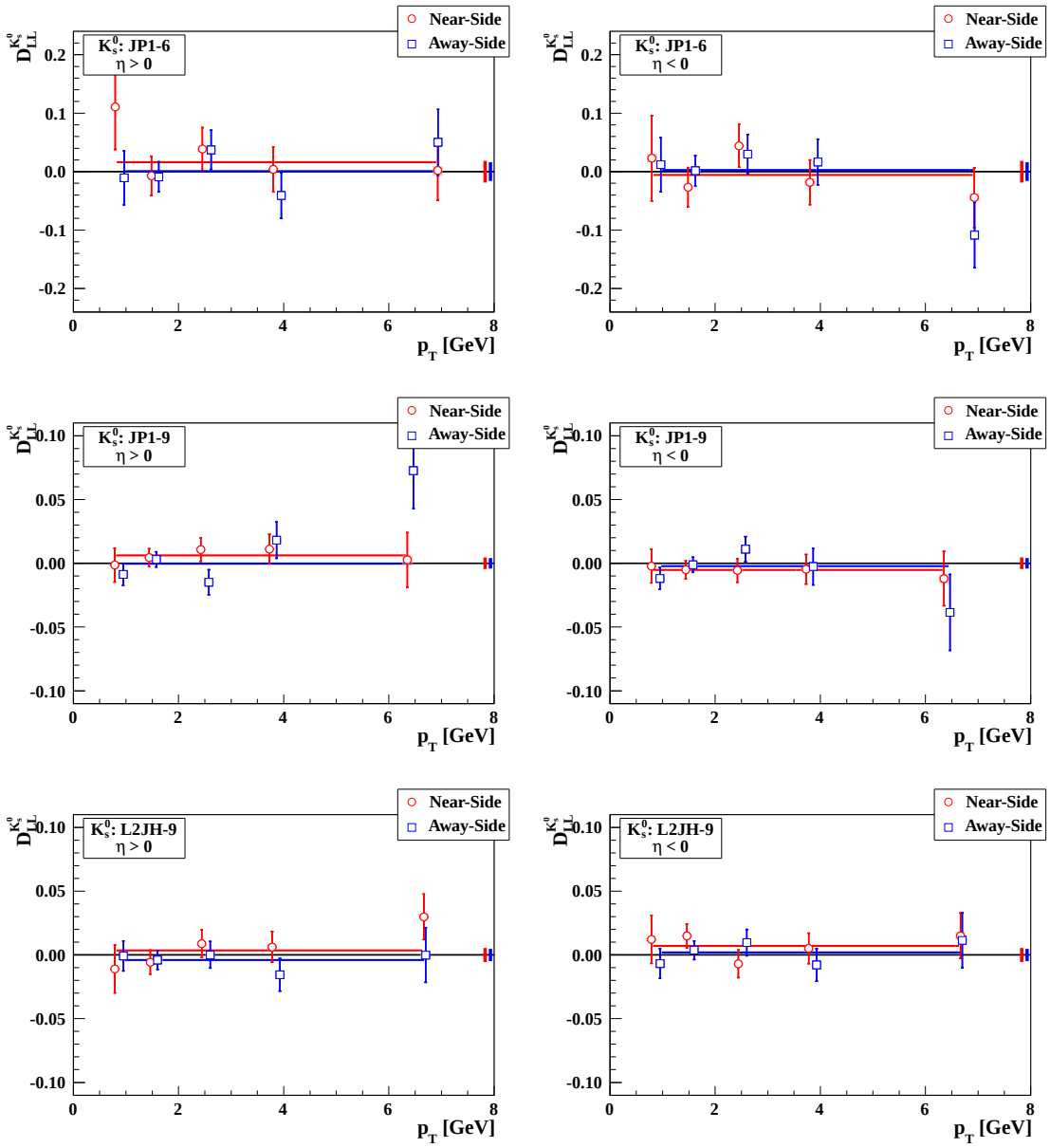

Figure 4.1: Near-side and away-side $D_{LL}^{K_s^0}$ values in the forward and backwards direction. The mean central values spanning all p_T intervals are shown as blue and red horizontal lines and their mean statistical uncertainty as vertical lines near $p_T = 8$ GeV.

tical precision than the $D_{LL}^{\Lambda(\overline{\Lambda})}$ measurements, since K_s^0 particles are produced more abundantly than $\Lambda(\overline{\Lambda})$. The reconstructed K_s^0 samples are over four times larger than the $\Lambda(\overline{\Lambda})$ samples and therefore form a stringent test for possible unaccounted systematics in the $\Lambda(\overline{\Lambda})$ measurement.

	$(\eta_{physics} > 0)$			$(\eta_{physics} < 0)$		
p_T GeV	D_{LL}	$\delta D_{LL}^{stat.}$	$\delta D_{LL}^{sys.}$	D_{LL}	$\delta D_{LL}^{stat.}$	$\delta D_{LL}^{sys.}$
			Near-Side			
$0.5 \leq p_T < 1.0$	0.111	0.073	0.002	0.023	0.073	0.006
$1.0 \leq p_T < 2.0$	−0.007	0.034	0.002	−0.027	0.034	0.002
$2.0 \leq p_T < 3.0$	0.039	0.037	0.004	0.044	0.036	0.001
$3.0 \leq p_T < 5.0$	0.004	0.038	0.002	−0.018	0.038	0.005
$5.0 \leq p_T$	0.002	0.051	0.007	−0.044	0.051	0.005
$0.5 \leq p_T$	0.016	0.019	0.001	−0.006	0.019	0.001
			Away-Side			
$0.5 \leq p_T < 1.0$	−0.011	0.046	0.002	0.012	0.046	0.004
$1.0 \leq p_T < 2.0$	−0.009	0.026	0.002	0.002	0.026	0.001
$2.0 \leq p_T < 3.0$	0.037	0.033	0.002	0.030	0.033	0.002
$3.0 \leq p_T < 5.0$	−0.041	0.039	0.003	0.017	0.039	0.002
$5.0 \leq p_T$	0.050	0.056	0.005	−0.108	0.056	0.009
$0.5 \leq p_T$	0.001	0.016	0.001	0.003	0.016	0.001

Table 4.1: Near-side and away-side values for $D_{LL}^{K_s^0}$ extracted in the forward and backwards direction for JP1–6 triggered data.

p_T GeV	D_{LL}	$\delta D_{LL}^{stat.}$	$\delta D_{LL}^{sys.}$	D_{LL}	$\delta D_{LL}^{stat.}$	$\delta D_{LL}^{sys.}$
	($\eta_{physics} > 0$)			($\eta_{physics} < 0$)		
			Near-Side			
$0.5 \leq p_T < 1.0$	-0.001	0.013	0.001	-0.002	0.013	0.001
$1.0 \leq p_T < 2.0$	0.004	0.007	0.001	-0.005	0.007	0.001
$2.0 \leq p_T < 3.0$	0.011	0.009	0.002	-0.006	0.009	0.001
$3.0 \leq p_T < 5.0$	0.011	0.012	0.002	-0.005	0.012	0.001
$5.0 \leq p_T$	0.003	0.021	0.004	-0.012	0.021	0.004
$0.5 \leq p_T$	0.006	0.005	0.001	-0.005	0.005	$<10^{-3}$
			Away-Side			
$0.5 \leq p_T < 1.0$	-0.009	0.009	0.001	-0.012	0.009	0.002
$1.0 \leq p_T < 2.0$	0.003	0.006	0.001	-0.001	0.006	$<10^{-3}$
$2.0 \leq p_T < 3.0$	-0.015	0.010	0.002	0.011	0.010	0.002
$3.0 \leq p_T < 5.0$	0.018	0.014	0.003	-0.003	0.014	0.002
$5.0 \leq p_T$	0.073	0.030	0.011	-0.039	0.030	0.006
$0.5 \leq p_T$	$<10^{-3}$	0.004	0.001	-0.002	0.004	$<10^{-3}$

Table 4.2: Near-side and away-side values for $D_{LL}^{K_s^0}$ extracted in the forward and backwards direction for JP1–9 triggered data.

p_T GeV	$(\eta_{physics} > 0)$ D_{LL}	$\delta D_{LL}^{stat.}$	$\delta D_{LL}^{sys.}$	$(\eta_{physics} < 0)$ D_{LL}	$\delta D_{LL}^{stat.}$	$\delta D_{LL}^{sys.}$
			Near-Side			
$0.5 \leq p_T < 1.0$	-0.011	0.019	0.002	0.012	0.019	0.002
$1.0 \leq p_T < 2.0$	-0.006	0.009	0.001	0.015	0.009	0.002
$2.0 \leq p_T < 3.0$	0.009	0.011	0.002	-0.007	0.011	0.001
$3.0 \leq p_T < 5.0$	0.006	0.012	0.002	0.005	0.012	0.001
$5.0 \leq p_T$	0.030	0.018	0.005	0.015	0.018	0.004
$0.5 \leq p_T$	0.004	0.006	0.001	0.007	0.006	0.001
			Away-Side			
$0.5 \leq p_T < 1.0$	-0.001	0.012	0.001	-0.007	0.012	0.001
$1.0 \leq p_T < 2.0$	-0.004	0.007	0.001	0.004	0.007	0.001
$2.0 \leq p_T < 3.0$	$<10^{-3}$	0.010	0.001	0.010	0.010	0.001
$3.0 \leq p_T < 5.0$	-0.016	0.013	0.002	-0.008	0.013	0.001
$5.0 \leq p_T$	$<10^{-3}$	0.022	0.002	0.011	0.022	0.002
$0.5 \leq p_T$	-0.004	0.005	$<10^{-3}$	0.002	0.005	0.001

Table 4.3: Near-side and away-side values for $D_{LL}^{K_s^0}$ extracted in the forward and backwards direction for L2JH–9 triggered data.

4.1.2 A_L Asymmetries

Single spin asymmetries, A_L, arise from parity-violating production processes. Such effects are expected to be negligible for the $\Lambda(\overline{\Lambda})$ and K^0_s particles produced in collisions at $\sqrt{s} = 200$ GeV [Bun00]. The data were analyzed for such asymmetries. The blue polarized beam A_L is extracted using

$$A_L^B = \frac{1}{P_B} \frac{(n^{++} + n^{-+}) - R_2 (n^{+-} + n^{--})}{(n^{++} + n^{-+}) + R_2 (n^{+-} + n^{--})}, \tag{4.5}$$

and the yellow polarized beam A_L is extracted in a similar way using

$$A_L^Y = \frac{1}{P_Y} \frac{(n^{++} + n^{+-}) - R_1 (n^{-+} + n^{--})}{(n^{++} + n^{+-}) + R_1 (n^{-+} + n^{--})}, \tag{4.6}$$

where the same notation is used for the counts, polarizations, and luminosities as before. Figures 4.2–4.4 show the near-side and away-side A_L asymmetries for run year 2006 and 2009. The numerical values are given in Tables 4.4–4.9. The data are generally found consistent with the zero expectation to within the statistical uncertainties. In particular, the precise K^0_s sample is found consistent with zero to within its statistical uncertainty. The $\Lambda(\overline{\Lambda})$ values show somewhat larger differences, with a largest mean A_L value for $\overline{\Lambda}$ that is 2.6σ away from zero for JP1–6 data. For the Λ sample, the largest A_L mean value reaches 3.7σ away from zero for JP1–9 data. The data in individual p_T intervals show no outliers. Further examination of the data yielded no pattern or other evidence, and hence the latter difference is ascribed to statistical fluctuation.

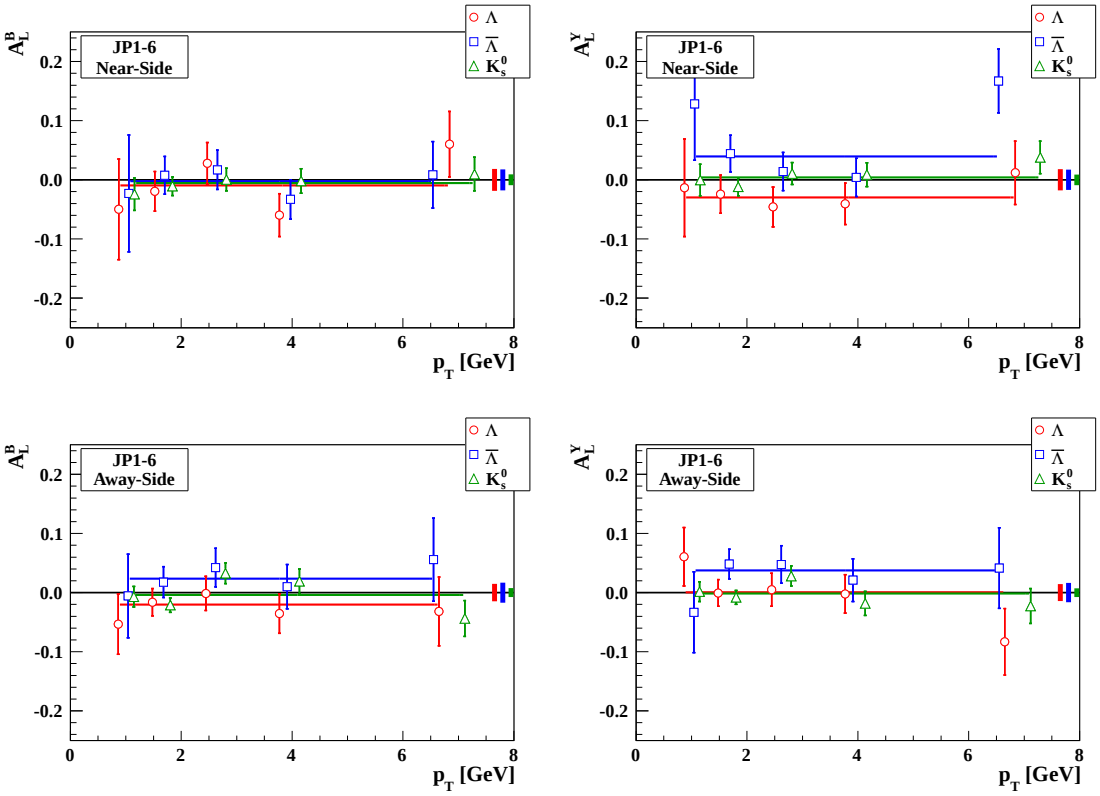

Figure 4.2: Near-side and away-side A_L^B and A_L^Y values from JP1–6 triggered data. The mean central values spanning all p_T intervals are shown as blue and red horizontal lines and their mean statistical uncertainty as vertical lines near $p_T = 8$ GeV.

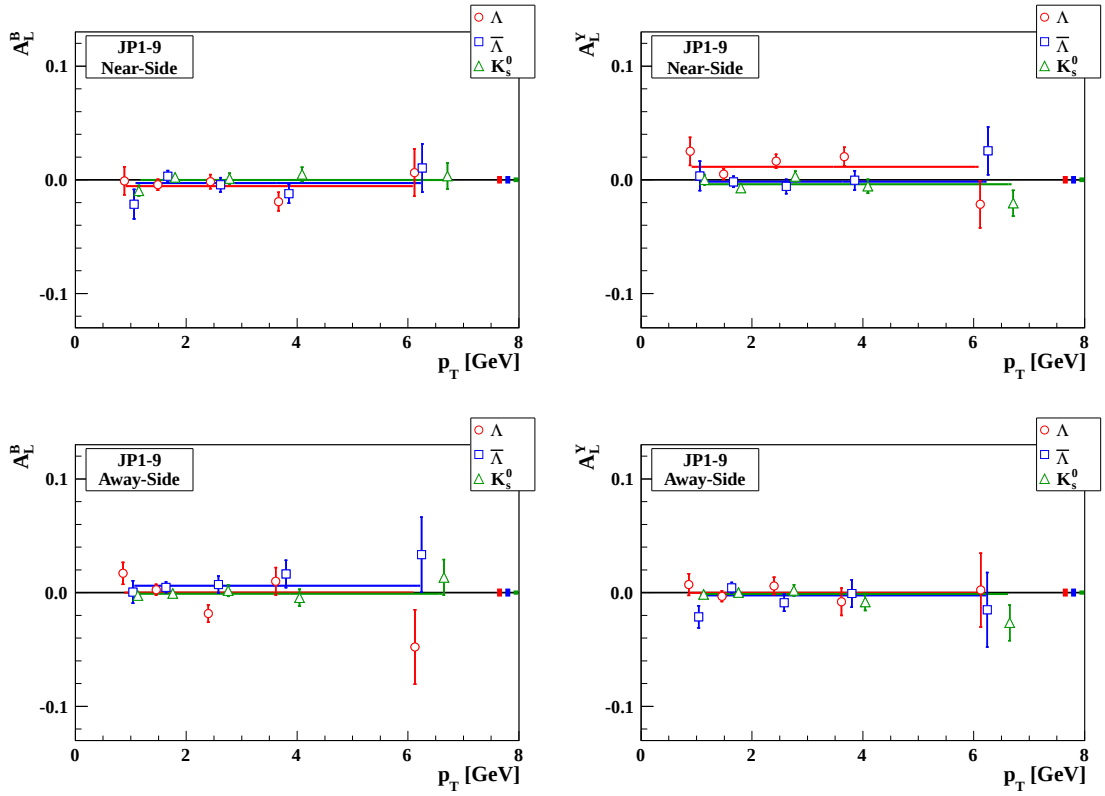

Figure 4.3: Near-side and away-side A_L^B and A_L^Y values from JP1–9 triggered data. The mean central values spanning all p_T intervals are shown as blue and red horizontal lines and their mean statistical uncertainty as vertical lines near $p_T = 8$ GeV.

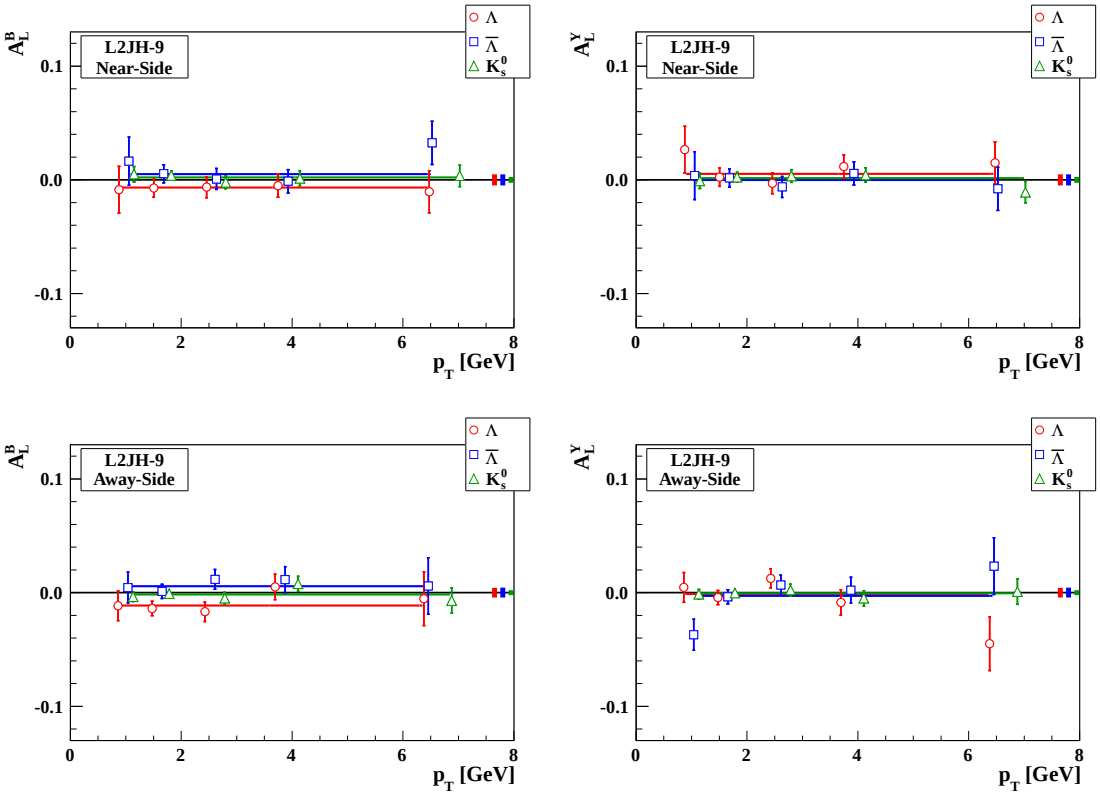

Figure 4.4: Near-side and away-side A_L^B and A_L^Y values from L2JH–9 triggered data. The mean central values spanning all p_T intervals are shown as blue and red horizontal lines and their mean statistical uncertainty as vertical lines near $p_T = 8$ GeV.

p_T GeV	(Near-Side) A_L^B	$\delta A_L^{B,stat.}$	(Away-Side) A_L^B	$\delta A_L^{B,stat.}$
		Λ		
$0.5 \leq p_T < 1.0$	-0.050	0.085	-0.053	0.051
$1.0 \leq p_T < 2.0$	-0.020	0.033	-0.016	0.023
$2.0 \leq p_T < 3.0$	0.028	0.035	-0.001	0.029
$3.0 \leq p_T < 5.0$	-0.060	0.036	-0.035	0.034
$5.0 \leq p_T$	0.060	0.055	-0.032	0.058
$0.5 \leq p_T$	-0.009	0.018	-0.020	0.015
		$\overline{\Lambda}$		
$0.5 \leq p_T < 1.0$	-0.023	0.099	-0.006	0.071
$1.0 \leq p_T < 2.0$	0.008	0.032	0.018	0.026
$2.0 \leq p_T < 3.0$	0.017	0.033	0.042	0.033
$3.0 \leq p_T < 5.0$	-0.033	0.033	0.010	0.037
$5.0 \leq p_T$	0.009	0.056	0.056	0.070
$0.5 \leq p_T$	-0.002	0.018	0.023	0.017
		K_s^0		
$0.5 \leq p_T < 1.0$	-0.024	0.028	-0.007	0.017
$1.0 \leq p_T < 2.0$	-0.011	0.016	-0.021	0.012
$2.0 \leq p_T < 3.0$	0.001	0.019	0.033	0.017
$3.0 \leq p_T < 5.0$	-0.002	0.021	0.019	0.021
$5.0 \leq p_T$	0.010	0.028	-0.044	0.030
$0.5 \leq p_T$	-0.006	0.009	-0.004	0.008

Table 4.4: Near-side and away-side values for A_L^B extracted from JP1–6 triggered data.

p_T GeV	(Near-Side) A_L^Y	$\delta A_L^{Y,stat.}$	(Away-Side) A_L^Y	$\delta A_L^{Y,stat.}$
		Λ		
$0.5 \leq p_T < 1.0$	-0.013	0.082	0.061	0.049
$1.0 \leq p_T < 2.0$	-0.024	0.032	-0.001	0.022
$2.0 \leq p_T < 3.0$	-0.046	0.034	0.005	0.028
$3.0 \leq p_T < 5.0$	-0.041	0.035	-0.002	0.032
$5.0 \leq p_T$	0.012	0.054	-0.083	0.056
$0.5 \leq p_T$	-0.030	0.018	$<10^{-3}$	0.014
		$\overline{\Lambda}$		
$0.5 \leq p_T < 1.0$	0.128	0.095	-0.033	0.068
$1.0 \leq p_T < 2.0$	0.044	0.031	0.048	0.025
$2.0 \leq p_T < 3.0$	0.014	0.032	0.048	0.032
$3.0 \leq p_T < 5.0$	0.004	0.032	0.021	0.036
$5.0 \leq p_T$	0.167	0.054	0.041	0.068
$0.5 \leq p_T$	0.039	0.017	0.038	0.016
		K_s^0		
$0.5 \leq p_T < 1.0$	$<10^{-3}$	0.027	0.002	0.017
$1.0 \leq p_T < 2.0$	-0.012	0.015	-0.008	0.012
$2.0 \leq p_T < 3.0$	0.011	0.018	0.028	0.017
$3.0 \leq p_T < 5.0$	0.009	0.020	-0.018	0.020
$5.0 \leq p_T$	0.038	0.027	-0.023	0.029
$0.5 \leq p_T$	0.004	0.009	-0.001	0.007

Table 4.5: Near-side and away-side values for A_L^Y extracted from JP1–6 triggered data.

p_T GeV	(Near-Side) A_L^B	$\delta A_L^{B,stat.}$	(Away-Side) A_L^B	$\delta A_L^{B,stat.}$
		Λ		
$0.5 \leq p_T < 1.0$	-0.001	0.012	0.017	0.010
$1.0 \leq p_T < 2.0$	-0.004	0.005	0.002	0.005
$2.0 \leq p_T < 3.0$	-0.002	0.006	-0.018	0.008
$3.0 \leq p_T < 5.0$	-0.019	0.008	0.010	0.012
$5.0 \leq p_T$	0.006	0.021	-0.048	0.033
$0.5 \leq p_T$	-0.005	0.003	$<10^{-3}$	0.004
		$\overline{\Lambda}$		
$0.5 \leq p_T < 1.0$	-0.022	0.013	0.001	0.010
$1.0 \leq p_T < 2.0$	0.003	0.005	0.005	0.005
$2.0 \leq p_T < 3.0$	-0.004	0.006	0.007	0.007
$3.0 \leq p_T < 5.0$	-0.012	0.008	0.016	0.012
$5.0 \leq p_T$	0.010	0.021	0.033	0.033
$0.5 \leq p_T$	-0.003	0.003	0.006	0.003
		K_s^0		
$0.5 \leq p_T < 1.0$	-0.010	0.005	-0.003	0.003
$1.0 \leq p_T < 2.0$	0.002	0.003	-0.001	0.003
$2.0 \leq p_T < 3.0$	0.001	0.005	0.002	0.005
$3.0 \leq p_T < 5.0$	0.005	0.006	-0.004	0.007
$5.0 \leq p_T$	0.003	0.011	0.013	0.016
$0.5 \leq p_T$	$<10^{-3}$	0.002	-0.001	0.002

Table 4.6: Near-side and away-side values for A_L^B extracted from JP1–9 triggered data.

p_T GeV	(Near-Side) A_L^Y	$\delta A_L^{Y,stat.}$	(Away-Side) A_L^Y	$\delta A_L^{Y,stat.}$
		Λ		
$0.5 \leq p_T < 1.0$	0.025	0.012	0.007	0.010
$1.0 \leq p_T < 2.0$	0.005	0.005	-0.003	0.005
$2.0 \leq p_T < 3.0$	0.016	0.006	0.006	0.008
$3.0 \leq p_T < 5.0$	0.020	0.008	-0.008	0.012
$5.0 \leq p_T$	-0.022	0.021	0.002	0.033
$0.5 \leq p_T$	0.011	0.003	$<10^{-3}$	0.004
		$\overline{\Lambda}$		
$0.5 \leq p_T < 1.0$	0.003	0.013	-0.021	0.010
$1.0 \leq p_T < 2.0$	-0.002	0.005	0.004	0.005
$2.0 \leq p_T < 3.0$	-0.006	0.006	-0.009	0.007
$3.0 \leq p_T < 5.0$	$<10^{-3}$	0.008	-0.001	0.012
$5.0 \leq p_T$	0.025	0.021	-0.015	0.033
$0.5 \leq p_T$	-0.002	0.003	-0.002	0.003
		K_s^0		
$0.5 \leq p_T < 1.0$	$<10^{-3}$	0.005	-0.002	0.003
$1.0 \leq p_T < 2.0$	-0.007	0.003	$<10^{-3}$	0.003
$2.0 \leq p_T < 3.0$	0.003	0.005	0.002	0.005
$3.0 \leq p_T < 5.0$	-0.006	0.006	-0.008	0.007
$5.0 \leq p_T$	-0.020	0.011	-0.027	0.016
$0.5 \leq p_T$	-0.004	0.002	-0.001	0.002

Table 4.7: Near-side and away-side values for A_L^Y extracted from JP1–9 triggered data.

p_T GeV	(Near-Side) A_L^B	$\delta A_L^{B,stat.}$	(Away-Side) A_L^B	$\delta A_L^{B,stat.}$
		Λ		
$0.5 \leq p_T < 1.0$	-0.009	0.021	-0.012	0.013
$1.0 \leq p_T < 2.0$	-0.007	0.008	-0.014	0.006
$2.0 \leq p_T < 3.0$	-0.006	0.009	-0.017	0.009
$3.0 \leq p_T < 5.0$	-0.005	0.010	0.005	0.011
$5.0 \leq p_T$	-0.010	0.018	-0.005	0.024
$0.5 \leq p_T$	-0.007	0.005	-0.011	0.004
		$\overline{\Lambda}$		
$0.5 \leq p_T < 1.0$	0.016	0.021	0.004	0.014
$1.0 \leq p_T < 2.0$	0.005	0.008	0.001	0.006
$2.0 \leq p_T < 3.0$	0.001	0.009	0.012	0.009
$3.0 \leq p_T < 5.0$	-0.001	0.010	0.011	0.011
$5.0 \leq p_T$	0.033	0.019	0.006	0.025
$0.5 \leq p_T$	0.005	0.005	0.006	0.004
		K_s^0		
$0.5 \leq p_T < 1.0$	0.005	0.007	-0.004	0.004
$1.0 \leq p_T < 2.0$	0.004	0.004	-0.001	0.003
$2.0 \leq p_T < 3.0$	-0.002	0.006	-0.005	0.005
$3.0 \leq p_T < 5.0$	0.001	0.006	0.008	0.007
$5.0 \leq p_T$	0.004	0.009	-0.007	0.011
$0.5 \leq p_T$	0.002	0.003	-0.002	0.002

Table 4.8: Near-side and away-side values for A_L^B extracted from L2JH–9 triggered data.

p_T GeV	(Near-Side) A_L^Y	$\delta A_L^{Y,stat.}$	(Away-Side) A_L^Y	$\delta A_L^{Y,stat.}$
		Λ		
$0.5 \leq p_T < 1.0$	0.026	0.021	0.005	0.013
$1.0 \leq p_T < 2.0$	0.002	0.008	-0.004	0.006
$2.0 \leq p_T < 3.0$	-0.003	0.009	0.012	0.009
$3.0 \leq p_T < 5.0$	0.012	0.010	-0.009	0.011
$5.0 \leq p_T$	0.015	0.018	-0.045	0.024
$0.5 \leq p_T$	0.005	0.005	-0.001	0.004
		$\overline{\Lambda}$		
$0.5 \leq p_T < 1.0$	0.004	0.021	-0.037	0.014
$1.0 \leq p_T < 2.0$	0.002	0.008	-0.004	0.006
$2.0 \leq p_T < 3.0$	-0.006	0.009	0.007	0.009
$3.0 \leq p_T < 5.0$	0.006	0.010	0.002	0.011
$5.0 \leq p_T$	-0.008	0.019	0.023	0.025
$0.5 \leq p_T$	$<10^{-3}$	0.005	-0.003	0.004
		K_s^0		
$0.5 \leq p_T < 1.0$	-0.001	0.007	-0.001	0.004
$1.0 \leq p_T < 2.0$	0.002	0.004	$<10^{-3}$	0.003
$2.0 \leq p_T < 3.0$	0.003	0.006	0.002	0.005
$3.0 \leq p_T < 5.0$	0.004	0.006	-0.005	0.007
$5.0 \leq p_T$	-0.011	0.009	0.001	0.011
$0.5 \leq p_T$	0.001	0.003	-0.001	0.002

Table 4.9: Near-side and away-side values for A_L^Y extracted from L2JH–9 triggered data.

4.1.3 Like-Sign and Unlike-Sign Asymmetries

The so-called like-sign and unlike-sign asymmetries are similar to the asymmetries A_L, expected to be negligible for all p_T intervals. The like-sign and unlike-sign asymmetries were extracted as a further cross check, using

$$A_{l.s.} = \frac{1}{P_B P_Y} \frac{n^{++} - R_4 n^{--}}{n^{++} + R_4 n^{--}}, \tag{4.7}$$

and

$$A_{u.s.} = \frac{1}{P_B P_Y} \frac{n^{+-} - R_5 n^{-+}}{n^{+-} + R_5 n^{-+}}, \tag{4.8}$$

where the same notation is used as before. Figures 4.5–4.7 show the near-side and away-side like-sign and unlike-sign asymmetries in different p_T intervals for the data obtained during run year 2006 and 2009. The numerical values are given in Tables 4.10–4.15 for run year 2006 and 2009. The data are generally found to be consistent with the expectation of a null measurement. The largest mean values are 2.5σ and 3.4σ away from zero for $A_{l.s.}^{\overline{\Lambda}}$ and $A_{u.s.}^{\Lambda}$ respectively. The precise K_s^0 sample is consistent with zero to within its statistical uncertainties. The asymmetries A_L, $A_{u.s.}$, and $A_{l.s.}$ are not fully independent, since at most three independent asymmetries can be formed from four event samples. The largest difference is indeed observed in the case of the near-side sample obtained with the same trigger as was the case for A_L. The difference is ascribed to the same statistical happenstance.

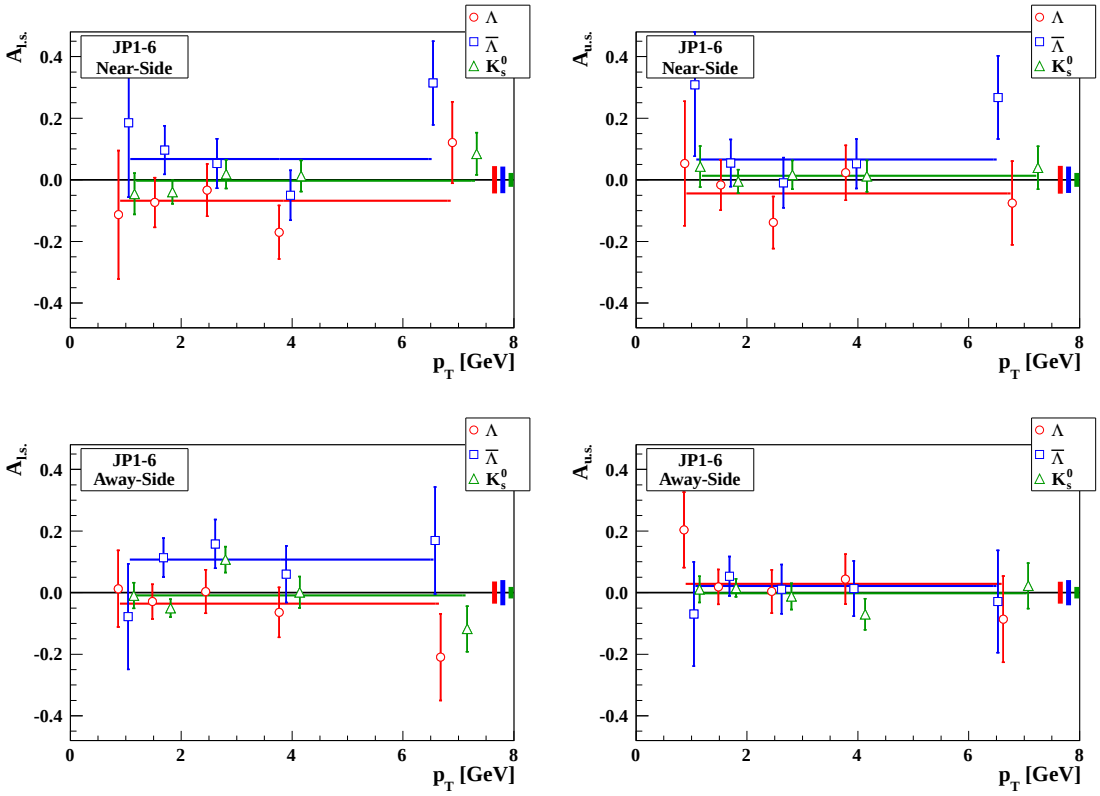

Figure 4.5: Near-side and away-side $A_{l.s.}$ and $A_{u.s.}$ values from JP1–6 triggered data. The mean central values spanning all p_T intervals are shown as blue and red horizontal lines and their mean statistical uncertainty as vertical lines near $p_T = 8$ GeV.

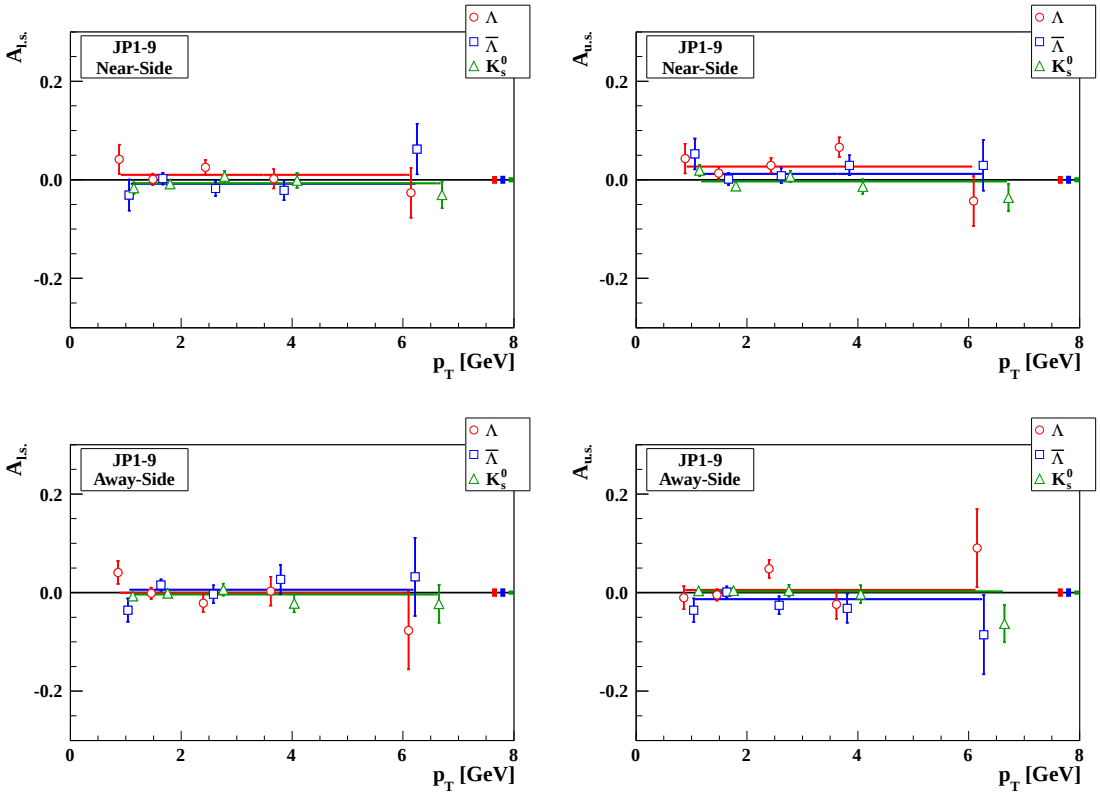

Figure 4.6: Near-side and away-side $A_{l.s.}$ and $A_{u.s.}$ values from JP1–9 triggered data. The mean central values spanning all p_T intervals are shown as blue and red horizontal lines and their mean statistical uncertainty as vertical lines near $p_T = 8$ GeV.

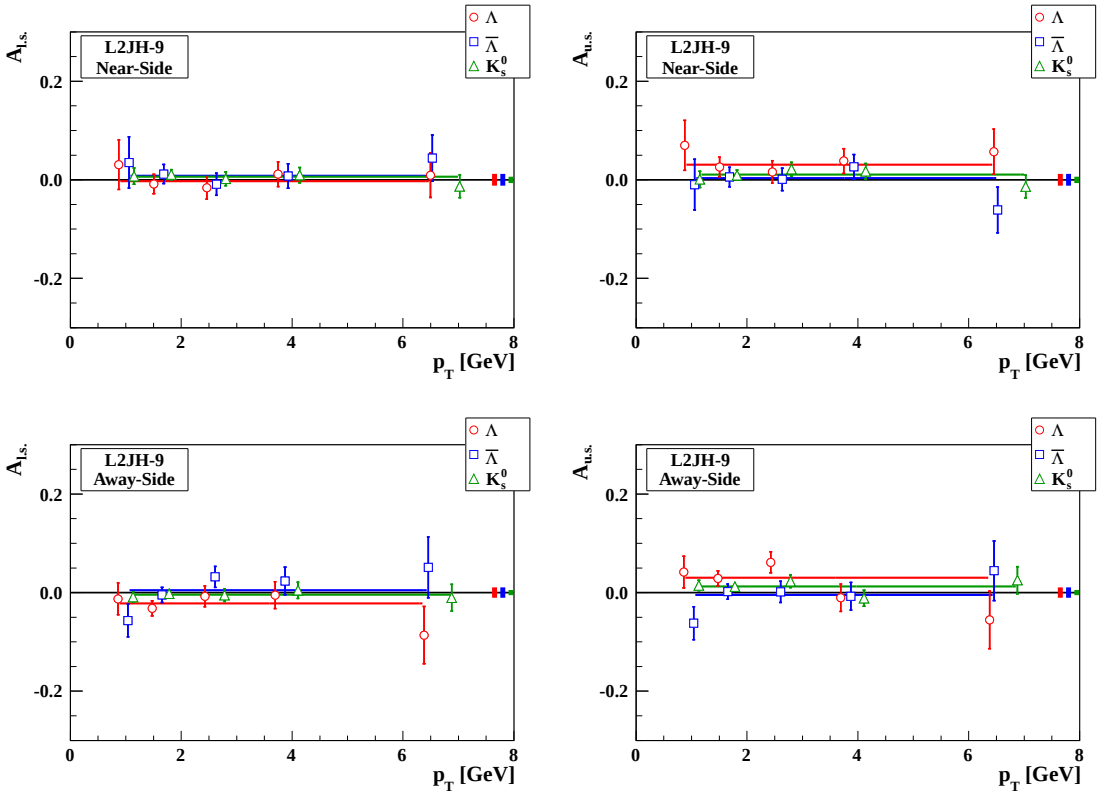

Figure 4.7: Near-side and away-side $A_{l.s.}$ and $A_{u.s.}$ values from L2JH–9 triggered data. The mean central values spanning all p_T intervals are shown as blue and red horizontal lines and their mean statistical uncertainty as vertical lines near $p_T = 8$ GeV.

p_T GeV	(Near-Side) $A_{l.s.}$	$\delta A_{l.s.}^{stat.}$	(Away-Side) $A_{l.s.}$	$\delta A_{l.s.}^{stat.}$
		Λ		
$0.5 \leq p_T < 1.0$	-0.113	0.208	0.013	0.124
$1.0 \leq p_T < 2.0$	-0.073	0.081	-0.029	0.056
$2.0 \leq p_T < 3.0$	-0.033	0.085	0.004	0.071
$3.0 \leq p_T < 5.0$	-0.170	0.087	-0.064	0.081
$5.0 \leq p_T$	0.121	0.132	-0.209	0.140
$0.5 \leq p_T$	-0.068	0.045	-0.036	0.036
		$\overline{\Lambda}$		
$0.5 \leq p_T < 1.0$	0.185	0.241	-0.078	0.172
$1.0 \leq p_T < 2.0$	0.097	0.079	0.114	0.063
$2.0 \leq p_T < 3.0$	0.053	0.081	0.158	0.079
$3.0 \leq p_T < 5.0$	-0.050	0.081	0.060	0.092
$5.0 \leq p_T$	0.314	0.136	0.169	0.174
$0.5 \leq p_T$	0.067	0.043	0.107	0.041
		K_s^0		
$0.5 \leq p_T < 1.0$	-0.046	0.067	-0.010	0.042
$1.0 \leq p_T < 2.0$	-0.040	0.038	-0.050	0.029
$2.0 \leq p_T < 3.0$	0.018	0.046	0.107	0.042
$3.0 \leq p_T < 5.0$	0.013	0.050	0.001	0.051
$5.0 \leq p_T$	0.085	0.068	-0.118	0.074
$0.5 \leq p_T$	-0.003	0.022	-0.009	0.019

Table 4.10: Near-side and away-side values for $A_{l.s.}$ extracted from JP1–6 triggered data.

p_T GeV	(Near-Side) $A_{u.s.}$	$\delta A_{u.s.}^{stat.}$	(Away-Side) $A_{u.s.}$	$\delta A_{u.s.}^{stat.}$
		Λ		
$0.5 \leq p_T < 1.0$	0.053	0.202	0.204	0.123
$1.0 \leq p_T < 2.0$	−0.017	0.082	0.019	0.057
$2.0 \leq p_T < 3.0$	−0.139	0.085	0.004	0.070
$3.0 \leq p_T < 5.0$	0.023	0.089	0.044	0.081
$5.0 \leq p_T$	−0.075	0.136	−0.086	0.140
$0.5 \leq p_T$	−0.044	0.045	0.028	0.036
		$\overline{\Lambda}$		
$0.5 \leq p_T < 1.0$	0.309	0.232	−0.070	0.169
$1.0 \leq p_T < 2.0$	0.054	0.077	0.053	0.064
$2.0 \leq p_T < 3.0$	−0.009	0.081	0.011	0.080
$3.0 \leq p_T < 5.0$	0.052	0.081	0.013	0.089
$5.0 \leq p_T$	0.267	0.135	−0.029	0.166
$0.5 \leq p_T$	0.066	0.043	0.022	0.041
		K_s^0		
$0.5 \leq p_T < 1.0$	0.043	0.067	0.011	0.042
$1.0 \leq p_T < 2.0$	−0.005	0.038	0.016	0.029
$2.0 \leq p_T < 3.0$	0.016	0.047	−0.012	0.042
$3.0 \leq p_T < 5.0$	0.012	0.051	−0.070	0.051
$5.0 \leq p_T$	0.039	0.069	0.022	0.073
$0.5 \leq p_T$	0.013	0.023	−0.002	0.019

Table 4.11: Near-side and away-side values for $A_{u.s.}$ extracted from JP1–6 triggered data.

p_T GeV	(Near-Side) $A_{l.s.}$	$\delta A_{l.s.}^{stat.}$	(Away-Side) $A_{l.s.}$	$\delta A_{l.s.}^{stat.}$
		Λ		
$0.5 \leq p_T < 1.0$	0.042	0.030	0.041	0.023
$1.0 \leq p_T < 2.0$	0.001	0.012	−0.001	0.011
$2.0 \leq p_T < 3.0$	0.025	0.015	−0.022	0.018
$3.0 \leq p_T < 5.0$	0.002	0.020	0.003	0.029
$5.0 \leq p_T$	−0.026	0.050	−0.077	0.079
$0.5 \leq p_T$	0.010	0.008	$<10^{-3}$	0.009
		$\overline{\Lambda}$		
$0.5 \leq p_T < 1.0$	−0.031	0.031	−0.036	0.024
$1.0 \leq p_T < 2.0$	0.002	0.012	0.015	0.011
$2.0 \leq p_T < 3.0$	−0.018	0.015	−0.003	0.018
$3.0 \leq p_T < 5.0$	−0.021	0.020	0.027	0.029
$5.0 \leq p_T$	0.062	0.051	0.032	0.079
$0.5 \leq p_T$	−0.008	0.008	0.006	0.008
		K_s^0		
$0.5 \leq p_T < 1.0$	−0.017	0.011	−0.007	0.008
$1.0 \leq p_T < 2.0$	−0.009	0.008	−0.001	0.006
$2.0 \leq p_T < 3.0$	0.007	0.011	0.006	0.012
$3.0 \leq p_T < 5.0$	−0.001	0.015	−0.022	0.018
$5.0 \leq p_T$	−0.030	0.028	−0.023	0.038
$0.5 \leq p_T$	−0.007	0.005	−0.004	0.004

Table 4.12: Near-side and away-side values for $A_{l.s.}$ extracted from JP1–9 triggered data.

p_T GeV	(Near-Side) $A_{u.s.}$	$\delta A_{u.s.}^{stat.}$	(Away-Side) $A_{u.s.}$	$\delta A_{u.s.}^{stat.}$
		Λ		
$0.5 \leq p_T < 1.0$	0.043	0.030	−0.011	0.023
$1.0 \leq p_T < 2.0$	0.014	0.012	−0.005	0.012
$2.0 \leq p_T < 3.0$	0.029	0.015	0.048	0.018
$3.0 \leq p_T < 5.0$	0.066	0.020	−0.024	0.029
$5.0 \leq p_T$	−0.043	0.051	0.090	0.079
$0.5 \leq p_T$	0.027	0.008	0.006	0.009
		$\overline{\Lambda}$		
$0.5 \leq p_T < 1.0$	0.053	0.031	−0.036	0.024
$1.0 \leq p_T < 2.0$	0.002	0.012	0.001	0.011
$2.0 \leq p_T < 3.0$	0.008	0.015	−0.026	0.018
$3.0 \leq p_T < 5.0$	0.029	0.020	−0.032	0.029
$5.0 \leq p_T$	0.029	0.051	−0.086	0.080
$0.5 \leq p_T$	0.012	0.008	−0.013	0.008
		K_s^0		
$0.5 \leq p_T < 1.0$	0.019	0.011	0.004	0.008
$1.0 \leq p_T < 2.0$	−0.013	0.008	0.004	0.006
$2.0 \leq p_T < 3.0$	0.007	0.012	0.004	0.012
$3.0 \leq p_T < 5.0$	−0.014	0.015	−0.003	0.018
$5.0 \leq p_T$	−0.036	0.028	−0.063	0.038
$0.5 \leq p_T$	−0.003	0.005	0.003	0.004

Table 4.13: Near-side and away-side values for $A_{u.s.}$ extracted from JP1–9 triggered data.

p_T GeV	(Near-Side) $A_{l.s.}$	$\delta A_{l.s.}^{stat.}$	(Away-Side) $A_{l.s.}$	$\delta A_{l.s.}^{stat.}$
		Λ		
$0.5 \leq p_T < 1.0$	0.031	0.050	-0.013	0.032
$1.0 \leq p_T < 2.0$	-0.008	0.020	-0.032	0.015
$2.0 \leq p_T < 3.0$	-0.016	0.023	-0.007	0.021
$3.0 \leq p_T < 5.0$	0.011	0.025	-0.005	0.027
$5.0 \leq p_T$	0.009	0.045	-0.086	0.058
$0.5 \leq p_T$	-0.003	0.012	-0.022	0.010
		$\overline{\Lambda}$		
$0.5 \leq p_T < 1.0$	0.035	0.052	-0.057	0.033
$1.0 \leq p_T < 2.0$	0.012	0.020	-0.005	0.015
$2.0 \leq p_T < 3.0$	-0.009	0.023	0.032	0.021
$3.0 \leq p_T < 5.0$	0.008	0.025	0.024	0.028
$5.0 \leq p_T$	0.044	0.047	0.051	0.062
$0.5 \leq p_T$	0.008	0.012	0.005	0.011
		K_s^0		
$0.5 \leq p_T < 1.0$	0.007	0.017	-0.009	0.010
$1.0 \leq p_T < 2.0$	0.010	0.010	-0.002	0.008
$2.0 \leq p_T < 3.0$	0.002	0.014	-0.005	0.013
$3.0 \leq p_T < 5.0$	0.009	0.015	0.005	0.016
$5.0 \leq p_T$	-0.013	0.023	-0.010	0.027
$0.5 \leq p_T$	0.006	0.006	-0.004	0.005

Table 4.14: Near-side and away-side values for $A_{l.s.}$ extracted from L2JH–9 triggered data.

p_T GeV	(Near-Side) $A_{u.s.}$	$\delta A_{u.s.}^{stat.}$	(Away-Side) $A_{u.s.}$	$\delta A_{u.s.}^{stat.}$
		Λ		
$0.5 \leq p_T < 1.0$	0.070	0.051	0.042	0.032
$1.0 \leq p_T < 2.0$	0.026	0.020	0.029	0.015
$2.0 \leq p_T < 3.0$	0.016	0.023	0.062	0.021
$3.0 \leq p_T < 5.0$	0.038	0.025	−0.010	0.028
$5.0 \leq p_T$	0.057	0.046	−0.055	0.058
$0.5 \leq p_T$	0.031	0.012	0.030	0.011
		$\overline{\Lambda}$		
$0.5 \leq p_T < 1.0$	−0.010	0.051	−0.062	0.033
$1.0 \leq p_T < 2.0$	0.006	0.020	0.002	0.015
$2.0 \leq p_T < 3.0$	0.001	0.023	0.001	0.022
$3.0 \leq p_T < 5.0$	0.026	0.025	−0.007	0.028
$5.0 \leq p_T$	−0.061	0.046	0.044	0.060
$0.5 \leq p_T$	0.004	0.012	−0.005	0.011
		K_s^0		
$0.5 \leq p_T < 1.0$	0.001	0.017	0.015	0.011
$1.0 \leq p_T < 2.0$	0.009	0.010	0.012	0.008
$2.0 \leq p_T < 3.0$	0.022	0.014	0.023	0.013
$3.0 \leq p_T < 5.0$	0.017	0.016	−0.011	0.016
$5.0 \leq p_T$	−0.014	0.023	0.025	0.028
$0.5 \leq p_T$	0.010	0.006	0.013	0.005

Table 4.15: Near-side and away-side values for $A_{u.s.}$ extracted from L2JH–9 triggered data.

4.1.4 Consistency of Sub-samples

The internal consistency of the asymmetry and spin transfer values were checked by analyzing the data for each fill separately and comparing the results and quality of fit for the average. This section focuses on the A_{LL} and forward D_{LL} asymmetries per fill, since these are of largest physics interest. In the fill-by-fill analyses, the yields were found too low to meaningfully extract background corrections. Therefore, the stability figures presented in this section are for $\Lambda(\overline{\Lambda})$ candidates in the signal region only. For the D_{LL} values presented in Section 4.3, the fills are summed over prior to extracting a D_{LL} value and the results in that section include background corrections.

The fill-by-fill results for $\Lambda(\overline{\Lambda})$-candidates residing within the signal region are shown in Figures 4.8–4.13. Both A_{LL} and D_{LL} values are given for the jet-patch triggered data obtained in run year 2006 and 2009. The correspondence of the fill indices used in these figures and the actual RHIC beam fill number is found in Appendix C. The mean value from all fills was calculated for A_{LL} and D_{LL} for each p_T interval independently and is shown as a red horizontal line in the corresponding figure. The quality of fit is found satisfactory, with somewhat better values for A_{LL} than for D_{LL}. No evidence is found for step-like behavior and possible trending was investigated by repeating the analysis and fitting first order polynomials rather than constants to the results. No evidence for trending was found.

The D_{LL} fit-quality is generally found lower than that for A_{LL}. This behavior was investigated and is ascribed to a combination of lower statistics and data treatment. In particular, the extraction of D_{LL} requires one to divide the $\Lambda(\overline{\Lambda})$ spin sorted yields into intervals in $\cos(\theta^*)$. The statistical fluctuations are correspondingly larger and selections imposing, for example, a minimum number of

counts are thought to propagate to deviations from ideal statistical behavior in the fill-by-fill values. Importantly, the outlier fills for D_{LL} at $1.0 \leq p_T < 2.0$ GeV in the JP1–6 data are not outliers throughout the other p_T intervals. No such correlations were found either by comparison of A_{LL} and D_{LL} outliers.

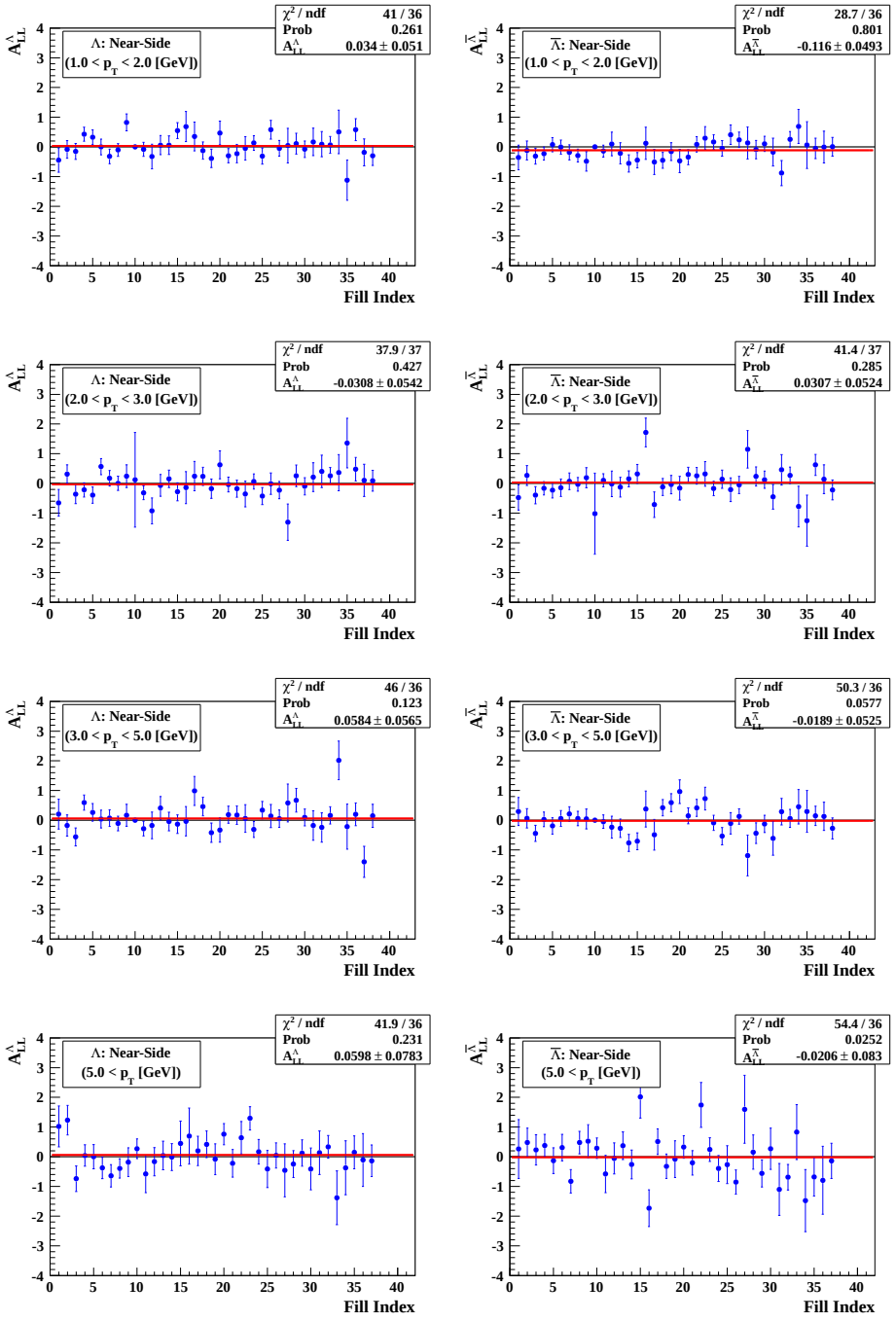

Figure 4.8: $A_{LL}^{\Lambda(\overline{\Lambda})}$ values from $\Lambda(\overline{\Lambda})$ candidates reconstructed on the near-side of the trigger jet in JP1–6 data. No corrections were applied to the $A_{LL}^{\Lambda(\overline{\Lambda})}$ asymmetries for background. The correspondence of the fill index and the RHIC fill numbers can be found in Section C.1.

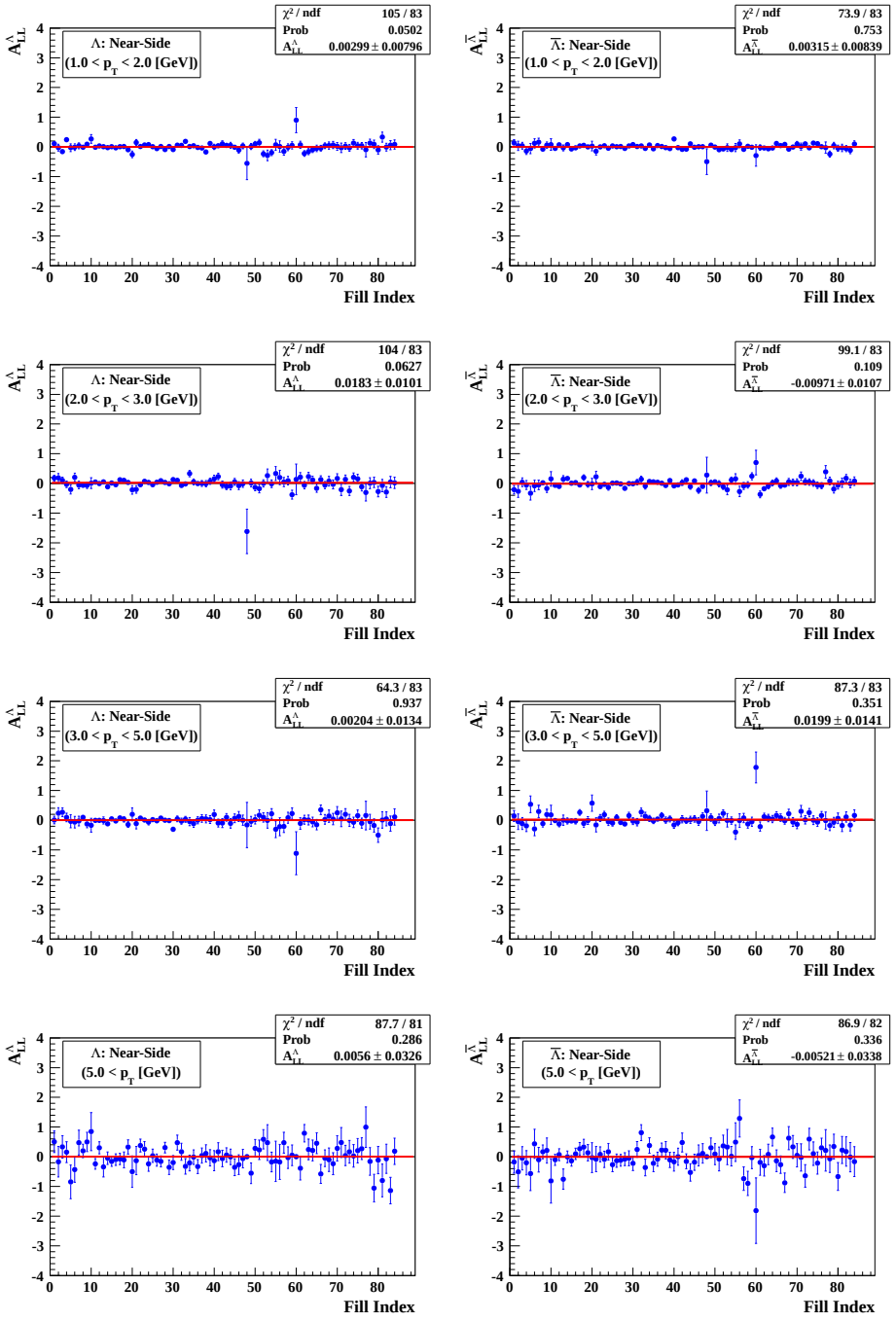

Figure 4.9: $A_{LL}^{\Lambda(\overline{\Lambda})}$ values from $\Lambda(\overline{\Lambda})$ candidates reconstructed on the near-side of the trigger jet in JP1–9 data. No corrections were applied to the $A_{LL}^{\Lambda(\overline{\Lambda})}$ asymmetries for background. The correspondence of the fill index and the RHIC fill numbers can be found in Section C.2.

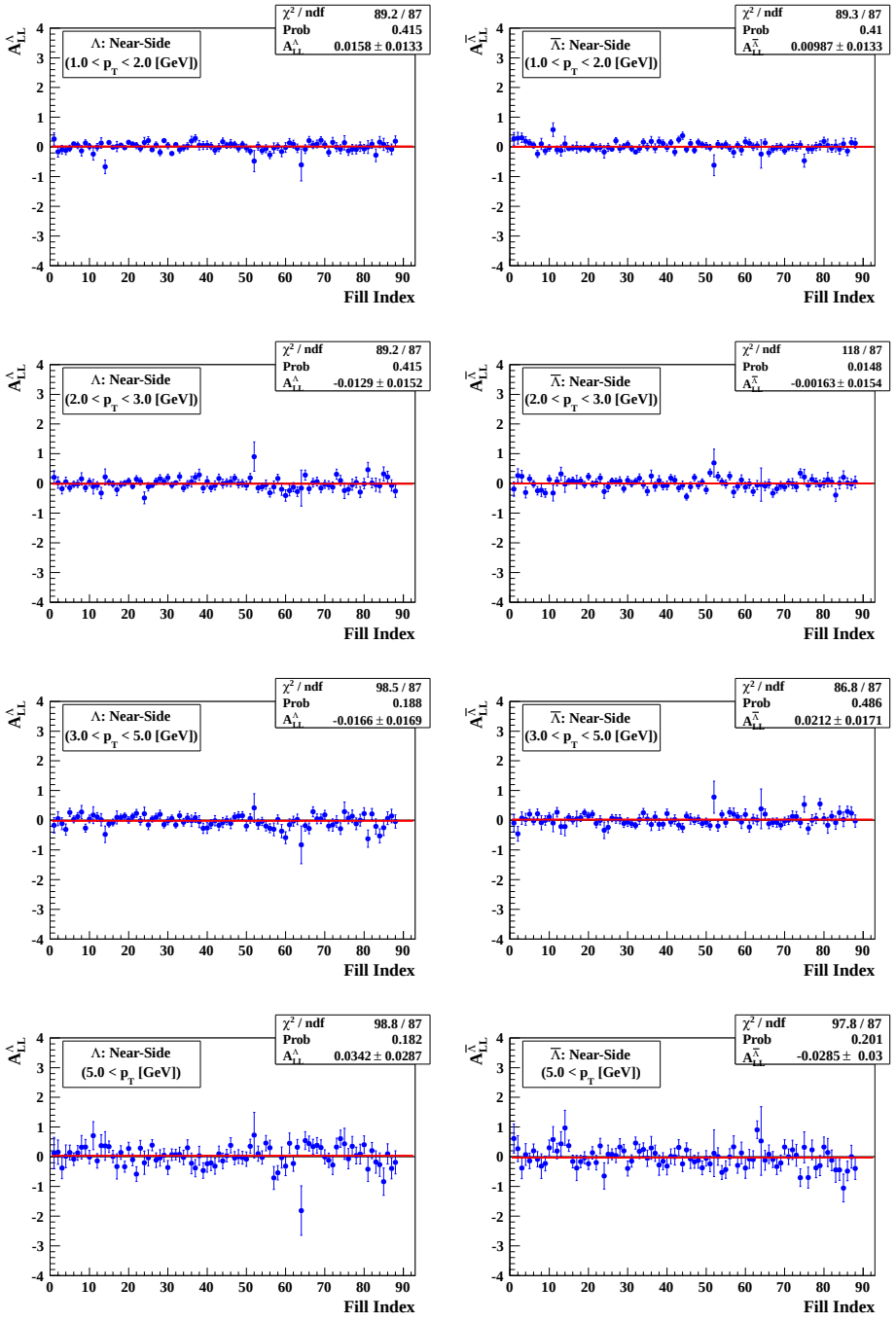

Figure 4.10: $A_{LL}^{\Lambda(\overline{\Lambda})}$ values from $\Lambda(\overline{\Lambda})$ candidates reconstructed on the near-side of the trigger jet in L2JH–9 data. No corrections were applied to the $A_{LL}^{\Lambda(\overline{\Lambda})}$ asymmetries for background. The correspondence of the fill index and the RHIC fill numbers can be found in Section C.3.

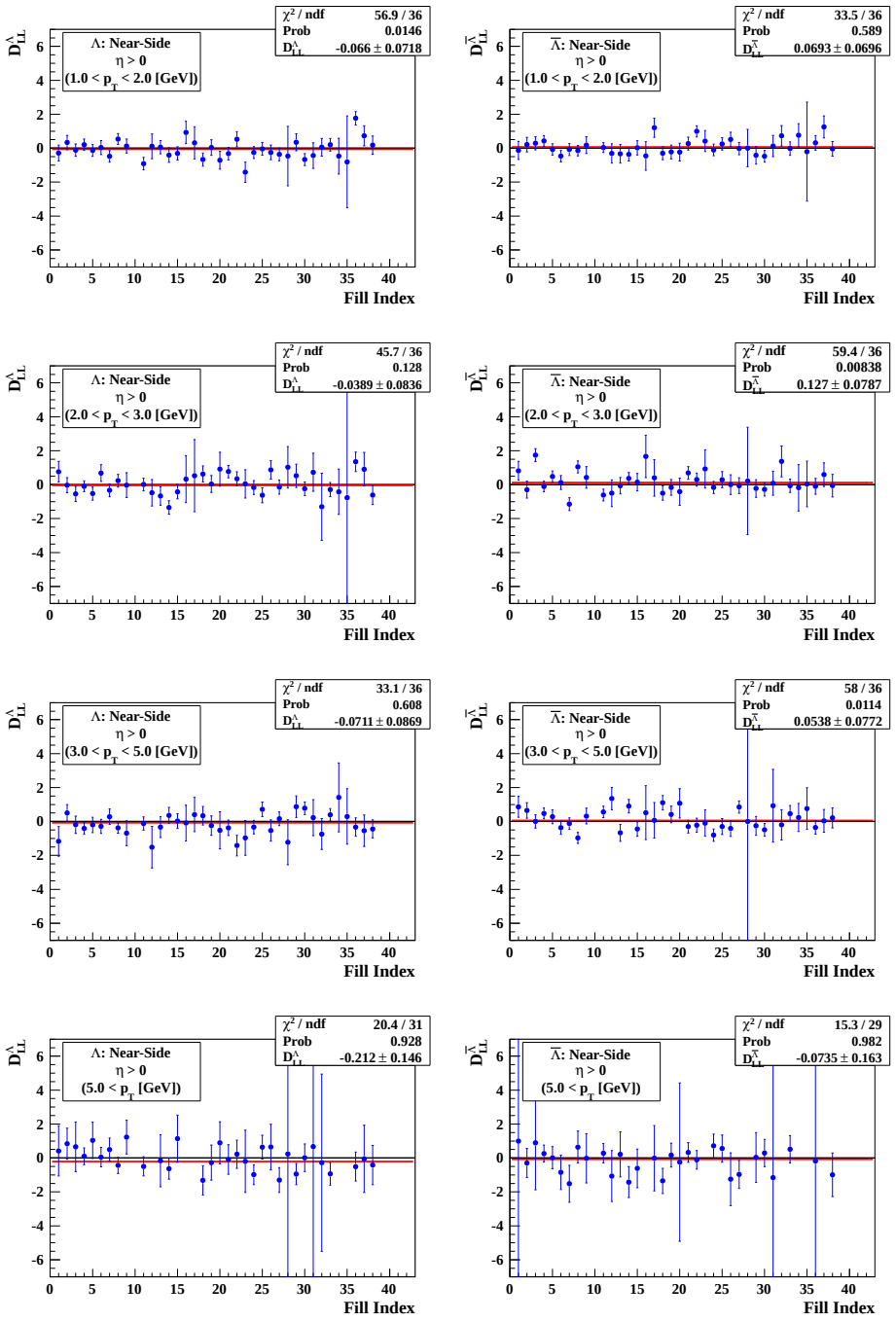

Figure 4.11: $D_{LL}^{\Lambda(\overline{\Lambda})}$ values from $\Lambda(\overline{\Lambda})$ candidates reconstructed on the near-side forward region of the trigger jet in JP1–6 data. No corrections were applied to the $D_{LL}^{\Lambda(\overline{\Lambda})}$ asymmetries for background. The correspondence of the fill index and the RHIC fill numbers can be found in Section C.1.

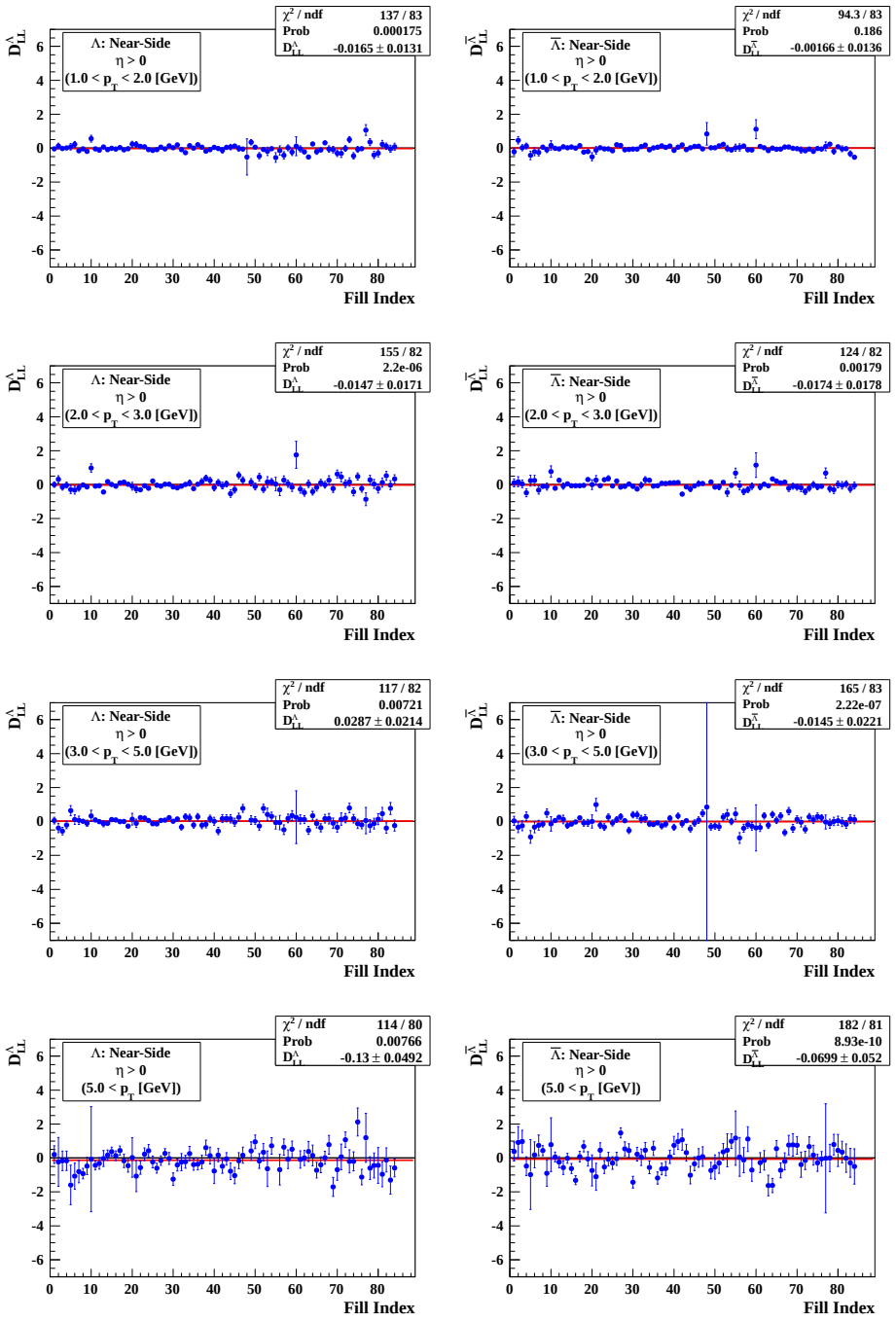

Figure 4.12: $D_{LL}^{\Lambda(\overline{\Lambda})}$ values from $\Lambda(\overline{\Lambda})$ candidates reconstructed on the near-side forward region of the trigger jet in JP1–9 data. No corrections were applied to the $D_{LL}^{\Lambda(\overline{\Lambda})}$ asymmetries for background. The correspondence of the fill index and the RHIC fill numbers can be found in Section C.2.

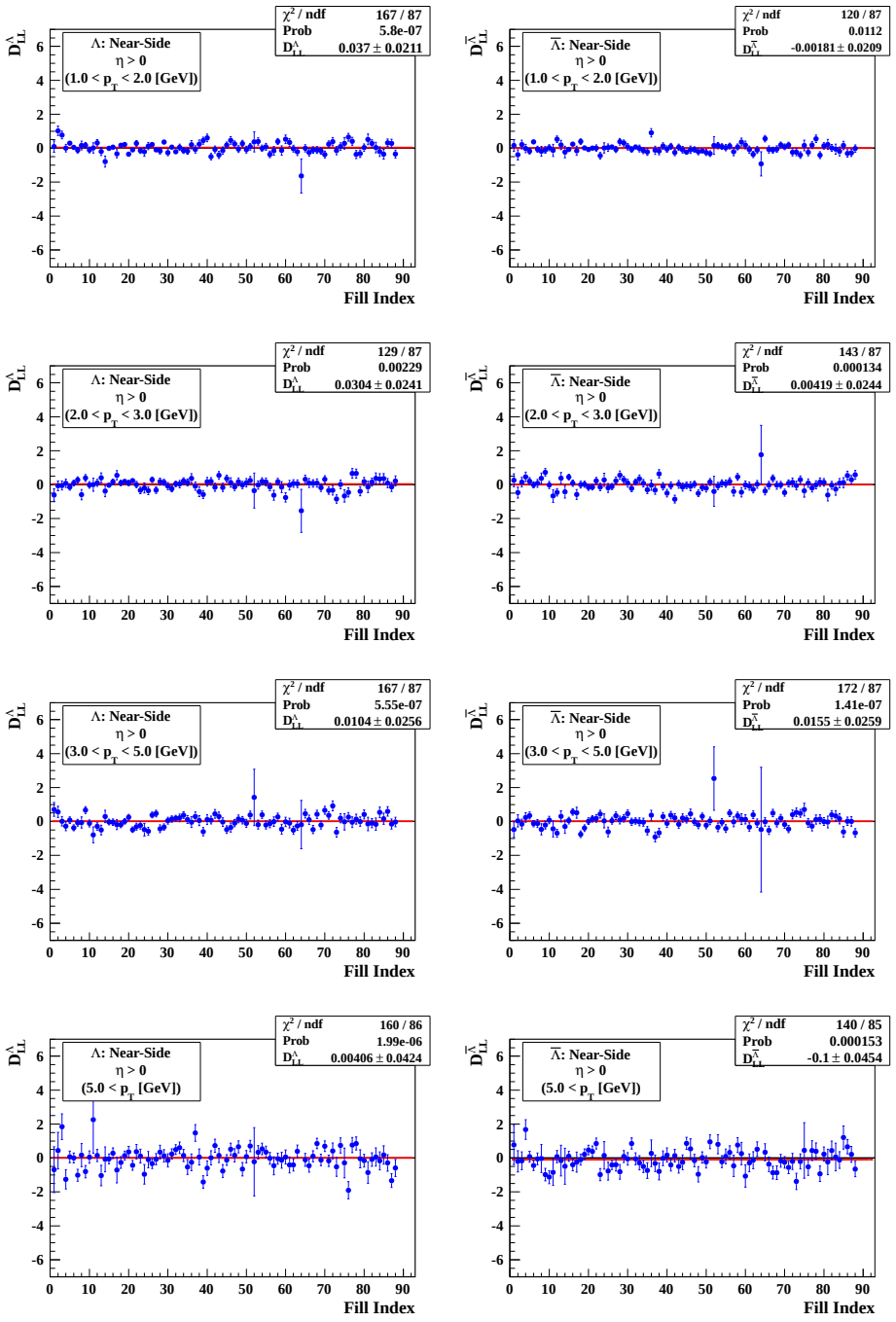

Figure 4.13: $D_{LL}^{\Lambda(\overline{\Lambda})}$ values from $\Lambda(\overline{\Lambda})$ candidates reconstructed on the near-side forward region of the trigger jet in L2JH–9 data. No corrections were applied to the $D_{LL}^{\Lambda(\overline{\Lambda})}$ asymmetries for background. The correspondence of the fill index and the RHIC fill numbers can be found in Section C.3.

4.2 A_{LL} Results

The double longitudinal spin asymmetry A_{LL} was measured for both Λ and $\overline{\Lambda}$ samples obtained from JP1–6, JP1–9, and L2JH–9 jet-patch triggered data. The measurements were made in different intervals in $\Lambda(\overline{\Lambda})$ p_T. Results were obtained separately for the samples with the $\Lambda(\overline{\Lambda})$ on the near-side and the away-side of the trigger jet. The extracted $A_{LL}^{\Lambda(\overline{\Lambda})}$ values for run year 2006 and 2009 are shown in Figure 4.14 for $0.5 < p_T \leq 6.5$ GeV. The numerical values are given in Tables 4.16–4.18 for run year 2006 and 2009. The 2009 data has superior statistical precision. The systematic uncertainty estimate dominates the total uncertainty for $p_T < 4$ GeV for both JP1–6 and JP1–9 data. The statistical uncertainty dominates at higher values of $\Lambda(\overline{\Lambda})$ p_T. The data provides no evidence for the existence of a sizable A_{LL}. The production cross-section for $\Lambda(\overline{\Lambda})$ is therefore found largely independent of the helicity configuration of the colliding proton beams.

	(Near-Side)			(Away-Side)		
p_T GeV	A_{LL}	$\delta A_{LL}^{stat.}$	$\delta A_{LL}^{sys.}$	A_{LL}	$\delta A_{LL}^{stat.}$	$\delta A_{LL}^{sys.}$
			Λ			
$0.5 \leq p_T < 1.0$	−0.119	0.147	0.092	−0.044	0.088	0.093
$1.0 \leq p_T < 2.0$	0.035	0.058	0.092	0.014	0.040	0.092
$2.0 \leq p_T < 3.0$	−0.035	0.060	0.091	−0.033	0.050	0.092
$3.0 \leq p_T < 5.0$	0.060	0.063	0.092	−0.007	0.058	0.092
$5.0 \leq p_T$	0.059	0.096	0.091	−0.043	0.100	0.091
			$\overline{\Lambda}$			
$0.5 \leq p_T < 1.0$	−0.149	0.170	0.093	−0.034	0.122	0.091
$1.0 \leq p_T < 2.0$	−0.115	0.055	0.092	0.025	0.045	0.092
$2.0 \leq p_T < 3.0$	0.022	0.058	0.092	0.015	0.057	0.092
$3.0 \leq p_T < 5.0$	−0.026	0.057	0.092	−0.089	0.064	0.092
$5.0 \leq p_T$	−0.024	0.097	0.094	−0.158	0.121	0.092

Table 4.16: Near-side and away-side values for $A_{LL}^{\Lambda(\overline{\Lambda})}$ extracted from JP1–6 triggered data.

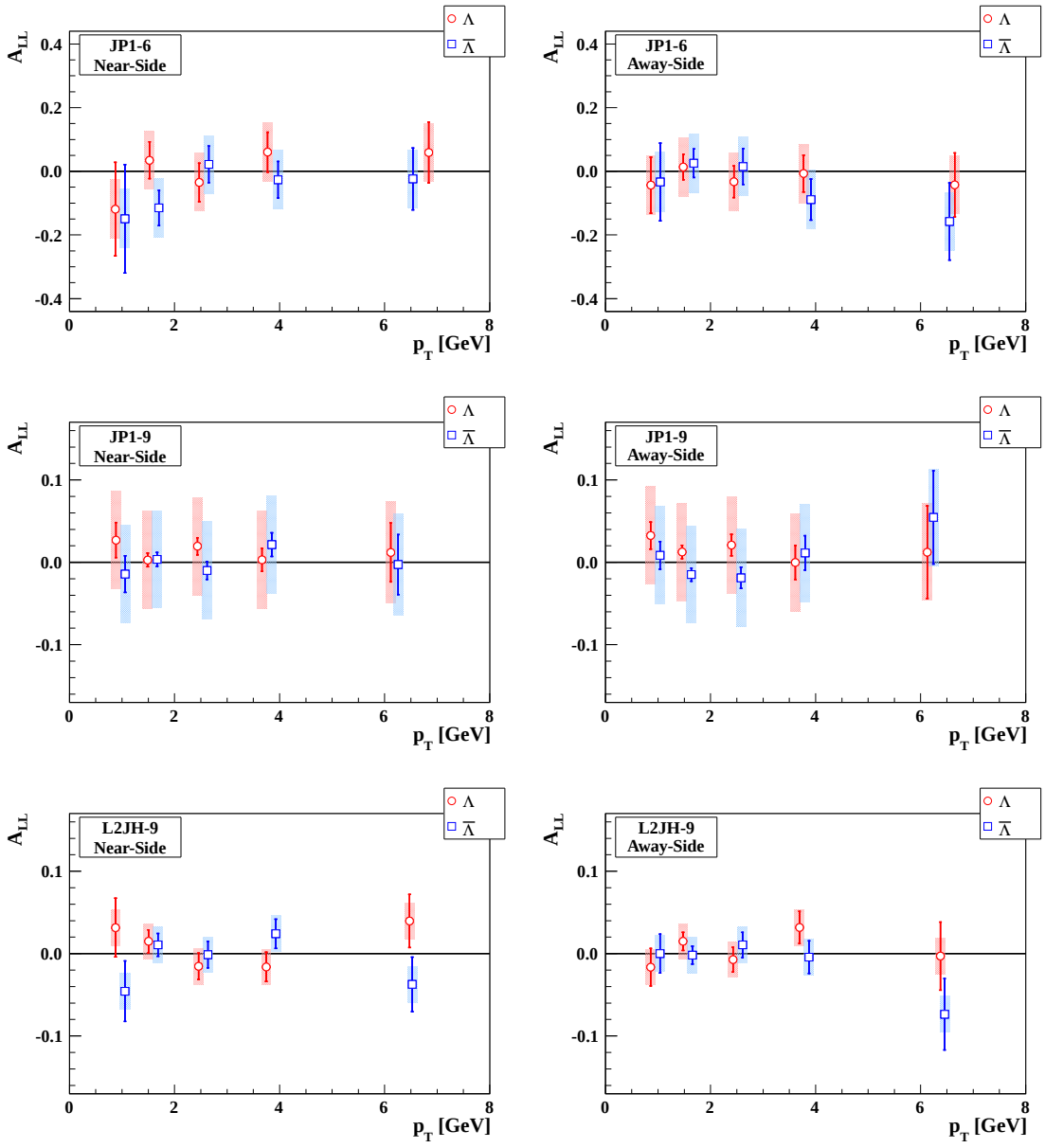

Figure 4.14: Near-side and away-side $A_{LL}^{\Lambda(\overline{\Lambda})}$ values from jet-patch triggered data.

p_T GeV	(Near-Side) A_{LL}	$\delta A_{LL}^{stat.}$	$\delta A_{LL}^{sys.}$	(Away-Side) A_{LL}	$\delta A_{LL}^{stat.}$	$\delta A_{LL}^{sys.}$
			Λ			
$0.5 \leq p_T < 1.0$	0.027	0.021	0.049	0.032	0.016	0.050
$1.0 \leq p_T < 2.0$	0.003	0.008	0.049	0.013	0.008	0.049
$2.0 \leq p_T < 3.0$	0.019	0.011	0.049	0.021	0.013	0.049
$3.0 \leq p_T < 5.0$	0.003	0.014	0.049	−0.000	0.021	0.050
$5.0 \leq p_T$	0.012	0.036	0.052	0.012	0.056	0.049
			$\overline{\Lambda}$			
$0.5 \leq p_T < 1.0$	−0.014	0.022	0.049	0.009	0.017	0.050
$1.0 \leq p_T < 2.0$	0.004	0.008	0.049	−0.015	0.008	0.049
$2.0 \leq p_T < 3.0$	−0.010	0.011	0.049	−0.019	0.013	0.050
$3.0 \leq p_T < 5.0$	0.021	0.014	0.049	0.011	0.021	0.050
$5.0 \leq p_T$	−0.003	0.036	0.049	0.054	0.057	0.052

Table 4.17: Near-side and away-side values for $A_{LL}^{\Lambda(\overline{\Lambda})}$ extracted from JP1–9 triggered data.

p_T GeV	(Near-Side) A_{LL}	$\delta A_{LL}^{stat.}$	$\delta A_{LL}^{sys.}$	(Away-Side) A_{LL}	$\delta A_{LL}^{stat.}$	$\delta A_{LL}^{sys.}$
			Λ			
$0.5 \leq p_T < 1.0$	0.032	0.036	0.020	−0.016	0.023	0.020
$1.0 \leq p_T < 2.0$	0.015	0.014	0.020	0.015	0.011	0.020
$2.0 \leq p_T < 3.0$	−0.015	0.016	0.020	−0.007	0.015	0.020
$3.0 \leq p_T < 5.0$	−0.016	0.018	0.020	0.032	0.020	0.020
$5.0 \leq p_T$	0.040	0.032	0.020	−0.003	0.041	0.020
			$\overline{\Lambda}$			
$0.5 \leq p_T < 1.0$	−0.046	0.037	0.020	0.000	0.024	0.020
$1.0 \leq p_T < 2.0$	0.011	0.014	0.020	−0.002	0.011	0.020
$2.0 \leq p_T < 3.0$	−0.001	0.016	0.020	0.011	0.015	0.020
$3.0 \leq p_T < 5.0$	0.024	0.018	0.020	−0.004	0.020	0.020
$5.0 \leq p_T$	−0.037	0.033	0.021	−0.074	0.043	0.023

Table 4.18: Near-side and away-side values for $A_{LL}^{\Lambda(\overline{\Lambda})}$ extracted from L2JH–9 triggered data.

4.3 D_{LL} Results

D_{LL} was measured for positive and negative $\eta_{physics}$ separately for $\Lambda(\overline{\Lambda})$ produced on the near-side and the away-side of a trigger jet. The $D_{LL}^{\Lambda(\overline{\Lambda})}$ values were extracted in dependence of $\Lambda(\overline{\Lambda})$ p_T and the fragmentation momentum fraction z. No corrections were made in the latter measurement for jet energy scale or resolution and only $\Lambda(\overline{\Lambda})$ with $p_T > 1$ GeV were used to extract the D_{LL} versus uncorrected z.

4.3.1 The Dependence of D_{LL} on Hyperon p_T

The results for $D_{LL}^{\Lambda(\overline{\Lambda})}$ in different p_T intervals are shown in Figures 4.15–4.17. The corresponding numerical values are given in Tables 4.19–4.24. The data in bins provide no evidence for sizeable transfer of proton beam spin to the $\Lambda(\overline{\Lambda})$. Nevertheless, the data may provide some indication of a p_T dependence. In particular, for the near-side central values of $D_{LL}^{\overline{\Lambda}}$ for $\eta_{physics} > 0$ with increasing p_T seems to decrease for the near-side sample obtained with each of the three trigger conditions (cf. Section 3.9.6). If confirmed, such a dependence is likely to have its origin in the underlying hard production mechanisms. An increase in (absolute) size of $D_{LL}^{\Lambda(\overline{\Lambda})}$ for $3 < p_T$ GeV would be consistent with the changes in the production from sub-process contributions found in studies of the mcJP1–6, mcJP1–9, and mcL2JH–9 triggered simulated data. Gluon-gluon scattering contributions are expected to decrease with p_T and are typically not expected to have a sizable spin transfer [Flo98a]. The statistical uncertainty is the dominant uncertainty for $2.0 < p_T$ GeV for both run year 2006 and 2009. The uncertainty contributions to the systematic uncertainty are typically smaller. Future large data sample taking will allow to confirm the existence of a p_T trend.

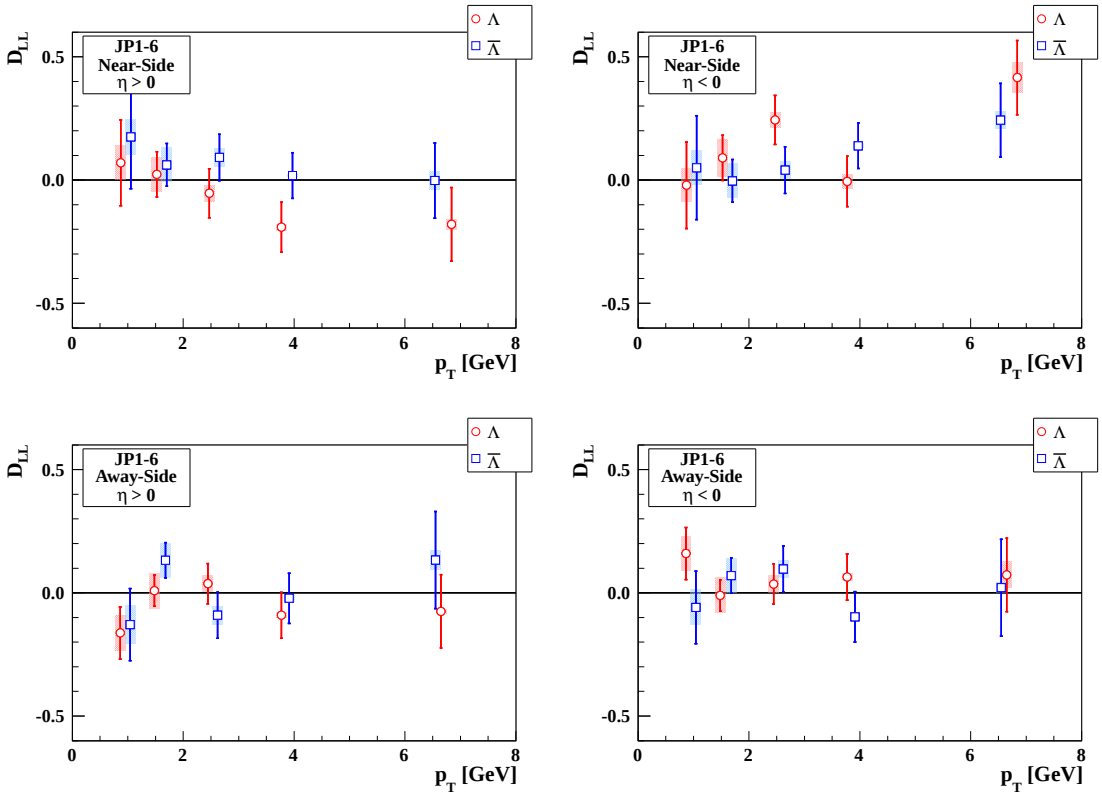

Figure 4.15: Near-side and away-side $D_{LL}^{\Lambda(\overline{\Lambda})}$ values in the forward and backwards direction from JP1–6 triggered data.

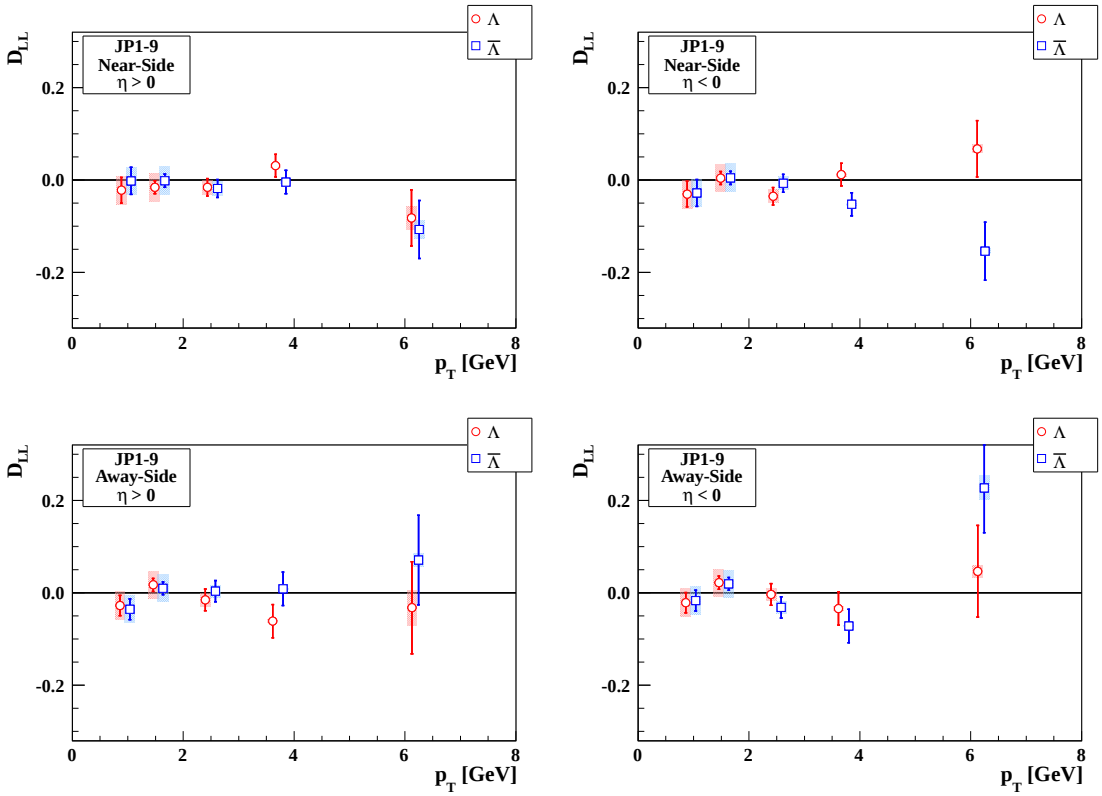

Figure 4.16: Near-side and away-side $D_{LL}^{\Lambda(\overline{\Lambda})}$ values in the forward and backwards direction from JP1–9 triggered data.

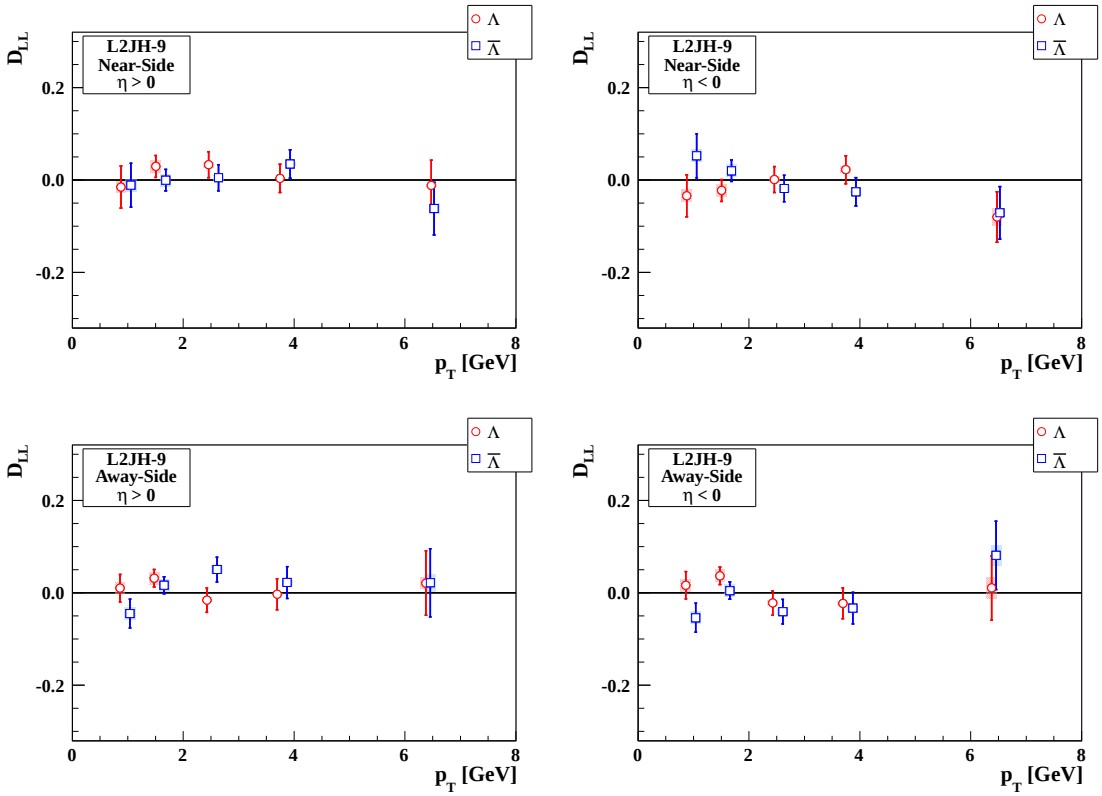

Figure 4.17: Near-side and away-side $D_{LL}^{\Lambda(\overline{\Lambda})}$ values in the forward and backwards direction from L2JH–9 triggered data.

p_T GeV	(Near-Side) D_{LL}	$\delta D_{LL}^{stat.}$	$\delta D_{LL}^{sys.}$	(Away-Side) D_{LL}	$\delta D_{LL}^{stat.}$	$\delta D_{LL}^{sys.}$
			Λ			
$0.5 \leq p_T < 1.0$	0.070	0.174	0.069	−0.163	0.106	0.072
$1.0 \leq p_T < 2.0$	0.023	0.092	0.070	0.009	0.063	0.071
$2.0 \leq p_T < 3.0$	−0.053	0.100	0.033	0.037	0.082	0.032
$3.0 \leq p_T < 5.0$	−0.191	0.101	0.023	−0.091	0.093	0.014
$5.0 \leq p_T$	−0.180	0.149	0.028	−0.075	0.149	0.011
			$\overline{\Lambda}$			
$0.5 \leq p_T < 1.0$	0.175	0.210	0.073	−0.011	0.046	0.078
$1.0 \leq p_T < 2.0$	0.062	0.087	0.069	−0.009	0.026	0.069
$2.0 \leq p_T < 3.0$	0.092	0.094	0.039	0.037	0.033	0.038
$3.0 \leq p_T < 5.0$	0.018	0.093	0.005	−0.041	0.039	0.015
$5.0 \leq p_T$	−0.002	0.152	0.035	0.050	0.056	0.042

Table 4.19: Near-side and away-side values for $D_{LL}^{\Lambda(\overline{\Lambda})}$ extracted from $\eta_{physics}>0$ JP1–6 triggered data.

p_T GeV	(Near-Side) D_{LL}	$\delta D_{LL}^{stat.}$	$\delta D_{LL}^{sys.}$	(Away-Side) D_{LL}	$\delta D_{LL}^{stat.}$	$\delta D_{LL}^{sys.}$
			Λ			
$0.5 \leq p_T < 1.0$	−0.021	0.176	0.067	0.160	0.106	0.071
$1.0 \leq p_T < 2.0$	0.090	0.092	0.075	−0.010	0.063	0.071
$2.0 \leq p_T < 3.0$	0.244	0.100	0.040	0.036	0.082	0.036
$3.0 \leq p_T < 5.0$	−0.006	0.102	0.029	0.064	0.093	0.014
$5.0 \leq p_T$	0.416	0.151	0.076	0.073	0.149	0.053
			$\overline{\Lambda}$			
$0.5 \leq p_T < 1.0$	0.050	0.211	0.070	−0.059	0.147	0.071
$1.0 \leq p_T < 2.0$	−0.003	0.087	0.069	0.070	0.072	0.068
$2.0 \leq p_T < 3.0$	0.041	0.095	0.034	0.097	0.094	0.035
$3.0 \leq p_T < 5.0$	0.139	0.092	0.017	−0.098	0.102	0.018
$5.0 \leq p_T$	0.243	0.150	0.043	0.021	0.197	0.020

Table 4.20: Near-side and away-side values for $D_{LL}^{\Lambda(\overline{\Lambda})}$ extracted from $\eta_{physics}<0$ JP1–6 triggered data.

p_T GeV	(Near-Side) D_{LL}	$\delta D_{LL}^{stat.}$	$\delta D_{LL}^{sys.}$	(Away-Side) D_{LL}	$\delta D_{LL}^{stat.}$	$\delta D_{LL}^{sys.}$
			Λ			
$0.5 \leq p_T < 1.0$	-0.022	0.028	0.039	-0.030	0.028	0.038
$1.0 \leq p_T < 2.0$	-0.016	0.014	0.038	0.004	0.014	0.037
$2.0 \leq p_T < 3.0$	-0.016	0.019	0.019	-0.035	0.019	0.017
$3.0 \leq p_T < 5.0$	0.031	0.024	0.006	0.012	0.024	0.010
$5.0 \leq p_T$	-0.082	0.061	0.028	0.068	0.061	0.039
			$\overline{\Lambda}$			
$0.5 \leq p_T < 1.0$	-0.002	0.029	0.038	-0.028	0.029	0.038
$1.0 \leq p_T < 2.0$	-0.001	0.014	0.038	0.005	0.014	0.037
$2.0 \leq p_T < 3.0$	-0.018	0.019	0.019	-0.007	0.019	0.017
$3.0 \leq p_T < 5.0$	-0.004	0.025	0.003	-0.052	0.025	0.002
$5.0 \leq p_T$	-0.107	0.063	0.025	-0.154	0.063	0.018

Table 4.21: Near-side and away-side values for $D_{LL}^{\Lambda(\overline{\Lambda})}$ extracted from $\eta_{physics}>0$ JP1–9 triggered data.

p_T GeV	(Near-Side) D_{LL}	$\delta D_{LL}^{stat.}$	$\delta D_{LL}^{sys.}$	(Away-Side) D_{LL}	$\delta D_{LL}^{stat.}$	$\delta D_{LL}^{sys.}$
			Λ			
$0.5 \leq p_T < 1.0$	-0.030	0.028	0.039	-0.021	0.022	0.038
$1.0 \leq p_T < 2.0$	0.004	0.014	0.038	0.022	0.014	0.038
$2.0 \leq p_T < 3.0$	-0.035	0.019	0.019	-0.003	0.023	0.017
$3.0 \leq p_T < 5.0$	0.012	0.024	0.004	-0.034	0.036	0.007
$5.0 \leq p_T$	0.068	0.061	0.014	0.047	0.099	0.015
			$\overline{\Lambda}$			
$0.5 \leq p_T < 1.0$	-0.028	0.029	0.038	-0.017	0.023	0.038
$1.0 \leq p_T < 2.0$	0.005	0.014	0.038	0.019	0.014	0.037
$2.0 \leq p_T < 3.0$	-0.007	0.019	0.019	-0.031	0.023	0.017
$3.0 \leq p_T < 5.0$	-0.052	0.025	0.008	-0.072	0.036	0.011
$5.0 \leq p_T$	-0.154	0.063	0.024	0.227	0.097	0.042

Table 4.22: Near-side and away-side values for $D_{LL}^{\Lambda(\overline{\Lambda})}$ extracted from $\eta_{physics}<0$ JP1–9 triggered data.

p_T GeV	(Near-Side) D_{LL}	$\delta D_{LL}^{stat.}$	$\delta D_{LL}^{sys.}$	(Away-Side) D_{LL}	$\delta D_{LL}^{stat.}$	$\delta D_{LL}^{sys.}$
			Λ			
$0.5 \leq p_T < 1.0$	-0.015	0.045	0.014	0.010	0.030	0.014
$1.0 \leq p_T < 2.0$	0.030	0.024	0.015	0.032	0.019	0.015
$2.0 \leq p_T < 3.0$	0.033	0.028	0.008	-0.016	0.026	0.006
$3.0 \leq p_T < 5.0$	0.004	0.031	0.001	-0.003	0.034	0.002
$5.0 \leq p_T$	-0.011	0.054	0.003	0.021	0.070	0.013
			$\overline{\Lambda}$			
$0.5 \leq p_T < 1.0$	-0.011	0.048	0.015	-0.045	0.031	0.016
$1.0 \leq p_T < 2.0$	-0.000	0.023	0.015	0.016	0.018	0.014
$2.0 \leq p_T < 3.0$	0.005	0.028	0.006	0.051	0.027	0.011
$3.0 \leq p_T < 5.0$	0.035	0.031	0.007	0.022	0.034	0.005
$5.0 \leq p_T$	-0.062	0.057	0.014	0.022	0.074	0.019

Table 4.23: Near-side and away-side values for $D_{LL}^{\Lambda(\overline{\Lambda})}$ extracted from $\eta_{physics}>0$ L2JH–9 triggered data.

p_T GeV	(Near-Side) D_{LL}	$\delta D_{LL}^{stat.}$	$\delta D_{LL}^{sys.}$	(Away-Side) D_{LL}	$\delta D_{LL}^{stat.}$	$\delta D_{LL}^{sys.}$
			Λ			
$0.5 \leq p_T < 1.0$	-0.034	0.045	0.015	0.016	0.030	0.014
$1.0 \leq p_T < 2.0$	-0.023	0.024	0.015	0.037	0.019	0.015
$2.0 \leq p_T < 3.0$	0.001	0.028	0.006	-0.022	0.026	0.007
$3.0 \leq p_T < 5.0$	0.022	0.031	0.007	-0.023	0.034	0.005
$5.0 \leq p_T$	-0.080	0.054	0.021	0.011	0.070	0.024
			$\overline{\Lambda}$			
$0.5 \leq p_T < 1.0$	0.052	0.048	0.016	-0.054	0.031	0.016
$1.0 \leq p_T < 2.0$	0.020	0.023	0.015	0.005	0.018	0.014
$2.0 \leq p_T < 3.0$	-0.018	0.028	0.007	-0.041	0.027	0.009
$3.0 \leq p_T < 5.0$	-0.025	0.031	0.004	-0.033	0.034	0.008
$5.0 \leq p_T$	-0.071	0.057	0.012	0.081	0.074	0.024

Table 4.24: Near-side and away-side values for $D_{LL}^{\Lambda(\overline{\Lambda})}$ extracted from $\eta_{physics}<0$ L2JH–9 triggered data.

4.3.2 The Dependence of D_{LL} on z

To gain insight in the dependence of $D_{LL}^{\Lambda(\overline{\Lambda})}$ on polarized fragmentation, measurements were made for different values of the fragmentation ratio z. Fragmentation z expresses the fraction of the hard scattering momentum carried by the produced $\Lambda(\overline{\Lambda})$. The ratio was obtained as the ratio of the $\Lambda(\overline{\Lambda})$ transverse momentum to the jet transverse momentum, and no corrections were made for the jet energy scale. The measurements were made for both run years and the results are shown in Figures 4.18–4.20. The corresponding numerical values are given in Tables 4.25–4.30. The $D_{LL}^{\Lambda(\overline{\Lambda})}$ values were extracted using $\Lambda(\overline{\Lambda})$ hyperons with $p_T > 1$ GeV. Statistical uncertainty is the dominant source of uncertainty for run year 2009. The away-side data extend to slightly larger values of z, as expected. The data provide no conclusive indication of a dependence.

	(Near-Side)			(Away-Side)		
p_T GeV	D_{LL}	$\delta D_{LL}^{stat.}$	$\delta D_{LL}^{sys.}$	D_{LL}	$\delta D_{LL}^{stat.}$	$\delta D_{LL}^{sys.}$
			Λ			
$0.0 \leq z < 0.15$	-0.025	0.094	0.050	-0.035	0.065	0.047
$0.15 \leq z < 0.30$	-0.055	0.079	0.039	0.053	0.066	0.018
$0.30 \leq z < 0.45$	-0.261	0.135	0.036	-0.075	0.125	0.031
$0.45 \leq z < 1.0$	-0.344	0.256	0.042	-0.283	0.206	0.024
			$\overline{\Lambda}$			
$0.0 \leq z < 0.15$	0.078	0.095	0.044	-0.009	0.026	0.051
$0.15 \leq z < 0.30$	0.016	0.074	0.023	0.004	0.027	0.030
$0.30 \leq z < 0.45$	0.053	0.121	0.007	0.014	0.051	0.028
$0.45 \leq z < 1.0$	0.332	0.215	0.025	0.078	0.078	0.032

Table 4.25: Near-side and away-side values from $D_{LL}^{\Lambda(\overline{\Lambda})}$ extracted from $\eta_{physics}>0$ JP1–6 triggered data. The $D_{LL}^{\Lambda(\overline{\Lambda})}$ values were extracted using $\Lambda(\overline{\Lambda})$ hyperons with $p_T > 1$ GeV. The z interval values are uncorrected.

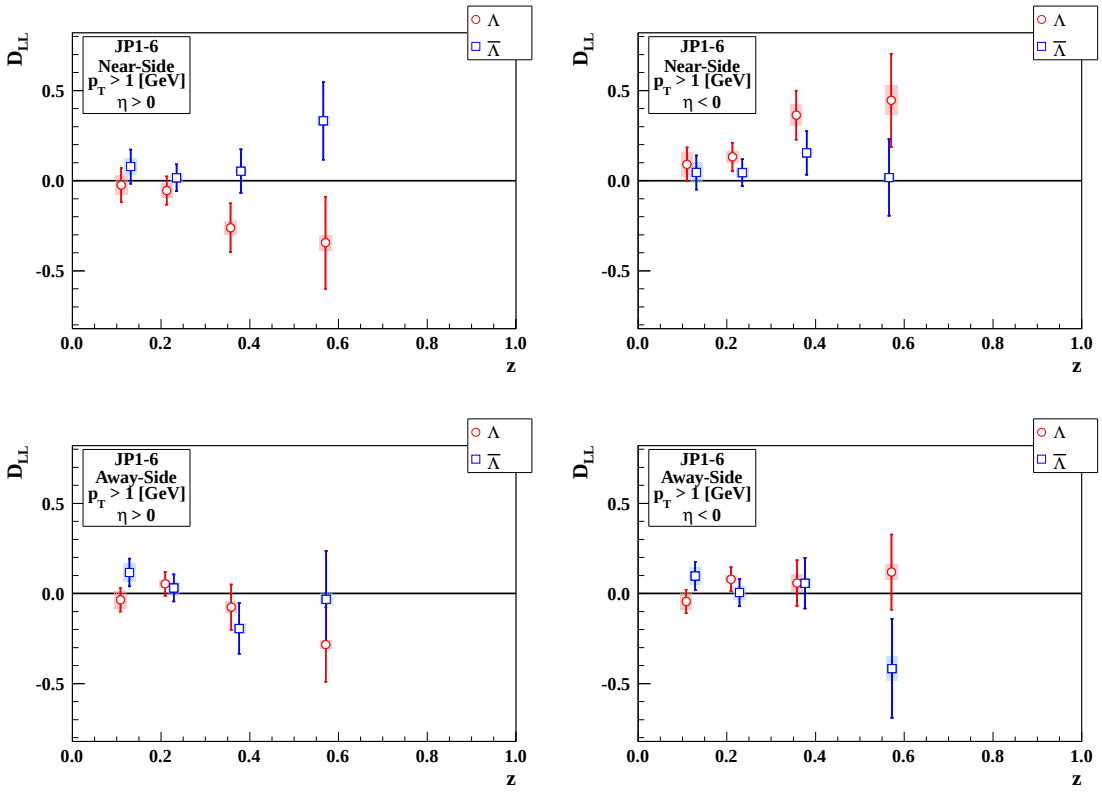

Figure 4.18: Near-side and away-side $D_{LL}^{\Lambda(\overline{\Lambda})}$ values in the forward and backwards direction for JP1–6 triggered data. The $D_{LL}^{\Lambda(\overline{\Lambda})}$ values were extracted using $\Lambda(\overline{\Lambda})$ hyperons with $p_T > 1$ GeV. The z values are uncorrected.

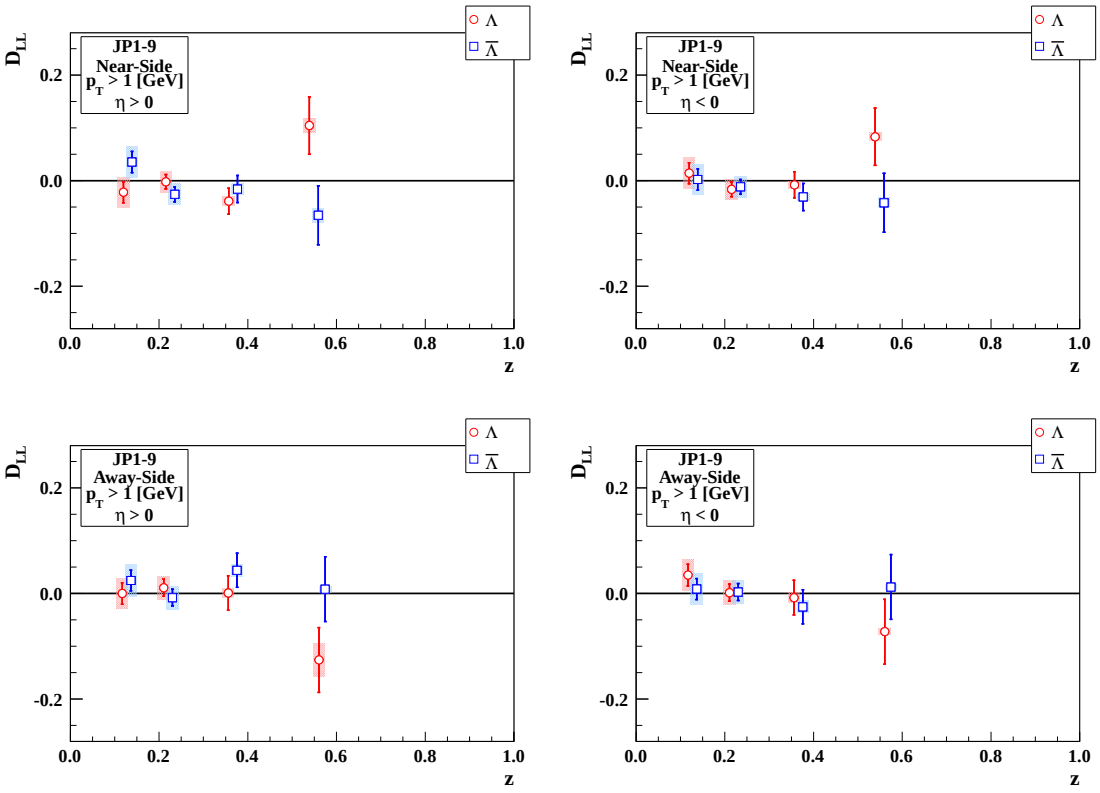

Figure 4.19: Near-side and away-side $D_{LL}^{\Lambda(\overline{\Lambda})}$ values in the forward and backwards direction for JP1–9 triggered data. The $D_{LL}^{\Lambda(\overline{\Lambda})}$ values were extracted using $\Lambda(\overline{\Lambda})$ hyperons with $p_T > 1$ GeV. The z values are uncorrected.

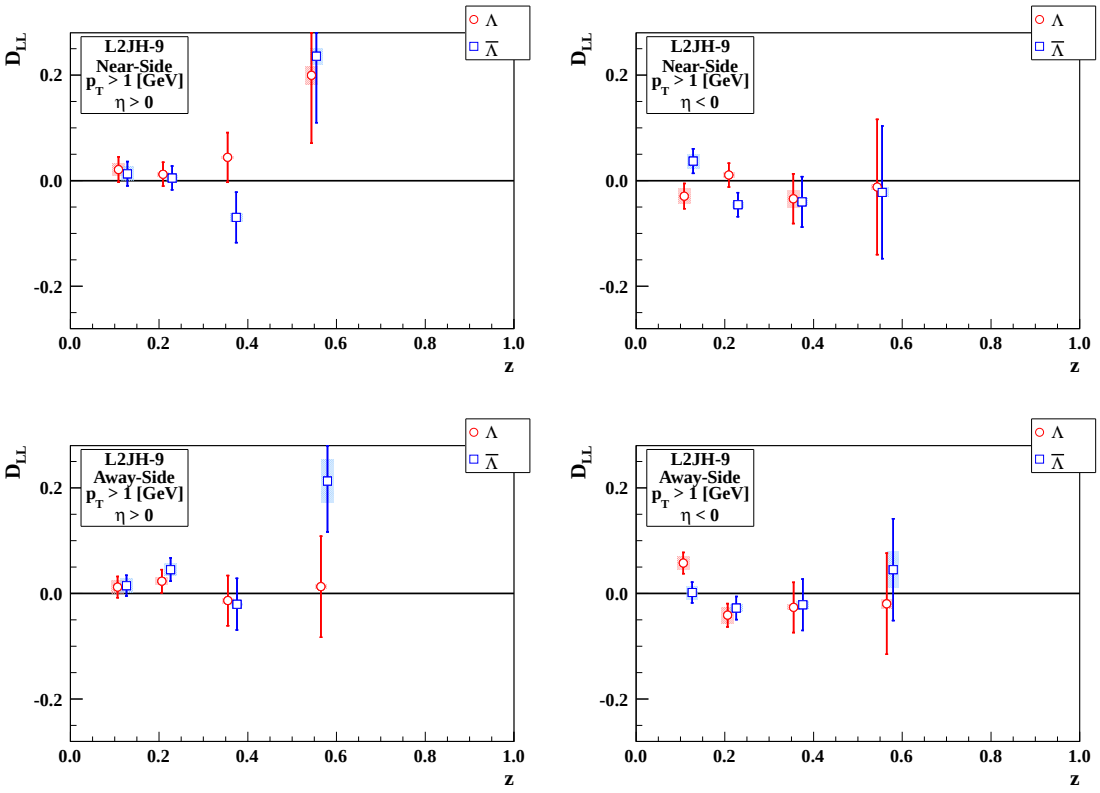

Figure 4.20: Near-side and away-side $D_{LL}^{\Lambda(\overline{\Lambda})}$ values in the forward and backwards direction for L2JH–9 triggered data. The $D_{LL}^{\Lambda(\overline{\Lambda})}$ values were extracted using $\Lambda(\overline{\Lambda})$ hyperons with $p_T > 1$ GeV. The z values are uncorrected.

p_T GeV	(Near-Side) D_{LL}	$\delta D_{LL}^{stat.}$	$\delta D_{LL}^{sys.}$	(Away-Side) D_{LL}	$\delta D_{LL}^{stat.}$	$\delta D_{LL}^{sys.}$
			Λ			
$0.0 \leq z < 0.15$	0.091	0.094	0.066	−0.044	0.066	0.046
$0.15 \leq z < 0.30$	0.132	0.079	0.032	0.079	0.066	0.019
$0.30 \leq z < 0.45$	0.363	0.136	0.060	0.057	0.127	0.047
$0.45 \leq z < 1.0$	0.445	0.258	0.081	0.119	0.209	0.042
			$\overline{\Lambda}$			
$0.0 \leq z < 0.15$	0.045	0.094	0.053	0.098	0.077	0.047
$0.15 \leq z < 0.30$	0.044	0.075	0.027	0.005	0.075	0.036
$0.30 \leq z < 0.45$	0.154	0.121	0.003	0.057	0.140	0.025
$0.45 \leq z < 1.0$	0.018	0.213	0.015	−0.416	0.274	0.069

Table 4.26: Near-side and away-side values from $D_{LL}^{\Lambda(\overline{\Lambda})}$ extracted from $\eta_{physics}<0$ JP1–6 triggered data. The $D_{LL}^{\Lambda(\overline{\Lambda})}$ values were extracted using $\Lambda(\overline{\Lambda})$ hyperons with $p_T > 1$ GeV. The z interval values are uncorrected.

p_T GeV	(Near-Side) D_{LL}	$\delta D_{LL}^{stat.}$	$\delta D_{LL}^{sys.}$	(Away-Side) D_{LL}	$\delta D_{LL}^{stat.}$	$\delta D_{LL}^{sys.}$
			Λ			
$0.0 \leq z < 0.15$	−0.022	0.020	0.029	0.014	0.020	0.029
$0.15 \leq z < 0.30$	−0.002	0.014	0.020	−0.016	0.014	0.022
$0.30 \leq z < 0.45$	−0.039	0.025	0.008	−0.008	0.025	0.009
$0.45 \leq z < 1.0$	0.104	0.054	0.013	0.083	0.054	0.031
			$\overline{\Lambda}$			
$0.0 \leq z < 0.15$	0.035	0.020	0.030	0.002	0.020	0.030
$0.15 \leq z < 0.30$	−0.026	0.014	0.020	−0.012	0.014	0.022
$0.30 \leq z < 0.45$	−0.016	0.026	0.010	−0.031	0.026	0.012
$0.45 \leq z < 1.0$	−0.066	0.056	0.013	−0.042	0.056	0.006

Table 4.27: Near-side and away-side values from $D_{LL}^{\Lambda(\overline{\Lambda})}$ extracted from $\eta_{physics}>0$ JP1–9 triggered data. The $D_{LL}^{\Lambda(\overline{\Lambda})}$ values were extracted using $\Lambda(\overline{\Lambda})$ hyperons with $p_T > 1$ GeV. The z interval values are uncorrected.

p_T GeV	(Near-Side) D_{LL}	$\delta D_{LL}^{stat.}$	$\delta D_{LL}^{sys.}$	(Away-Side) D_{LL}	$\delta D_{LL}^{stat.}$	$\delta D_{LL}^{sys.}$
			Λ			
$0.0 \leq z < 0.15$	0.014	0.020	0.030	0.035	0.020	0.030
$0.15 \leq z < 0.30$	−0.016	0.014	0.020	0.002	0.016	0.023
$0.30 \leq z < 0.45$	−0.008	0.025	0.008	−0.008	0.033	0.009
$0.45 \leq z < 1.0$	0.083	0.054	0.008	−0.072	0.061	0.006
			$\overline{\Lambda}$			
$0.0 \leq z < 0.15$	0.002	0.020	0.030	0.008	0.020	0.030
$0.15 \leq z < 0.30$	−0.012	0.014	0.020	0.003	0.016	0.022
$0.30 \leq z < 0.45$	−0.031	0.026	0.006	−0.025	0.032	0.011
$0.45 \leq z < 1.0$	−0.042	0.056	0.009	0.012	0.061	0.004

Table 4.28: Near-side and away-side values from $D_{LL}^{\Lambda(\overline{\Lambda})}$ extracted from $\eta_{physics}<0$ JP1–9 triggered data. The $D_{LL}^{\Lambda(\overline{\Lambda})}$ values were extracted using $\Lambda(\overline{\Lambda})$ hyperons with $p_T > 1$ GeV. The z interval values are uncorrected.

p_T GeV	(Near-Side) D_{LL}	$\delta D_{LL}^{stat.}$	$\delta D_{LL}^{sys.}$	(Away-Side) D_{LL}	$\delta D_{LL}^{stat.}$	$\delta D_{LL}^{sys.}$
			Λ			
$0.0 \leq z < 0.15$	0.021	0.024	0.012	0.012	0.020	0.013
$0.15 \leq z < 0.30$	0.012	0.022	0.004	0.023	0.022	0.007
$0.30 \leq z < 0.45$	0.044	0.047	0.002	−0.013	0.047	0.005
$0.45 \leq z < 1.0$	0.199	0.128	0.018	0.013	0.096	0.003
			$\overline{\Lambda}$			
$0.0 \leq z < 0.15$	0.013	0.023	0.013	0.015	0.020	0.013
$0.15 \leq z < 0.30$	0.005	0.023	0.004	0.045	0.022	0.012
$0.30 \leq z < 0.45$	−0.070	0.048	0.007	−0.020	0.049	0.002
$0.45 \leq z < 1.0$	0.236	0.126	0.015	0.213	0.096	0.041

Table 4.29: Near-side and away-side values from $D_{LL}^{\Lambda(\overline{\Lambda})}$ extracted from $\eta_{physics}>0$ L2JH–9 triggered data. The $D_{LL}^{\Lambda(\overline{\Lambda})}$ values were extracted using $\Lambda(\overline{\Lambda})$ hyperons with $p_T > 1$ GeV. The z interval values are uncorrected.

p_T GeV	(Near-Side) D_{LL}	$\delta D_{LL}^{stat.}$	$\delta D_{LL}^{sys.}$	(Away-Side) D_{LL}	$\delta D_{LL}^{stat.}$	$\delta D_{LL}^{sys.}$
			Λ			
$0.0 \leq z < 0.15$	-0.029	0.024	0.015	0.058	0.020	0.013
$0.15 \leq z < 0.30$	0.011	0.022	0.004	-0.041	0.022	0.015
$0.30 \leq z < 0.45$	-0.034	0.047	0.016	-0.026	0.047	0.005
$0.45 \leq z < 1.0$	-0.012	0.128	0.004	-0.019	0.096	0.008
			$\overline{\Lambda}$			
$0.0 \leq z < 0.15$	0.037	0.023	0.013	0.002	0.020	0.012
$0.15 \leq z < 0.30$	-0.045	0.023	0.005	-0.028	0.022	0.007
$0.30 \leq z < 0.45$	-0.040	0.048	0.006	-0.021	0.049	0.007
$0.45 \leq z < 1.0$	-0.022	0.126	0.008	0.045	0.096	0.034

Table 4.30: Near-side and away-side values from $D_{LL}^{\Lambda(\overline{\Lambda})}$ extracted from $\eta_{physics}<0$ L2JH–9 triggered data. The $D_{LL}^{\Lambda(\overline{\Lambda})}$ values were extracted using $\Lambda(\overline{\Lambda})$ hyperons with $p_T > 1$ GeV. The z interval values are uncorrected.

4.4 Comparison of D_{LL} to Prior Results

In 2005, the first measurement of D_{LL} for longitudinally polarized proton-proton collisions at $\sqrt{s} = 200$ GeV was performed [Abe09] by STAR. A comparison between the 2005 triggered data samples, JP1–6, JP1–9, and L2JH–9 is presented. Several improvements to the experiment setup were made each year and the main differences are summarized in Table 4.31. The east half of the BEMC detector

	JP1–5	JP1–6	JP1–9	L2JH–9
BEMC η	[0, 1]	[−1, 1]	[−1, 1]	[−1, 1]
# Jet Patches	6	12	18	18
E_T GeV	6.5	7.8/8.3	4.7/5.4	6.4/7.3
BBC Rate kHz	45-205	270-520	200-800	200-800

Table 4.31: Key differences between experiment setup for triggered data sets.

was commissioned, extending the pseudo-rapidity range from [0,1] to [−1,1] and doubling(tripling) the number of jet patches for run year 2006(2009). JP1–6 triggered events were required to have a larger jet patch E_T threshold than for JP1–5 events from run year 2005, reducing the number of events recorded. The rate of collisions more than doubled(quadrupled) for run year 2006(2009) compared to run year 2005. The higher jet E_T threshold counteracts the increase of pileup incurred by the higher collision rate. Table 4.32 summarizes the key differences in the analysis for all three run years. The average residual background is denoted as $\langle r \rangle$, η_{Jet} is the jet pseudo-rapidity, and R_T is the jet neutral energy fraction. The residual background was on average reduced by 81%(96%) for run year 2006(2009).

No away-side measurements were made for run year 2005 $D_{LL}^{\Lambda(\overline{\Lambda})}$, unlike for run year 2006 and 2009. Only near-side $D_{LL}^{\Lambda(\overline{\Lambda})}$ measurements from run year 2006 and 2009 are compared with 2005 $D_{LL}^{\Lambda(\overline{\Lambda})}$ values and are shown in Figures 4.21–4.22. The results for run year 2006 and 2009 were separated into similar p_T sized intervals

	JP1–5	JP1–6	JP1–9	L2JH–9
$\langle r \rangle$	9%	1.7%	0.3%	1.0%
η_{Jet}	[0.2, 0.8]	[−0.7, 0.7]	[−0.7, 0.7]	[−0.7, 0.7]
R_T	[0.1, 0.8]	[0.03, 0.94]	[0.01, 0.94]	[0.01, 0.94]

Table 4.32: Differences between analysis for triggered data sets.

as run year 2005. The D_{LL} measurements for run year 2006 and 2009 extend the p_T range of the data to about 7 GeV, one additional p_T interval compared to run year 2005. The results obtained from the 2005 and 2006 run years have comparable D_{LL}^{Λ} statistical uncertainties in the region of kinematic overlap. The $D_{LL}^{\overline{\Lambda}}$ values from 2005 were extracted using two triggered data samples, resulting in smaller run year 2005 $D_{LL}^{\overline{\Lambda}}$ statistical uncertainties compared to run year 2006, which used only a jet trigger. The significant increase in statistics for run year 2009 results in an improvement by more than a factor of four in statistical uncertainty compared to run year 2005.

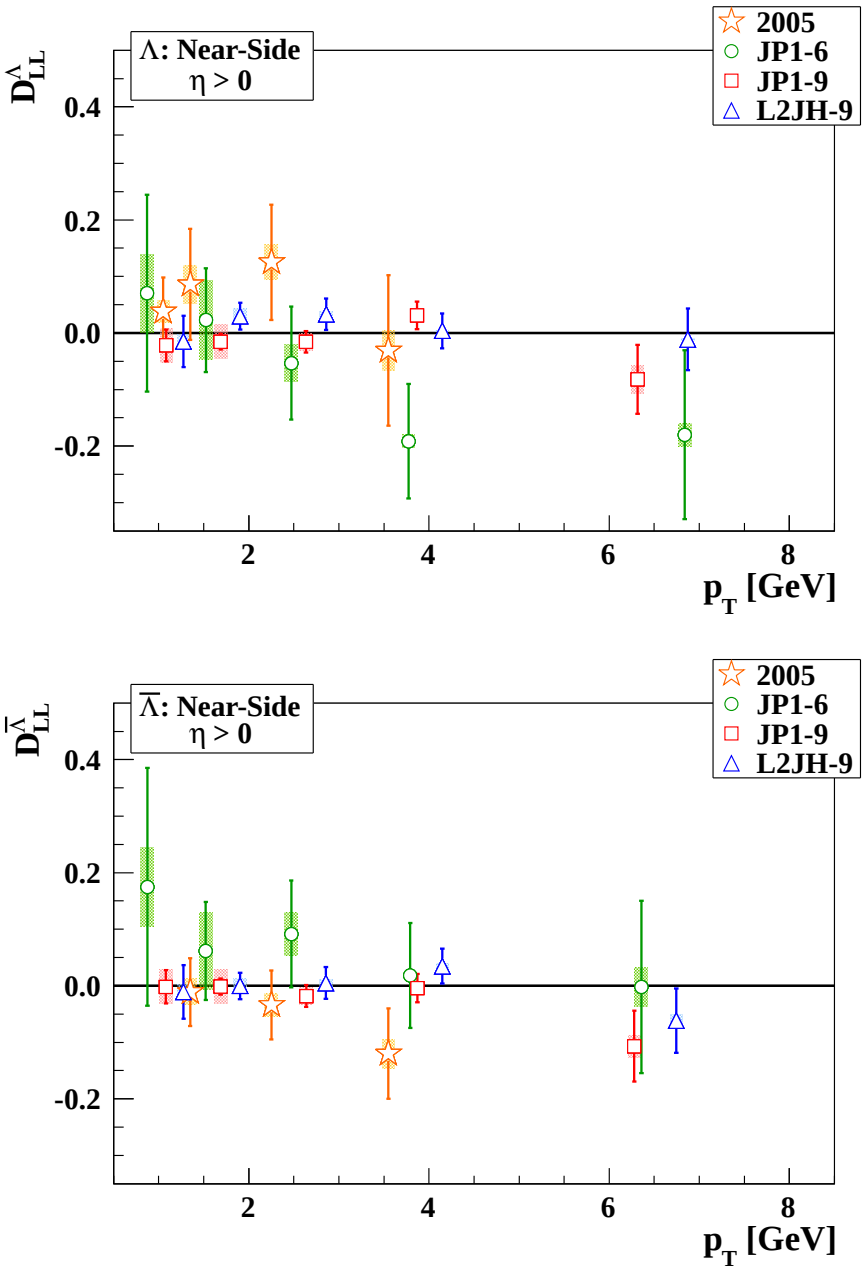

Figure 4.21: Comparison of 2005 published, run year 2006, and 2009 near-side D_{LL} measurements for $\eta_{physics} > 0$. 2005 published D_{LL} results is comprised of multiple trigger conditions.

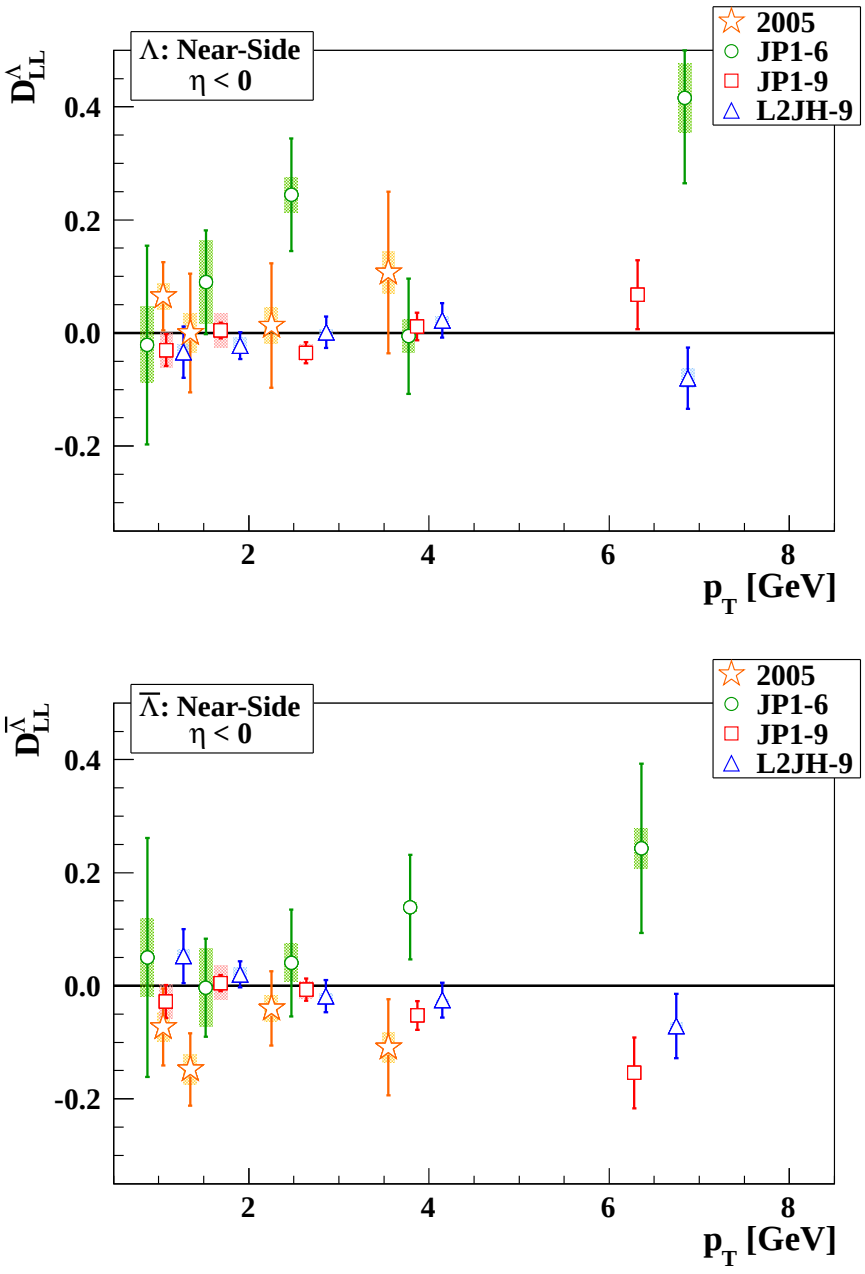

Figure 4.22: Comparison of 2005 published, run year 2006, and 2009 near-side D_{LL} measurements for $\eta_{physics} < 0$. 2005 published D_{LL} results is comprised of multiple trigger conditions.

4.5 Comparison of Data and Model Calculations

Several model calculations exist for D_{LL} [Flo98a, Xu06] and in two cases the numerical values for the relevant kinematics and acceptance are available to the analysis. Specifically, the $D_{LL}^{\Lambda+\overline{\Lambda}}$ model predictions from [Flo98a] were re-evaluated for this analysis with the unpolarized and polarized parton distributions CTEQ6L [Nad08] and DSSV [Flo09] for $\sqrt{s} = 200$ GeV [Flo98a]. The comparisons focus on the results from run year 2009 and omit the 2006 results in view of their limited precision. The two jet-patch triggered data samples, JP1–9 and L2JH–9, from run year 2009 have been merged to one data sample after performing trigger bias studies between the two triggers as described in Section 3.9.6. An upper limit of 0.007 is placed on the systematic uncertainty pertaining to the flavor-separated sub-process contribution and 0.0002 from the change in z between the two triggers. Tables 4.33–4.34 summarizes the $D_{LL}^{\Lambda(\overline{\Lambda})}$ values for the run year 2009 merged jet-patch triggered sample.

The resulting $D_{LL}^{\Lambda+\overline{\Lambda}}$ curves are shown as a function of p_T^{Λ} for [2.0,7.5] GeV in Figures 4.23–4.24, together with the data on D_{LL}^{Λ} and $D_{LL}^{\overline{\Lambda}}$. The $D_{LL}^{\Lambda(\overline{\Lambda})}$ values at $p_T < 3$ GeV are consistent with the model curves. At the largest measured p_T, however, the near-side D_{LL}^{Λ} and $D_{LL}^{\overline{\Lambda}}$ values for run year 2009 tend to be below the curves for the three model scenarios considered in Ref. [Flo98a]. This holds also for the less precise near-side $D_{LL}^{\overline{\Lambda}}$ values for run year 2006. Although the D_{LL} model evaluations are strictly for $\Lambda + \overline{\Lambda}$, the data for both Λ and $\overline{\Lambda}$ individually tend to be below the model values at the highest p_T. In this sense, and in view of the precision of the data, the equivalent contribution scenario of Ref. [Flo98a] is disfavored. In this scenario, the up, down, and strange quarks contribute equally to D_{LL}. Such a seemingly implausible scenario could be realized in nature if feed-down contributions are large. The away-side results do not distinguish the various

model curves.

In addition, numerical values of the model calculation of Ref. [Xu06] are available to the analysis. In these calculations, the Λ and $\overline{\Lambda}$ are considered separately. This model does not consider an equivalent contribution scenario, and the absolute values are therefore smaller. Furthermore, numerical values are available also as a function of z so that additional comparisons with the data can be made. The $\overline{\Lambda}$ model curves [Xu06] were generated using the GRSV2000 [G01] polarized parton distributions for hyperon production at $\sqrt{s} = 200$ GeV in association with jets with $p_T^{Jet} > 5$ GeV. The forward near-side and away-side $D_{LL}^{\Lambda(\overline{\Lambda})}$ values are compared against the model curves and are shown in Figures 4.25–4.26. At the highest p_T interval, the statistical uncertainty becomes comparable to the model spread. Both near-side Λ and $\overline{\Lambda}$ samples tend to prefer the GRSV2000-standard curves, although no definitive conclusions can be drawn. The away-side results are based on smaller data samples than the near-side results and their central values do not allow one to discriminate between the model curves. A requirement of $p_T^{\overline{\Lambda}} > 8$ GeV was imposed on the $\overline{\Lambda}$ hyperons for the generated model curves as a function of z. A similar selection in the 2009 data sample would eliminate nearly all events, and instead a lower limit of 1 GeV on $p_T^{\overline{\Lambda}}$ was imposed. It should furthermore be noted that the D_{LL} values extracted in different z intervals were not corrected for jet energy scale and resolution. The data are shown together with the model evaluations in Figure 4.27. The near-side data at highest raw z once again tends to (slightly) prefer the models based on the GRSV2000-standard polarized parton distribution functions. The away-side data versus z, however, is closest to the GRSV2000-valence curves for the highest raw z interval. Significant continued data collection is required to conclusively discriminate between the model curves.

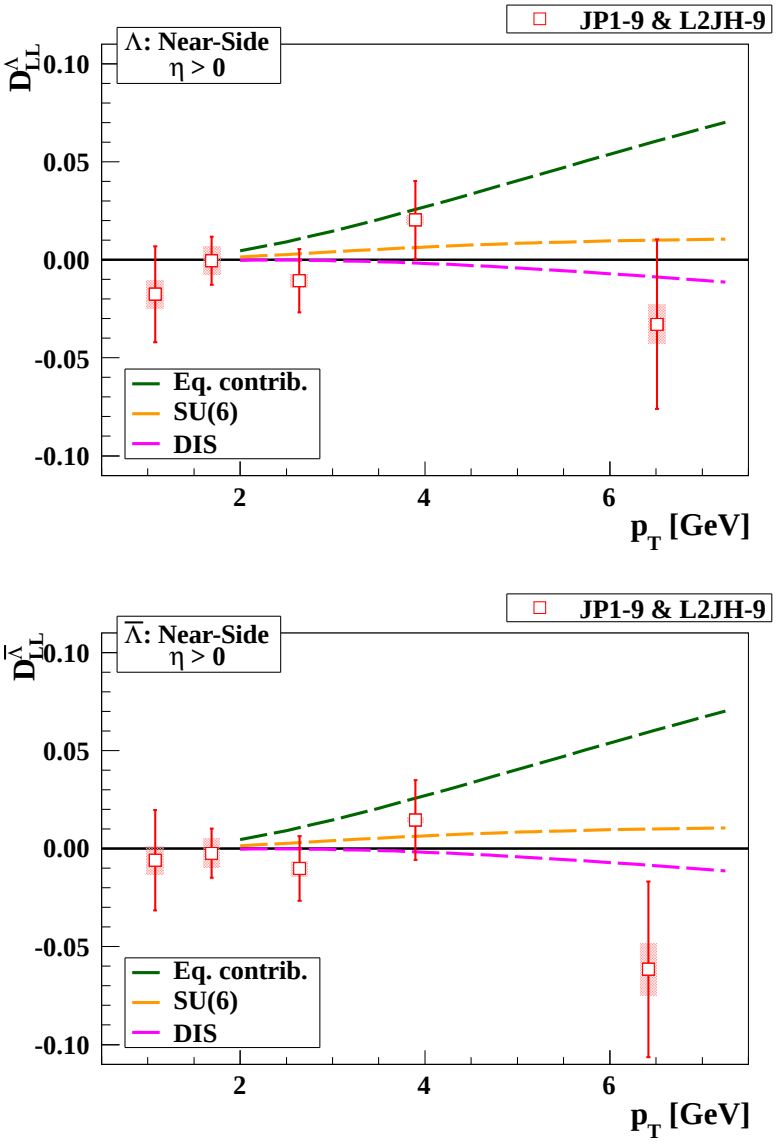

Figure 4.23: Comparison of the model curves of Ref. [Flo98a] and the near-side D_{LL} data at $\eta_{physics} > 0$. The model curves represent the expected D_{LL} values for $\Lambda + \overline{\Lambda}$ sample at average $\eta_{physics} = 0.5$.

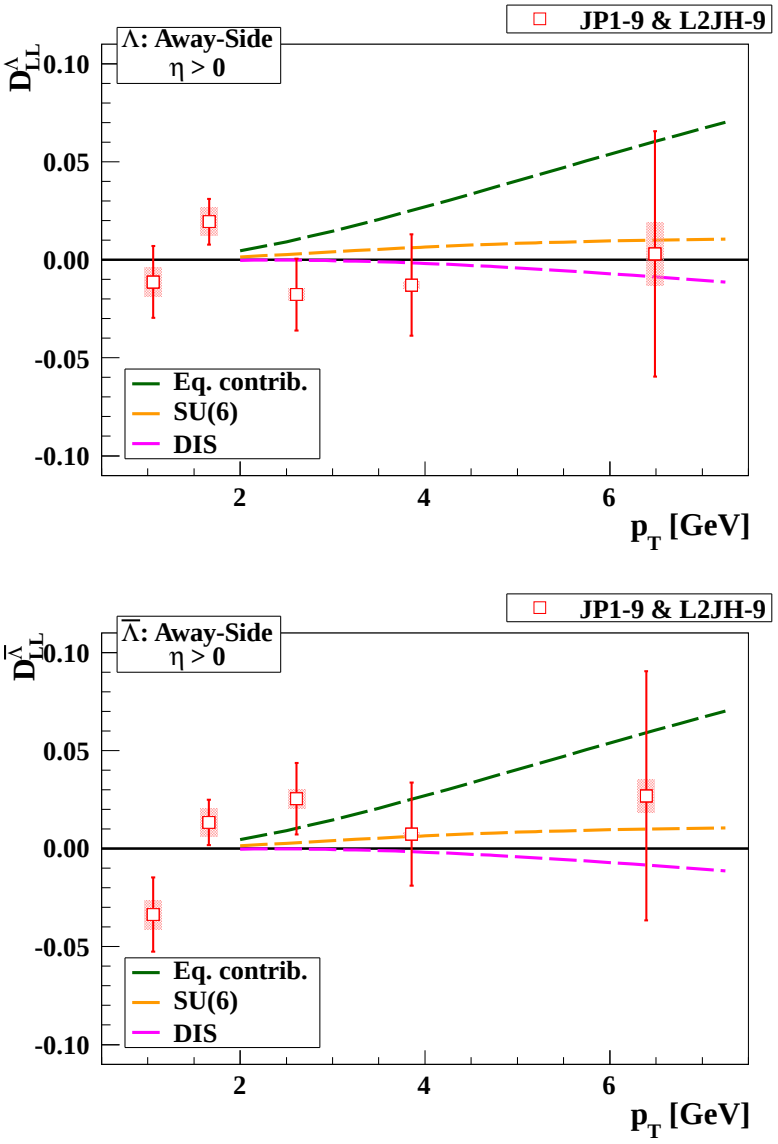

Figure 4.24: Comparison of the model curves of Ref. [Flo98a] and the away-side D_{LL} data at $\eta_{physics} > 0$. The model curves represent the expected D_{LL} values for $\Lambda + \overline{\Lambda}$ sample at average $\eta_{physics} = 0.5$.

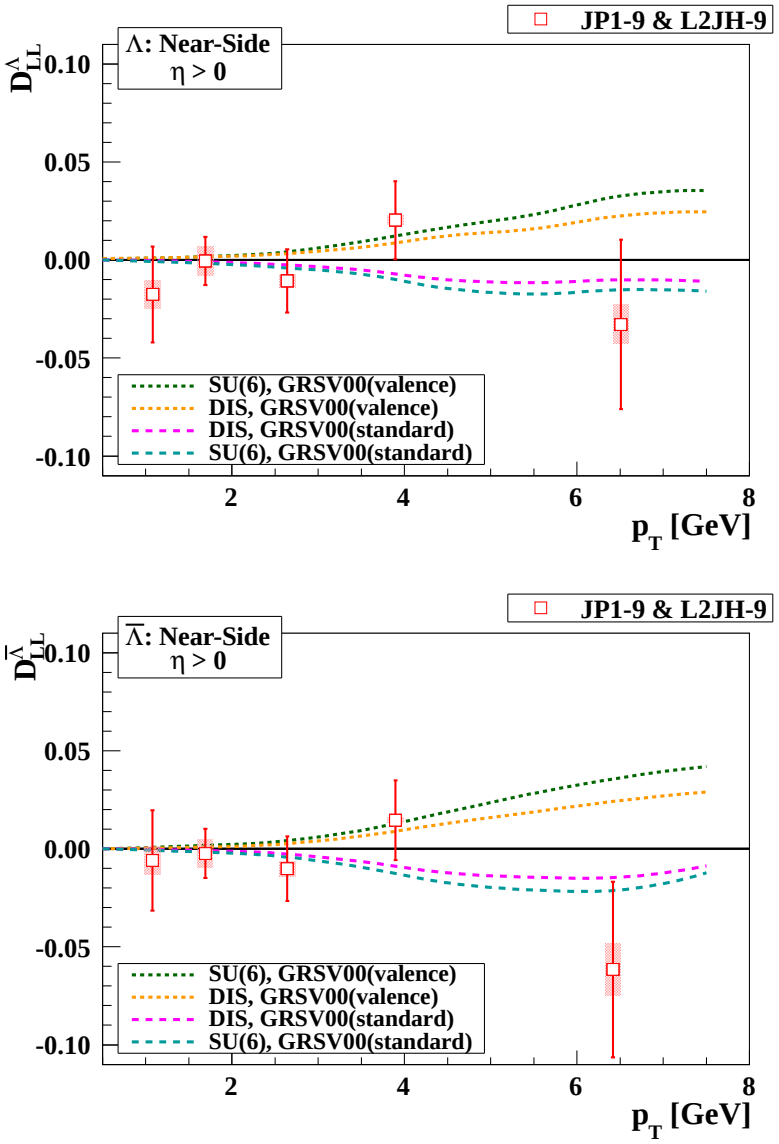

Figure 4.25: Comparison of model curves of Ref. [Xu06] and extracted D_{LL} values for near-side at $\eta_{physics} > 0$. The model curves describe Λ and $\overline{\Lambda}$ separately.

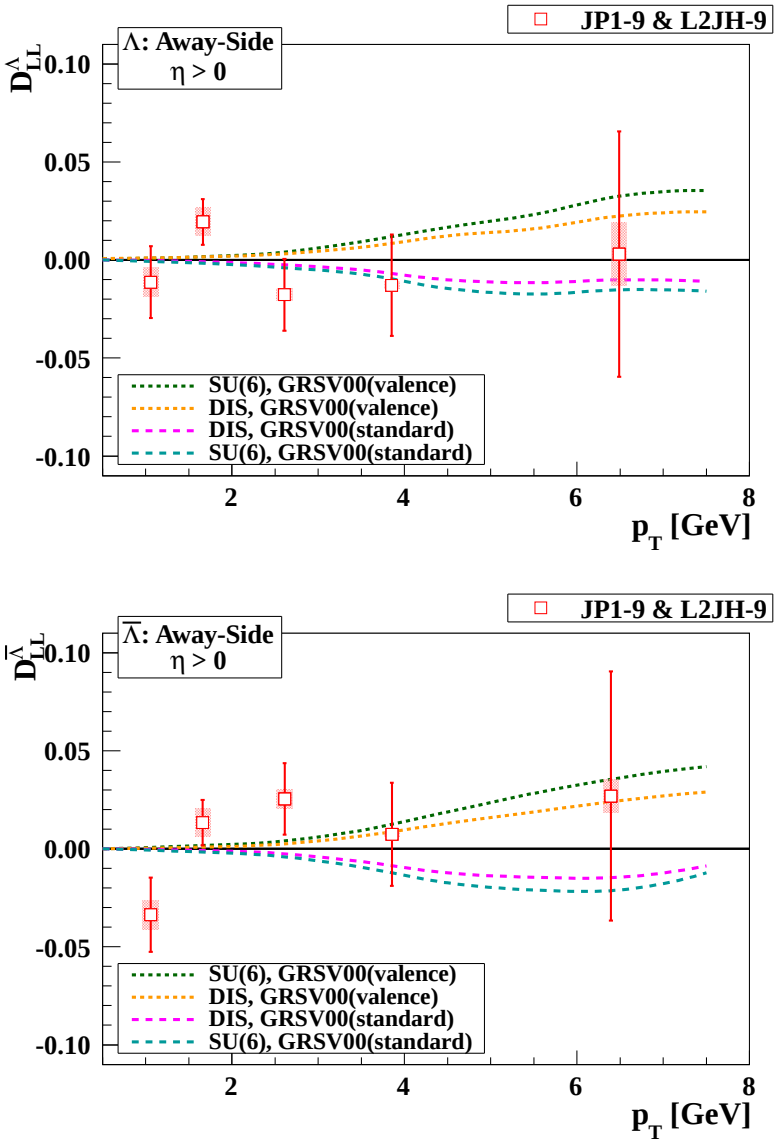

Figure 4.26: Comparison of model curves of Ref. [Xu06] and extracted D_{LL} values for away-side at $\eta_{physics} > 0$. The model curves describe Λ and $\overline{\Lambda}$ separately.

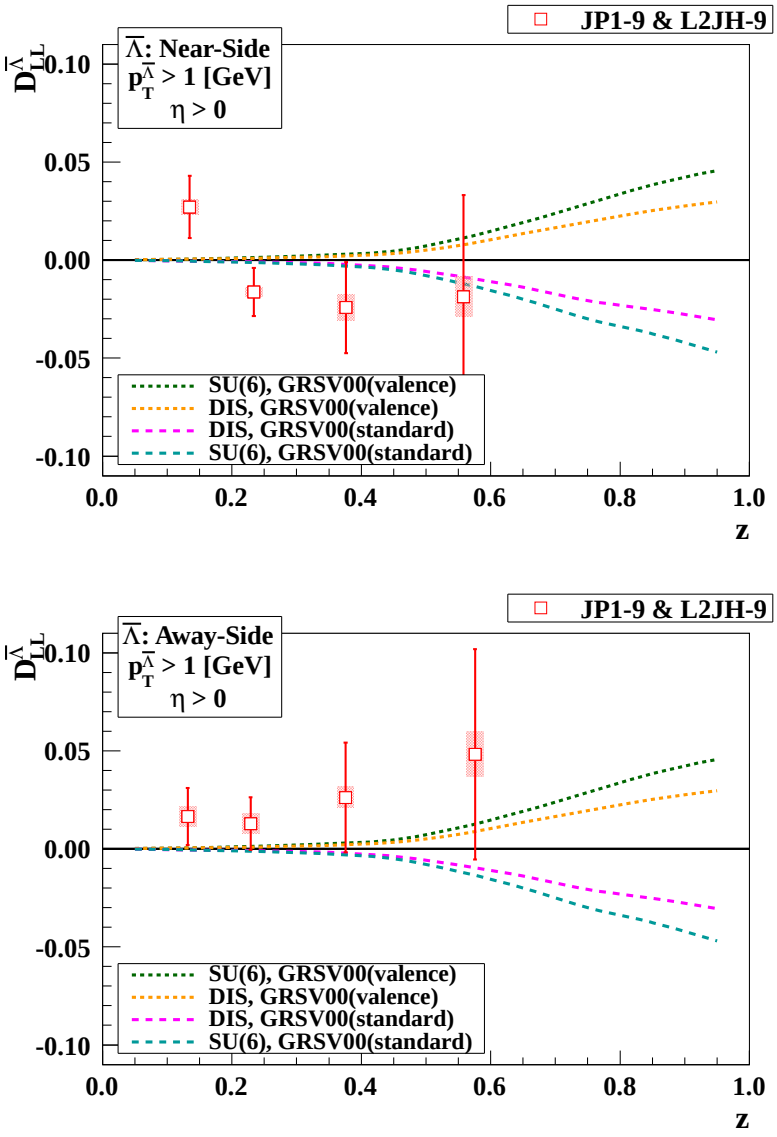

Figure 4.27: Comparison of model curves of Ref. [Xu06] and extracted D_{LL} values for near-side and away-side at $\eta_{physics} > 0$. The model curves describe the $D_{LL}^{\overline{\Lambda}}$ values for $p_T^{\overline{\Lambda}} > 8$ GeV. The $\overline{\Lambda}$ sample was required to satisfy $p_T^{\overline{\Lambda}} > 1$ GeV for extracted $D_{LL}^{\overline{\Lambda}}$ values. The data z intervals are uncorrected.

p_T GeV	(Near-Side) D_{LL}	$\delta D_{LL}^{stat.}$	$\delta D_{LL}^{sys.}$	(Away-Side) D_{LL}	$\delta D_{LL}^{stat.}$	$\delta D_{LL}^{sys.}$
			Λ			
$0.5 \leq p_T < 1.0$	-0.018	0.024	0.007	-0.011	0.018	0.007
$1.0 \leq p_T < 2.0$	-0.001	0.012	0.007	0.019	0.012	0.007
$2.0 \leq p_T < 3.0$	-0.011	0.016	0.003	-0.018	0.018	0.003
$3.0 \leq p_T < 5.0$	0.020	0.020	0.002	-0.013	0.026	0.002
$5.0 \leq p_T$	-0.033	0.043	0.010	0.003	0.063	0.016
			$\overline{\Lambda}$			
$0.5 \leq p_T < 1.0$	-0.006	0.026	0.007	-0.034	0.019	0.007
$1.0 \leq p_T < 2.0$	-0.002	0.012	0.007	0.013	0.012	0.007
$2.0 \leq p_T < 3.0$	-0.010	0.016	0.004	0.025	0.018	0.005
$3.0 \leq p_T < 5.0$	0.015	0.020	0.001	0.007	0.026	0.001
$5.0 \leq p_T$	-0.062	0.045	0.013	0.027	0.064	0.008

Table 4.33: Near-side and away-side values for $D_{LL}^{\Lambda(\overline{\Lambda})}$ extracted from merged $\eta_{physics}$>0 run year 2009 triggered data.

p_T GeV	(Near-Side) D_{LL}	$\delta D_{LL}^{stat.}$	$\delta D_{LL}^{sys.}$	(Away-Side) D_{LL}	$\delta D_{LL}^{stat.}$	$\delta D_{LL}^{sys.}$
			Λ			
$0.0 \leq z < 0.15$	-0.004	0.016	0.004	-0.000	0.015	0.005
$0.15 \leq z < 0.30$	-0.000	0.012	0.002	0.019	0.014	0.003
$0.30 \leq z < 0.45$	-0.018	0.022	0.004	-0.003	0.028	0.001
$0.45 \leq z < 1.0$	0.115	0.051	0.002	-0.071	0.054	0.016
			$\overline{\Lambda}$			
$0.0 \leq z < 0.15$	0.027	0.016	0.004	0.017	0.015	0.005
$0.15 \leq z < 0.30$	-0.016	0.012	0.002	0.013	0.013	0.005
$0.30 \leq z < 0.45$	-0.024	0.023	0.007	0.026	0.028	0.005
$0.45 \leq z < 1.0$	-0.019	0.052	0.010	0.048	0.054	0.011

Table 4.34: Near-side and away-side values from $D_{LL}^{\Lambda(\overline{\Lambda})}$ extracted from merged $\eta_{physics}$>0 for run year 2009. The $D_{LL}^{\Lambda(\overline{\Lambda})}$ values were extracted using $\Lambda(\overline{\Lambda})$ hyperons with $p_T > 1$ GeV . The z interval values are uncorrected.

CHAPTER 5

Summary and Outlook

The EMC observation that the quark spins carry only a small fraction of about 30% of the proton spin has motivated considerable theoretical and experimental efforts to study the nucleon spin. Of particular interest, thus far, have been the flavor decomposition of the quark spin contribution and the contribution of gluon spins. The flavor helicity structure of the polarized nucleon, in particular the strange quark and anti-quark polarization, has been studied in polarized DIS and SIDIS experiments such as HERMES [Air05] and COMPASS [Ale09]. The spin physics program at RHIC [Bun00] has provided stringent constraints on gluon polarization and the effort to determine the up and down quark and anti-quark polarizations through measurements of leptonic W decay has started. Measurements of Λ and $\overline{\Lambda}$ have been proposed to gain insights in the polarization of strange quarks and anti-quarks. The longitudinal spin transfer, D_{LL}, of Λ and $\overline{\Lambda}$ hyperons in longitudinally polarized proton-proton collisions is sensitive to the polarization of strange quarks and anti-quarks in the polarized proton, as well as polarized fragmentation.

The analysis performed in this dissertation focuses on data taken during longitudinally polarized proton-proton collisions at $\sqrt{s} = 200$ GeV for run year 2006 and 2009. It was preceded by a proof-of-concept analysis of 2005 data, which has been published [Abe09]. Improvements for run year 2006 and 2009 include higher integrated luminosities of 6.5 pb^{-1} and 25 pb^{-1} with average beam polarization values of 57%. The completion of the second half of the barrel electromagnetic

calorimeter pseudo-rapidity coverage and DAQ upgrades at STAR increased the trigger acceptance. The tracking and particle identification capabilities of the TPC are used to reconstruct the dominant weak decay channels, $\Lambda \to p + \pi^-$ and $\overline{\Lambda} \to \overline{p} + \pi^+$. Kinematic and geometrical selections were applied and tuned per p_T interval to reduce combinatorial backgrounds, and an improvement in background rejection was achieved compared to the proof-of-concept analysis based on 2005 data. The background of spin-zero K^0_s particles in the $\Lambda(\overline{\Lambda})$ samples results in a non-uniform dilution throughout the $\Lambda(\overline{\Lambda})$ mass spectra, which was also reduced. To sample hard scattering events, hyperons were associated with high p_T jets that triggered the experiment. The jet associated hyperons are separated into two sub-samples, hyperons residing within the cone of the trigger jet are labeled near-side whereas hyperons within a ϕ range opposite to the trigger jet are labeled away-side hyperons. The away-side sample complements the near-side jet associated hyperon sample.

The transfer of longitudinal spin, D_{LL}, from a beam proton to a hyperon produced in association with a jet in longitudinally polarized proton-proton collisions was measured. In addition to D_{LL}, the double longitudinal beam-spin asymmetry, A_{LL}, in the production of hyperons was measured. The run year 2006 sample is of similar size as the published 2005 data sample, and is statistics limited. The run year 2009 data sample is considerably larger. The measurements extend to a hyperon p_T of 7 GeV. A null-measurement of D_{LL} for the more abundantly produced spin-zero K^0_s was found consistent with zero, as expected. The A_{LL} results for Λ and $\overline{\Lambda}$ are systematics limited and provide no evidence for a dependence of the production cross-sections on the proton beam helicity configuration.

The near-side and away-side hyperon samples are analyzed for positive and negative physics pseudo-rapidity. The near-side forward longitudinal spin transfer

is measured to be $D_{LL}^{\Lambda} = -0.03 \pm 0.04_{stat} \pm 0.01_{syst}$ and $D_{LL}^{\overline{\Lambda}} = -0.06 \pm 0.05_{stat} \pm 0.01_{syst}$ at the highest p_T interval from run year 2009 data. The D_{LL} values for Λ and $\overline{\Lambda}$ are consistent with each other and with the results from earlier run years. The dependence of D_{LL} on p_T, η, and the fragmentation ratio, z, were studied. The ratio z was obtained from the transverse momentum of the $\Lambda(\overline{\Lambda})$ and the transverse momentum of the trigger jet with no corrections made for jet energy scale or resolution. The near-side forward longitudinal spin transfer for $z \simeq 0.5$ is measured to be $D_{LL}^{\Lambda} = 0.12 \pm 0.05_{stat} \pm 0.01_{syst}$ and $D_{LL}^{\overline{\Lambda}} = -0.02 \pm 0.05_{stat} \pm 0.01_{syst}$ from run year 2009 data. No conclusive dependence on p_T or z is observed. The data remain mostly statistics limited.

The D_{LL} data were compared with the numerical values from the model calculations in Refs. [Flo98a] and [Xu06]. The $D_{LL}^{\Lambda+\overline{\Lambda}}$ model calculations from [Flo98a] were re-evaluated as a function of p_T for the analysis at $\sqrt{s} = 200$ GeV with updated fragmentation functions. The largest measured p_T interval from forward near-side Λ and $\overline{\Lambda}$ are below the three model curves in Refs. [Flo98a]. Although the model curves describe $\Lambda + \overline{\Lambda}$, the measured D_{LL} from Λ and $\overline{\Lambda}$ at highest p_T each disfavor the model scenario in which the up, down, and strange quark spins contribute equally to the polarized $\Lambda + \overline{\Lambda}$ fragmentation. The model curves in [Xu06] are evaluated separately for Λ and $\overline{\Lambda}$ as a function of p_T and trigger jet $p_T > 5.0$ GeV. The current precision of the data, however, does not allow conclusive discrimination between these models.

The D_{LL} data from run year 2009 improve the precision by a factor of 4–5 compared to the previously published results from 2005 in the region of overlap and extend to larger hyperon p_T of 7 GeV. A further increase in statistics is required to further discriminate between the various model predictions. The model predictions of Ref. [Flo98a] predict that D_{LL} increases with higher forward

physics pseudo-rapidities. The inclusion of the Endcap Electromagnetic Calorimeter (EEMC) [All03] in a future analysis may make it possible to slightly extend the acceptance range. Polarized proton-proton collisions have been achieved at higher center-of-mass energies of $\sqrt{s} = 500$ GeV at RHIC and STAR has successfully recorded and reconstructed particles at this center-of-mass energy. Very significant data samples at this energy are anticipated from run year 2012 and 2013. Furthermore, the addition of a Forward Hadron Calorimeter (FHC) to STAR would make it possible to directly trigger on the decay products of the Λs with large transverse momenta [Bla09]. Model curves exist for D_{LL} for the relevant pseudo-rapidities of up to 3.5 [Zho10] and predict asymmetries at the level of several percent. In this case, the Λ hyperons are reconstructed from $\Lambda \to n + \pi^0$ and $\overline{\Lambda} \to \overline{n} + \pi^0$ decays where the π^0s will be detected with the existing Forward Meson Spectrometer (FMS) and the (anti-)neutrons with the FHC upgrade to STAR.

APPENDIX A

Run Indices

A.1 Run Indices Year 2006

1::7132001	19::7133019	37::7133066	55::7134055	73::7136033
2::7132005	20::7133022	38::7133068	56::7134056	74::7136034
3::7132007	21::7133025	39::7134001	57::7134065	75::7136035
4::7132009	22::7133035	40::7134005	58::7134066	76::7136039
5::7132010	23::7133036	41::7134006	59::7134067	77::7136040
6::7132018	24::7133039	42::7134007	60::7134068	78::7136041
7::7132023	25::7133041	43::7134009	61::7134072	79::7136042
8::7132026	26::7133043	44::7134013	62::7134074	80::7136045
9::7132027	27::7133044	45::7134015	63::7134075	81::7136073
10::7132062	28::7133045	46::7134026	64::7134076	82::7136075
11::7132066	29::7133046	47::7134027	65::7135003	83::7136076
12::7132068	30::7133047	48::7134030	66::7135004	84::7136079
13::7132071	31::7133049	49::7134043	67::7136017	85::7136080
14::7133008	32::7133050	50::7134046	68::7136022	86::7136084
15::7133009	33::7133052	51::7134047	69::7136023	87::7137012
16::7133011	34::7133053	52::7134048	70::7136024	88::7137013
17::7133012	35::7133064	53::7134049	71::7136027	89::7137035
18::7133018	36::7133065	54::7134052	72::7136031	90::7137036

91::7138001
92::7138002
93::7138003
94::7138004
95::7138008
96::7138009
97::7138010
98::7138011
99::7138012
100::7138017
101::7138029
102::7138032
103::7138034
104::7138043
105::7139017
106::7139018
107::7139019
108::7139022
109::7139025
110::7139031
111::7139032
112::7139033
113::7139034
114::7139035
115::7139036
116::7139037
117::7139043
118::7140007
119::7140008
120::7140009
121::7140010
122::7140011
123::7140014
124::7140015
125::7140016
126::7140017
127::7140018
128::7140022
129::7140023
130::7140024
131::7140042
132::7140045
133::7140046
134::7140051
135::7140052
136::7141010
137::7141011
138::7141015
139::7141016
140::7141034
141::7141038
142::7141039
143::7141042
144::7141043
145::7141044
146::7141064
147::7141066
148::7141069
149::7141070
150::7141071
151::7141074
152::7141075
153::7141076
154::7141077
155::7142001
156::7142005
157::7142016
158::7142017
159::7142018
160::7142022
161::7142024
162::7142025
163::7142028
164::7142029
165::7142033
166::7142034
167::7142035
168::7142036
169::7142045
170::7142046
171::7142047
172::7142048
173::7142049
174::7142059
175::7142060
176::7142061
177::7143001
178::7143004
179::7143005
180::7143006
181::7143007
182::7143008
183::7143011
184::7143012
185::7143013
186::7143014
187::7143025
188::7143043
189::7143044
190::7143047
191::7143049
192::7143054
193::7143055
194::7143056
195::7143057
196::7143060
197::7144009
198::7144011
199::7144014
200::7144015
201::7144018
202::7145007
203::7145009
204::7145010
205::7145013
206::7145017
207::7145018
208::7145019
209::7145022
210::7145023
211::7145024
212::7145025
213::7145026
214::7145030
215::7145057
216::7145064
217::7145067
218::7145068
219::7145069
220::7145070
221::7146001
222::7146004
223::7146006
224::7146008
225::7146009

226::7146017	245::7148027	264::7149026	283::7153103	302::7155042
227::7146019	246::7148028	265::7150005	284::7154004	303::7155043
228::7146020	247::7148032	266::7150007	285::7154005	304::7155044
229::7146024	248::7148036	267::7150008	286::7154044	305::7155046
230::7146025	249::7148037	268::7150013	287::7154047	306::7155048
231::7146066	250::7148054	269::7152035	288::7154051	307::7155052
232::7146067	251::7148057	270::7152037	289::7154052	308::7155053
233::7146068	252::7148059	271::7152049	290::7154068	309::7156006
234::7146069	253::7148063	272::7152051	291::7154069	310::7156010
235::7146075	254::7148064	273::7152062	292::7154070	311::7156017
236::7146076	255::7148065	274::7153001	293::7155009	312::7156018
237::7146077	256::7148066	275::7153002	294::7155010	313::7156019
238::7146078	257::7148067	276::7153008	295::7155011	314::7156024
239::7147052	258::7149003	277::7153014	296::7155013	315::7156025
240::7147055	259::7149004	278::7153015	297::7155016	316::7156026
241::7147083	260::7149005	279::7153021	298::7155018	317::7156027
242::7148014	261::7149018	280::7153025	299::7155019	318::7156028
243::7148020	262::7149019	281::7153032	300::7155022	
244::7148024	263::7149023	282::7153035	301::7155023	

A.2 Run Indices Year 2009

1::10120063	5::10120082	9::10120097	13::10121020	17::10121040
2::10120065	6::10120085	10::10120100	14::10121022	18::10121043
3::10120078	7::10120086	11::10121001	15::10121029	19::10121044
4::10120079	8::10120093	12::10121017	16::10121039	20::10121045

21::10121051
22::10121052
23::10121053
24::10122006
25::10122007
26::10122010
27::10122013
28::10122014
29::10122015
30::10122016
31::10122017
32::10122019
33::10122022
34::10122023
35::10122024
36::10122025
37::10122031
38::10122047
39::10122048
40::10122049
41::10122050
42::10122054
43::10122055
44::10122060
45::10122061
46::10122065
47::10122067
48::10122071
49::10122072
50::10122074
51::10122075
52::10122086
53::10122087
54::10122095
55::10122099
56::10123004
57::10123007
58::10123010
59::10123013
60::10123015
61::10123016
62::10123017
63::10123019
64::10123022
65::10123023
66::10123024
67::10123086
68::10123087
69::10123088
70::10123090
71::10124013
72::10124014
73::10124024
74::10124025
75::10124026
76::10124037
77::10124038
78::10124044
79::10124045
80::10124046
81::10124049
82::10124050
83::10124053
84::10124055
85::10124057
86::10124110
87::10124111
88::10124113
89::10125001
90::10125008
91::10125009
92::10125010
93::10125014
94::10125015
95::10125016
96::10125017
97::10125022
98::10125023
99::10125024
100::10125026
101::10125027
102::10125075
103::10125076
104::10125080
105::10125083
106::10125091
107::10126003
108::10126004
109::10126005
110::10126012
111::10126016
112::10126017
113::10126018
114::10126019
115::10126024
116::10126025
117::10126026
118::10126083
119::10126084
120::10126087
121::10126088
122::10126089
123::10126090
124::10127007
125::10127008
126::10127009
127::10127011
128::10128041
129::10128043
130::10128046
131::10128047
132::10128048
133::10128049
134::10128050
135::10128052
136::10128053
137::10128054
138::10128055
139::10128056
140::10128059
141::10128060
142::10128061
143::10128063
144::10128065
145::10128066
146::10128070
147::10128072
148::10128094
149::10128098
150::10128099
151::10128100
152::10128101
153::10128102
154::10129003
155::10129005

156::10129006 183::10134086 210::10135083 237::10136077 264::10139007
157::10129007 184::10134101 211::10136001 238::10136078 265::10139008
158::10129008 185::10134102 212::10136010 239::10136079 266::10139009
159::10129011 186::10134103 213::10136011 240::10136092 267::10139010
160::10131029 187::10135001 214::10136012 241::10136096 268::10139014
161::10131030 188::10135002 215::10136017 242::10136097 269::10139015
162::10131031 189::10135005 216::10136019 243::10136099 270::10139017
163::10131034 190::10135006 217::10136020 244::10136100 271::10139018
164::10131039 191::10135007 218::10136021 245::10137003 272::10141008
165::10131040 192::10135008 219::10136024 246::10137004 273::10141010
166::10131041 193::10135009 220::10136025 247::10137006 274::10141013
167::10131043 194::10135011 221::10136026 248::10137008 275::10141018
168::10131045 195::10135016 222::10136027 249::10137045 276::10141019
169::10131047 196::10135017 223::10136028 250::10137046 277::10141020
170::10131052 197::10135018 224::10136029 251::10137048 278::10141023
171::10134021 198::10135058 225::10136030 252::10137049 279::10141025
172::10134024 199::10135059 226::10136031 253::10138047 280::10141026
173::10134025 200::10135063 227::10136035 254::10138049 281::10141027
174::10134026 201::10135064 228::10136036 255::10138052 282::10141030
175::10134027 202::10135065 229::10136037 256::10138053 283::10141031
176::10134028 203::10135066 230::10136061 257::10138054 284::10141032
177::10134030 204::10135070 231::10136063 258::10138055 285::10142011
178::10134035 205::10135072 232::10136069 259::10138098 286::10142029
179::10134036 206::10135076 233::10136070 260::10138099 287::10142031
180::10134037 207::10135077 234::10136071 261::10138100 288::10142034
181::10134044 208::10135081 235::10136073 262::10139002 289::10142035
182::10134085 209::10135082 236::10136074 263::10139003 290::10142036

291::10142041 318::10143054 345::10144027 372::10145012 399::10146047
292::10142042 319::10143058 346::10144028 373::10145013 400::10146048
293::10142043 320::10143062 347::10144029 374::10145016 401::10146049
294::10142044 321::10143063 348::10144030 375::10145018 402::10146050
295::10142047 322::10143064 349::10144034 376::10145027 403::10146051
296::10142050 323::10143065 350::10144035 377::10145030 404::10146052
297::10142056 324::10143076 351::10144036 378::10145032 405::10146054
298::10142057 325::10143077 352::10144037 379::10145034 406::10146055
299::10142058 326::10143078 353::10144038 380::10145036 407::10146073
300::10143007 327::10143082 354::10144044 381::10145038 408::10146084
301::10143008 328::10143083 355::10144045 382::10145042 409::10146086
302::10143009 329::10143085 356::10144046 383::10145046 410::10146087
303::10143014 330::10143086 357::10144072 384::10145047 411::10146091
304::10143015 331::10143090 358::10144074 385::10145070 412::10147124
305::10143018 332::10143092 359::10144075 386::10145071 413::10148002
306::10143023 333::10143095 360::10144076 387::10145072 414::10148005
307::10143025 334::10143098 361::10144083 388::10145073 415::10148006
308::10143026 335::10143099 362::10144085 389::10145076 416::10148021
309::10143027 336::10143102 363::10144086 390::10145078 417::10148025
310::10143029 337::10143103 364::10144087 391::10145079 418::10148026
311::10143043 338::10143104 365::10144090 392::10145081 419::10148027
312::10143044 339::10143106 366::10144091 393::10145082 420::10148028
313::10143045 340::10144001 367::10144092 394::10145083 421::10148033
314::10143047 341::10144002 368::10144093 395::10146040 422::10148034
315::10143051 342::10144003 369::10144098 396::10146041 423::10148035
316::10143052 343::10144022 370::10144099 397::10146043 424::10149001
317::10143053 344::10144026 371::10145011 398::10146046 425::10149008

426::10149012 453::10150056 480::10154060 507::10156090 534::10158047
427::10149023 454::10150057 481::10154061 508::10156092 535::10158048
428::10149024 455::10151001 482::10154064 509::10156093 536::10158049
429::10149025 456::10151002 483::10154065 510::10156095 537::10158050
430::10149026 457::10151003 484::10154066 511::10156096 538::10158051
431::10149028 458::10151004 485::10154067 512::10157001 539::10158054
432::10149031 459::10151005 486::10154068 513::10157004 540::10158055
433::10149032 460::10151006 487::10154069 514::10157005 541::10158074
434::10149033 461::10151034 488::10154083 515::10157015 542::10158075
435::10149034 462::10151035 489::10155001 516::10157016 543::10158076
436::10149035 463::10151039 490::10155010 517::10157019 544::10158079
437::10149036 464::10151040 491::10155014 518::10157020 545::10158080
438::10150005 465::10151041 492::10155015 519::10157021 546::10158082
439::10150008 466::10151042 493::10155016 520::10157022 547::10158083
440::10150009 467::10151043 494::10155018 521::10157023 548::10158086
441::10150010 468::10151044 495::10155019 522::10157027 549::10158087
442::10150011 469::10151045 496::10155020 523::10158010 550::10158089
443::10150012 470::10151046 497::10155022 524::10158013 551::10158090
444::10150013 471::10151047 498::10156031 525::10158014 552::10159006
445::10150018 472::10152001 499::10156034 526::10158015 553::10159039
446::10150021 473::10152004 500::10156037 527::10158016 554::10159040
447::10150022 474::10152005 501::10156038 528::10158017 555::10159044
448::10150024 475::10152006 502::10156039 529::10158018 556::10159045
449::10150025 476::10152007 503::10156040 530::10158021 557::10159046
450::10150051 477::10152008 504::10156058 531::10158042 558::10159048
451::10150052 478::10152009 505::10156086 532::10158043 559::10159049
452::10150053 479::10152010 506::10156087 533::10158046 560::10160005

561::10160006 588::10161021 615::10164002 642::10165077 669::10167048
562::10160009 589::10161025 616::10164009 643::10165078 670::10167049
563::10160010 590::10161026 617::10164010 644::10165079 671::10167050
564::10160011 591::10161027 618::10164011 645::10165080 672::10167053
565::10160012 592::10161030 619::10164013 646::10165081 673::10167054
566::10160013 593::10162024 620::10164016 647::10166001 674::10167056
567::10160014 594::10162025 621::10164017 648::10166003 675::10167057
568::10160016 595::10162028 622::10164018 649::10166012 676::10167058
569::10160017 596::10162029 623::10164025 650::10166021 677::10167059
570::10160069 597::10162030 624::10164026 651::10166022 678::10167067
571::10160071 598::10162031 625::10164029 652::10166023 679::10167068
572::10160072 599::10162032 626::10164030 653::10166024 680::10167069
573::10160075 600::10162033 627::10164031 654::10166025 681::10169005
574::10160077 601::10162034 628::10164034 655::10166026 682::10169006
575::10160078 602::10162035 629::10165041 656::10166027 683::10169009
576::10160079 603::10162036 630::10165042 657::10166061 684::10169010
577::10160081 604::10162037 631::10165043 658::10166067 685::10169011
578::10160084 605::10162038 632::10165046 659::10167007 686::10169012
579::10161005 606::10162040 633::10165047 660::10167008 687::10169013
580::10161006 607::10163048 634::10165049 661::10167009 688::10169014
581::10161010 608::10163051 635::10165050 662::10167012 689::10169021
582::10161011 609::10163052 636::10165051 663::10167013 690::10169030
583::10161014 610::10163053 637::10165052 664::10167014 691::10169031
584::10161015 611::10163054 638::10165053 665::10167015 692::10169032
585::10161016 612::10163055 639::10165054 666::10167016 693::10169033
586::10161019 613::10163056 640::10165057 667::10167017 694::10169041
587::10161020 614::10163059 641::10165070 668::10167020 695::10169042

696::10169043 723::10170029 750::10171043 777::10172077 804::10174044
697::10169044 724::10170045 751::10171044 778::10172079 805::10174045
698::10169047 725::10170046 752::10171045 779::10172082 806::10174048
699::10169048 726::10170047 753::10171048 780::10172083 807::10174049
700::10169049 727::10170050 754::10171060 781::10172085 808::10174050
701::10169065 728::10170052 755::10171061 782::10172089 809::10174051
702::10169070 729::10170053 756::10171068 783::10172090 810::10174052
703::10169074 730::10170054 757::10171069 784::10172094 811::10174093
704::10169075 731::10170060 758::10171070 785::10173031 812::10174094
705::10169076 732::10170061 759::10171071 786::10173032 813::10175001
706::10169077 733::10170064 760::10171078 787::10173033 814::10175005
707::10169078 734::10170065 761::10172001 788::10173039 815::10175008
708::10169079 735::10171008 762::10172002 789::10173046 816::10175009
709::10169080 736::10171009 763::10172003 790::10173048 817::10175010
710::10170003 737::10171011 764::10172007 791::10173051 818::10175011
711::10170011 738::10171014 765::10172018 792::10173053 819::10175012
712::10170012 739::10171015 766::10172021 793::10173055 820::10175013
713::10170013 740::10171016 767::10172023 794::10174012 821::10175014
714::10170016 741::10171019 768::10172054 795::10174013 822::10175019
715::10170017 742::10171021 769::10172055 796::10174016 823::10175038
716::10170018 743::10171022 770::10172056 797::10174021 824::10176001
717::10170019 744::10171025 771::10172057 798::10174023 825::10176008
718::10170020 745::10171034 772::10172058 799::10174025 826::10176016
719::10170023 746::10171036 773::10172059 800::10174026 827::10176017
720::10170024 747::10171037 774::10172060 801::10174027 828::10176018
721::10170025 748::10171041 775::10172061 802::10174028 829::10176020
722::10170026 749::10171042 776::10172064 803::10174031 830::10176022

831::10176025 841::10178026 851::10179010 861::10179044 871::10180007

832::10176028 842::10178029 852::10179018 862::10179045 872::10180021

833::10177014 843::10178036 853::10179019 863::10179085 873::10180022

834::10177016 844::10178037 854::10179022 864::10179086 874::10180027

835::10177017 845::10179002 855::10179031 865::10179088 875::10180028

836::10177018 846::10179005 856::10179032 866::10179096 876::10180029

837::10177019 847::10179006 857::10179033 867::10179097 877::10180030

838::10177022 848::10179007 858::10179036 868::10179098

839::10178022 849::10179008 859::10179042 869::10180003

840::10178023 850::10179009 860::10179043 870::10180004

APPENDIX B

Analysis Run Lists

B.1 Run Year 2006

7132001	7133022	7134001	7134065	7136035	7138003	7139034	7140042
7132005	7133025	7134005	7134066	7136039	7138004	7139035	7140045
7132007	7133035	7134006	7134067	7136040	7138008	7139036	7140046
7132009	7133036	7134007	7134068	7136041	7138009	7139037	7140051
7132010	7133039	7134009	7134072	7136042	7138010	7139043	7140052
7132018	7133041	7134013	7134074	7136045	7138011	7140007	7141010
7132023	7133043	7134015	7134075	7136073	7138012	7140008	7141011
7132026	7133044	7134026	7134076	7136075	7138017	7140009	7141015
7132027	7133045	7134027	7135003	7136076	7138029	7140010	7141016
7132062	7133046	7134030	7135004	7136079	7138032	7140011	7141038
7132066	7133047	7134043	7136017	7136080	7138034	7140014	7141039
7132068	7133049	7134046	7136022	7136084	7138043	7140015	7141042
7132071	7133050	7134047	7136023	7137012	7139018	7140016	7141043
7133008	7133052	7134048	7136024	7137013	7139019	7140017	7141064
7133011	7133064	7134049	7136027	7137035	7139025	7140018	7141066
7133012	7133065	7134052	7136031	7137036	7139031	7140022	7141069
7133018	7133066	7134055	7136033	7138001	7139032	7140023	7141070
7133019	7133068	7134056	7136034	7138002	7139033	7140024	7141071

7141074	7142048	7143056	7145057	7146075	7148066	7153008	7155018
7141075	7142049	7143057	7145064	7146076	7148067	7153014	7155019
7141076	7142060	7143060	7145067	7146077	7149003	7153015	7155022
7141077	7142061	7144011	7145068	7146078	7149004	7153021	7155023
7142001	7143001	7144014	7145069	7147052	7149005	7153025	7155042
7142005	7143004	7144015	7145070	7147055	7149018	7153032	7155043
7142016	7143005	7144018	7146001	7147083	7149019	7153035	7155044
7142017	7143006	7145007	7146004	7148020	7149023	7153103	7155048
7142018	7143007	7145009	7146006	7148024	7149026	7154004	7155052
7142022	7143008	7145010	7146008	7148027	7150005	7154005	7156006
7142024	7143011	7145013	7146009	7148028	7150007	7154051	7156010
7142025	7143012	7145017	7146017	7148032	7150008	7154052	7156017
7142028	7143013	7145018	7146019	7148036	7150013	7154068	7156018
7142029	7143014	7145019	7146020	7148037	7152035	7154069	7156019
7142033	7143025	7145022	7146024	7148054	7152037	7154070	7156024
7142034	7143044	7145023	7146025	7148057	7152049	7155009	7156025
7142035	7143047	7145024	7146066	7148059	7152051	7155010	7156026
7142045	7143049	7145025	7146067	7148063	7152062	7155011	7156027
7142046	7143054	7145026	7146068	7148064	7153001	7155013	
7142047	7143055	7145030	7146069	7148065	7153002	7155016	

B.2 Run Year 2009

10120063	10120079	10120086	10120100	10121020	10121039	10121044
10120065	10120082	10120093	10121001	10121022	10121040	10121045
10120078	10120085	10120097	10121017	10121029	10121043	10121051

10121052	10122072	10124037	10125076	10128046	10129007	10134101
10121053	10122074	10124038	10125080	10128047	10129008	10134102
10122006	10122075	10124044	10125083	10128048	10129011	10134103
10122007	10122086	10124045	10125091	10128049	10131029	10135001
10122010	10122087	10124046	10126003	10128050	10131030	10135002
10122013	10122095	10124049	10126004	10128052	10131031	10135005
10122014	10122099	10124050	10126005	10128053	10131034	10135006
10122015	10123004	10124053	10126012	10128054	10131039	10135007
10122016	10123007	10124055	10126016	10128055	10131040	10135008
10122017	10123010	10124057	10126017	10128056	10131041	10135009
10122019	10123013	10124110	10126018	10128059	10131043	10135011
10122022	10123015	10124111	10126019	10128060	10131045	10135016
10122023	10123016	10124113	10126024	10128061	10131047	10135017
10122024	10123017	10125001	10126025	10128063	10131052	10135018
10122025	10123019	10125008	10126026	10128065	10134021	10135058
10122031	10123022	10125009	10126083	10128066	10134024	10135059
10122047	10123023	10125010	10126084	10128070	10134025	10135063
10122048	10123024	10125014	10126087	10128072	10134026	10135064
10122049	10123086	10125015	10126088	10128094	10134027	10135065
10122050	10123087	10125016	10126089	10128098	10134028	10135066
10122054	10123088	10125017	10126090	10128099	10134030	10135070
10122055	10123090	10125022	10127007	10128100	10134035	10135072
10122060	10124013	10125023	10127008	10128101	10134036	10135076
10122061	10124014	10125024	10127009	10128102	10134037	10135077
10122065	10124024	10125026	10127011	10129003	10134044	10135081
10122067	10124025	10125027	10128041	10129005	10134085	10135082
10122071	10124026	10125075	10128043	10129006	10134086	10135083

10136001	10136078	10139008	10142044	10143063	10144030	10145034
10136010	10136079	10139009	10142047	10143064	10144034	10145036
10136011	10136092	10139010	10142050	10143065	10144035	10145038
10136012	10136096	10139014	10142056	10143076	10144036	10145042
10136017	10136097	10139015	10142057	10143077	10144037	10145046
10136019	10136099	10139017	10142058	10143078	10144044	10145047
10136020	10136100	10139018	10143007	10143082	10144045	10145070
10136021	10137003	10141008	10143008	10143083	10144046	10145071
10136024	10137004	10141010	10143009	10143085	10144072	10145072
10136025	10137006	10141013	10143014	10143086	10144074	10145073
10136026	10137008	10141018	10143015	10143090	10144075	10145076
10136027	10137045	10141019	10143018	10143092	10144076	10145078
10136028	10137046	10141020	10143023	10143095	10144083	10145079
10136029	10137048	10141023	10143025	10143098	10144085	10145081
10136030	10137049	10141025	10143026	10143099	10144087	10145082
10136031	10138047	10141026	10143027	10143102	10144090	10145083
10136035	10138049	10141027	10143029	10143103	10144091	10146040
10136036	10138052	10141030	10143043	10143104	10144092	10146043
10136037	10138053	10141031	10143044	10143106	10144093	10146046
10136061	10138054	10141032	10143045	10144001	10145011	10146047
10136063	10138055	10142031	10143047	10144002	10145012	10146048
10136069	10138098	10142034	10143051	10144003	10145013	10146049
10136070	10138099	10142035	10143052	10144022	10145016	10146050
10136071	10138100	10142036	10143053	10144026	10145018	10146051
10136073	10139002	10142041	10143054	10144027	10145027	10146052
10136074	10139003	10142042	10143058	10144028	10145030	10146054
10136077	10139007	10142043	10143062	10144029	10145032	10146055

10146073	10149034	10151040	10155016	10157023	10158089	10160084
10146084	10149035	10151042	10155018	10157027	10158090	10161005
10146086	10150005	10151043	10155019	10158010	10159006	10161006
10146087	10150008	10151044	10155020	10158013	10159039	10161010
10146091	10150009	10151045	10155022	10158014	10159040	10161011
10147124	10150010	10151046	10156031	10158015	10159044	10161015
10148002	10150011	10151047	10156034	10158016	10159045	10161016
10148005	10150012	10152001	10156038	10158017	10159046	10161019
10148006	10150013	10152004	10156039	10158018	10159048	10161020
10148021	10150021	10152005	10156040	10158021	10159049	10161021
10148025	10150022	10152006	10156058	10158042	10160005	10161025
10148026	10150024	10152007	10156086	10158043	10160006	10161026
10148027	10150025	10152008	10156087	10158047	10160009	10161027
10148028	10150051	10152009	10156090	10158048	10160010	10161030
10148033	10150052	10152010	10156092	10158049	10160011	10162024
10148034	10150053	10154060	10156093	10158050	10160012	10162025
10148035	10150056	10154061	10156095	10158051	10160013	10162028
10149008	10150057	10154064	10156096	10158054	10160014	10162029
10149012	10151001	10154065	10157001	10158055	10160016	10162030
10149023	10151002	10154066	10157004	10158075	10160017	10162031
10149024	10151003	10154067	10157005	10158076	10160071	10162032
10149025	10151004	10154068	10157015	10158079	10160072	10162033
10149026	10151005	10154083	10157016	10158080	10160075	10162034
10149028	10151006	10155001	10157019	10158082	10160077	10162035
10149031	10151034	10155010	10157020	10158083	10160078	10162036
10149032	10151035	10155014	10157021	10158086	10160079	10162037
10149033	10151039	10155015	10157022	10158087	10160081	10162038

10162040	10165051	10167013	10169030	10170019	10171034	10172085
10163048	10165052	10167014	10169031	10170020	10171036	10172089
10163051	10165053	10167015	10169032	10170023	10171037	10172090
10163052	10165054	10167016	10169033	10170024	10171041	10172094
10163053	10165057	10167017	10169041	10170025	10171042	10173031
10163054	10165070	10167020	10169042	10170026	10171043	10173032
10163055	10165077	10167048	10169043	10170029	10171044	10173033
10163056	10165078	10167049	10169044	10170045	10171045	10173039
10163059	10165079	10167050	10169047	10170046	10171048	10173046
10164002	10165080	10167053	10169048	10170047	10171060	10173048
10164009	10165081	10167054	10169049	10170050	10171061	10173051
10164010	10166001	10167056	10169065	10170052	10171068	10173053
10164011	10166003	10167057	10169070	10170053	10171069	10173055
10164013	10166012	10167058	10169074	10170054	10171070	10174012
10164016	10166021	10167059	10169075	10170060	10171071	10174013
10164017	10166022	10167067	10169076	10170061	10171078	10174016
10164025	10166023	10167068	10169077	10170064	10172001	10174021
10164026	10166024	10167069	10169078	10170065	10172002	10174023
10164029	10166025	10169005	10169079	10171008	10172003	10174025
10164030	10166026	10169006	10169080	10171011	10172007	10174026
10164031	10166027	10169009	10170003	10171014	10172060	10174027
10164034	10166061	10169010	10170011	10171015	10172061	10174028
10165041	10166067	10169011	10170012	10171016	10172064	10174031
10165043	10167007	10169012	10170013	10171019	10172077	10174044
10165046	10167008	10169013	10170016	10171021	10172079	10174045
10165047	10167009	10169014	10170017	10171022	10172082	10174048
10165050	10167012	10169021	10170018	10171025	10172083	10174049

10174050	10175011	10176018	10178022	10179008	10179042	10180004
10174051	10175012	10176020	10178023	10179009	10179043	10180007
10174052	10175013	10176022	10178026	10179010	10179044	10180021
10174093	10175014	10176025	10178029	10179018	10179045	10180022
10174094	10175019	10176028	10178036	10179019	10179086	10180027
10175001	10175038	10177016	10178037	10179022	10179088	10180028
10175005	10176001	10177017	10179002	10179031	10179096	10180029
10175008	10176008	10177018	10179005	10179032	10179097	10180030
10175009	10176016	10177019	10179006	10179033	10179098	
10175010	10176017	10177022	10179007	10179036	10180003	

APPENDIX C

Fill Indices

C.1 Fill Indices Year 2006: JP1–6

1::7847	6::7855	11::7871	16::7889	21::7896	26::7911	31::7922	36::7952
2::7850	7::7856	12::7872	17::7890	22::7898	27::7913	32::7926	37::7954
3::7851	8::7863	13::7883	18::7891	23::7901	28::7916	33::7944	38::7957
4::7852	9::7864	14::7886	19::7892	24::7908	29::7918	34::7949	
5::7853	10::7865	15::7887	20::7893	25::7909	30::7921	35::7951	

C.2 Fill Indices Year 2009: JP1–9

1::10685	11::10712	21::10761	31::10789	41::10855	51::10889	61::10935
2::10688	12::10713	22::10763	32::10790	42::10866	52::10890	62::10937
3::10689	13::10729	23::10773	33::10791	43::10869	53::10904	63::10951
4::10690	14::10746	24::10777	34::10800	44::10870	54::10919	64::10952
5::10695	15::10748	25::10781	35::10806	45::10876	55::10920	65::10953
6::10700	16::10753	26::10782	36::10814	46::10877	56::10921	66::10954
7::10703	17::10754	27::10783	37::10820	47::10878	57::10926	67::10955
8::10704	18::10755	28::10784	38::10825	48::10880	58::10928	68::10959
9::10706	19::10756	29::10785	39::10826	49::10881	59::10930	69::10960
10::10708	20::10758	30::10786	40::10854	50::10884	60::10932	70::10961

71::10963	73::10968	75::10971	77::10986	79::10995	81::11002	83::11005
72::10964	74::10970	76::10973	78::10987	80::11001	82::11003	84::11006

C.3 Fill Indices Year 2009: L2JH–9

1::10682	14::10708	27::10773	40::10814	53::10881	66::10937	79::10971
2::10683	15::10712	28::10777	41::10820	54::10884	67::10951	80::10973
3::10684	16::10713	29::10781	42::10825	55::10889	68::10952	81::10986
4::10685	17::10729	30::10782	43::10826	56::10890	69::10953	82::10987
5::10688	18::10746	31::10783	44::10854	57::10904	70::10954	83::10995
6::10689	19::10748	32::10784	45::10855	58::10919	71::10955	84::11001
7::10690	20::10753	33::10785	46::10866	59::10920	72::10959	85::11002
8::10695	21::10754	34::10786	47::10869	60::10921	73::10960	86::11003
9::10696	22::10755	35::10789	48::10870	61::10926	74::10961	87::11005
10::10700	23::10756	36::10790	49::10876	62::10928	75::10963	88::11006
11::10703	24::10758	37::10791	50::10877	63::10930	76::10964	
12::10704	25::10761	38::10800	51::10878	64::10932	77::10968	
13::10706	26::10763	39::10806	52::10880	65::10935	78::10970	

References

[Abe03] J. Abele et al. "The laser system for the STAR time projection chamber." *Nucl.Instrum.Meth.*, **A499**:692–702, 2003.

[Abe07] B.I. Abelev et al. "Strange particle production in $p + p$ collisions at $\sqrt{s} = 200$ GeV." *Phys.Rev.*, **C75**:064901, 2007.

[Abe08] B.I. Abelev et al. "Longitudinal double-spin asymmetry for inclusive jet production in p+p collisions at $\sqrt{s} = 200$ GeV." *Phys.Rev.Lett.*, **100**, 2008.

[Abe09] B. I. Abelev et al. "Longitudinal spin transfer to Λ and $\overline{\Lambda}$ hyperons in polarized proton-proton collisions at $\sqrt{s} = 200$ GeV." *Phys. Rev. D 80*, 2009.

[Ack98] K. Ackerstaff et al. "Polarization and forward-backward asymmetry of Lambda baryons in hadronic Z0 decays." *Eur. Phys. J.*, 1998.

[Air05] A. Airapetian et al. "Quark helicity distributions in the nucleon for up, down, and strange quarks from semi-inclusive deep-inelastic scattering." *Phys.Rev.*, 2005.

[Air08] A. Airapetian et al. "Measurement of Parton Distributions of Strange Quarks in the Nucleon from Charged-Kaon Production in Deep-Inelastic Scattering on the Deuteron." *Phys.Lett.*, **B666**:446–450, 2008.

[Alb05] S. Albino et al. "Fragmentation functions for light charged hadrons with complete quark flavor separation." *Nucl.Phys.*, **B725**:181–206, 2005.

[Alb08] S. Albino et al. "AKK Update: Improvements from New Theoretical Input and Experimental Data." *Nucl.Phys.*, **B803**:42–104, 2008.

[Ale01] I. Alekseev et al. "Configuration Manual Polarized Proton Collider at RHIC." p. 171, 2001.

[Ale03] I. Alekseev et al. "Polarized proton collider at RHIC." *Nucl.Instrum.Meth.*, **A499**:392–414, 2003.

[Ale09] M. Alekseev et al. "Flavour Separation of Helicity Distributions from Deep Inelastic Muon-Deuteron Scattering." *Phys.Lett.*, **B680**:217–224, 2009.

[All03] C.E. Allgower et al. "The STAR endcap electromagnetic calorimeter." *Nucl.Instrum.Meth.*, **A499**:740–750, 2003.

[Ams08] C. Amsler et al. volume B667. 2008.

[And03] M. Anderson et al. "The Star time projection chamber: A Unique tool for studying high multiplicity events at RHIC." *Nucl.Instrum.Meth.*, **A499**:659–678, 2003.

[Ash88] J. Ashman et al. "A Measurement of the Spin Asymmetry and Determination of the Structure Function g_1 in Deep Inelastic Muon-Proton Scattering." *Phys. Lett.*, 1988.

[Ash89] J. Ashman et al. "An investigation of the spin structure of the proton in deep inelastic scattering of polarised muons on polarised protons." *Nucl. Phys.*, 1989.

[Bai03] M. Bai et al. "RHIC beam instrumentation." *Nucl.Instrum.Meth.*, **A499**:372–387, 2003.

[Baz07] A. Bazilevsky et al. "Single Transverse-Spin Asymmetry in Very Forward and Very Backward Neutral Particle Production for Polarized Proton Collisions at $\sqrt{s} = 200$ GeV." *Phys.Lett.*, **B650**:325–330, 2007.

[Bed03] M. Beddo et al. "The STAR barrel electromagnetic calorimeter." *Nucl.Instrum.Meth.*, **A499**:725–739, 2003.

[Ber03] F. Bergsma et al. "The STAR detector magnet subsystem." *Nucl.Instrum.Meth.*, **A499**:633–639, 2003.

[Bit09] M.B. Bitters et al. "SN0480 : Analysis of STAR ZDC SMD Data for Polarimetry.", 2009. http://drupal.star.bnl.gov/STAR/starnotes/public/sn0480.

[Bjo69] J.D. Bjorken. "Asymptotic Sum Rules at Infinite Momentum." *Phys.Rev.*, **179**:1547–1553, 1969.

[Bla00] Gerald C. Blazeya et al. "Run II Jet Physics." *arXiv:hep-ex/0005012v2*, 2000.

[Bla09] L.C. Bland et al. "FHC proposal update.", 2009. http://drupal.star.bnl.gov/STAR/system/files/ upgrade_documents_nu_memo_091005.pdf.

[Bor98a] C. Boros et al. "Spin content of Lambda and its longitudinal polarization in e+ e- annihilation at high-energies." *Phys.Rev.*, **D57**:4491–4494, 1998.

[Bor98b] C. Boros et al. "Spin content of Lambda and its longitudinal polarization in e^+e^- annihilation at high-energies." *Phys.Rev.*, **D57**:4491–4494, 1998.

[Bor00] C. Boros et al. "Lambda polarization in polarized proton proton collisions at RHIC." *Phys.Rev.*, 2000.

[Bou83] M. Bourquin et al. "Measurements of Hyperon Semileptonic Decays at the CERN Super Proton Synchrotron. 4. Tests of the Cabibbo Model." *Z.Phys.*, **C21**:27, 1983.

[Bun00] Gerry Bunce et al. "Prospects for spin physics at RHIC." *Ann.Rev.Nucl.Part.Sci.*, **50**, 2000.

[Cal68] C.G. Callan et al. "Crucial Test of a Theory of Currents." *Phys.Rev.Lett.*, **21**:311–313, 1968.

[Che08] Ye Chen et al. "Anti-Hyperon polarization in high energy pp collisions with polarized beams." *Phys.Rev.*, 2008.

[Clo88] F.E. Close et al. "The Spin Content of the Proton." *Phys.Rev.Lett.*, **60**:1471, 1988.

[Clo93] F.E. Close et al. "Consistent analysis of the spin content of the nucleon." *Phys.Lett.*, **B316**:165–171, 1993.

[Col88] John C. Collins et al. "Factorization of Hard Processes in QCD." *Adv.Ser.Direct.High Energy Phys.*, **5**, 1988.

[Col93] John C. Collins. "Hard scattering in QCD with polarized beams." *Nucl.Phys.*, **B394**:169–199, 1993.

[Cor02] T.M. Cormier et al. "STAR barrel electromagnetic calorimeter absolute calibration using 'minimum ionizing particles' from collisions at RHIC." *Nucl.Instrum.Meth.*, **A483**:734–746, 2002.

[Cro63] James W. Cronin et al. "Measurement of the decay parameters of the Λ^0 particle." *Phys.Rev.*, 1963.

[Cro00] D. Cronin-Hennessy et al. "Luminosity monitoring and measurement at CDF." *Nucl.Instrum.Meth.*, **443**:37–50, 2000.

[Eis57] F. Eisler et al. "Demonstration of Parity Nonconservation in Hyperon Decay." *Phys. Rev.*, 1957.

[Ell74] John R. Ellis et al. "A Sum Rule for Deep Inelastic Electroproduction from Polarized Protons." *Phys.Rev.*, **D9**, 1974.

[Eys07] K.O. Eyser et al. "Absolute polarization measurements at RHIC in the Coulomb nuclear interference region." *AIP Conf.Proc.*, **915**:916–919, 2007.

[Fie05] Rick Field et al. "PYTHIA tune A, HERWIG, and JIMMY in Run 2 at CDF." *hep-ph/0510198*, 2005.

[Flo98a] Daniel de Florian et al. "Polarized Lambda baryon production in p p collisions." *Phys.Rev.Lett.*, **81**:530–533, 1998.

[Flo98b] Daniel de Florian et al. "QCD analysis of unpolarized and polarized Lambda baryon production in leading and next-to-leading order." *Phys.Rev.*, **D57**:5811–5824, 1998.

[Flo05] Daniel de Florian et al. "Sea quark and gluon polarization in the nucleon at NLO accuracy." *Phys.Rev.*, **D71**:094018, 2005.

[Flo09] Daniel de Florian et al. "Extraction of Spin-Dependent Parton Densities and Their Uncertainties." *Phys.Rev.*, **D80**:034030, 2009.

[G01] M. Glück, , et al. "Models for the polarized parton distributions of the nucleon." *Phys. Rev. D*, **63**, 2001.

[Goo93] Michel Goossens et al. *GEANT Detector Description and Simulation Tool*, 1993.

[Gro11a] CNI Polarimeter Group. "Run06Offline." 2011. http://www4.rcf.bnl.gov/čnipol/pubdocs/Run06Offline/NOTE_2006_Polarizations_RHIC.txt.

[Gro11b] CNI Polarimeter Group. "Run09Offline." 2011. http://www4.rcf.bnl.gov/čnipol/pubdocs/Run09Offline/NOTE_2009_Polarizations_RHIC.txt.

[Has09] D. Hasch. "The spin of the nucleon from the HERMES point of view." *Nucl.Phys.Proc.Suppl.*, **191**:79–87, 2009.

[Hay11] James Hays-Wehle et al. "PSN0528 : 2009 Relative Luminosity at STAR at $\sqrt{s} = 200$ GeV Draft v1.2.", 2011. http://drupal.star.bnl.gov/STAR/starnotes/private/psn0528.

[Hil86] H.J. Hilke. "Detector calibration with lasers-A review." *Nucl.Instrum.Meth.*, **252**:169–179, 1986.

[Hsu88] S.Y. Hsueh et al. "A High Precision Measurement of Polarized Sigma-beta Decay." *Phys.Rev.*, 1988.

[Hua94] H. Huang et al. "Preservation of Proton Polarization by a Partial Siberian Snake." *Phys. Rev. Lett.*, **73**:2982–2985, 1994.

[Hua08] H. Huang et al. "p-Carbon CNI Polarimetry in the AGS and RHIC." *Conf.Proc.*, **C0806233**:TUPC039, 2008.

[Ji97] Xiang-Dong Ji. "Gauge-invariant decomposition of nucleon spin and its spin-off." *Phys.Rev.Lett.*, **78**:610–613, 1997.

[Jin04] O. Jinnouchi et al. "Measurement of the analyzing power of proton-carbon elastic scattering in the CNI region at RHIC." pp. 515–518, 2004.

[Kir03] Joanna Kiryluk. "Relative luminosity measurement in STAR and implications for spin asymmetry determinations." *AIP Conf.Proc.*, **675**:424–428, 2003.

[Kir05] Joanna Kiryluk. "Local polarimetry for proton beams with the STAR beam beam counters." pp. 718–721, 2005.

[Kur02] K. Kurita. "Proton carbon CNI polarimeter for RHIC." *Nucl.Phys.Proc.Suppl.*, **105**:164–167, 2002.

[Lai00] H.L. Lai et al. "Global QCD analysis of parton structure of the nucleon: CTEQ5 parton distributions." *Eur.Phys.J.*, **C12**:375–392, 2000.

[Lan05] J. Landgraf et al. "Proposal for the TPC Electronics and Data Acquisition Upgrade for STAR DAQ1000.", 2005. http://drupal.star.bnl.gov/STAR/files/future/proposals/daq1000-3-22-2005.pdf.

[Lea06] Elliot Leader et al. "Longitudinal polarized parton densities updated." *Phys.Rev.*, **D73**:034023, 2006.

[Leb02] A. Lebedev. "A laser calibration system for the STAR TPC." *Nucl.Instrum.Meth.*, **A478**:163–165, 2002.

[Lee57] T. D. Lee et al. "General Partial Wave Analysis of the Decay of a Hyperon of Spin ." *Phys. Rev.*, 1957.

[Nad08] Pavel M. Nadolsky et al. "Implications of CTEQ global analysis for collider observables." *Phys.Rev.*, **D78**:013004, 2008.

[Nak08a] I. Nakagawa et al. "p-carbon polarimetry at RHIC." *AIP Conf.Proc.*, **980**:380–389, 2008.

[Nak08b] I. Nakagawa et al. "RHIC polarimetry." *Eur.Phys.J.ST*, **162**:259–265, 2008.

[Oka00] M. Okamura et al. "Half-length model of a Siberian Snake magnet for RHIC." *Nucl.Instrum.Meth.*, **A452**:53–60, 2000.

[Oka06a] H. Okada et al. "Measurement of the analyzing power A(N) in pp elastic scattering in the CNI region with a polarized atomic hydrogen gas jet target." 2006.

[Oka06b] H. Okada et al. "Measurement of the analyzing power in pp elastic scattering in the peak CNI region at RHIC." *Phys.Lett.*, **B638**:450–454, 2006.

[Oka08] H. Okada et al. "Absolute polarimetry at RHIC." *AIP Conf.Proc.*, **980**:370–379, 2008.

[par87] *Introduction to Elementary Particles*. John Wiley & Sons, 1987.

[par00] *Introduction to High Energy Physics*. Cambridge University Press, 2000.

[Pod94] J. Podolanski et al. "Analysis of V-Events." *The Philosophical Magazine*, **45**, 1594.

[Rus07] T. Russo et al. "The RHIC hydrogen jet luminescence monitor." *Particle Accelerator Conference, 2007. PAC. IEEE*, pp. 2648–2652, 2007.

[Sai01] N. Saito. "Spin Physics Program at RHIC: The First Polarized-Proton Collider." *Nucl.Phys.*, **A698**:275–286, 2001.

[Sak11] Tai Sakuma et al. "Run-6 Relative Luminosity at STAR.", 2011. http://scripts.mit.edu/r̃hic/scaler/2006/prelim_release2.shtml.

[Sas07] Murad Sasrour et al. "Relative luminosity systematic.", 2007. http://cyclotron.tamu.edu/star/2006Jets/jul31_2007/.

[See11] Joseph Seele et al. "Relative Luminosity Studies.", 2011. http://drupal.star.bnl.gov/STAR/blog/seelej/2011/feb/01/relative-luminosity-studies-viii.

[Sj06] Torbjrn Sjstrand et al. *PYTHIA 6.4 Physics and Manual*, 2006.

[Ste77] George F. Sterman et al. "Jets from Quantum Chromodynamics." *Phys.Rev.Lett.*, **39**, 1977.

[Tan86] Ching-Hua Tan. *Inclusive Production of Strange Particles at CERN Proton-Antiproton Collider*. PhD thesis, Wuhan University, 1986.

[Tog08] Manabu Togawa. *Measurements of the leading neutron production in polarized pp collision at* $\sqrt{s}$ *= 200* GeV. PhD thesis, Kyoto University, 2008.

[Whi08] C.A. Whitten. "The beam-beam counter: A local polarimeter at STAR." *AIP Conf.Proc.*, **980**:390–396, 2008.

[Xu06] Qing-hua Xu et al. "Anti-lambda polarization in high energy pp collisions with polarized beam." *Phys.Rev.*, **D73**, 2006.

[Xu09] Qinghua Xu et al. "Analysis Note: Longitudinal spin transfer to Λ and $\overline{\Lambda}$ hyperons in polarized proton-proton collisions at $\sqrt{s}$ = 200 GeV." 2009.

[Zel05] A. Zelenski et al. "Absolute polarized H-jet polarimeter development, for RHIC." *Nucl.Instrum.Meth.*, **A536**:248–254, 2005.

[Zel07] Anatoli Zelenski. "Optically-pumped polarized electron, H^- (proton), deuteron and $^3He^{++}$ ion source development at BNL." *AIP Conf.Proc.*, **915**:987–991, 2007.

[Zho10] Wei Zhou et al. "The longitudinal polarization of hyperons in the forward region in polarized *pp* collisions." *Phys.Rev.*, **D81**, 2010.